Accretion and Star Formation in Quasars

Sarah Virginia White

New College

Department of Physics

University of Oxford

A thesis submitted for the degree of

Doctor of Philosophy

Trinity Term, 2015

Abstract

Accretion and Star Formation in Quasars

Sarah Virginia White

New College, University of Oxford

Submitted for the degree of Doctor of Philosophy

Trinity Term, 2015

Studying the interplay of accretion and star formation is crucial to our understanding of galaxy evolution. The new generation of radio surveys are able to play a key role in this area, since both processes produce radio emission. As we probe low radio-luminosities, the two main populations are star-forming galaxies and radio-quiet quasars (RQQs). How they contribute to the total radio emission is under debate, with previous authors arguing that star formation dominates. In this thesis I investigate the relative levels of radio emission due to accretion and star formation in RQQs.

Firstly, I select a sample of 74 quasars from the VISTA Deep Extragalactic Observations (VIDEO) survey, whose depth allows me to study very low accretion rates and/or lower-mass black holes. By comparing radio emission from the quasars with that from a control sample of galaxies, and calculating two independent estimates of star-formation rate, I show that this emission is predominantly related to the accretion process. A second sample of 72 RQQs is obtained from the *Spitzer-Herschel* Active Galaxy Survey, spanning a factor of ∼100 in optical luminosity over a narrow redshift range at $z \sim 1$. This enables evolutionary effects to be decoupled when comparisons are made with the VIDEO sample. I reduce radio data from the Karl G. Jansky Very Large Array (JVLA) for these objects, and find further support that accretion makes a significant contribution to the radio emission in RQQs. In addition, the levels of accretion and star formation appear to be weakly correlated with each other, and with optical luminosity.

These findings offer an insight into how the mechanisms behind galaxy evolution may interact differently in RQQs compared to their radio-loud counterparts. They also have important implications for modelling radio populations below 1 mJy, which is necessary for the development of the Square Kilometre Array.

This thesis is dedicated to my Mum and Dad,
for their continued support and inspiring influence.
I also wish to dedicate this work to my former supervisor,
the late Steve Rawlings, whose enthusiasm I will always cherish.

Acknowledgements

First and foremost I'd like to thank my supervisor, Matt Jarvis, who has been excellent fun to work with and a true fountain of knowledge. This includes knowing when to give me a little nudge of encouragement, and when to let me get on with things(!). I'm ever so grateful that you accepted the job at Oxford, taking me on as a student following an unfortunate start to my DPhil. Thanks also go to Mairi Brookes (a.k.a. "the Boss") for her part, and for playing in the New College MCR cricket team.

Thank you to Jas and Lance, for looking after me during the interim period, and to Paul for being by my side. You've been an awesome-cool office buddy. Special thanks to David, for also getting excited by radio astronomy, answering all my questions, and carefully proof-reading several chapters of this thesis. Danielle, Luke, your cheerfulness has stopped me going crazy at times. Thanks to Will, Tessa and Phil, for acting as mentors, always eager to help. Nikhi, I've loved your little visits and the vegetarian momos that they bring.

A huge hug for Ian, the radio-interferometry ninja, and for Jonathan, who has come to the rescue on many an occasion. High-fives to Aprajita and Ryan, for explaining things when I'm not sure what's going on. Thank you John, for fascinating chats about black holes, and Jocelyn, for putting your pretty pulsar painting outside The Tower office. Also thanks to Vanessa, Ashling, Dan, Eric, Boris, Boon, Aris and Natasha, for your kind words and advice.

Outside of the 'Astro family', thanks go to Fenner, Guy and Fred, for lending an ear. Also to Mum, Dad, Lisa, Emma and Chris, all of whom I love dearly. Last but not least, thanks to Dominic, for giving me my first taste of astrophysics research, and introducing me to Python all those years ago.

Declaration of Authorship

I hereby declare that this thesis, submitted for the degree of *Doctor of Philosophy* at the University of Oxford, is the result of my own work unless stated otherwise.

A part of the research described is based on the following paper:

Chapters 2 and 3 - Sarah V. White, Matt J. Jarvis, Boris Häußler and Natasha Maddox, 2015, MNRAS, Volume 448, Issue 3, p.2665-2686.

Accordingly, each of the sections within these two chapters were written in collaboration, with the exception of Sections 2.3.2 and 2.4.2.

Sarah White

Trinity Term, 2015

Contents

Abbreviations

A list of abbreviations that are used throughout this thesis:

AGN - Active Galactic Nucleus (/Nuclei)

CASA - Common Astronomy Software Applications

FIR - Far-InfraRed

FIRC - Far-Infrared–Radio Correlation

FIRST - Faint Images of the Radio Sky at Twenty-centimetres

FT - Fourier Transform

IFT - Inverse Fourier Transform

ISM - InterStellar Medium

JVLA - Karl G. Jansky Very Large Array

KS - Kolmogorov–Smirnov

PACS - Photodetector Array Camera and Spectrometer

QSO - Quasi-Stellar Object

RFI - Radio-Frequency Interference

RQQ - Radio-Quiet Quasar

SALT - Southern African Large Telescope

SDSS - Sloan Digital Sky Survey

SED - Spectral Energy Distribution

SFR - Star-Formation Rate

SHAGS - *Spitzer-Herschel* Active Galaxy Survey

SKA - Square Kilometre Array

SMBH - Super-Massive Black Hole

SNR - Signal-to-Noise Ratio

SPIRE - Spectral and Photometric Imaging REceiver

ULIRG - Ultra-Luminous InfraRed Galaxy

VIDEO - VISTA Deep Extragalactic Observations

VISTA - Visible and Infrared Survey Telescope for Astronomy

WENSS - WEsterbork Northern Sky Survey

1

Introduction

“Black holes and revelations”

– Muse, *Starlight*

The work presented in this thesis concerns accretion and star formation, as present in quasars. In this introductory chapter I will explain the importance of these two processes for galaxy evolution, and describe studies that argue for and against their interdependence. I will then provide the scientific background for how active galactic nuclei (AGN) and star-forming regions produce radio emission. Radio interferometry enables such emission to be observed with high angular resolution, allowing AGN activity and star-formation histories to be investigated well beyond the local Universe. The theory behind this technique is described in Chapter 4.

1.1 Galaxy evolution

At the start of the 20th century, astronomers were debating the significance of cloud-like objects observed throughout the sky. The uncertainty was over whether they were gas clouds within the Milky Way galaxy or external collections of stars, and therefore galaxies in their own right. The spiral structure of some of these ‘nebulae’ was first recorded by William Parsons in 1845, but it was not until the work of Edwin Hubble that their extragalactic nature could be proven [e.g. Hubble, 1925] and confirmed beyond doubt [Hubble, 1929]. As more and more galaxies were discovered it became necessary to develop classification schemes, based on their appearance, to help understand the variety of shapes and sizes observed. The most enduring of these is Hubble's 'Tuning Fork', in which the majority of galaxies belong to one of two categories: 'ellipticals' and 'spirals' (Figure 1.1). Ellipticals are so-called because of their ellipsoidal shape, and have a brightness profile that varies smoothly with radius. Spirals, meanwhile, have a central concentration of stars (referred to as the 'bulge') around which a flat disc of stars, dust and gas rotates. A subset of these objects have an additional bar-like structure, and so they are named 'barred spirals'. A common misinterpretation [e.g. Masters, 2013] of the Hubble Tuning Fork was that galaxy evolution results in a changing morphology, from left to right along the sequence shown. For this reason, ellipticals are often referred to as 'early-type' galaxies and spirals as 'late-type' galaxies.

In reality it is more likely that spiral galaxies, during a merger, lose the angular momentum associated with their rotation, forming an elliptical galaxy. However, recent simulations show that if there is sufficient gas in the system, or it is replenished by the environment, then it is possible for a disc to reform following either a major [Governato et al., 2009] or a minor [Moster et al., 2010] merger. ('Major' is used to describe a merger where the two interacting bodies are of comparable mass, while the mass ratio in a minor merger is typically >10:1.) The merging of matter is the result of self-similar 'condensation' predicted by the cold dark matter (CDM) model [e.g. Peebles, 1982]. This is where small halos of dark matter collapse due to self-gravitation, followed by their merging into larger halos as illustrated by the halo merger tree in Figure 1.2. These CDM models therefore imply hierarchical structure in the Universe, and with the assumption that the amount of baryonic matter scales with the mass of dark matter, they provide the theoretical base for models of galaxy evolution.

As with any model, its success is judged by how well it is able to reproduce observations of the Universe. Relevant for galaxy evolution, Figure 1.3 illustrates the differences between the luminosity function based on the halo-mass function (the theoretical model) and the observed galaxy-luminosity function. It is clear that the method for incorporating baryonic matter is over-simplistic, as the model predicts both too many faint galaxies and too many bright galaxies. 'Feedback processes' are therefore invoked to explain these

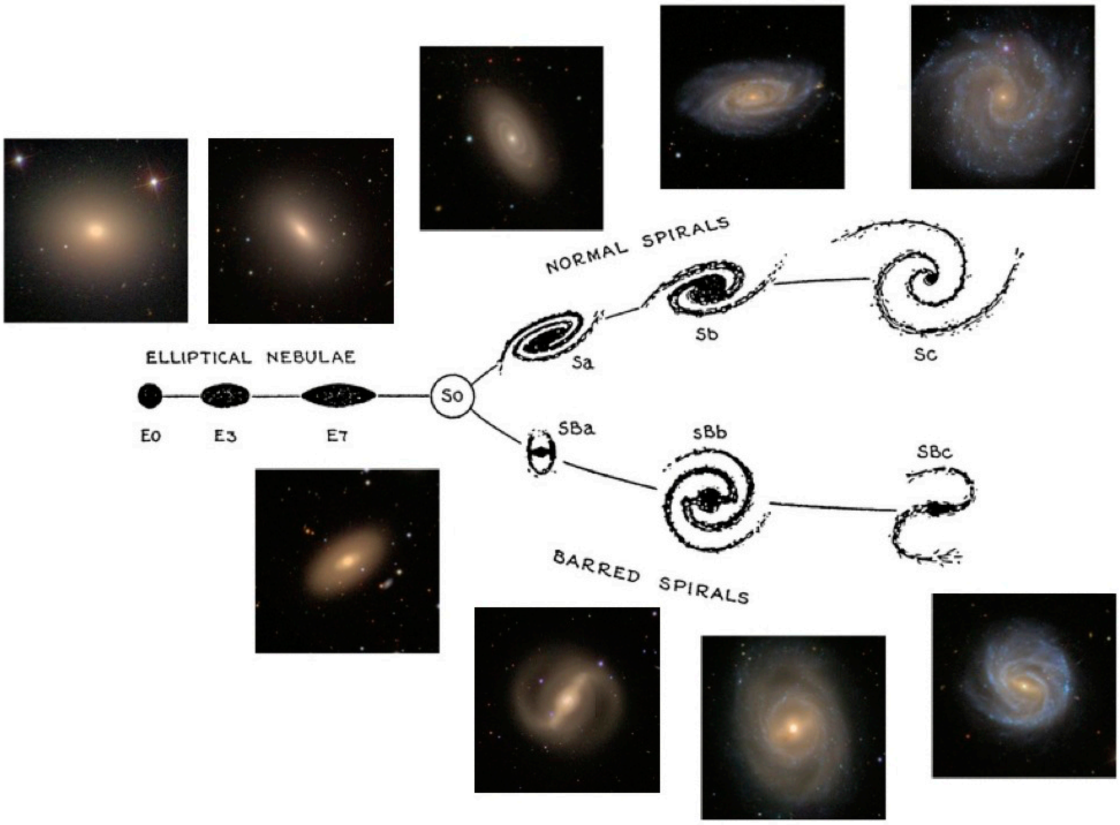

Figure 1.1: The original ‘Hubble Tuning Fork’, as presented in the book *Realm of the Nebulae* [Hubble, 1936], with example images of the different galaxy types from the Sloan Digital Sky Survey (SDSS). The elliptical galaxies on the left-hand side are labelled E0 (the most round in shape) to E7 (the most elliptical). The galaxy type classified as S0 are termed ‘lenticular galaxies’. These are undergoing a transition between elliptical and spiral morphology, having a central bulge and disc but no spiral arms. Towards the right-hand side, along the two spiral branches, the prominence of the bulge decreases and the spiral arms become increasingly open. Another category, ‘irregulars’ (Irr), is not shown in this diagram. These have no symmetric properties and so do not fit into the above sequence. Credit: Masters [2013].

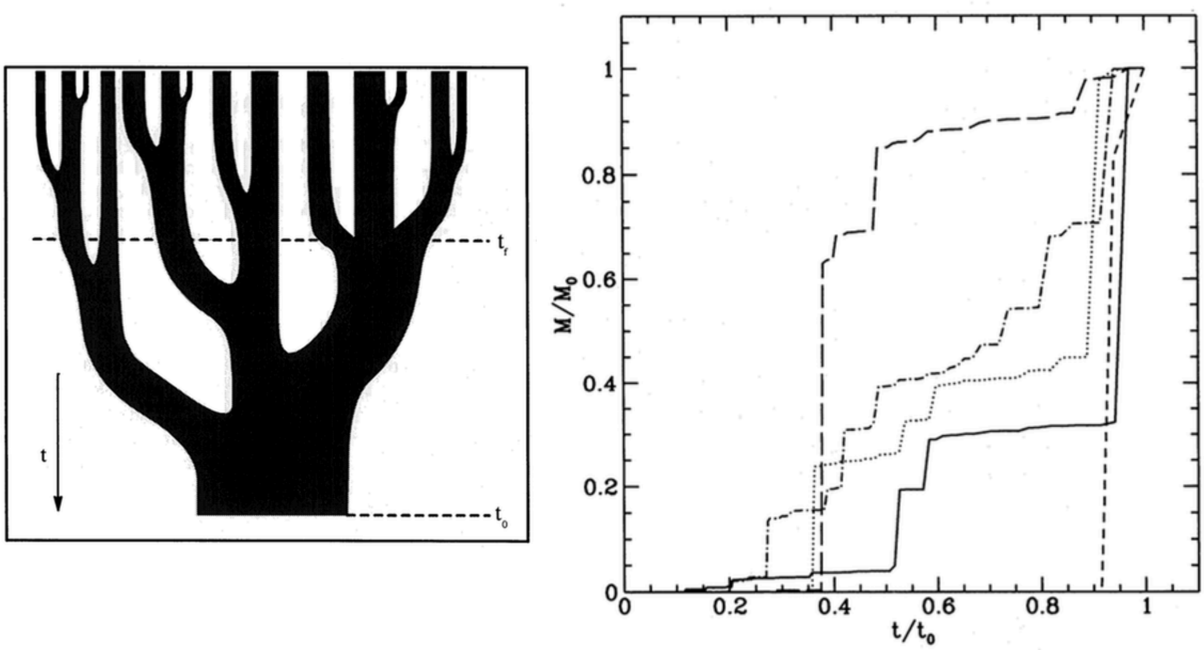

Figure 1.2: An illustration of a halo merger tree (left), with the flow of time indicated by the arrow and the branch width corresponding to the mass of the halo. This therefore shows the progenitors at the time of formation, t_f, and how they merge to form the final halo at the present time, t_0. For a halo constrained to have mass M_0 at time t_0, there are a number of possible trajectories that a particle within the halo may have taken (right). Credit: Lacey and Cole [1993].

discrepancies, which I describe further in the next subsection.

There are two main approaches for modelling galaxy evolution, these being through hydrodynamical simulations and semi-analytic models. In the former, the properties of each particle or 'box' (such as the total mass and angular momentum) are evolved numerically, as prescribed by fluid-dynamic equations. This allows the interaction of gas, stars and black holes to be treated at a very small scale, but such N-body calculations are computationally expensive. Semi-analytic models [e.g. Benson 2012] fare better, in this respect, as they involve modelling baryonic physics on the galactic scale and then combining this in post-processing to purely-analytic models (such as that by Lacey and Cole 1993). The primary disadvantage is that a greater degree of approximation is used, and so this may mask the underlying physics of feedback processes. However, even in current simulations, from the Millennium Simulation [Springel et al., 2005] to the EAGLE (Evolution and Assembly of GaLaxies and their Environments) Project [Schaye et al., 2015], the parameters governing such processes are adjusted post-hoc on a trial-and-error basis. Although this leads to much better agreement with observations, further

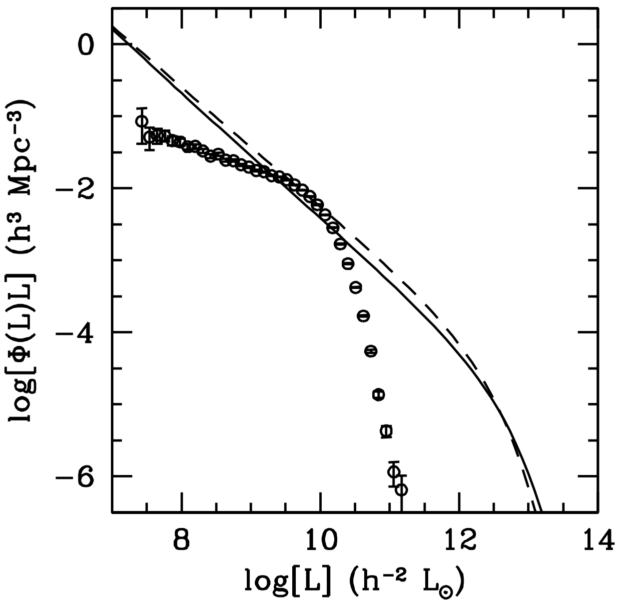

Figure 1.3: A comparison of theoretical and observed galaxy-luminosity functions (LFs), the latter being the 2dFGRS (Two-degree-Field Galaxy Redshift Survey) LF in the b_J band (open circles with error bars). The solid line represents the LF derived from the halo-mass function of Sheth and Tormen [1999], while the dashed line corresponds to the halo-mass function of Press and Schechter [1974]. In both cases it is assumed that there is exactly one galaxy with $M/L = 100h\,(\mathrm{M}_\odot/\mathrm{L}_\odot)$ in each halo, where $h = H_0/(100\,\mathrm{km\,s^{-1}})$. Credit: Yang et al. [2003].

understanding of the exact physical mechanisms is hindered by the computational cost of simulating large cosmological volumes at the required resolution. Instead, the macroscale properties of these mechanisms are parametrised and implemented via a 'black box' of sub-grid physics (where 'grid' refers to the simulation's resolution).

1.1.1 The role of feedback

Feedback, in this case, refers to the secondary effects of physical processes that either promote galaxy growth (i.e. 'positive feedback') or suppress it ('negative feedback'). Note that this growth could be referring to either the supermassive black-hole, thought to be at the centre of every galaxy, or the host galaxy in which the black hole resides. As such, the main mechanisms for growth are black-hole accretion and star formation (respectively), and their interaction is often cited to explain the tightness of the relation between the black-hole mass, M, and the velocity dispersion of the host-galaxy bulge, σ (M–σ; Ferrarese and Merritt 2000; Gebhardt et al. 2000; Figure 1.4). Silk and Rees [1998] proposed a feedback model in which a wind, driven by the black hole, is countering the infalling gas. However the energy associated with the formation of a supermassive black-hole far exceeds that required to unbind the bulge, leading to the normalisation of the M–σ relation being a factor 1000 too small. King [2003] attempted to remedy this by suggesting that the black hole's wind is momentum-driven rather than energy-driven, and so the majority of the output energy is dissipated as radiation. The remainder is then sufficient to balance the inflow of energy, giving the correct normalisation.

Returning to Figure 1.3, the lack of low-mass galaxies in the simulations, compared to observations, is thought to be related to star formation. Halos need to have a minimum mass of $\sim 10^5\,\mathrm{M}_\odot$[Silk, 2011] if they are to have a potential well deep enough to trap baryons and allow them to undergo cooling, eventually forming stars. However, the energetic output from supernovae also has to be considered. These cause material to be easily expelled from low-mass halos, reducing the available gas and thus preventing further stellar-mass growth. Meanwhile, the discrepancy at the high-mass (i.e. bright) end is thought to be due to active galactic nuclei (AGN, Section 1.2). The thermal energy of the accretion disc, and mechanical energy of the jets, cause heating of the halo. As a result, cold molecular clouds may not be able to collapse to form stars, and so this feedback effectively 'quenches' star formation. In this scenario, the AGN has a self-regulating effect on the growth of a galaxy [Silk and Mamon, 2012].

The interplay of accretion and star formation may also be able to explain the phenomenon of 'cosmic downsizing'. In the case of AGN, this is the observation that the fastest-growing black holes were much larger in the early Universe than they are now [Babić et al., 2007; Steffen et al., 2003]. This is likely due to the greater availability of gas, fuelling the accretion, at earlier epochs. The same downsizing trend is seen for the stellar mass of galaxies [Cowie et al. 1996; Figure 1.5], where the typical stellar-mass shifts to lower values at lower redshifts. Clearly this goes against the expected hierarchical structure predicted by theorists. The cause of this trend is the quenching of star formation in the most massive galaxies [Peng et al. 2010; Lilly et al. 2013], which may point towards AGN-related feedback. (See Section 1.3 for further details.)

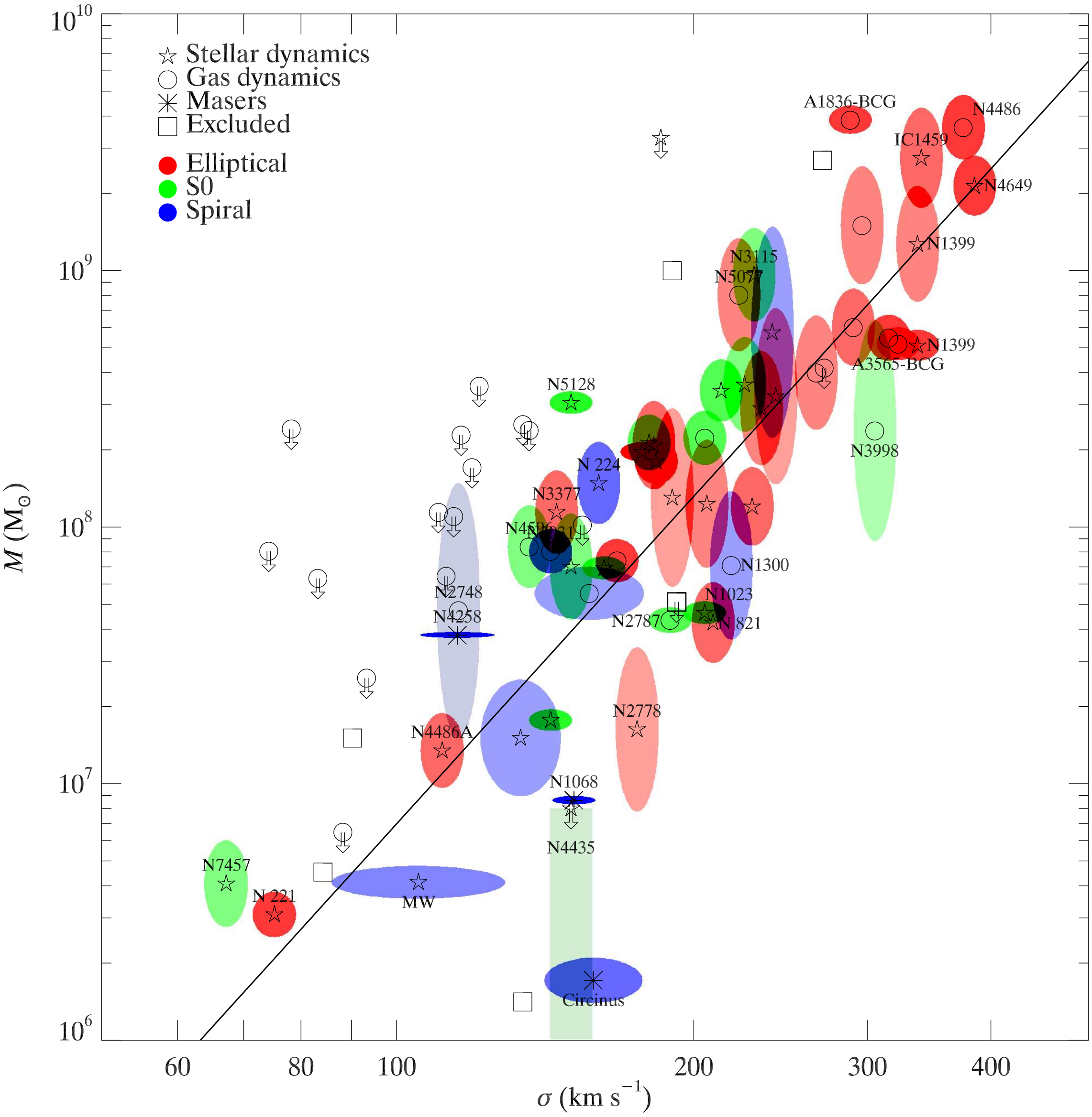

Figure 1.4: The M-σ relation, indicating a connection between the mass of the supermassive black-hole (M) and the velocity dispersion of the host-galaxy bulge (σ). Values of M were measured using various dynamical techniques, as shown by the legend in the top-left corner. Each datapoint is accompanied by an error ellipse, the colour of which represents the host galaxy's Hubble type: elliptical (red), S0 (green) and spiral (blue). Credit: Gültekin et al. [2009].

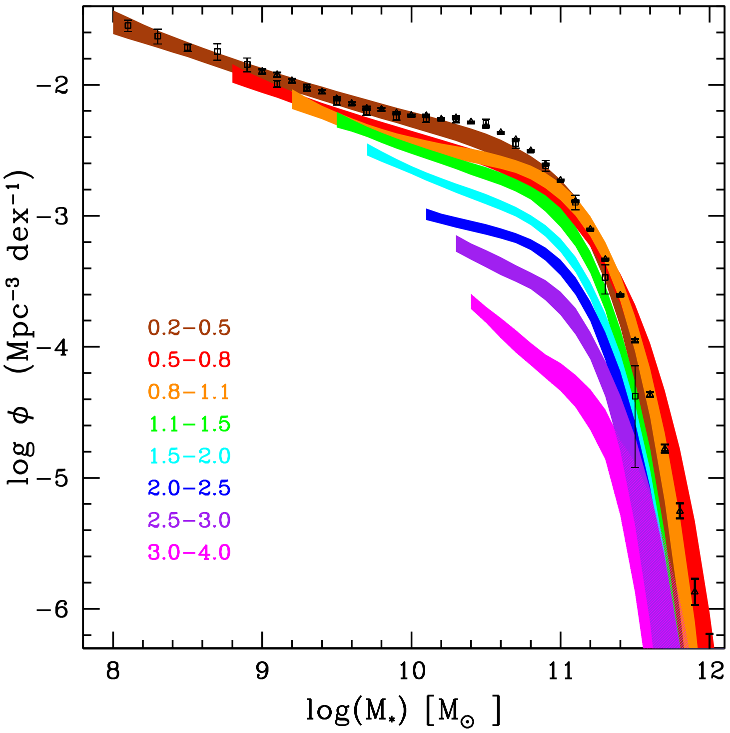

Figure 1.5: Stellar-mass functions for 220,000 galaxies, binned in redshift over the range $0.2 < z < 4.0$ using variable step-size. The sample consists of both star-forming and quiescent galaxies, down to a depth of $K_S < 24$. The coloured areas indicate the extent of the 68% confidence level, and the datapoints correspond to local estimates (triangles from Moustakas et al. 2013, squares from Baldry et al. 2012). Credit: Ilbert et al. [2013].

1.2 Active galactic nuclei

A galaxy is said to have an AGN when there is material accreting onto a supermassive black-hole at the centre. The accretion process is crucial to this 'active' description and, in objects where fuelling is discontinuous, the AGN may exhibit variability over a range of timescales [Hickox et al., 2014]. Similarly, a reservoir of gas may be exhausted completely, and so the galaxy is only active for a finite period of time. Taking the typical age of a normal galaxy to be about the Hubble time ($\sim 10^{10}$ yr), and that approximately 1% of all galaxies are active at any one time, it follows that the average lifetime of activity is $\sim 10^{8}$ yr [Woltjer, 1959]. This is also known as the 'duty cycle' of the AGN, and is consistent with the time it may take destabilised gas to travel across a halo [Fiore et al., 2012].

Due to the angular momentum of the infalling material, an accretion disc forms around the black hole. In order for gas to move to smaller radii, this angular momentum must be transported outwards, which is achieved via magnetorotational instabilities [Balbus and

Hawley, 1991]. Other key features of the AGN are shown in Figure 1.6, such as the dusty torus thought to surround the accretion disc. Its presence enables various degrees of AGN obscuration to be unified by a single model, as optical observations of this axisymmetric system are then highly dependent on the viewing angle. Unobscured AGN, for which the 'central engine' (i.e. black hole and accretion disc) can be seen, are labelled 'Type 1', while 'Type-2 AGN' are those that appear obscured. However, there is disagreement over the structure of the torus itself, with some authors suggesting that a clumpy distribution of dust is more realistic than the simplified smoothly-varying distribution [Schartmann et al., 2008]. If the torus does consist of individual dust clouds, then the Bayesian method used by Alonso-Herrero et al. [2011] is a more reliable way of classifying the type of AGN. This is because tight constraints can be placed on parameters describing the dust-cloud distribution, and (for example) the small probability of a cloud intersecting the line-of-sight, when viewing the accretion disc *face-on*, is taken into account.

The high temperatures associated with an AGN lead to strong emission-lines being observed for the surrounding gas. Based on the widths of these lines, it is possible to divide AGN into two populations again: those exhibiting narrow-line emission and those with broad emission-lines also. As the velocity of the gas dictates the linewidth, it follows that broad emission-lines ($\Delta v_{\rm FWHM} > 1000\,{\rm km\,s^{-1}}$) originate from gas clouds in the central region of the AGN (the broad-line region, BLR) and narrow emission-lines ($\Delta v_{\rm FWHM} \simeq$ 200–900 $\rm km\,s^{-1}$) are emitted by gas clouds further out in the narrow-line region, NLR [Peterson, 1997]. The location of the BLR means that it may be obscured by the torus, and so the orientation angle is again an important factor in the classification.

Another division highlighted in Figure 1.6 is that regarding radio loudness. The terms 'radio-quiet' and 'radio-loud' arise from the dichotomy initially thought to exist in the AGN population [Peacock et al. 1986; Xu et al. 1999]. However there are different definitions for radio loudness, historically this being a straight-forward boundary of $10^{25}\,{\rm W\,Hz^{-1}}$ at radio frequency 8.4 GHz [Hooper et al., 1996]. More common, and perhaps more physically meaningful, is the ratio between radio luminosity and optical luminosity [Kellermann et al., 1989]. This is discussed further in Section 1.4.1, whilst here I consider the role of radio loudness in AGN classification. Although radio jets have been detected in radio-quiet AGN [e.g. Blundell et al., 2003], they are largely associated with the radio-loud population. If the viewing angle is such that we are looking down the jet of a quasar (see Section 1.2.2), then the object is referred to as a 'blazar'. They appear as compact sources and have highly-energetic properties that vary rapidly. Two blazar subtypes are OVVs (optically-violent variable quasars) and BL Lacs. As suggested by the name, flares mean that the optical output of an OVV can vary drastically over timescales as short as one day Sikora et al. [2001]. BL Lacs are also highly-variable, but differ in that they lack the strong emission lines seen for OVVs.

There is still debate as to how jets from AGN are formed, but it is thought they are powered by the rotation of magnetic fields [Blandford, 1990]. Spin is therefore a key component, and the strength of these fields is also dependent on accretion rate and the thickness of the accretion disc close to the black hole. As material spirals in towards the black hole, gravitational energy is converted to thermal energy. Emission from the accretion disc is due to bremsstrahlung radiation, which is proportional to the square of the density, ρ. Therefore if the density is low, the thermal energy is retained, causing the disc to stay geometrically thick. As the density increases, radiation is more efficient, allowing the disc to cool and become thinner.

1.2.1 Seyfert galaxies

Seyfert galaxies and quasars are the two main groups of AGN, with the former having low-luminosity nuclear emission and a detectable host galaxy. As such, observations of these objects are largely confined to the local Universe, allowing the various processes involved in galaxy evolution to be resolved. For example, Davies et al. [2014] exploited SINFONI (Spectrograph for INtegral Field Observations in the Near Infrared) to study the kinematics of molecular gas, with the aim of understanding how gas is driven into the nuclear region.

In visible light, most Seyferts resemble normal spiral galaxies, but it is emission at other wavelengths that reveals the large luminosity of their cores. As indicated in Figure 1.6, the labels 'Sey 1' and 'Sey 2' refer to the level of orientation-dependent dust-obscuration. There are also intermediate classes of Seyfert galaxies, which are defined based on the

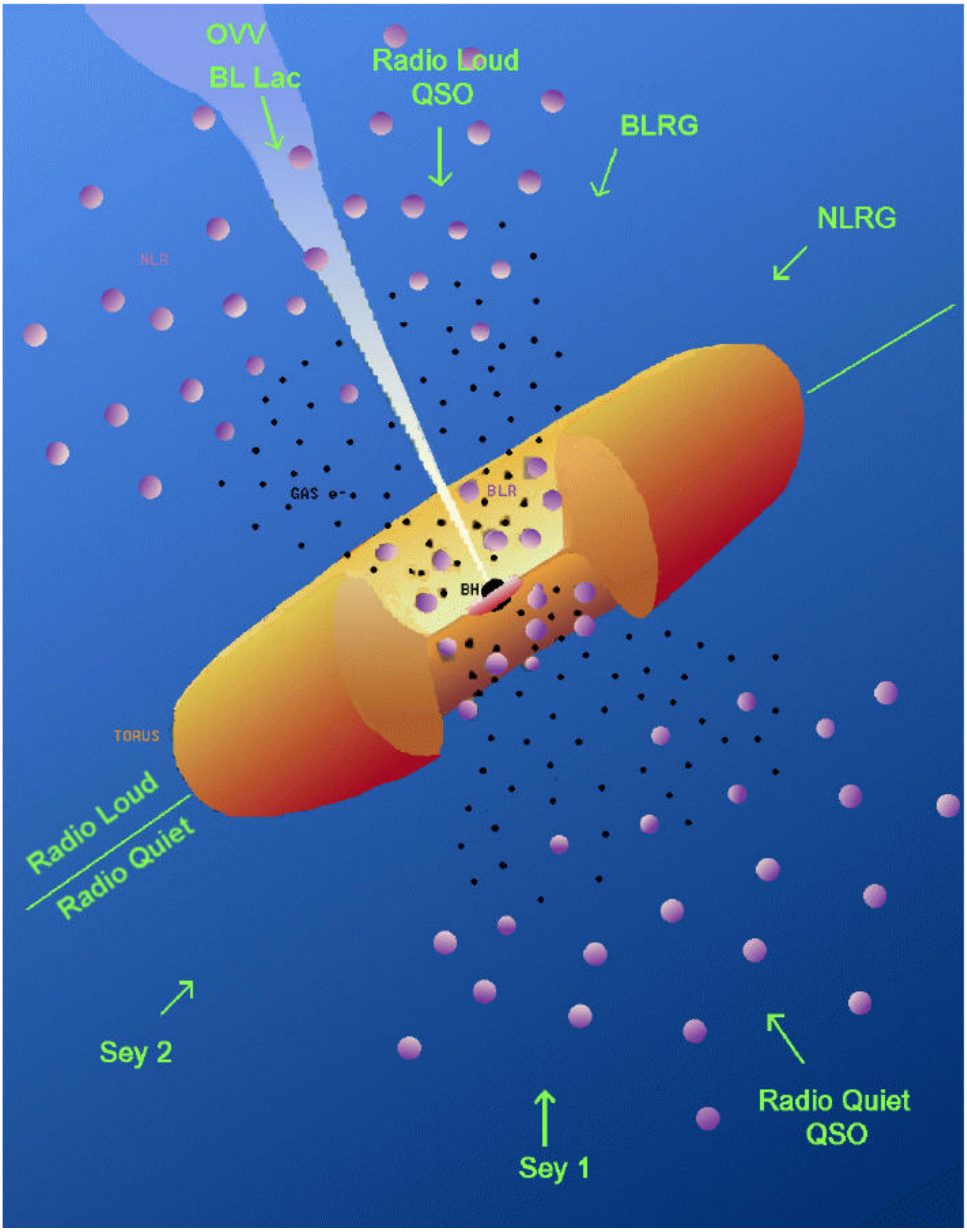

Figure 1.6: A model of the general structure of an AGN, with the aim to unify various classification schemes. These are the terms used when the object is viewed along the line-of-sight indicated by the green arrows. Although a radio jet is evident on the radio-loud side of the illustration, this may not always be present. 'OVV' stands for an optically-violent variable quasar, and 'BL Lacs' are a group of objects named after BL Lacertae, their prototype. Other abbreviations used in the diagram are: QSO - quasi-stellar object; BLRG - broad emission-line radio galaxy; NLRG - narrow emission-line radio galaxy; Sey 1/2 - two types of Seyfert galaxy; BH - black hole; BLR - broad-line region; and NLR - narrow-line region. (See the text for further description.) Credit: NRAO, with image retrieved from http://imagine.gsfc.nasa.gov/science/toolbox/spectra2.html and based on that by Urry and Padovani [1995].

relative strengths of the emission lines' broad and narrow components [Osterbrock, 1981].

1.2.2 Quasars

Extremely luminous, unobscured AGN appear point-like at high redshifts, and so are called quasi-stellar objects (QSOs) or 'quasars'. By definition these are Type-1 QSOs, with Type-2 QSOs being their obscured counterparts. Unlike Seyfert galaxies, the emission from the central engine strongly outshines that from the host galaxy. Some quasars may be dust-reddened, for which there are two popular explanations. Already discussed is the orientation argument, that the dusty nuclear torus surrounding the accretion disc provides a large amount of extinction along certain lines of sight to the quasar [see Antonucci 1993 for a review]. On the 'evolution side', the quasar begins life highly-obscured, following a galaxy merger and associated starburst, but then gradually expels its dusty envelope [Sanders et al. 1988; Hopkins et al. 2008]. This being the case, it is expected that many galaxies may undergo a quasar phase, as illustrated in Figure 1.7.

Being the high-luminosity analogues of Seyferts, quasars host the most-rapidly accreting supermassive black-holes, and so are excellent objects for studying extreme accretion events. However there is a limit to their brightness, which is determined by the Eddington limit, L_{Edd} (Equation 1.1). This is where the outward radiation pressure, caused by the heating of the infalling gas, is balanced by the gravitational force of the black hole (hence the dependence on black-hole mass, M_{BH}). Spherical accretion is assumed, and if there is too much gas accreting at once, the resulting pressure will counteract the inflow of gas, slowing it so that the quasar's luminosity is $\leq L_{\mathrm{Edd}}$. The Eddington ratio for a quasar with bolometric luminosity, L_{bol}, is then defined as $L_{\mathrm{bol}}/L_{\mathrm{Edd}}$. Its mean value is 0.1, for quasars at $z < 1$, rising to higher values at higher redshift and (as expected) reaching an upper limit of $\sim$1 [McLure and Dunlop, 2004].

$$L_{\mathrm{Edd}} = \frac{4\pi G M_{\mathrm{BH}} m_p c}{\sigma_{\mathrm{T}}} \tag{1.1}$$

where G is the gravitational constant, and c is the speed of light. For infalling material that is pure ionised hydrogen, the opacity is $\kappa = \sigma_{\mathrm{T}}/m_p$, where σ_{T} is the Thomson

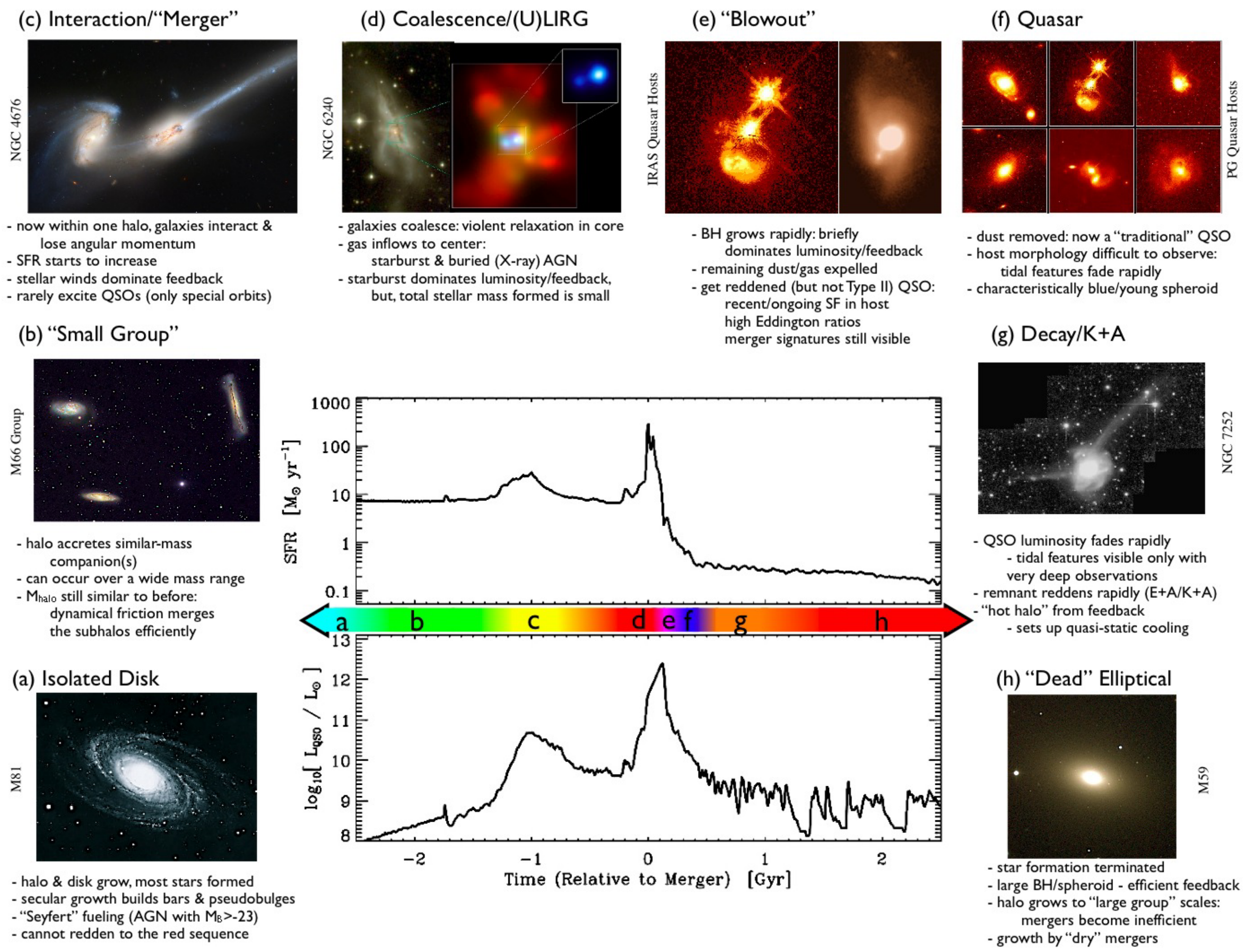

Figure 1.7: An outline of the different stages of growth that a 'typical' galaxy undergoes before, during, and after a gas-rich major merger. Figure taken from Hopkins et al. [2008], with credits as follows: (a) NOAO/AURA/NSF; (b) REU program/NOAO/AURA/NSF; (c) NASA/STScI/ACS Science Team; (d) Optical (left): NASA/STScI/R. P. van der Marel & J. Gerssen; X-ray (right): NASA/CXC/MPE/S. Komossa et al.; (e) Left: J. Bahcall/M. Disney/NASA; Right: Gem- ini Observatory/NSF/University of Hawaii Institute for Astronomy; (f) J. Bahcall/M. Disney/NASA; (g) F. Schweizer (CIW/DTM); (h) NOAO/AURA/NSF.

scattering cross-section for the electron, and m_p is the mass of a proton.

1.3 AGN-related feedback

As introduced in Section 1.1.1, investigating feedback mechanisms has become an integral part of galaxy-evolution studies. In this thesis I am particularly interested in how the AGN interacts with its host galaxy, if at all. This feedback can be described as being 'mechanical' or 'radiative', and these two pathways are explained below.

1.3.1 Mechanical feedback

Mechanical feedback from an AGN is in the form of radio jets or outflows driven by the central engine. In low-redshift objects these are seen to inflate 'bubbles' in the surrounding hot gas, creating cavities that are observed in the X-ray [e.g. Fabian et al., 2000]. By dividing the cavity enthalpy by a characteristic timescale, such as the duty cycle of the AGN, an estimate of the time-averaged mechanical power can be derived. Such a calculation is carried out by Bîrzan et al. [2004], who show that the rate at which the AGN injects energy into its environment correlates with the radio luminosity, although with large scatter. Furthermore, the lower density within the cavities gives them buoyancy, and as they 'rise', kinetic energy is likely dissipated as heat [McNamara and Nulsen, 2007]. Through heating of the galaxy halo and interstellar medium (ISM), mechanical feedback may therefore suppress star formation [Croston et al. 2007; Best 2007].

The jets and outflows may also expel material from a galaxy, cutting off the fuel that would otherwise accrete onto the central supermassive black-hole or collapse to form stars [Combes et al. 2013; Morganti et al. 2013]. On the other hand, the jet could *cause* a molecular cloud to collapse, initiating star formation [e.g. Silk, 2013]. Statistical evidence of positive feedback in high-redshift quasars comes from Kalfountzou et al. [2012, 2014], and an excellent individual example is Minkowski's Object [Croft et al., 2006]. This is a region of star formation, appearing blue in the left-hand panel of Figure 1.8, with radio lobes from a nearby AGN highlighted in purple. When inspecting a HI map of the region that has radio contours overlaid (right-hand panel), the interaction between the gas and

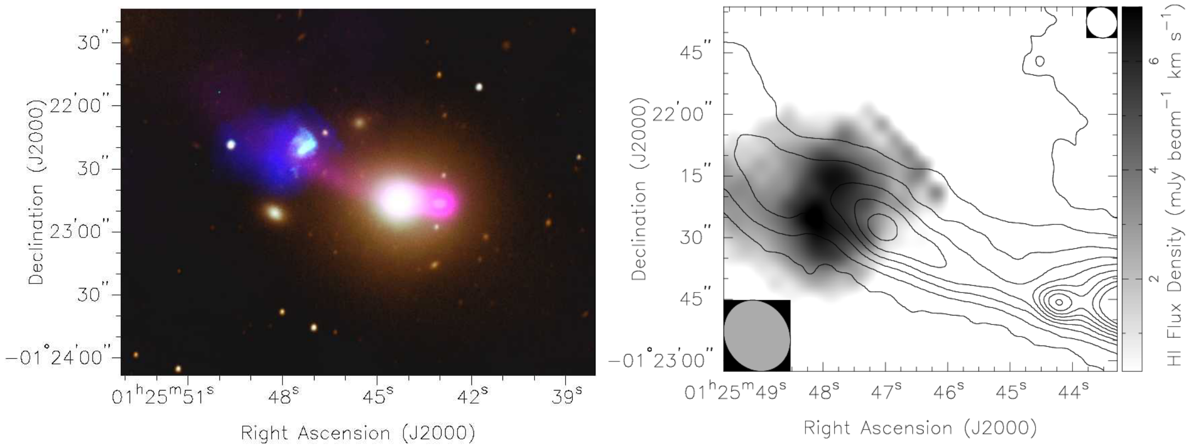

Figure 1.8: A *BR* image of the Abell 194 field (left), with radio continuum (purple), HI (dark blue) and Hα (light blue) data overlaid. Minkowski's Object (MO) is at 1h25m47s, -1°22'20", lying in the path of a jet from NGC541, at 1h25m44s, -1°22'46". The HI cloud associated with MO is mapped in greyscale in the right-hand panel, with contours of radio emission (observed with the VLA) overplotted. These are at 2 mJy/beam intervals, covering the range 1–17 mJy/beam. Credit: Croft et al. [2006].

the radio jet becomes much clearer.

1.3.2 Radiative feedback

Even without jets, the radiation associated with the accretion disc is sufficient to prevent the cooling of gas. The significance of this AGN-heating is suggested by Croton et al. [2006] using Figure 1.9. They show that by incorporating this mechanism into their semi-analytic models, the predicted galaxy luminosity functions are in much better agreement with the observations. However, it can be difficult to decouple radiative effects from other processes associated with negative feedback, such as the expulsion of gas by jets or supernovae, where the star formation in the host galaxy is truncated. Much work over the past decade has revolved around understanding such feedback mechanisms, with similar semi-analytic models being developed to understand the observations [e.g. Benson et al. 2003; Bower et al. 2006]. These help to inform high-resolution simulations [e.g. Dubois et al., 2011; Li and Bryan, 2014], but debate continues over how star-formation and accretion processes interact. For example, the EAGLE simulation [Schaye et al., 2015] still fails to match the galaxy luminosity function at high redshift, and cannot resolve the multi-phase ISM. Also, like many models, the power output of the AGN is simply mapped from the accretion rate, which itself is forced to be Eddington-limited, and there is no

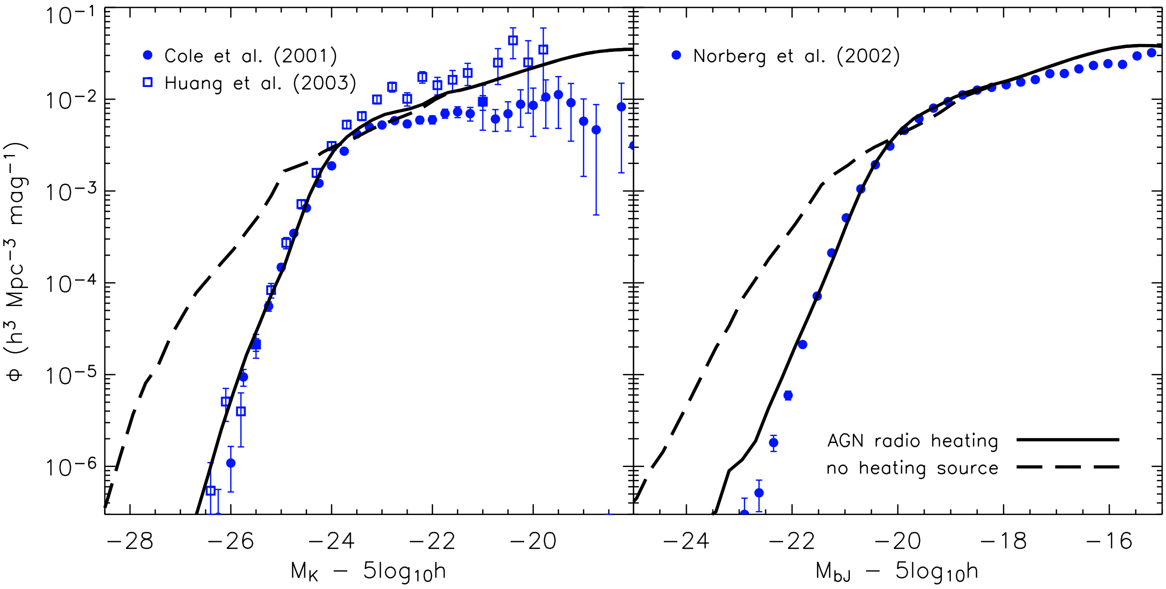

Figure 1.9: Galaxy luminosity functions in the photometric bands K (left) and b_J (right), with observational data from the studies stated in each panel. The solid and dashed lines represent the semi-analytic model with and without radiative feedback, respectively. Credit: Croton et al. [2006].

prescription for the production of radio emission, largely due to the origin and evolution of cosmic magnetism being poorly understood.

1.3.3 Impact on the star-formation rate

The impact of the AGN, through feedback, may be reflected by the way in which the accretion rate correlates with the star-formation rate. Figure 1.10 is taken from Rosario et al. [2012], who show that in each redshift bin, *no* correlation is seen between the AGN luminosity, L_AGN, and the star-formation luminosity, given by $\nu L_\nu(60\,\mu\mathrm{m})$, except for systems with high values of each. However, the AGN luminosities here refer to the *instantaneous* accretion rate, when this could be varying over timescales comparable with the star-formation activity [Hickox et al., 2014]. In contrast, Chen et al. [2013] find that a correlation does exist between the star-formation rate (SFR) and the black-hole accretion rate if the latter is averaged over each SFR bin. Another example is the work by Bonfield et al. [2011], showing a shallow but significant correlation between star-formation rate (SFR) and average accretion rate. These studies suggest that the two processes may be interlinked, either through feedback processes or as a consequence of being fuelled by a common gas-reservoir.

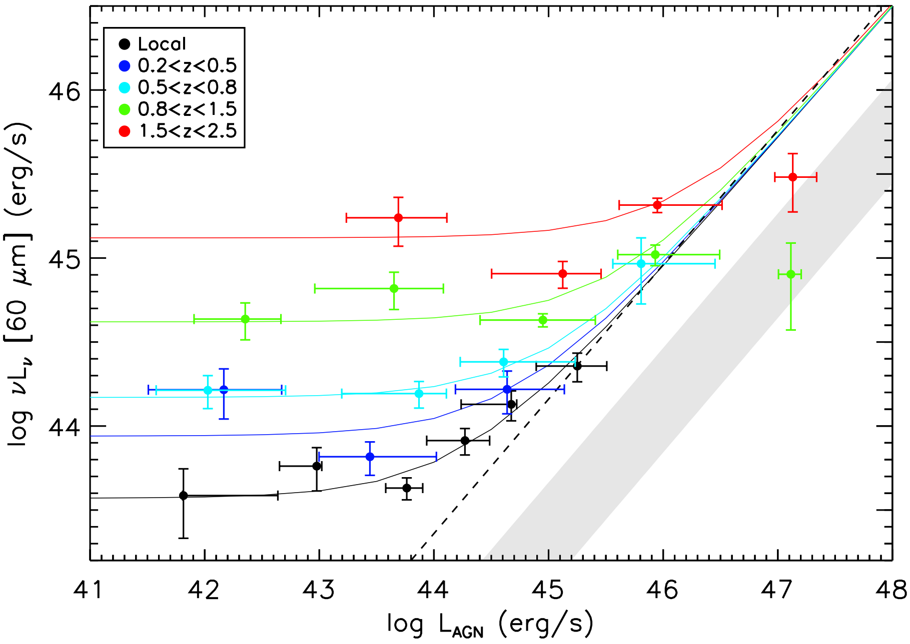

Figure 1.10: Mean 60 µm-luminosity, $\nu L_\nu(60\,\mu\mathrm{m})$, against AGN luminosity, L_{AGN}, for X-ray selected AGN. They are binned in redshift over the range $0 < z < 2.5$, with functional fits to the mean measurements (solid lines). A correlation line for AGN-dominated systems is shown (dashed line, Netzer 2009) and the shaded region indicates the $\sim$1-σ range over which the spectral energy distributions (SEDs) for empirical pure-AGN lie. Credit: Rosario et al. [2012].

1.4 Radio emission

Synchrotron emission is produced when charged particles are moving at relativistic speeds through a magnetic field (Figure 1.11). The force exerted by the field on the particle is in a direction perpendicular to the particle's motion, causing it to change direction and therefore accelerate. As with all charges undergoing acceleration, electromagnetic energy is radiated as a result, and in this case it is called synchrotron radiation. The frequencies of the emitted photons depend on both the energies of the particles involved and the strength of magnetic field, with the combination of lower-energy electrons and magnetic fields present in AGN and star-forming regions leading to radio photons being emitted. Since the field continues to exert a perpendicular force as the particle travels, its motion follows a spiral path through the field. As a result, the radiation is polarised in the plane perpendicular to the magnetic field, and so information about the radio source's magnetism can be determined from the polarisation of radio emission.

Figure 1.12 shows the typical spectrum, from the radio through to the far-infrared

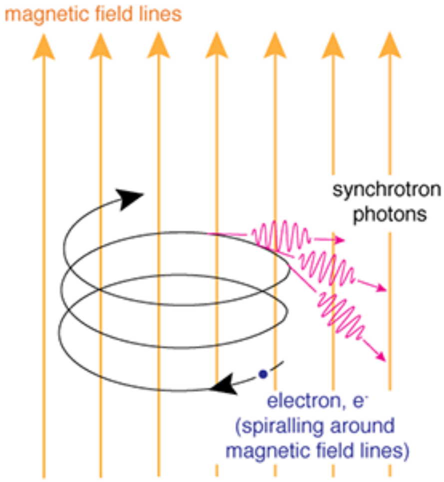

Figure 1.11: An illustration of synchrotron radiation being produced when electrons are accelerated by a magnetic field. Credit: NASA's Imagine the Universe, image retrieved from http://imagine.gsfc.nasa.gov/science/toolbox/spectra2.html.

(FIR), for a starburst galaxy. This is a galaxy in which the star-formation rate is very high and at its most efficient (with respect to the amount of available gas). The synchrotron emission has a power-law spectrum, $S_\nu \propto \nu^\alpha$, which reflects the underlying power-law distribution of electron energies. For most optically-thin extragalactic radio-sources the spectral index is $\alpha = -0.7$. Also shown in Figure 1.12 is the spectrum for free-free emission (this being another name for bremsstrahlung radiation) and that for dust re-radiating in the far-infrared.

1.4.1 Radio emission from AGN

There are two main pathways by which AGN produce radio emission, the most common being connected to the accretion disc. As electrons and other charged particles orbit and accrete onto the central supermassive black-hole, they are accelerated by magnetic fields [Blandford and Znajek, 1977] and so produce synchrotron radiation. The other route is via radio jets. Radio emission is associated with the acceleration of electrons entrained within the jet but also with regions where the surrounding environment is dense enough to *decelerate* the jet's relativistic particles. The properties of both the AGN and its environment therefore determine the morphology and luminosity [Hardcastle et al., 2013] as observed in the radio. AGN that are 'edge-darkened', where radio jets appear brightest at the source centre, are classed as 'FRI' objects. Those with radio lobes that are 'edge-

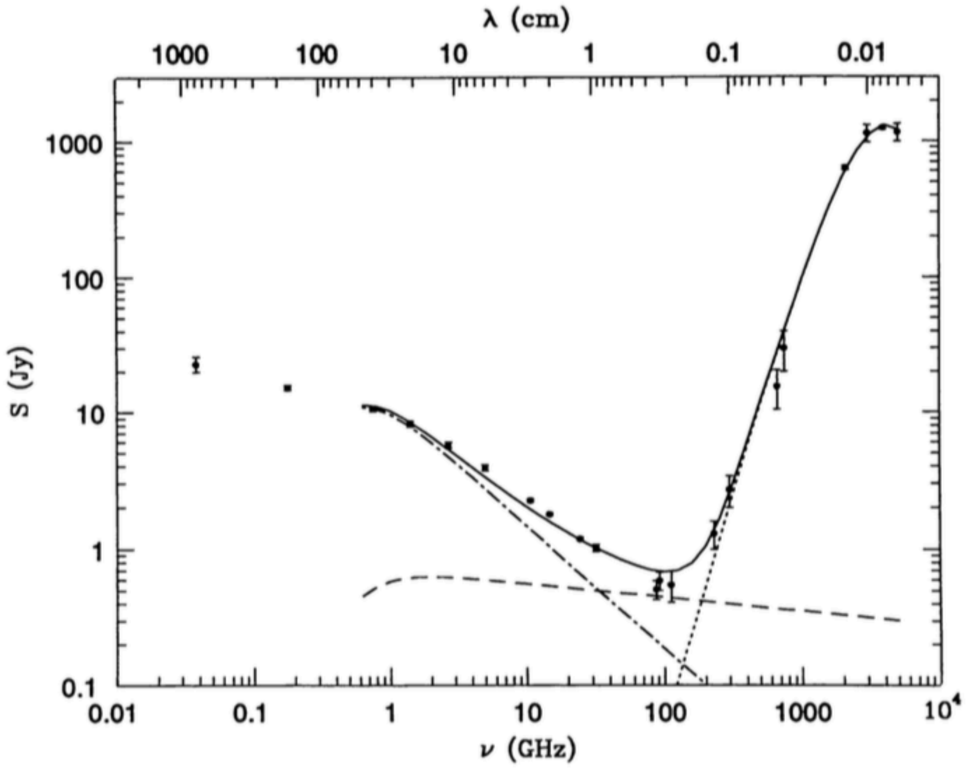

Figure 1.12: The spectrum for the starburst galaxy M82, as observed in the radio and far-infrared (solid line). This is produced by the sum of synchrotron radiation (dash-dotted line), free-free emission (dashed line) and re-radiation from dust (dotted line). Credit: Condon [1992].

brightened', where the emission peaks well away from the actual AGN, are labelled 'FRII' [Fanaroff and Riley, 1974].

However, not all radio sources have strong jets and the distinctive morphologies associated with them. Therefore a useful classification scheme is that by Best and Heckman [2012], who divide radio galaxies into those that are 'low excitation' (LERG) and those that are 'high excitation' (HERG), primarily based on the strength of emission lines. For LERGs the accretion rate onto the black hole is less than 1% of the Eddington accretion rate, $\dot{M}_{\rm Edd}$, and the object is referred to as being in 'radio mode'. In HERGs the black hole is fuelled by cold gas at high rates of 1-10% $\dot{M}_{\rm Edd}$, through radiatively-efficient accretion discs. Hence 'cold mode' and 'accretion mode' are alternative names for this 'quasar mode'. HERGs are seen to evolve strongly at all radio luminosities, and tend to have host galaxies that have younger stellar populations, lower stellar mass, lower black-hole mass, and bluer colours than the LERGs. This is consistent with observations of quasars out to very high redshifts, where the Universe is still relatively young, star formation dominates, and there hasn't been enough time for numerous mergers.

1.4.1.1 Radio loudness

The FRI/FRII classifications above refer to objects that are radio-loud (Section 1.2). However, the distinction between these and radio-quiet objects remains an arbitrary concept as a bimodality in radio loudness has not been convincingly proven [e.g. Cirasuolo et al. 2003; Baloković et al. 2012]. Ivezić et al. [2004] argue that the bimodality in the radio-to-optical luminosity ratio is genuine, whilst others suggest it is a result of selection effects, with objects actually found across the full range of radio powers [Lacy et al., 2001]. There is also uncertainty surrounding the exact physical mechanism that turns energy from accreted material into well-collimated jets, and why some systems show no jets at all. For example, the influence of the spin of the black hole is still an open question. Several theoretical and observational studies suggest that it may play a role [e.g. Blandford and Znajek 1977; Wilson and Colbert 1995; McLure and Jarvis 2004; Volonteri et al. 2007; King et al. 2008; Fernandes et al. 2011], whilst van Velzen and Falcke [2013] present evidence that it could be irrelevant. Meanwhile, Lin et al. [2010] find that different radio morphologies are more dependent on the accretion rate than the galaxy's structure, with highly-extended, lobe-dominated radio galaxies having higher accretion rates than their less-extended counterparts.

1.4.1.2 A minimum accretion rate

Fernandes et al. [2011] investigated whether there is a connection between the accretion rate and the radio power for a set of radio galaxies. Figure 1.13 is taken from their work, and shows the radio luminosity at 151 MHz on the x-axis, tracing jet power, and the mid-infrared luminosity at 12 µm along the y-axis. The latter is demonstrated to be tightly correlated with the oxygen [OII] emission line, and so acts as a proxy for the accretion rate onto the black hole. The effectiveness of [OII] as an indicator of accretion rate is that it originates from the NLR (Figure 1.6), and so is unaffected by obscuration from the torus.

With the addition of bright optically-selected quasars to the various samples of radio

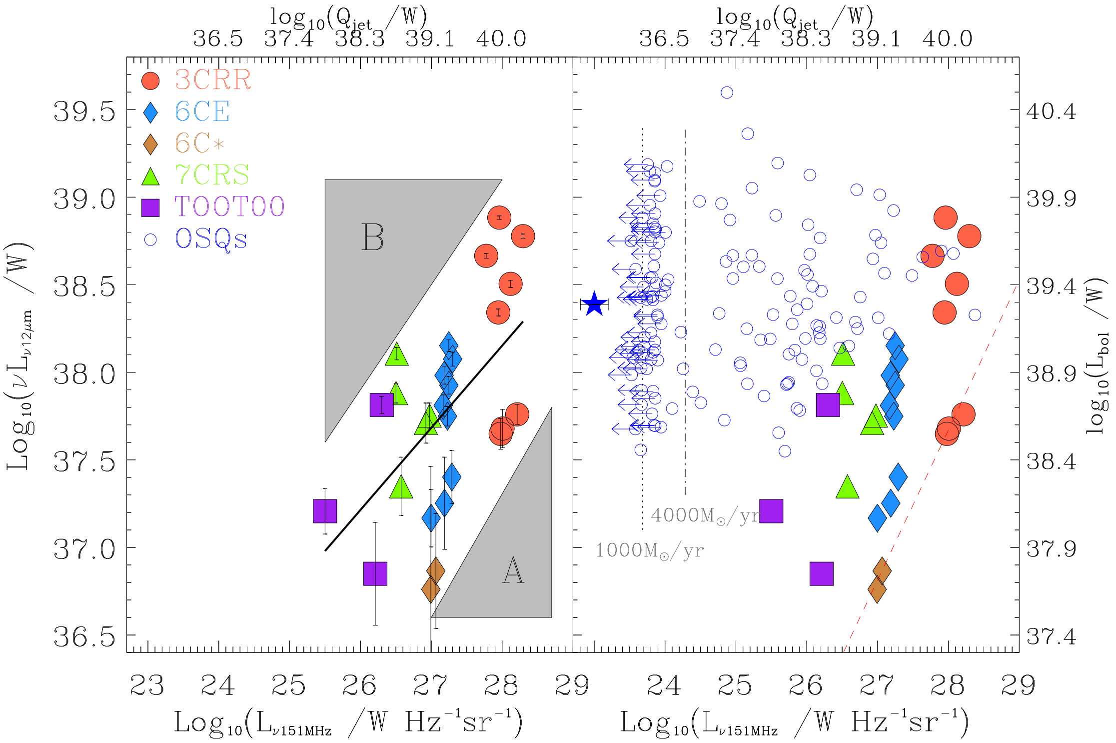

Figure 1.13: Mid-infrared (12 µm) rest-frame luminosity, $\nu L_{\nu 12\mu\rm m}$, against low-frequency radio luminosity, $L_{\nu 151\rm MHz}$, for $z \sim 1$ radio galaxies from different surveys (see legend). In the left-hand panel, the best-fit line (solid, black line) is given by $\log_{10}(\nu L_{\nu 12\mu\rm m}) = (0.47 \pm 0.13)\log_{10}(L_{\nu 151\rm MHz}) + 25.0 \pm 3.6$. A sample of optically-selected quasars, taken from Falder et al. [2010], are overplotted in the right-hand panel (open, blue circles). Those with upper limits, given to $2\,\sigma$, are stacked to give the result represented by a blue star. Vertical lines indicate the radio luminosity of a starburst and the associated star-formation rate. Drawing attention to the alternative axes: Jet power, $Q_{\rm jet}$, is estimated from the radio luminosity, whilst the mid-infrared luminosity is used to estimate the bolometric luminosity, $L_{\rm bol}$. The maximum jet efficiency, $\eta \sim 2.5$, is represented by the red, dashed line. Credit: Fernandes et al. [2011].

galaxies, the region labelled ‘A’ in the left-hand panel of Figure 1.13 is proven to be truly absent of objects. (That is, it is not the result of radio-selection effects, as is the case for region ‘B’.) Therefore the lower envelope in the correlation shows that for a given radio luminosity, there is a minimum accretion rate. Assuming that the black hole is accreting at the Eddington limit, this implies that there is a maximum efficiency with which the black hole is able to produce jets from the infalling material.

This study uses a thin slice in redshift ($0.9 < z < 1.1$), and it is unclear whether the result extends over a larger redshift range and, moreover, to the lower radio-luminosities of RQQs. It is possible that an alternative mechanism determines the relation between accretion rate and radio power in these objects, and that this is connected to RQQs having a lower threshold in their black-hole mass than radio-loud quasars [e.g. Dunlop et al., 2003]. Also, probing the minimum accretion-rate envelope for all AGN, whether obscured or unobscured, entails removing contamination by star formation in the host galaxy. This is because star formation can make a significant contribution to the radio flux (see Section 1.4.2), and is thought to make a large contribution to the total radio emission of radio-quiet AGN [Kimball et al. 2011; Condon et al. 2012].

1.4.1.3 Radio-quiet quasars

Quasars are (naturally) a component of ‘quasar mode’ accretors, belonging to the HERG population as described by Best and Heckman [2012]. Although they were discovered using radio observations, only $\sim 10\%$ have significant radio emission [Hooper et al., 1996]. The remaining radio-quiet quasars (RQQs), that do not show strong jets, need to be better-studied at radio wavelengths to investigate their contribution to the overall radio-source counts [e.g. Jarvis and Rawlings 2004; Simpson et al. 2006; Padovani et al. 2014] and the underlying physical processes that may provide a different source of relativistic electrons [e.g. Fernandes et al. 2011; Condon et al. 2012].

Figure 1.14 shows the number density of radio sources as a function of their flux density at 1.4 GHz. Two ‘bumps’ are evident, with the one on the right due to AGN dominating the bright end. As for the fainter bump, below 1 mJy, consensus holds that the total radio population is dominated by star-forming (SF) galaxies [Condon et al., 2002]. However,

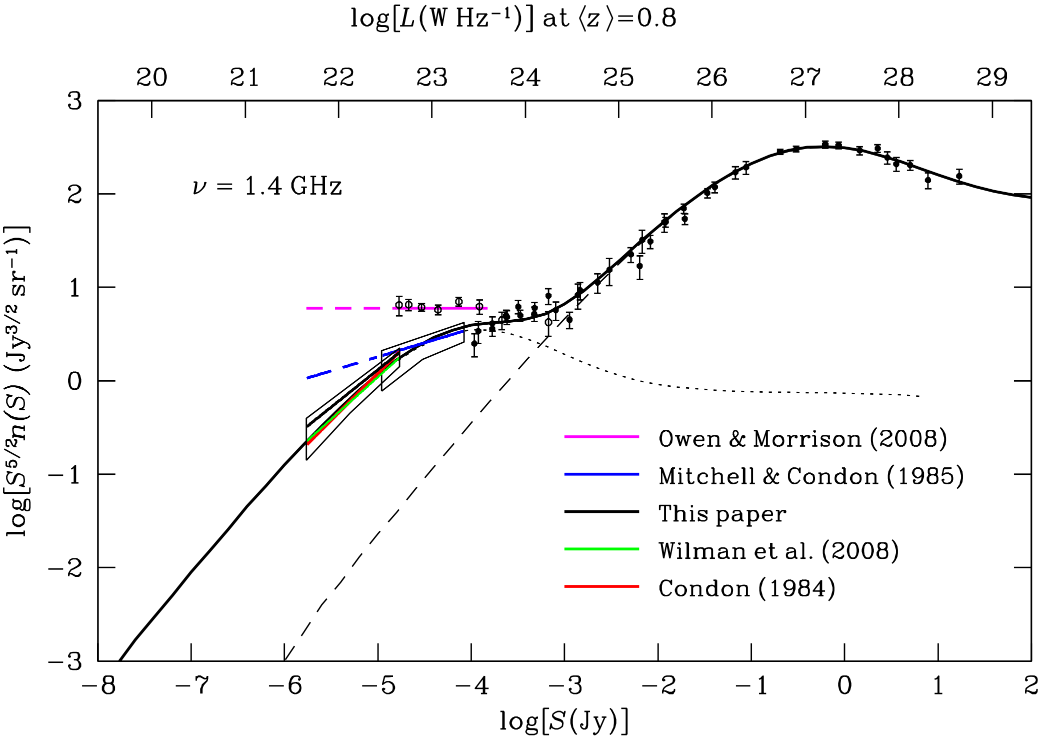

Figure 1.14: The source counts at 1.4 GHz based on individual objects (datapoints), and the 1.4 GHz $P(D)$ distribution from Mitchell and Condon [1985] (blue line and error box) and that based on Condon et al. [2012] (black line and error box). The latter is converted from the 3.0 GHz $P(D)$ distribution using a mean spectral index, $\alpha = -0.7$. Power-law approximations to the 1.4 GHz models of Condon [1984] and Wilman et al. [2008] are represented by red and green lines, respectively. Also shown are the relative contributions of AGN (dashed line) and star-forming galaxies (dotted line), according to the Condon [1984] model. Credit: Condon et al. [2012].

this is based on the assumption that the approximate power-law describing the AGN number counts, over the range $-2.5 < \log_{10}[S/\text{Jy}] < -1.0$ [Condon et al., 2013], simply extends to lower luminosities (dashed line in Figure 1.14). It also assumes that the AGN and SF populations are uncorrelated, which may not be the case (as illustrated through various feedback scenarios). Meanwhile Wilman et al. [2008], whose total source-counts are consistent with Condon et al. [2012], show that a combination of SF galaxies and RQQs are able to reproduce the faint 'bump' in their simulations. This is also backed up by observations [e.g. Simpson et al. 2006; Smolčić et al. 2008; Padovani et al. 2014]. However, we are yet to understand the relative levels of accretion and star formation in RQQs, in terms of their contributions to the total radio emission.

1.4.2 Radio emission from star-forming regions

A tight correlation between the far-infrared and radio emission (Figure 1.15) was first discovered by Helou et al. [1985], and is (aptly) known as the far-infrared–radio correlation (FIRC). The reason it exists is that both types of emission are mediated by star formation. This process produces large quantities of dust that, being at cool temperatures ($\sim 30\,\mathrm{K}$), radiates in the far-infrared via black-body radiation. As for the radio emission, supernova remnants are naturally co-located with regions of star formation. When electrons traverse these aging shock fronts, they are decelerated rapidly, thus producing synchrotron radiation. However, given that the far-infrared traces *ongoing* star-formation, one might expect the correlation to be affected by the delay between stars forming and supernovae occurring. This is not the case, though, as the supernovae in question are only produced by stars more massive than $\sim 8\,\mathrm{M}_{\odot}$. These stars have lifetimes of $\leq 3 \times 10^{7}\,\mathrm{yr}$, which is a factor ten shorter than the lifetimes of relativistic electrons [Condon et al., 1991]. Therefore stellar populations older than approximately $10^{8}\,\mathrm{yr}$ do not contribute to the radio emission from galaxies, meaning that radio observations are indeed probes of recent star-formation.

A great advantage of radio emission over other indicators of star-formation rate (SFR) is that it is unaffected by dust obscuration, and so could be crucial for determining the SFRs of high-redshift objects (for which far-infrared data is too poor in resolution and becomes confusion-limited). Also, at high redshift the molecular-gas content of galaxies is much larger [Carilli and Walter, 2013]. Since dust largely traces the gas, the increased dust content means that there is a greater likelihood that optical observations will be obscured. This obscuration is in addition to that associated with an AGN's torus being viewed edge-on, which may itself have some redshift dependence if the shape of the torus evolves. As a result, the biases associated with using optical emission-lines for sample selection, and analysis, worsen.

1.4.3 Disentangling accretion and star formation

As stated previously, two crucial aspects of galaxy evolution are black-hole accretion and star formation. That the two processes are connected is suggested by the cosmic

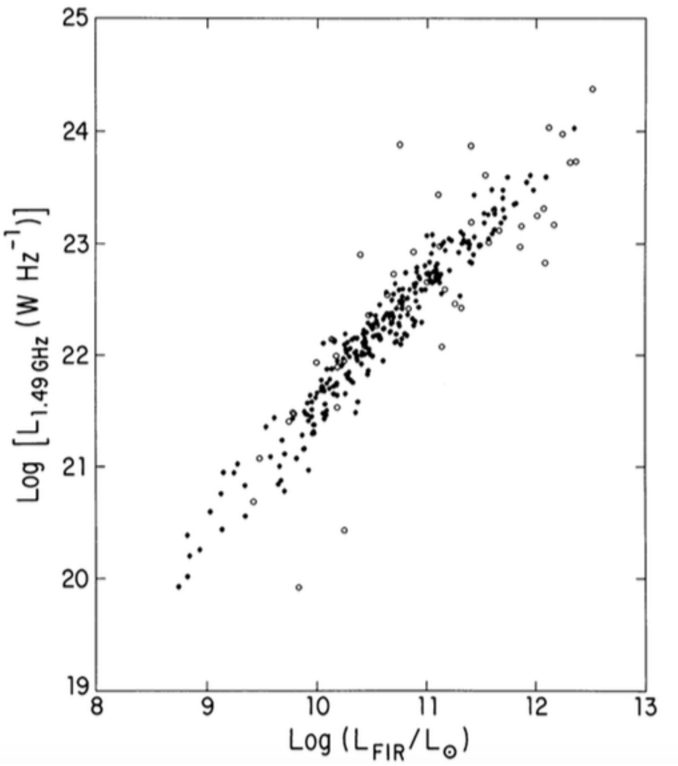

Figure 1.15: The far-infrared–radio correlation for 313 infrared-selected galaxies, with $S_{60\,\mu m} \geq 5.24$ Jy. The unfilled circles are galaxies known to have AGN, and so are excluded from the sample, leaving 258 galaxies without known AGN (filled circles). Credit: Condon et al. [1991].

history of star formation following a similar trajectory as the cosmic history of accretion (Figure 1.16). Along with the peak at $z \sim 1-2$ for both accretion [e.g. Ueda et al. 2003; Wolf et al. 2003] and star-formation [e.g. Madau et al. 1996; Hopkins and Beacom 2006] activity, the interaction of these processes is thought to explain, for example, why black-hole mass is correlated with the bulge mass [Ferrarese and Merritt 2000; Gebhardt et al. 2000; Gültekin et al. 2009]. However it is not yet well-understood how the two phenomena interact or whether their similar histories are simply due to a common factor: the availability of gas.

Many previous studies that investigated the interplay between AGN and star formation have used optical and infrared data [e.g. Bonfield et al. 2011; Hardcastle et al. 2013]. The strength of emission lines produced by gas is often used as a proxy for accretion rate [Rawlings and Saunders, 1991], as the intense, hot environments of accretion discs lead to the ionisation of multi-electron atoms. The disc's thermal emission contributes to the continuum, which is measured in the X-ray through to the mid-infrared. Optical

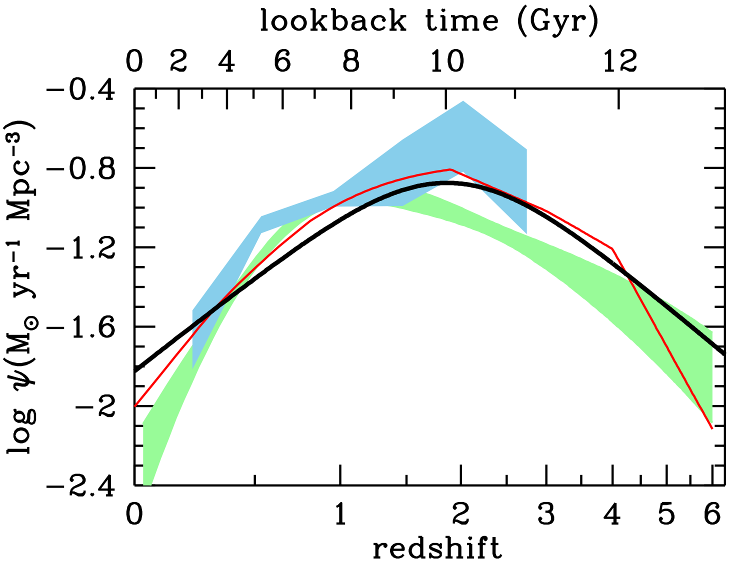

Figure 1.16: A comparison of the best-fit star formation history (thick black line) with the black-hole accretion history from X-ray data [thin red line, Shankar et al. 2009; light-green shading, Aird et al. 2010]. These have been scaled by a factor of 3,300 to aid comparison, as has the black-hole accretion history from infrared data [light-blue shading, Delvecchio et al. 2014]. Credit: Madau and Dickinson [2014].

and near-infrared bands also provide information on the degree of any ongoing star-formation, either directly from stellar light or indirectly, through energy being absorbed by the surrounding dust and re-radiated at longer wavelengths. Emission measured in the mid-infrared is indicative of warm dust [∼100–1000 K; Mathis 1990], mostly in the torus, which has been heated via the accretion process. Meanwhile, star formation is largely responsible for cooler dust [∼10–100 K; Kirkpatrick et al. 2012; Scoville 2013], whose emission is observed in the far-infrared.

The ‘Baldwin, Phillips & Terlevich’ (BPT) diagram (Figure 1.17) is traditionally used to provide object classification via diagnostic line-ratios [Baldwin et al., 1981], allowing AGN to be separated from starbursts. The emission lines used for this method are sufficiently close that the effect of (moderate) dust obscuration is negated. However, the presence of dust means that ultra-violet and optical samples are prone to missing the most-obscured objects. As such, without the necessary emission lines appearing in the spectrum, employing the BPT diagram is insufficient for distinguishing AGN from star-forming galaxies. Instead, near-infrared or mid-infrared photometry is needed to remove star-forming contaminants (or, conversely, to remove AGN contaminants when studying the star-forming population). Another way is to observe obscured AGN in the radio part of the spectrum, since emission at these long wavelengths is unaffected by dust. As explained earlier in this section, electrons accelerated in magnetic fields lead to radio emission being produced via synchrotron radiation [Kellermann and Owen 1988; Condon 1992], providing the means to measure both star formation and AGN activity at ∼GHz frequencies.

However, for objects without obvious jets, separating star formation and accretion components is difficult at radio wavelengths. Therefore, multi-wavelength data can be used to help disentangle the two contributions to the total radio emission. For example, using far-infrared data from *Herschel* in combination with deep radio-data breaks the degeneracy in the radio emission. This is because Helou et al. [1985] and de Jong et al. [1985] showed that a tight correlation exists between the far-infrared and radio (the FIRC, Section 1.4.2), allowing us to determine the star-formation rate directly from radio emission. Any 'excess' radio emission is then attributed to the AGN.

As mentioned in Section 1.4.1.3, studies of the radio-source populations as a function of radio flux-density suggest that as we probe fainter radio-sources, the population changes from being AGN-dominated (FRIs, FRIIs) to being dominated by star-forming galaxies [Hopkins et al. 2003; Wilman et al. 2008; Condon et al. 2012]. However, there are obviously cases in which AGN are hosted in galaxies with ongoing star-formation [e.g. Canalizo and Stockton, 2001; Netzer et al., 2007; Silverman et al., 2009]. This is investigated further by Kimball et al. [2011] and Condon et al. [2013], who study the radio emission from samples of optically-selected quasars, leading them to propose that the radio emission from these quasars is due to star formation within the host galaxy, rather than from the AGN. Complementary studies at other wavelengths also suggest that there is at least some ongoing star-formation in quasar host-galaxies. Using far-infrared observations from *Herschel*, Bonfield et al. [2011] find a modest correlation between accretion luminosity and star formation, and Rosario et al. [2013] show that the mean star-formation rate (SFR) of quasar hosts is consistent with typical massive star-forming galaxies.

On the other hand, Zakamska and Greene [2014] use emission-line kinematics, from quasars and their host galaxies, to show that star formation in quasar hosts is insufficient to explain the observed radio emission. Instead they argue that the synchrotron emission

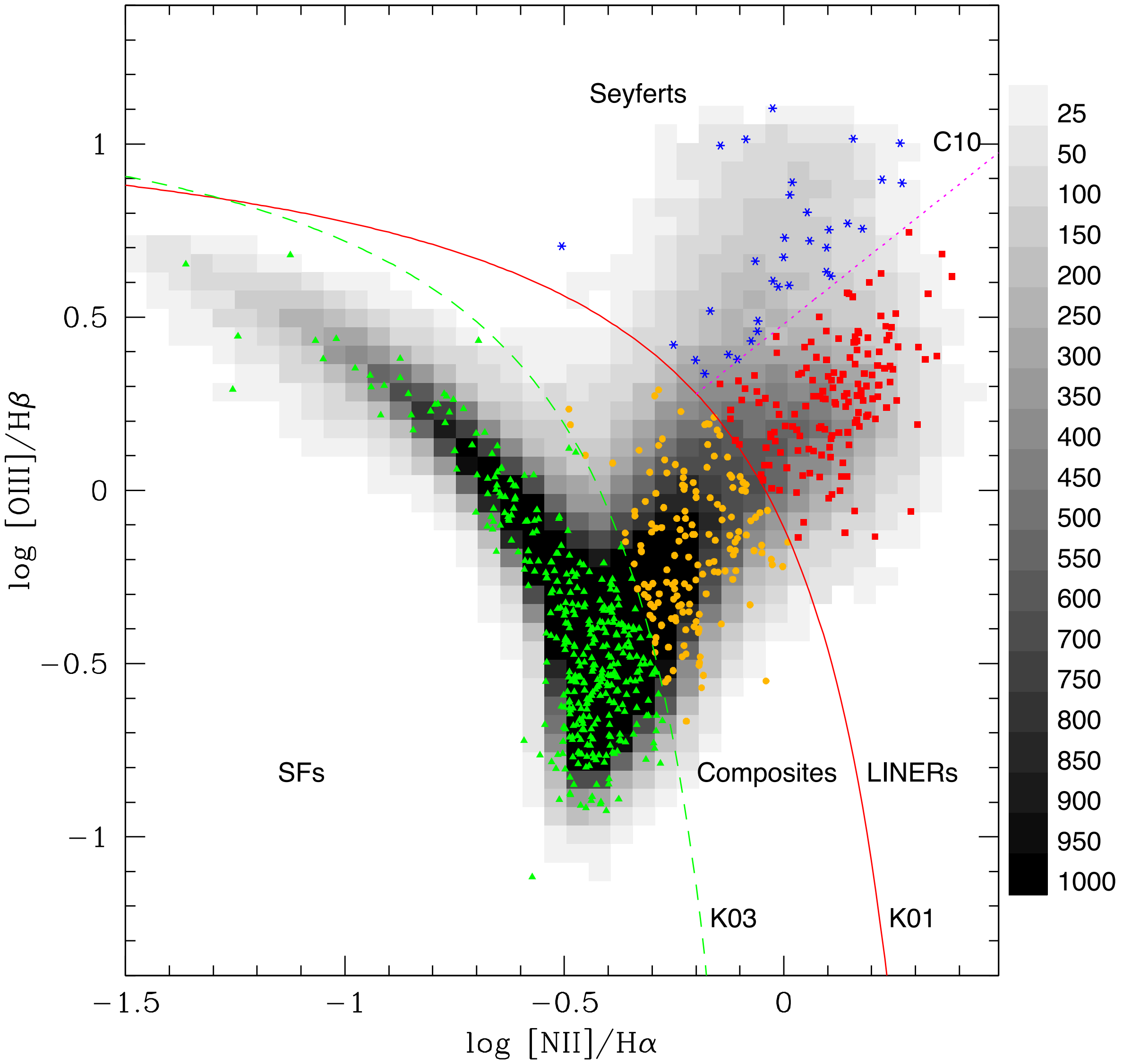

Figure 1.17: A 'Baldwin, Phillips & Terlevich' (BPT) diagram [Baldwin et al., 1981], used to spectrally diagnose a sample of 727 galaxies. They occupy the regions of star-forming (SF) galaxies (green triangles), composite galaxies (orange circles), LINERs (Low-Ionization Nuclear Emission-line Regions, red squares), and Seyferts (blue asterisks). The solid line labelled 'K01' is the theoretical divide proposed by Kewley et al. [2001], separating AGN from SF galaxies, while the 'K03' line (dashed line) is the empirical line from Kauffmann et al. [2003]. The dotted line ('C10') demarcates the divide between Seyferts and LINERs, as defined by Cid Fernandes et al. [2010]. Beneath the datapoints is the distribution of emission-line galaxies from the SDSS, whose number density is given by the grayscale bar on the right-hand side. Credit: Hakobyan et al. [2012].

is radiated from the shock fronts of quasar-driven outflows. Also, Simpson et al. [2006] cite radio-quiet AGN as responsible for the changing number counts, with their contribution towards the faint ($100 \leq S_{1.4\,\mathrm{GHz}} < 300\,\mu\mathrm{Jy}$) radio-source population thought to be at least 20%. However no distinction is made with respect to the source of the radio emission in these objects.

1.5 Thesis structure

In this thesis I conduct a thorough investigation of the cause of radio emission in RQQs, and in the next chapter explain the selection criteria used to create a new sample of quasars. For this I exploit the greater depth of the VISTA Deep Extragalactic Observations (VIDEO) compared to the Sloan Digital Sky Survey (SDSS), and include spectroscopic confirmation from the Southern African Large Telescope (SALT). The analysis of these objects, in terms of their radio emission, is described in Chapter 3. In Chapter 4 I detail the reduction of radio data from the Karl G. Jansky Very Large Array (JVLA), for a sample of RQQs belonging to the *Spitzer-Herschel* Active Galaxy Survey (SHAGS). This is followed by analysis of their emission in Chapter 5. Finally, in Chapter 6 I present a summary of my findings and suggestions for future work. AB magnitudes are used throughout this thesis (see Table 2.1 for conversions to Vega), and I use a ΛCDM cosmology, with $H_0 = 70\,\mathrm{km\,s^{-1}\,Mpc^{-1}}$, $\Omega_m = 0.3$, $\Omega_\Lambda = 0.7$.

2

Quasar selection with VIDEO, and SALT spectroscopy

> "When we first came here, we were cold and we were clear,
> with no colours on our skin, we were light and paper thin"
> – Florence + the Machine, *Spectrum*

Many quasar studies over the past decade have been based on photometry and spectroscopy from the Sloan Digital Sky Survey [SDSS; York et al. 2000]. However, this limits the science to those systems that have high accretion-rates and/or large supermassive black-holes (SMBHs). In order to understand what processes govern the emission from quasars with low accretion-rates and/or lower black-hole masses, we must exploit deep, multi-wavelength data. In this chapter I describe how I use the VISTA Deep Extragalactic Observations (VIDEO) survey to construct a sample of 74 candidate quasars (Section 2.2), followed by the optical spectroscopy that is used to confirm 26% of the sample (Section 2.3). I then outline how I derive photometric redshifts and absolute i-band magnitudes via a template quasar spectrum (Section 2.4). The analysis of these quasars is presented in Chapter 3.

Table 2.1: Multi-wavelength data used over the XMM3 tile of the VIDEO survey, which is centred at RA(J2000) = 02:26:18, DEC(J2000) = -04:44:00. CFHTLS–D1 = Canada–France–Hawaii Telescope Legacy Survey Deep field 1, covering 1 deg^2 within the XMM3 tile. VIDEO = VISTA Deep Extragalactic Observations. SWIRE = *Spitzer* Wide-area InfraRed Extragalactic. IRAC = InfraRed Array Camera

Survey name	Band	Wavelength (μm)	Point-source sensitivity (AB mag, 5σ)	Vega offset
CFHTLS–D1	u	0.38	27.4	-0.434
CFHTLS–D1	g	0.48	27.9	0.078
CFHTLS–D1	r	0.63	27.6	-0.165
CFHTLS–D1	i	0.77	27.4	-0.402
CFHTLS–D1	z	0.89	26.1	-0.536
VIDEO	Z	0.88	25.7	-
VIDEO	Y	1.02	24.5	-0.614
VIDEO	J	1.25	24.4	-0.929
VIDEO	H	1.65	24.1	-1.375
VIDEO	K_S	2.15	23.8	-1.836
SWIRE	IRAC 1	3.60	22.5	-
SWIRE	IRAC 2	4.50	22.1	-
SWIRE	IRAC 3	5.80	19.7	-
SWIRE	IRAC 4	8.00	20.0	-

2.1 Data

The aim is to study the radio properties of a sample of quasars, with zero contamination from inactive galaxies, as a function of luminosity and redshift. (Hereafter I describe such a sample as being ‘clean’.) For this I require multi-wavelength observations for the initial selection and for determining photometric redshifts. I also use follow-up spectroscopy of a subsample of the quasars, as a check on the selection to low fluxes and photometric-redshift accuracy. These data are described below, and a summary of the imaging data, used for Chapters 2 and 3, is provided in Table 2.1. This table also gives the values used to convert between the AB and Vega magnitude systems, i.e. $\mathrm{mag}_{\mathrm{Vega}} = \mathrm{mag}_{\mathrm{AB}}+$Vega offset. Such offsets are calculated only for the bands used in SED-fitting (Section 2.2.2). The final area over which I select the candidate quasars is 1 deg^2, as determined by the extent of the Canada–France–Hawaii Telescope Legacy Survey Deep field 1 (CFHTLS-D1; see Section 2.1.2).

2.1.1 Near-infrared: VIDEO

My primary selection relies on near-infrared photometry and I use the 5-band near-infrared $ZYJHK_\mathrm{S}$ data from the VISTA Deep Extragalactic Observations (VIDEO) Survey [Jarvis et al., 2013], over the XMM3 tile, which spans 1.5 deg^2 in area. The VIDEO imaging has a typical seeing of <0.9 arcsec, and a 2-arcsec diameter aperture was used for the measurements. The photometric uncertainties were determined by placing the aperture on regions of blank sky within the VIDEO images and constructing a histogram of the flux values. The 1-σ uncertainties, measured by fitting a Gaussian to this histogram, were used directly during the fitting of spectral energy distributions (SEDs, Section 2.2.2).

2.1.2 Optical: CFHTLS and VVDS

The CFHTLS provides photometry in $ugriz$ over 1 deg^2 of the VIDEO–XMM3 field [Gwyn, 2012]. This deep field (labelled 'D1') is centred at RA(J2000) = 02:25:59, DEC(J2000) = -04:29:40, and again I use a 2-arcsec aperture for the photometry. Note that the MegaCam filters used are not identical to those of SDSS, and that the i filter needed to be replaced partway through the survey. The band referred to in Table 2.1 is the original i'_1 filter, as images with the new, slightly bluer, i'_2 filter were not used for the Deep Field stacks.

The Visible Multi-Object Spectrograph (VIMOS) VLT Deep Survey (VVDS) provides a catalogue of spectroscopic redshifts selected with $17.5 \leq i \leq 24.75$, with a spectral resolution of $R \approx 230$ in two deep fields, VVDS–CDFS and VVDS–02h [Le Fèvre et al., 2013]. I use data from the VVDS–02h field, which overlaps entirely with the VIDEO–XMM3 and CFHTLS–D1 fields over an area of 0.61 deg^2.

2.1.3 Radio: VLA

To investigate the level of radio emission in the quasars I use radio data, at 1.4 GHz, from the VLA–VIRMOS Deep Field [Bondi et al., 2003]. The area covered is 1 deg^2, centred at RA(J2000) = 02:26:00, DEC(J2000) = -04:30:00, again completely contained within the VIDEO–XMM3 field. The average rms noise of the radio map is 17.5 μJy and the restoring beam is a 6-arcsec × 6-arcsec Gaussian. Bondi et al. [2003] create a catalogue of all radio components with peak flux $S_P > 60\,\mu\mathrm{Jy}$ ($\sim 3.5\sigma$), resulting in 1054 radio sources, with 19 thought to be multi-component. These data have previously been cross-matched with the VIDEO survey data by McAlpine et al. [2012].

2.1.4 Mid-infrared: SWIRE

To check my quasar selection method, I use *Spitzer*/IRAC (InfraRed Array Camera) imaging from the *Spitzer* Wide-area InfraRed Extragalactic (SWIRE) survey that completely overlaps with the VIDEO–XMM3 field. This allows dust, associated with star-forming regions and AGN, to be traced out to $z \sim 3$ [Lonsdale et al., 2003]. The IRAC fluxes (in µJy) are from Version 2 of the SWIRE catalogue and have already had aperture corrections applied. I follow the recommendation to use 'aperture 2', which gives the flux measured with an aperture of radius 1.9 arcsec and results in the signal-to-noise ratio being maximised. Note that the SWIRE data do not need to be aperture-matched with the VIDEO and CFHTLS photometry as they are not used alongside these two datasets during the SED-fitting procedure (Section 2.2.2).

2.2 Quasar selection

Many studies have used multi-colour photometry to define clean samples of quasars, free from contamination by stars and galaxies. Mortlock et al. [2012] used optical and near-infrared data, whilst Richards et al. [2006a] used optical and mid-infrared data. In this chapter I use a combination of optical and near-infrared for my selection, to fainter magnitudes than previous work, and check the robustness of my selection using mid-infrared data.

In assessing whether radio emission from quasars is due to star formation in the host or from the accretion process, my key concern is to ensure a high reliability, at the expense of completeness. I therefore impose a series of cuts to maximise the reliability of my sample. Maddox et al. [2008] showed that the $J - K$ colour is very effective at selecting quasars, with the fraction being missed due to dust-reddening determined to be less than 10%. This is because there is an excess in the $J-K$ colour for quasars – even those reddened by dust – compared to that for foreground stars. Such stars may have *optical* colours similar to the quasars, but near-infrared colour allows them to be distinguished [Warren et al., 2000]. To exploit this, I therefore start by selecting all objects in the VIDEO K_S-band brighter than the 5-σ limit of $K_S = 23.8$, as detailed in Jarvis et al. [2013].

2.2.1 K-band selection

I expect the vast majority of quasars to outshine their host galaxies in the K_S band, and therefore impose a morphology cut based on the SExtractor K_CLASS_STAR parameter [Bertin and Arnouts, 1996]. This is a measure of the compactness of a source on a scale of 0 to 1, with 1 representing a point-like appearance. To check the effectiveness of K_CLASS_STAR as a morphology indicator, I select stars from the VIDEO catalogue using $giJK_S$ colours (Figure 2.1). Following the method of Baldry et al. [2010], Jarvis et al. [2013] show that the region of colour space defined as $J - K_S - f_{\rm locus}(g - i) < 0.1$ provides a clean stellar-sample, free from contamination by galaxies. Figure 2.2 shows the value of K_CLASS_STAR as a function of K_S-band magnitude for these objects, and I see that my point-source classification is robust down to $K_S = 22.8$. Therefore imposing a restriction on the morphological parameter, K_CLASS_STAR > 0.9, effectively means that I should eliminate objects with $K_S \geq 22.8$.

As a further check, since I will rely on this morphology parameter for quasars rather than stars, Boris Häussler created a set of simulated AGN for me to analyse. This was done by adding a point source, representing the output from the quasar nucleus, to the image of a model host galaxy. The latter are simulated following the methodology of Häussler et al. [2007], using a Sérsic index of 4. For numerous steps in the total K_S-band magnitude, different values of AGN magnitude ($m_{\rm AGN}$), galaxy magnitude ($m_{\rm galaxy}$), and effective radius for the host ($r_{\rm eff}$) are assigned. Exact details for the parameters used to simulate the AGN-plus-host-galaxies are shown in Table 2.2.

Boris Häussler then ran SExtractor on the simulated images, outputting the K_CLASS_STAR value for each object. Next, for each subset of the resulting catalogue – defined by a particular combination of total magnitude (K_S), $m_{\rm AGN}$ and $m_{\rm galaxy}$ – I calculated the fraction of objects with K_CLASS_STAR > 0.9 (Table 2.3). This provides an estimate of the de-

Table 2.2: The parameter values used to simulate AGN and their host galaxies. The magnitudes of the AGN and the host are constrained by the assigned combination of total magnitude, K_S, and flux ratio, $f_\mathrm{AGN}/f_\mathrm{total}$. To clarify, $f_\mathrm{total} = f_\mathrm{AGN} + f_\mathrm{galaxy}$.

Parameter	Min.	Max.	Distribution
K_S magnitude	18.0	23.5	In steps of 0.5
$f_\mathrm{AGN}/f_\mathrm{total}$	0.0	1.0	In steps of 0.1
r_eff/arcsec	0.3	2.1	In steps of 0.3

tection completeness (with respect to the AGN), for different ratios of AGN flux (f_AGN) to total flux (f_total), when this morphological cut is made.

A simulated AGN that has been correctly classified as point-like will have a K_CLASS_STAR value close to 1. My results show that for the brightest objects, with $K_\mathrm{S} < 19.0$, the AGN must account for at least 90% of the total flux if over 90% are to have K_CLASS_STAR > 0.9. This corresponds to the AGN needing to outshine its host galaxy by over two orders of magnitude. The reason for this is that the host galaxies belonging to such bright systems are themselves bright, and so their extended appearance influences the K_CLASS_STAR measurement. However, I do not expect this to greatly bias my sample as very few quasars in my sample have $K_\mathrm{S} < 19.0$. Over the more-populated range of $19.0 \leq K_\mathrm{S} \leq 21.5$ (due to the shape of the quasar luminosity function and depth of our data), I am able to recover over 90% of the simulated AGN provided that their flux is $\geq 50\%$ of the total flux. I find that the distribution of r_eff for the host galaxy over this regime has no influence on the K_CLASS_STAR values.

To achieve $\geq 90\%$ completeness over $21.5 \leq K_\mathrm{S} \leq 22.5$, I find that the AGN's contribution to the total flux must rise again to at least 70%. This means that I should be aware of possible contamination from the host galaxy, as a consequence of using the K_CLASS_STAR > 0.9 cut across this magnitude range. For total magnitude $K_\mathrm{S} > 22.4$, no level of contribution from AGN to the total flux ($f_\mathrm{AGN}/f_\mathrm{total}$) allows me to attain even 50% completeness. Therefore I impose a cut of $K_\mathrm{S} \leq 22.4$, in addition to using K_CLASS_STAR > 0.9 as a selection criterion, which ensures that the morphology of the candidates is reliable. Whilst this means that I may be biased towards the brightest quasars and faintest host galaxies, such a conservative approach is sufficient for the purpose of this investigation. Such a bias works in a way that strengthens the conclusions I

Table 2.3: The fraction of simulated objects having K_CLASS_STAR > 0.9, for a given combination of AGN flux (f_{AGN}) and total flux (f_{total}), as a function of total magnitude, K_{S}.

	Total magnitude, K_{S}											
$f_{\mathrm{AGN}}/f_{\mathrm{total}}$	**18.0**	**18.5**	**19.0**	**19.5**	**20.0**	**20.5**	**21.0**	**21.5**	**22.0**	**22.5**	**23.0**	**23.5**
0.0	0.00	0.00	0.00	0.00	0.00	0.00	0.00	0.00	0.01	0.00	0.00	0.00
0.1	0.00	0.00	0.01	0.03	0.02	0.06	0.03	0.04	0.04	0.00	0.00	0.00
0.2	0.00	0.09	0.10	0.14	0.09	0.12	0.15	0.13	0.06	0.00	0.00	0.00
0.3	0.03	0.25	0.36	0.31	0.31	0.36	0.49	0.35	0.04	0.00	0.00	0.00
0.4	0.75	0.85	0.98	0.94	0.82	0.85	0.83	0.69	0.20	0.00	0.00	0.00
0.5	0.86	0.88	1.00	1.00	1.00	1.00	0.98	0.88	0.37	0.00	0.00	0.00
0.6	0.68	0.83	1.00	1.00	1.00	1.00	1.00	0.99	0.64	0.00	0.00	0.00
0.7	0.07	0.24	1.00	1.00	1.00	1.00	1.00	1.00	0.91	0.00	0.00	0.00
0.8	0.21	0.99	1.00	1.00	1.00	1.00	1.00	1.00	0.95	0.02	0.00	0.00
0.9	1.00	1.00	1.00	1.00	1.00	1.00	1.00	1.00	0.99	0.13	0.00	0.00
1.0	1.00	1.00	1.00	1.00	1.00	1.00	1.00	1.00	1.00	0.17	0.00	0.00

draw regarding the radio emission, as explained in Section 3.1.4.

2.2.2 Photometric fitting

Optical bands alone have in the past been used to define a colour space for quasar selection [e.g. Richards et al., 2001]. However their success in separating the regions occupied by stars and quasars diminishes at high redshifts, and they are especially affected by dust-reddening. Instead I follow the method of Maddox et al. [2008] and use gJK_{S} colour space (Figure 2.3). I also use full SED modelling, as inactive galaxies may still be present amongst the potential quasar candidates, contaminating my sample. Fitting SED templates to the VIDEO–CFHTLS–D1 data was carried out using Le PHARE [Ilbert et al., 2006].

There are 62 galaxy templates, based on the SEDs compiled by Coleman et al. [1980] and those of starburst galaxies. In combination with different extinction law values, these produce 187 sets of model photometry that are then redshifted. A range of extinction values are also used in conjunction with the stellar library, consisting of 254 templates, and the 10 empirical SEDs that make up the AGN library.

These AGN templates are taken from the SWIRE template library [Polletta et al., 2007]. Two of them, 'Sey18' and 'Sey2', represent moderately-luminous Seyfert galaxies. The 'I19254' template is from IRAS19254-7245, a starburst/ULIRG (ultra-luminous infrared galaxy) with Seyfert-2 galaxy properties. Another ULIRG is included in the form of 'Mrk231', which has a heavily-obscured quasar at the centre. Like 'I19254' and the 'N6240' AGN template, its SED is an AGN-starburst composite.

Hatziminaoglou et al. [2005] used an optically-selected sample of 35 SDSS/SWIRE Type-1 quasars to construct the three Type-1 quasar templates ('QSO1', 'BQSO1', 'TQSO1'), via a quasar composite spectrum in addition to rest-frame infrared data. The difference between them is their IR/optical flux ratios, with 'BQSO1' representing the bottom quartile and 'TQSO1' the top quartile. Finally, the 'QSO2' and 'Torus' templates are typical SEDs for Type-2 quasars, with the second of these having greater dust obscuration. I determine the best fit for both redshift and extinction using each of the SED libraries ('star', 'galaxy' and 'AGN').

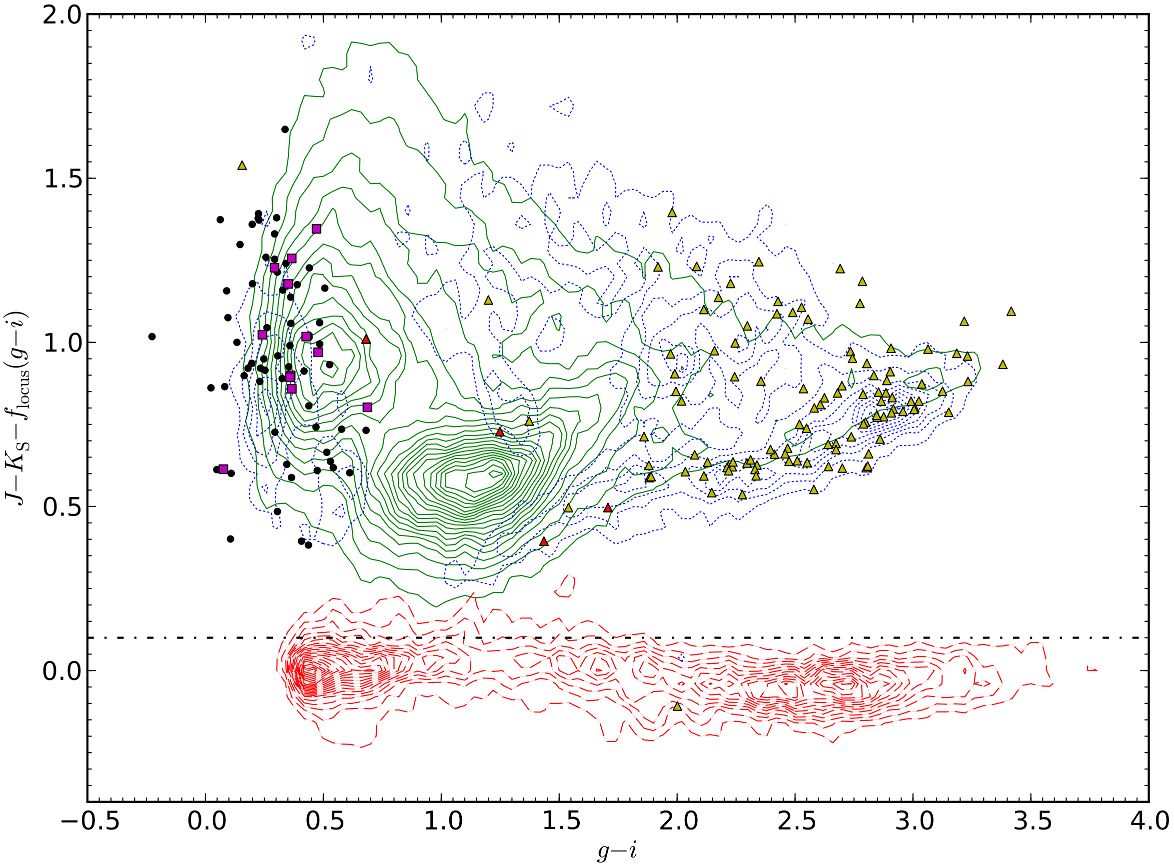

Figure 2.1: The position of all VIDEO objects in $giJK_S$ colour space. Red contours (dashed, with interval of 2 objects) correspond to the number of objects best fit by a star template, via the LE PHARE code (Section 2.2.2). Green contours (solid, interval = 10) are for those best fit by a galaxy template, and blue contours (dotted, interval = 2) correspond to an AGN template. The AGN and galaxy loci begin to blend into one another, whilst the objects below the black (dash-dotted) line are used to create a clean sample of stars (Figure 2.2). Overplotted are objects from the 'Gold' candidate quasar subsample (black dots, Section 2.2.2), including those that are cross-matched with VVDS (magenta squares, Section 2.3.1). In addition are VIDEO objects cross-matched with VVDS but lying outside the Gold selection region, either with broad emission-lines (red triangles) or without (yellow triangles). The definition of $f_{\rm locus}(x)$, where $x = g - i$, is as follows: for $x \leq 0.3$, $f_{\rm locus}(x) = -0.6127$; for $0.3 < x \leq 2.3$, $f_{\rm locus}(x) = -0.79 + 0.615x - 0.13x^2$; for $x > 2.3$, $f_{\rm locus}(x) = -0.0632$.

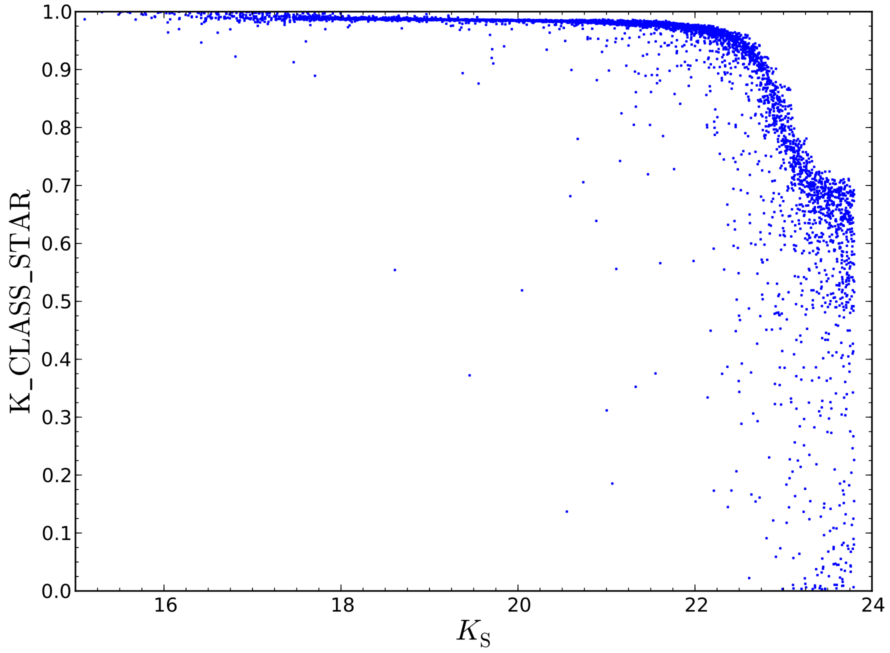

Figure 2.2: The variation in K_CLASS_STAR, an indicator of compactness (1 = point-like), for a clean sample of stars. Each of these objects are K_S-band selected ($K_S \leq 23.8$) in the VIDEO catalogue, and have stellar colours using the locus shown in Figure 2.1.

Figure 2.3 shows the gJK_S colour space for the point sources in the VIDEO K_S-band selected catalogue where one of the ten AGN SEDs provides a better fit to the photometry than the galaxy or star templates. Point-like objects that are best fit by a stellar template are predominantly found in the light-blue, hatched region. Therefore the data points that lie within this region represent objects with stellar gJK_S colours, despite their photometry being better-modelled by an AGN SED. The blue, dotted line in Figure 2.3 is the evolution track for a model quasar that has no host-galaxy contamination, and follows a path that lies between the star and galaxy regions.

I also show the broad region occupied by the galaxy tracks that are used by Le PHARE (shaded grey in Figure 2.3). Some of the AGN template-fitted data points are well-separated from the galaxy region, whilst others have greater overlap. Those that remain 'clear' from the galaxy locus are subsequently referred to as the 'Gold candidate quasar sample'. This Gold selection region is demarcated by a green, dashed line in Figure 2.3, as defined by the following straight-line equations, where $x = J - K$ and

$y = g - J$:

$$x = -0.30, \tag{2.1}$$

$$y = -1.00 \qquad -0.30 < x < 1.10, \tag{2.2}$$

$$y = 0.65 \qquad -0.30 < x < 1.10, \tag{2.3}$$

$$x = 1.10. \tag{2.4}$$

I use the descriptor ‘Gold’ simply to distinguish the candidates that I am confident of being quasars. (Additional samples, labelled ‘Silver’ for example, could be constructed using more-relaxed selection criteria.) The Gold sample comprises 75 quasars, with one later being removed as the result of an absolute i-band magnitude cut (Section 2.4.2). I deem the slight overlap with the galaxy tracks (shaded region) as acceptable given the photometric uncertainties. The selected objects are best-fitted by Type-1 quasar models: ‘QSO1’, ‘BQSO1’ and ‘TQSO1’, and I later see where they lie in mid-infrared colour space (Section 2.2.3). Valuing reliability over completeness, I choose not to extend the selection region downwards to include a few extra points fitted by Type-1 quasar models. This is because, with their positions lying well within the shaded region, there is a greater chance of their gJK_{S} colours being confused for galaxies. Similarly, the selection region is not extended bluewards to include the BQSO1 objects around $J - K_{\mathrm{S}} = 0.5$, $g - J = 0.5$, as doing so may introduce contamination by stars.

A similar method is used by Maddox et al. [2012] to construct a sample of quasars, whose K-band magnitude range is $15.8 \leq K \leq 18.4$. They are able to achieve $> 95\%$ efficiency and $> 95\%$ completeness with respect to known SDSS quasars. In addition, both methods incorporate information from SED fitting. Doing so enables me to be conservative in my selection, resulting in a clean sample of candidates. However, in contrast, my candidates are much fainter due to the depth of the photometry used, spanning $18.4 \leq K_{\mathrm{S}} \leq 22.4$. The light from the host galaxy could lead to greater contamination as I go deeper, but my selection (via morphology and colour information) ensures that the quasar is dominating the total flux from the system.

As a result of my selection criteria, I actually have very good completeness with

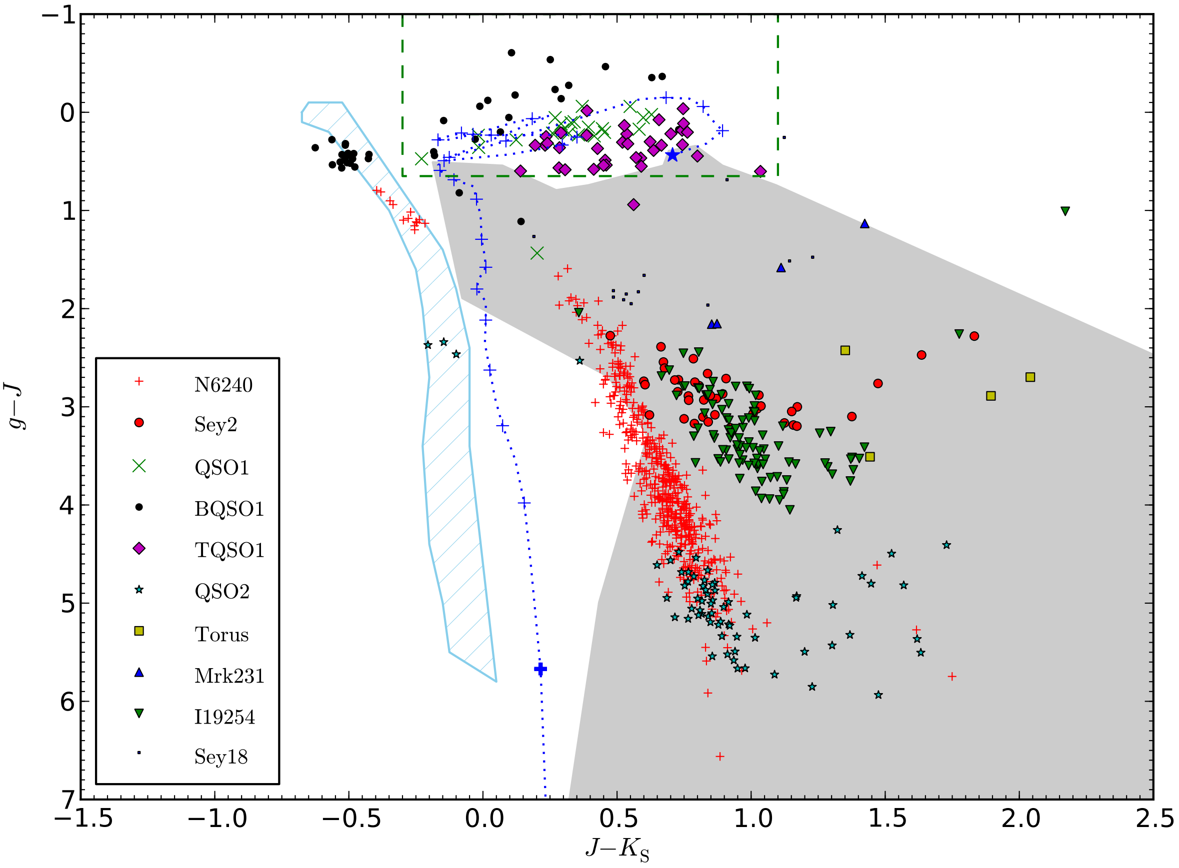

Figure 2.3: The positions of point-like objects (i.e. those with K_CLASS_STAR > 0.9) in gJK_s colour space, following Maddox et al. [2008]. Each of these data points has photometry that is best fit by one of 10 AGN templates (see legend, and their description in Section 2.2.2). The light-blue, hatched region represents the stellar locus, occupied by VIDEO objects for which a stellar template provides the best fit to the photometry. The blue dotted track is a model for how a quasar with no host-galaxy contamination evolves with redshift, lying between the stellar and galaxy loci (to the left and right, respectively). The redshift range of this track is $0.0 \leq z < 5.0$, with a blue star marking $z = 0.0$ and blue '+' markers every $\Delta z = 0.2$ (with a bold marker denoting $z = 4.8$). The grey, shaded region is the area covered by evolution tracks for the photometric fitting code's library of galaxy templates. The redshift range of these galaxy tracks is $0 \leq z < 6$, with colours evolved for each step of $\Delta z = 0.04$ taken. The region used to select 'Gold' candidate quasars is demarcated by a green, dashed line.

respect to *unobscured* quasars, as the majority of Type-1 sources lie in the selection region (demarcated by the green, dashed line in Figure 2.3). The SEDs that I have excluded are for composite systems or obscured AGN. This means that my sample is not representative of the entire quasar population, and so I emphasise that my investigation accounts for the radio emission from Type-1 quasars only. Also, the use of near-infrared data may lead to a bias towards bright quasars residing in faint host-galaxies. This is because a host that is bright in the K_S band may have an extended appearance in the imaging data, causing the object to be eliminated by the morphological cut. This potential bias is discussed in the context of my final results in Section 3.1.4.

2.2.3 Mid-infrared colour

As an additional check on the validity of my selection, I use *Spitzer* data to investigate where the Gold candidate quasars lie in mid-infrared colour space. Dust extinction is not a problem when measuring emission in the mid-infrared, and so both unobscured and obscured AGN can be detected. However, I note that my Gold candidates are biased towards the *unobscured* population, given the photometric fit to Type-1 quasar SEDs. To check what proportion are indeed active-galaxy candidates, I use the work of Lacy et al. [2004] and Stern et al. [2005].

Lacy et al. [2004] use the 8.0 µm/4.5 µm ratio versus the 5.8 µm/3.6 µm ratio to separate stars, low-redshift galaxies, SDSS quasars and radio-selected quasars. Within this colour space they find that there are two distinct sequences, the quasars belonging to one and the remaining objects to the other. I refer to the region that contains the quasar sequence as the 'Lacy wedge'.

The tendency of AGN to be redder than galaxies in the mid-infrared is also exploited by Stern et al. [2005], who use a [3.6] – [4.5] versus [5.8] – [8.0] colour-colour space. The combination of restricted [5.8] – [8.0] colours observed for powerful AGN (due to a lack of strong PAH emission) with their [3.6] – [4.5] colour (much redder than that of low-redshift galaxies) leads to another clear selection region. I call this the 'Stern wedge'.

I find that 62 of my 75 Gold quasar sample have cross-matches in the SWIRE catalogue. Due to the depth of the mid-infrared data, only 35 of these have detections in

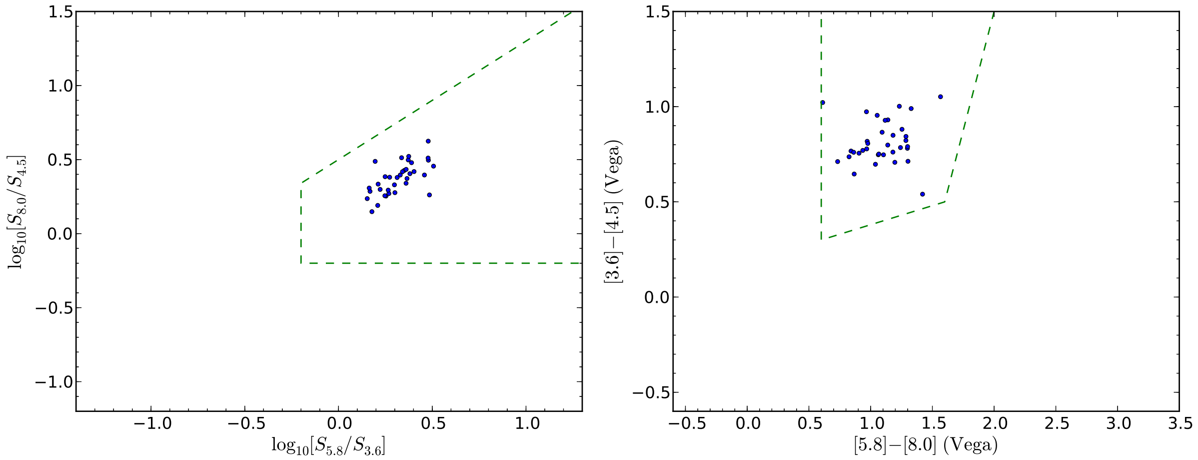

Figure 2.4: Gold objects that have mid-infrared data are shown, following Lacy et al. [2004] (left) and Stern et al. [2005] (right). The dashed lines outline the regions that these authors use to select active-galaxy candidates.

each of the 4 bands, IRAC 1-4. Hence I use this as a consistency check on the brighter candidates, rather than an additional step in the selection. Figure 2.4 shows that all of the Gold sample (with detections in all 4 bands) lie within the Lacy and Stern wedges. This provides further evidence that my quasar selection method is robust.

2.3 Spectroscopy

Spectroscopy enables the properties of objects to be studied with much finer wavelength-resolution than can be obtained with photometry. This allows broad emission-lines to be detected, leading to the straight-forward identification of quasars. However, blind spectroscopic-surveys like the Visible Multi-Object Spectrograph (VIMOS) VLT Deep Survey (VVDS) are expensive to conduct, and so must be confined to small areas. It is therefore worthwhile investing effort into optical and infrared selection, so that the efficiency of spectroscopic follow-up is improved.

In this section I use spectroscopic data to carry out a further check of the robustness of my sample selection, in addition to obtaining accurate redshift information. Existing spectroscopy comes from the VVDS, over the XMM3 tile within the VIDEO field. This is complemented by new spectroscopy for objects belonging to the Gold sample, using the Southern African Large Telescope (SALT). I discuss how the spectroscopic redshifts compare to the photometric redshifts obtained from the template fitting in Section 2.4.1.1.

2.3.1 VVDS data

I cross-matched all of the objects that had best-fit SEDs of an AGN (obscured, unobscured, or Seyfert-like) with the VVDS, using a matching radius of 1 arcsec. This identifies 127 objects with spectroscopic redshifts over the 0.61 deg^2 covered by the VVDS–02h field, twelve of which are in the Gold sample. Each of these 12 objects have broad emission-lines, again showing that I have a good basis for selecting quasars. They also lie in the quasar region of $giJK_{\mathrm{S}}$ colour space (magenta squares in Figure 2.1), as identified by Baldry et al. [2010].

The remaining 115 cross-matches lie in the galaxy locus of both $giJK_{\mathrm{S}}$ space (triangles in Figure 2.1) and gJK_{S} space (Figure 2.3). According to the VVDS redshift flags, 7 of them have broad emission-lines, meaning that they are more likely to be quasars. However, inspection by eye reveals that this is actually the case for only 5 of the objects, one of which is a broad absorption line (BAL) quasar. I also confirm that reliable redshifts have been obtained for each of these 5. They appear as red triangles in Figure 2.1, with one lying beyond the plot range of the figure. Their colours are redder than the Gold quasar candidates, and lie in the region of gJK_{S} colour space covered by galaxy evolution tracks, hence their exclusion from my sample. These extra quasars highlight the incompleteness of the Gold sample, although I emphasise my aim for a highly-reliable selection method instead. The 110 cross-matched objects that show no broad emission-lines, yet are best fit by an AGN template, may be obscured AGN.

2.3.2 SALT spectra

13 quasars from the Gold sample were observed between 4th November 2012 and 6th January 2013, using the Robert Stobie Spectrograph [Kobulnicky et al., 2003] on SALT [Buckley et al., 2006]. The PG0900 grating was used with the PC03850 filter, to obtain coverage over 4500–7500 Å. A 2-arcsec slit, and a resolving power of $R = \lambda/\Delta\lambda \approx 600$, provided adequate resolution (10 Å) for measuring redshifts from broad emission-lines.

I completed 'Phase II' of the corresponding proposal, which involved compiling the scheduling blocks, based on the observing conditions required for each object and constrained by the total time that had been allocated. I also needed to provide finding charts,

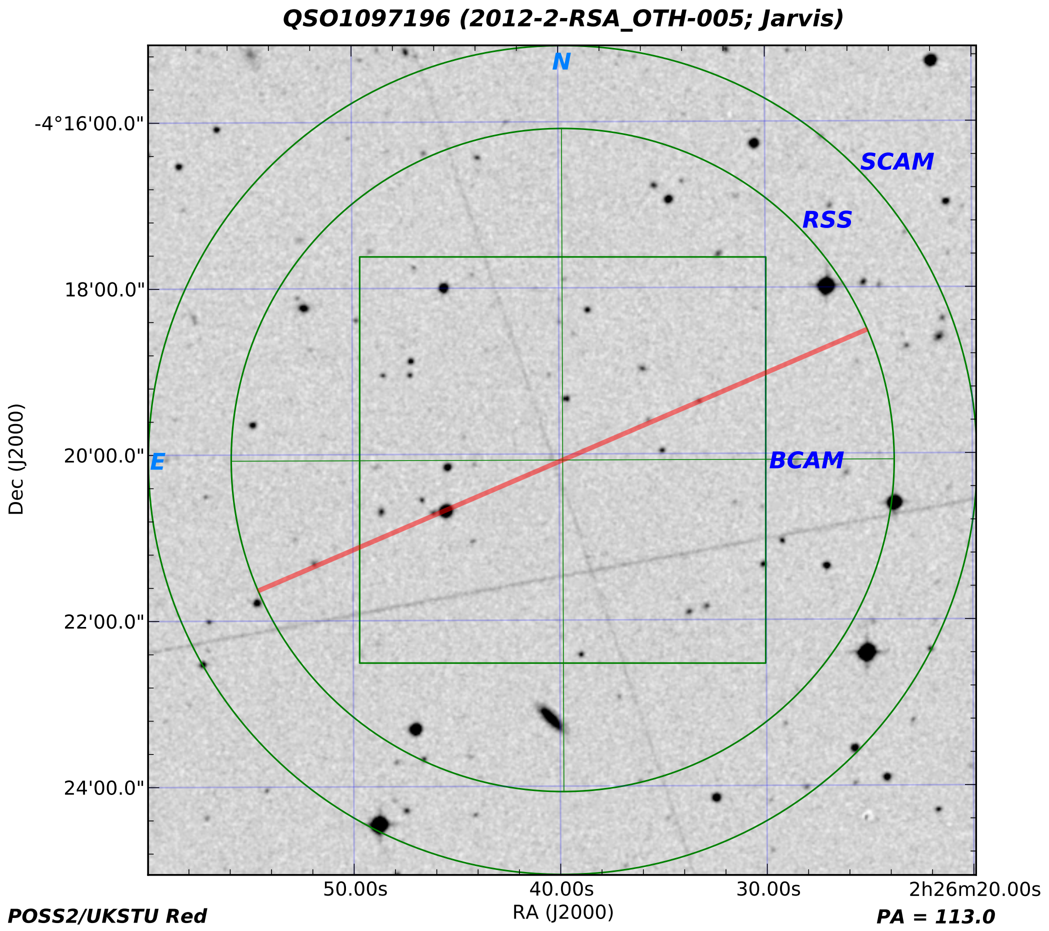

Figure 2.5: A SALT finding chart for acquisition of a quasar, located at the cross-hairs (RA = 02:26:39.83, Dec = -04:20:04.4). The spectrum for this object appears in panel (iii) of Figure 2.6.

such as Figure 2.5, since most targets are fainter than the $V = 17$ magnitude limit of the acquisition camera. The position angle of the long slit (represented by the red line in Figure 2.5) was set so that it intersected both the target and a nearby bright star. The target was then placed at the centre, to mitigate vignetting effects.

As part of the reduction of SALT spectra, the steps listed in the left-hand column of Table 2.4 are completed when raw data is passed through the SALT PyRAF pipeline [Crawford et al., 2010]. I then performed the tasks listed in the right-hand column, using standard procedures in IRAF software. The importance of these steps is explained below.

1. **Flat-fielding:** Spectroscopic lamp flats were obtained, although unfortunately not for each night of observation. These enable variations in pixel-to-pixel sensitivity to be removed, and distortions in the optical path to be corrected for. Given that the flat images have a large number of photon counts per pixel, compared to the counts

Table 2.4: The steps used to reduce SALT spectra.

Within the SALT pipeline	Completed by end user
Fidelity checking	Flat-fielding
Gain correction	Cosmic-ray rejection
Cross-talk correction	Wavelength calibration
Bias subtraction	Background subtraction
Amplifier mosaicing	Flux calibration

per pixel for the science images, it is important to first normalise the flats using the median value. Therefore, when they are used to correct the science frames, the multiplicative errors are transferred without significantly changing the pixel values.

2. **Cosmic-ray rejection:** Cosmic rays appear in the images usually as very bright spots, as a result of hitting only a single pixel of the detector. Those arriving at a more-inclined angle may lead to a bright streak instead. To eliminate these artefacts, three exposures were made for each target, with individual exposure times of 150, 200 and 400 seconds, according to the apparent magnitude of the object. The count for a particular pixel is compared across the three images, with a sigma-threshold set to remove unusually high pixel-values. In addition, the sharp-edge appearance of cosmic rays in an image also allows them to be easily identified and removed.

3. **Wavelength calibration:** Also referred to as 'arc calibration', this involves shining a lamp with emission lines at known wavelengths – an argon lamp in this case – onto the grating used. The angle of the grating with respect to the slit leads to the emission lines having a curved appearance in the 2D image. By correcting for this distortion, and applying it to the science targets, it is possible to create images where all pixels along the slit (i.e. along the non-dispersion axis) correspond to a single wavelength. Such calibration is vital for obtaining an accurate redshift later. Since IRAF struggled with fitting a polynomial to the large curvature of the emission lines seen with SALT, the 2D images were cropped in the slit direction, closer to the target, to avoid this problem.

4. **Background subtraction:** So that an accurate spectrum can be extracted, where all of the light is solely due to the science target concerned, the thermal contribution

made by the sky background needs to be removed. This is done by defining regions either side of the target, along the slit dimension. A polynomial is then fitted to these strips, extrapolated over the target itself, and subtracted from the 'total flux' spectrum. Doing so also removes the sky emission-lines that originate from elements such as oxygen in the atmosphere. An added advantage for this setup is that I could also fit the profile of the bright star used to acquire the target, as its light smoothly varied as a function of slit position.

5. **Flux calibration:** For flux calibration, LTT 1020 was used as the standard star. Observing such a spectrophotometric standard, whose spectrum is well-known, means that photon counts can be converted into flux units and the intensity calibrated as a function of wavelength. To do this, the above reduction steps are carried out for the standard in addition to the science targets. The continuum emission of the extracted spectrum is then fitted, and scaled to match that of the known spectrum. A test that this calibration has been successful is to integrate the total flux and check that the V-band magnitude, derived from this flux, agrees with the expected value of $V = 11.52$. Once satisfied, the same scaling/unit conversion can be applied to each of the targets.

The resulting fully-reduced spectra, extracted from the calibrated images, are presented in Figure 2.6. (Chip gaps are over the ranges $5500 \lesssim \lambda/\text{Å} \lesssim 5545$ and $6550 \lesssim \lambda/\text{Å} \lesssim 6585$.) They have been smoothed with a Gaussian window that covers 20 pixels, and correspond to the 8 Gold candidates for which it was possible to determine reliable spectroscopic redshifts. These are discussed further in Section 2.4.1.1.

Prominent emission-lines are labelled, except in panel (v) where the two labels indicate resonant absorption features. As such, each of these candidates are confirmed to be quasars. C III]$_{1909}$ is found to be the most common emission-line, and also present is either a C IV$_{1549}$ or Mg II$_{2799}$ broad line. Spectra for the other 5 objects observed with SALT were poor, due to being badly affected by weather and technical difficulties. A cross-correlation method was attempted for these, to extract the most-likely redshift, but their spectra were too strongly affected by noise.

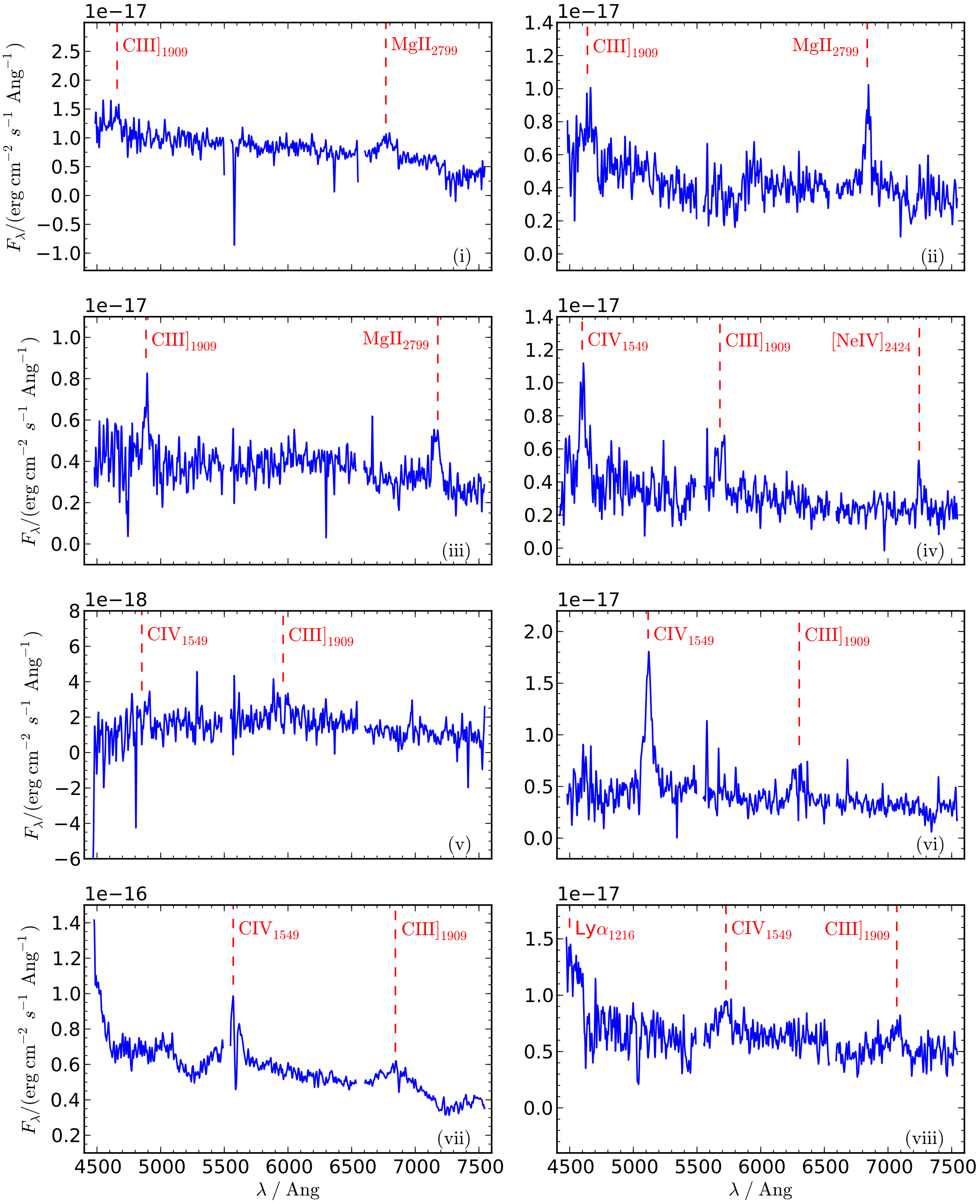

Figure 2.6: SALT spectra for 8 Gold objects: (i) A quasar at $z = 1.4$ (RA = 02:26:52.14, Dec = -04:05:57.1). (ii) A quasar at $z = 1.4$ (RA = 02:25:52.16, Dec = -04:05:16.1). (iii) A quasar at $z = 1.6$ (RA = 02:26:39.83, Dec = -04:20:04.4). (iv) A quasar at $z = 2.0$ (RA = 02:26:18.59, Dec = -04:11:01.1). (v) A quasar at $z = 2.1$ (RA = 02:26:33.31, Dec = -04:29:47.8). (vi) A quasar at $z = 2.3$ (RA = 02:26:12.64, Dec = -04:34:01.4). (vii) A quasar at $z = 2.6$ (RA = 02:27:40.55, Dec = -04:02:51.1), with possible Lyα emission at the spectrum's blue end. This is the brightest object in the Gold sample, and the only one to appear in both FIRST and NVSS radio catalogues. (viii) A quasar at $z = 2.7$ (RA = 02:27:09.03, Dec = -04:55:10.1).

2.4 The quasar sample

2.4.1 Photometric redshifts

The photometric redshifts (z_p), fitted using Le PHARE (Section 2.2.2), were compared to the spectroscopic redshifts (z_s) of the Gold objects, obtained with the VVDS and SALT. The majority are in good agreement (see Table 2.5), but there are a few cases where the photometric fitting severely underestimated the true redshift. Using the normalised median absolute deviation in $\Delta z/(1+z)$, where $\Delta z = (z_s - z_p)$, I find $\sigma_{\Delta z/(1+z)} = 0.082$ and four catastrophic outliers, where a catastrophic outlier is defined as having $|\Delta z|/(1+z) > 0.15$ [Ilbert et al., 2006]. Such inaccuracies prompted me to seek an alternative method for determining photometric redshifts.

2.4.1.1 χ^2 minimisation

I proceeded with a model quasar template provided by Paul Hewett, created so that it has no host-galaxy contribution. The colours associated with this template were evolved over the redshift range $0 < z < 7$ in steps of 0.1. I also included 0.2 mag of uncertainty to the quasar template colours to account for the variation in emission-line strength and the intrinsic quasar spectral shape. This was added in quadrature to the measured photometric uncertainties. The best fit was found through χ^2 minimisation, and I name the corresponding redshift 'Colour-z'. Colour-z values calculated for the objects with spectroscopic redshifts are presented in Table 2.5.

Figure 2.7 shows the correlation between the spectroscopic redshift, from both SALT and VVDS, and my photometric redshift. Two of the VVDS redshifts were highly discrepant, quoted to be 0.1 and 0.2 (Table 2.5). Inspection of their spectra showed that a $\mathrm{Mg{\small II}}_{2799}$ line had been mis-identified as a $\mathrm{H}\alpha_{6563}$ line. I therefore corrected the redshifts and used these values for Figure 2.7, which placed them in line with their corresponding Colour-z value. Using all of the objects with spectroscopic redshifts, the accuracy of Colour-z is $\sigma_{\Delta z/(1+z)} = 0.046$. Out of the 19 objects I find there to be three catastrophic outliers (circled in Figure 2.7). I investigated whether confusion between the $\mathrm{Mg{\small II}}_{2799}$ line and the $\mathrm{C{\small IV}}_{1549}$ line led to the catastrophic outliers with Colour-z = 0.7, and similarly

Table 2.5: Summary of redshifts for the QSOs spectroscopically confirmed by the VVDS, and those observed by SALT (except 5 for which a redshift could not be determined). * denotes a VVDS object assigned an incorrect redshift; the redshift given is my measurement (see text for details).

R.A. (hms)	Dec. (dms)	Le PHARE z	Colour z	VVDS/ SALT z
02:25:25.68	-04:35:09.6	0.4	2.1	2.1
02:25:45.53	-04:34:45.6	1.7	1.7	1.7*
02:25:50.38	-04:33:24.6	2.8	2.5	2.7
02:25:52.16	-04:05:16.1	1.5	1.4	1.4
02:26:09.62	-04:24:38.0	2.6	2.8	2.7
02:26:12.64	-04:34:01.4	2.2	0.7	2.3
02:26:18.59	-04:11:01.1	0.4	1.9	2.0
02:26:22.15	-04:22:21.8	2.0	1.8	2.0
02:26:24.64	-04:20:02.4	2.0	0.7	2.2
02:26:33.31	-04:29:47.8	2.4	2.4	2.1
02:26:39.83	-04:20:04.4	1.9	1.5	1.6
02:26:52.14	-04:05:57.1	1.4	1.4	1.4
02:27:07.54	-04:32:03.2	1.6	1.5	1.5*
02:27:09.03	-04:55:10.1	3.0	2.7	2.7
02:27:33.99	-04:25:23.5	1.8	1.5	1.6
02:27:36.93	-04:26:31.5	0.6	1.8	1.8
02:27:38.99	-04:09:40.8	1.4	1.3	1.4
02:27:40.55	-04:02:51.1	2.4	2.6	2.6
02:27:47.34	-04:27:53.7	0.2	2.4	1.1

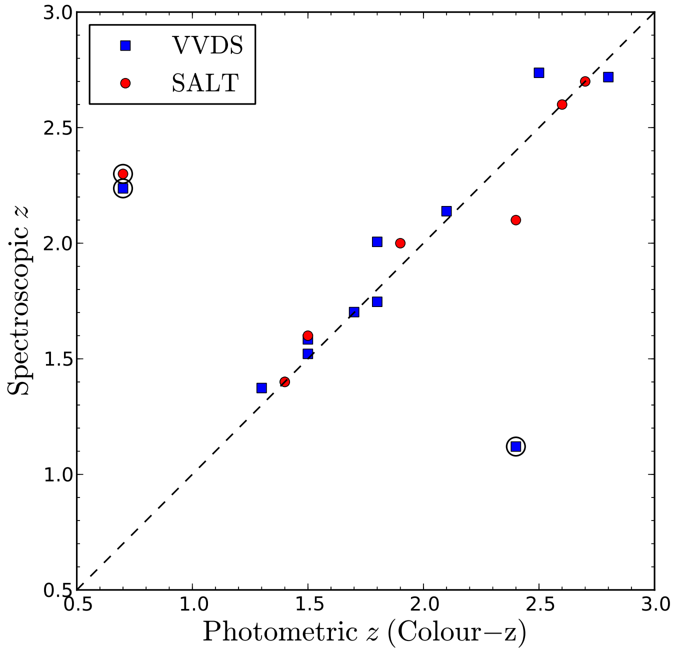

Figure 2.7: Spectroscopic redshifts, from SALT and VVDS, showing the accuracy of Colour-z as a photometric redshift, including the catastrophic outliers (circled, see text for details).

whether a C III]$_{1909}$ line was being confused for a Mg II$_{2799}$ line, resulting in the third outlier (with Colour-z = 2.4). However, in each case, the absence/presence of other expected emission-lines confirmed the previously-determined spectroscopic redshifts.

Therefore my Colour-z photometric redshift estimates perform well for the majority of quasars observed by the VVDS and SALT. However, a single spectrum is not enough to describe the variety found in the Type-1 quasar population, and for this reason I still find a number of outliers. As such, I cannot simply assume these best-fit values for the remainder of the photometric sample, for which I do not have spectroscopy. Instead I note that each of these outliers have a double-peaked probability distribution function (PDF) produced by the photometric fitting, with the secondary peak overlapping the spectroscopic redshift. This prompted me to generate 1000 Monte Carlo redshifts per Gold quasar, according to the full PDFs calculated for the Colour-z redshifts. These redshifts are used for the distribution in absolute i-band magnitudes (Section 2.4.2) and the subsequent analysis of the radio emission associated with the quasars. This therefore allows my final results to take the redshift uncertainties into account.

2.4.2 Absolute i-band magnitudes

The absolute i-band magnitude of an object (M), by definition, is a measure of its intrinsic brightness, having corrected the *apparent* magnitude (m) for the distance its light has travelled. This is done using the following equation, where D_L is the luminosity distance:

$$M = m - 5\log_{10}(D_L/10\,\mathrm{pc}). \tag{2.5}$$

Determining absolute magnitudes is necessary for understanding the underlying physical processes that take place in the object's rest frame. However, due to the finite bandwidth of filters, it is necessary to apply a K-correction function when comparing the measurements of objects at different redshifts.

2.4.2.1 K-correction

The K-correction accounts for bandwidth-smearing and spectral features that pass through the observed band. It therefore depends on the shape of the filter in question, the typical

SED for that population of objects, and the redshift. It is then possible to calculate the *K-corrected* absolute magnitude for an object at any redshift. Equation 2.5 then becomes

$$M = m - 5\log_{10}(D_L/10\,\mathrm{pc}) - K(z), \tag{2.6}$$

with the K-correction, $K(z)$, given by

$$K(z) = 2.5\log_{10}[1+z] + 2.5\log_{10}\left[\frac{\int F(\lambda')S(\lambda)\mathrm{d}\lambda}{\int F(\lambda'/(1+z))S(\lambda)\mathrm{d}\lambda}\right]. \tag{2.7}$$

The flux, $F(\lambda)$, is in units erg s^{-1} cm^{-2} Hz^{-1} and $S(\lambda)$ is the reference filter's response function [Hogg et al. 2002, Oke and Sandage 1968]. In this work, the reference filter is for the i band, and interpolations are calculated at 1 Å intervals. (A reminder that this is the original i_1 filter used by the CFHTLS, whose transmission function is closer to that of the SDSS i-filter, rather than the i_2 filter of the CFHTLS.) The redshift, z, that I use is the Colour-z value calculated in Section 2.4.1.1, and the same quasar spectrum [Hewett et al., in prep.] is used for determining the K-correction, and thus the K-corrected absolute i-band magnitudes (M_i) of my quasar sample.

For comparison, the calibration of the SDSS Data Release 9 Quasar (DR9Q) catalogue [Pâris et al., 2014] followed Richards et al. [2006a], who use a power-law spectral index of $\alpha = -0.5$ as the basis of their quasar SED. I note that the quasar spectrum used in my study is much bluer, closely following a power-law with $\alpha = -0.25$. This may be explained by existing models being empirically-derived from quasar samples of varying AGN fractions. That is, a greater proportion of the light originating from the host galaxy will lead to a reddening of the resultant spectrum. This is further pronounced for low-redshift objects, which dominate the SDSS catalogue. I therefore proceed with the model spectrum provided by Paul Hewett, as this is more suitable for the Gold quasar sample. Doing so also maintains consistency with the Colour-z values used.

2.4.2.2 The final quasar sample

To help finalise the quasar sample, I use the redshift probability distributions to calculate the probability distribution for M_i per quasar. I then impose the criterion $M_i \leq -22$, a magnitude cut that approximately splits quasars from Seyfert galaxies [e.g. Schneider et al., 2003]. I find one quasar has *no* part of its redshift probability distribution with $M_i < -22$, and so this object is removed from the sample. The properties of the final 74 quasars are given in Table 2.6. They are used for the remainder of this chapter and the analysis in Chapter 3 (Figure 2.8).

61 of these 74 objects are beyond $z = 1$ and brighter than $M_i = -22$, demonstrating the effectiveness of VIDEO+CFHTLS in detecting quasars. However, some of the objects may have an incorrect M_i, arising from an incorrect Colour-z. This is why it is important to note that I take this into account via my sampling of the photometric-redshift probability distribution. For example, the fraction of simulated objects that have $M_i \leq -22$ is used to weight the Gold quasars when analysing their radio emission in the next section. In Figure 2.9 I also show the K_S-band magnitude distribution of the final 74 quasars. Note that the majority are indeed in the range $19.0 \leq K_\mathrm{S} \leq 21.5$, as previously mentioned in Section 2.2.1.

To understand the proportion of the total quasar population that I have selected with my criteria, I use the quasar luminosity functions of Croom et al. [2009][1]. These are integrated over the redshift range of the final Gold sample, $0.5 \leq z \leq 3.1$ (Figure 2.8), for objects brighter than $M_g(z = 2) = -22.8$, which corresponds to my cut of $M_i(z = 0) = -22.0$. Using the luminosity dependent density evolution (LDDE) and luminosity evolution + density evolution (LEDE) models as lower and upper limits, respectively, these luminosity functions predict there to be between 338 and 381 quasars over 1 deg^2. My sample is therefore approximately 20% complete.

2.5 Conclusions

In this chapter I have described a robust method for the selection of RQQs in the VIDEO survey [Jarvis et al., 2013].

1. By applying a morphology cut and combining AGN template fitting with photometry, a region within gJK_S colour space is defined that successfully selects Type-1

---

[1] Note that the value given in table 4 of Croom et al. [2009] should be $\log_{10}(\Phi_0^*) = -5.99 \pm 0.07$ (S. Croom, private communication).

Table 2.6: Positions, AB magnitudes, radio flux-densities, and redshifts for the final 74 Gold quasars. z_{spec} is the SALT or VVDS redshift, where available. * This VVDS object is thought to have been assigned an incorrect redshift. The corrected value is given here.

R.A. (hms)	Dec. (dms)	u	g	r	i	z	Z	Y	J	H	K_{S}	$S_{1.4\,\mathrm{GHz}}/\mu\mathrm{Jy}$	z_{spec}
02:24:07.43	-04:45:55.5	23.08	22.83	22.67	22.34	22.27	22.52	22.06	22.42	22.27	21.88	39.69	-
02:24:09.79	-04:34:04.9	22.20	21.93	21.57	21.59	21.57	22.32	21.82	21.81	21.52	21.16	-37.39	-
02:24:09.81	-04:29:48.7	22.05	21.67	21.59	21.58	21.43	21.31	21.49	21.44	21.17	20.89	-24.96	-
02:24:09.89	-04:47:18.1	20.59	20.19	20.07	19.72	19.74	19.94	19.87	19.89	19.96	19.81	180.21	-
02:24:13.47	-04:52:10.4	21.80	21.09	21.13	21.06	20.89	21.01	20.66	20.65	20.59	20.40	-1.92	-
02:24:14.93	-04:43:53.7	22.85	22.41	22.38	22.05	22.10	21.91	22.18	22.07	21.69	21.67	-21.51	-
02:24:15.30	-04:29:55.9	22.99	22.71	22.50	22.38	22.13	22.36	22.21	22.01	21.55	20.96	21.27	-
02:24:19.75	-04:03:15.7	22.38	22.12	22.21	21.89	21.61	21.80	21.82	21.81	21.61	21.03	20.92	-
02:24:24.17	-04:32:30.0	19.99	19.81	19.66	19.28	19.50	19.71	19.96	19.89	19.62	19.75	17.35	-
02:24:30.91	-04:29:57.6	22.30	22.07	21.58	21.54	21.51	21.51	21.49	21.39	20.88	20.96	18.19	-
02:24:32.47	-04:30:37.2	21.21	21.24	20.85	20.80	21.11	20.77	20.86	20.94	20.72	20.47	5.98	-
02:24:32.93	-04:47:42.2	20.68	20.43	20.38	20.28	20.11	20.50	20.61	20.69	20.52	20.01	14.95	-
02:24:34.34	-04:32:00.4	20.56	19.87	19.85	19.82	19.65	19.78	19.56	19.53	19.48	19.53	78.54	-
02:24:34.90	-04:35:49.9	23.28	22.40	22.22	22.11	22.23	22.49	22.30	22.25	22.20	22.13	-13.70	-
02:24:36.91	-04:47:09.3	22.32	21.77	21.70	21.63	21.59	21.99	21.66	21.73	21.70	21.34	34.00	-
02:24:55.05	-04:50:44.0	23.81	22.72	23.04	22.94	22.67	22.83	22.72	22.63	22.29	22.23	-24.33	-
02:24:59.17	-04:41:52.7	21.80	21.58	21.66	21.33	21.24	21.87	22.02	21.84	21.64	21.19	39.68	-
02:25:01.69	-04:07:54.4	20.09	19.87	19.61	19.54	19.64	19.82	19.56	19.71	19.58	19.43	1.77	-
02:25:02.48	-04:05:58.1	21.84	21.39	21.23	21.20	21.05	21.24	21.32	20.71	20.77	20.38	6.88	-
02:25:03.60	-04:58:28.1	21.99	21.71	21.53	21.19	21.16	21.26	21.17	21.01	20.86	20.85	15.56	-
02:25:08.57	-04:25:12.8	22.13	22.01	22.04	21.71	21.62	21.80	21.92	21.95	21.60	21.19	-2.54	-
02:25:09.55	-04:08:38.4	20.78	20.47	20.29	20.00	20.03	20.08	20.19	20.03	19.76	19.82	45.99	-
02:25:12.09	-04:19:06.9	22.55	22.46	22.18	21.98	21.86	21.98	21.90	21.87	21.76	21.40	26.21	-
02:25:14.39	-04:47:00.1	18.72	18.66	18.58	18.30	18.27	18.49	18.48	18.62	18.72	18.62	94.18	-
02:25:15.35	-04:40:08.9	20.28	19.99	19.98	19.64	19.73	19.90	19.96	20.01	20.17	19.97	-4.54	-
02:25:16.60	-04:05:12.0	21.11	20.70	20.45	20.12	20.12	20.30	20.44	20.28	19.98	20.02	47.26	-
02:25:23.28	-04:00:38.3	21.73	21.47	21.25	21.21	21.01	21.05	21.04	21.13	21.05	20.69	19.93	-

Table 2.6: *continued*

R.A. (hms)	Dec. (dms)	u	g	r	i	z	Z	Y	J	H	K_S	$S_{1.4\,\mathrm{GHz}}/\mu\mathrm{Jy}$	z_{spec}
02:25:25.68	-04:35:09.6	21.24	21.02	20.92	20.72	20.62	20.90	20.85	20.86	20.67	20.25	360.74	2.1
02:25:27.52	-03:59:54.4	21.87	21.76	21.66	21.22	21.26	22.61	22.48	22.27	21.79	22.14	27.18	-
02:25:31.94	-04:06:59.8	22.66	22.29	22.35	22.19	22.10	22.22	22.19	22.02	21.89	21.56	12.48	-
02:25:37.16	-04:21:32.9	20.02	19.60	19.46	19.50	19.41	19.35	19.50	19.03	19.38	19.24	-21.31	-
02:25:38.11	-04:28:11.0	23.26	22.22	22.14	22.14	21.93	22.16	21.94	21.87	21.68	21.62	8.21	-
02:25:40.57	-04:38:25.2	20.68	20.07	20.01	19.89	19.81	20.08	19.87	19.85	19.81	19.54	40.77	-
02:25:45.53	-04:34:45.6	22.06	21.55	21.57	21.20	21.29	21.36	21.44	21.24	21.02	20.94	8.39	1.7*
02:25:50.38	-04:33:24.6	23.32	22.58	22.33	22.34	22.29	22.56	22.19	22.33	22.15	21.92	-19.73	2.7
02:25:50.97	-04:02:47.2	22.06	21.87	21.61	21.54	21.51	21.91	21.69	21.45	21.06	20.89	4.95	-
02:25:52.16	-04:05:16.1	21.76	21.83	21.56	21.40	21.42	21.43	21.40	21.19	20.80	20.72	45.88	1.4
02:25:55.43	-04:39:18.3	21.35	21.12	20.82	20.73	20.62	20.92	20.79	20.56	20.38	19.95	47.31	-
02:25:57.62	-04:50:05.3	20.10	19.74	19.54	19.49	19.45	19.77	19.82	19.91	19.83	19.57	83.74	-
02:25:58.87	-04:18:01.0	22.53	22.39	22.29	22.10	21.82	22.01	21.84	21.74	21.53	21.14	38.93	-
02:26:09.62	-04:24:38.0	21.83	20.91	20.80	20.83	20.62	20.63	20.43	20.45	20.50	20.45	17.84	2.7
02:26:12.64	-04:34:01.4	20.82	20.84	20.81	20.62	20.39	20.67	20.67	20.62	20.43	19.86	9.04	2.3
02:26:15.90	-04:10:11.3	22.17	21.87	21.56	21.51	21.59	21.47	21.55	21.55	21.35	21.22	14.79	-
02:26:17.85	-04:31:09.1	19.90	19.49	19.35	19.18	19.09	19.31	19.42	19.28	19.24	18.93	74.06	-
02:26:18.59	-04:11:01.1	21.67	21.53	21.49	21.16	21.10	21.88	21.89	21.89	21.72	21.42	7.52	2.0
02:26:19.65	-04:46:09.2	23.37	22.31	22.38	22.25	22.02	22.21	22.14	21.88	21.60	21.12	18.84	-
02:26:22.15	-04:22:21.8	19.87	19.69	19.59	19.01	18.98	19.21	19.29	19.36	19.32	18.99	16.34	2.0
02:26:24.64	-04:20:02.4	21.84	21.65	21.47	21.28	21.10	21.45	21.48	21.47	21.37	20.80	56.27	2.2
02:26:29.26	-04:30:57.2	20.12	19.84	19.90	19.67	19.52	19.82	19.78	19.97	20.02	19.68	13.27	-
02:26:32.38	-04:38:09.0	22.88	22.48	22.45	22.04	22.05	22.35	22.22	22.05	21.80	21.36	-29.17	-
02:26:33.31	-04:29:47.8	22.73	22.15	22.00	21.86	21.60	21.76	21.77	21.75	21.54	21.11	22.73	2.1
02:26:35.48	-04:51:04.8	20.58	20.55	20.45	20.25	20.12	20.49	20.30	20.28	20.15	19.68	13.19	-
02:26:36.07	-04:34:29.1	20.82	20.00	19.77	19.59	19.63	19.60	19.48	19.50	19.60	19.67	33.11	-
02:26:39.83	-04:20:04.4	21.78	21.95	21.67	21.34	21.42	21.54	21.78	21.57	21.20	21.43	22.22	1.6

Table 2.6: *continued*

R.A. (hms)	Dec. (dms)	u	g	r	i	z	Z	Y	J	H	K_S	$S_{1.4\,\mathrm{GHz}}/\mu\mathrm{Jy}$	z_{spec}
02:26:41.46	-03:59:49.8	22.10	21.82	21.83	21.59	21.41	21.61	21.68	21.86	21.88	21.55	34.03	-
02:26:48.19	-04:03:14.5	23.01	22.60	22.53	22.31	22.09	22.38	22.39	22.28	21.96	21.56	6.44	-
02:26:52.14	-04:05:57.1	21.22	20.95	20.66	20.51	20.46	20.35	20.55	20.31	19.93	19.84	31.34	1.4
02:26:55.57	-04:42:17.9	22.60	22.26	22.16	22.04	21.73	22.10	22.06	21.98	21.76	21.22	6.67	-
02:26:57.25	-03:59:44.5	20.08	20.08	20.03	19.66	19.59	19.74	19.77	19.88	19.84	19.52	7.89	-
02:27:07.54	-04:32:03.2	21.27	20.98	20.77	20.50	20.51	20.83	20.75	20.51	20.16	20.07	28.38	1.5*
02:27:09.03	-04:55:10.1	22.19	21.51	21.25	21.08	21.09	21.08	20.95	20.97	20.96	21.14	19.39	2.7
02:27:11.36	-04:58:15.1	23.03	22.75	22.51	22.25	22.14	22.89	22.76	22.26	21.80	21.61	-0.82	-
02:27:22.19	-04:52:21.8	21.84	21.79	21.81	21.59	21.40	21.62	21.61	21.75	21.60	21.18	18.32	-
02:27:23.71	-04:58:08.3	22.79	21.95	21.86	21.70	21.38	21.79	21.58	21.49	21.24	21.19	13.44	-
02:27:23.80	-04:02:14.8	20.39	19.91	19.89	19.68	19.78	20.26	20.37	20.35	20.33	20.08	96.93	-
02:27:25.72	-04:18:37.5	23.56	22.64	22.48	22.53	22.37	22.85	22.39	22.27	22.36	22.28	0.14	-
02:27:33.99	-04:25:23.5	20.64	20.50	20.40	20.13	20.21	20.32	20.42	20.22	19.91	19.90	14.33	1.6
02:27:36.93	-04:26:31.5	21.87	21.53	21.49	21.16	21.29	21.35	21.31	21.21	21.13	20.94	23.80	1.8
02:27:38.99	-04:09:40.8	22.19	22.00	21.71	21.64	21.53	21.61	21.62	21.43	20.97	20.85	-21.24	1.4
02:27:40.55	-04:02:51.1	19.00	18.41	18.19	18.10	18.05	18.33	18.15	18.22	18.20	18.35	2381.60	2.6
02:27:46.46	-04:01:00.7	22.14	22.00	21.94	21.56	21.53	21.65	21.64	21.62	21.53	21.36	20.99	-
02:27:47.16	-04:45:20.1	22.13	22.02	21.83	21.34	21.43	21.72	21.49	21.36	21.27	21.06	72.35	-
02:27:47.34	-04:27:53.7	22.32	22.00	21.68	21.53	21.46	21.74	21.40	21.45	21.07	20.64	13.33	1.1
02:27:49.46	-04:59:25.6	22.39	22.03	21.75	21.67	21.54	21.56	21.70	21.71	21.58	21.15	-13.53	-

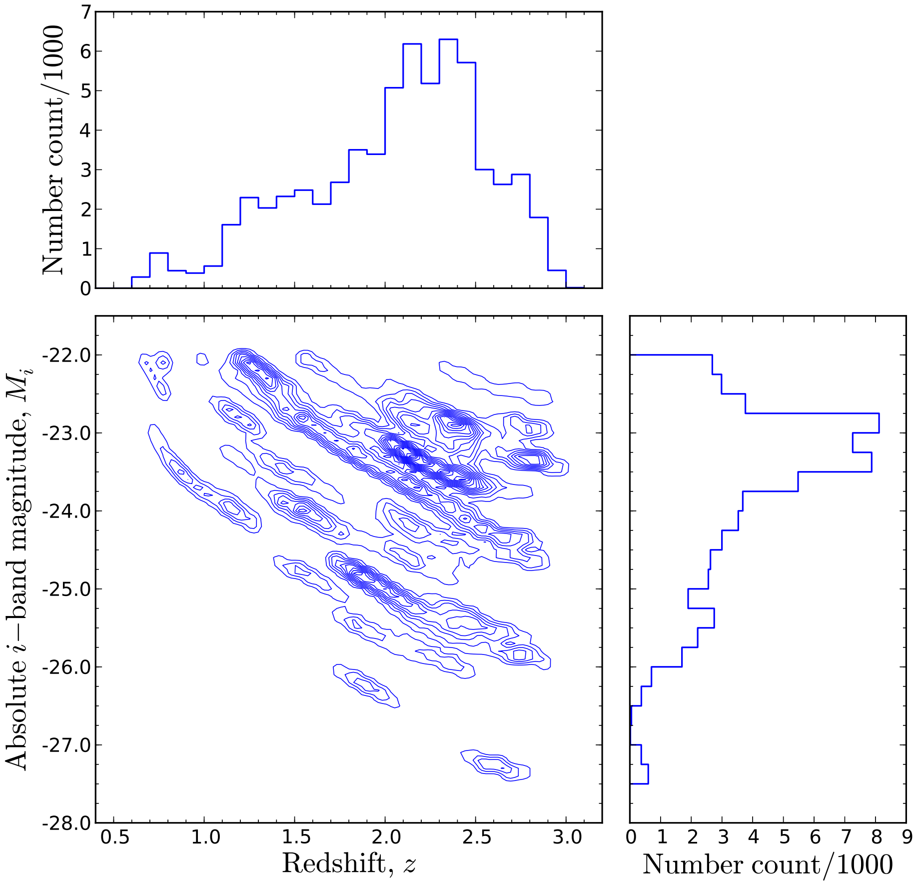

Figure 2.8: The distribution of photometric redshifts (Colour-z) and K-corrected absolute i-band magnitudes for the final 74 Gold quasars with $M_i \leq -22$ (contour interval=10), determined using the full redshift probability distributions.

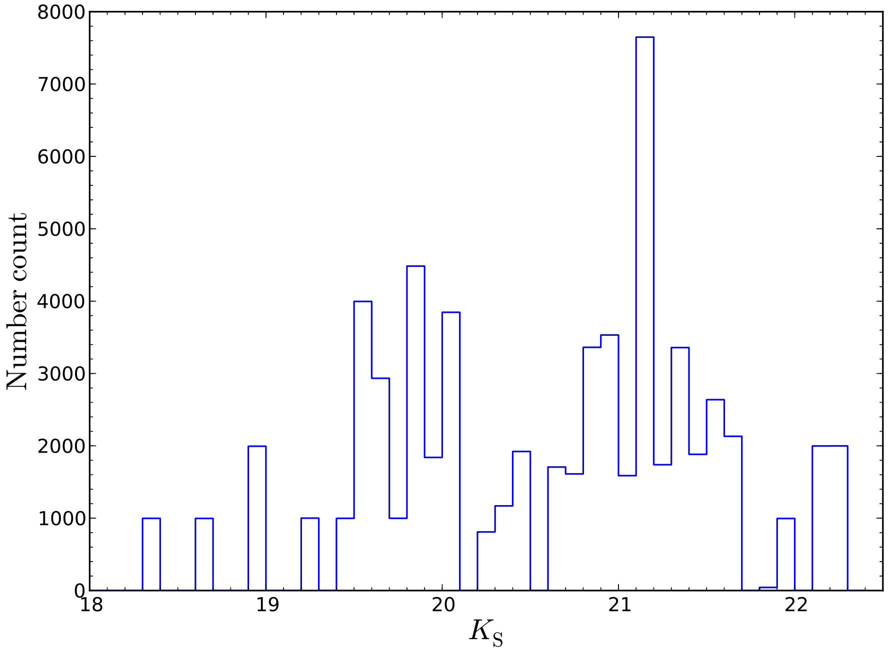

Figure 2.9: The K_S-band magnitude distribution for the final 74 Gold quasars, for those that have $M_i \leq -22$ generated from sampling the redshift probability distribution.

(i.e. unobscured) quasars. These make up my 'Gold' candidate quasar sample, which (following an absolute i-band magnitude cut, $M_i \leq -22$) comprises 74 quasars.

2. For follow-up, I use optical spectroscopy from both the SALT and VVDS, which provides accurate redshifts for 26% of the Gold objects. My photometric redshifts are shown to be reliable, with $\sigma_{\Delta z/(1+z)} = 0.046$ when calculated across the quasars with spectroscopic redshifts.

3

Analysis of the quasars selected using VIDEO

> "I'm scanning all my radars, well she said she's from a quasar,
> forty thousand million light-years away"
> – Jamiroquai, *Cosmic Girl*

In this chapter I explain the methods I use to investigate the radio emission from the quasar sample described in Chapter 2. This work extends the previous studies of Kimball et al. [2011] and Condon et al. [2013], who use photometry and spectroscopy from the relatively shallow SDSS. The quasars in my sample are selected from much deeper and narrower optical and near-infrared surveys, and here I determine whether there is evidence for star formation in the quasar hosts, as a function of redshift and absolute i-band magnitude. In Section 3.1 I analyse the radio emission from the quasar sample, both by stacking and by adopting a parametric description of the radio source counts for the quasars. I then discuss the origin of the emission in radio-quiet quasars, and present conclusions in Section 3.2.

3.1 Radio emission from radio-quiet quasars

3.1.1 Radio flux-density measurement

To obtain the radio properties of the RQQs in my sample, I initially performed a stacking analysis. I used 1.4 GHz flux densities extracted from the VLA–VIRMOS Deep Field map [Bondi et al., 2003] on a single-pixel basis, at the positions of the quasars. Due to the conversion from right ascension and declination to an integer pixel number, the positional error of the quasar associated with the chosen pixel is 1.5 arcsec for both co-ordinates. This error is comparable to the angular size of the objects in question, but deemed negligible given the 6-arcsec resolution of the data.

The mean and median radio flux-density values obtained at the positions of the Gold objects are shown in Table 3.1, noting that the radio map has an average rms noise of 17.5 μJy [Bondi et al., 2003]. In order to take the noise variation across the map into account, a random sample is also created, using pixels between 17 and 42 arcsec away (in a random direction) from each Gold quasar position. This was to ensure that the new position was well outside the synthesised beam covering the Gold candidate position (i.e. more than two beam sizes away), and so avoid any possible correlation in the flux values. Also, using a fixed direction would have introduced a systematic error due to artefacts arising during the radio imaging process, caused by the 6-order symmetry of the VLA's $u-v$ coverage. Repeated 1000 times per Gold candidate, this method ensures that all of the random pixels lie within annular loci, centred on a Gold position.

The fraction of negative flux density values is an indication of the level of non-detections, and is significantly lower for the Gold positions than the random positions (Table 3.1). Since the Gold quasar candidates are part of a clean sample, their median radio flux density being higher than that for the random positions is expected. Figure 3.1 shows flux-density histograms for the quasars and the random positions, and clearly shows a positive tail in the case of the former, reinforcing the evidence for excess radio emission at the positions of the quasars. Within this tail are 10 objects with detections at $> 3\sigma$, one of which is above 1 mJy and appears in both the FIRST and NVSS catalogues [White et al. 1997; Condon et al. 1998]. Assuming a typical spectral index of $\alpha = -0.7$ (where

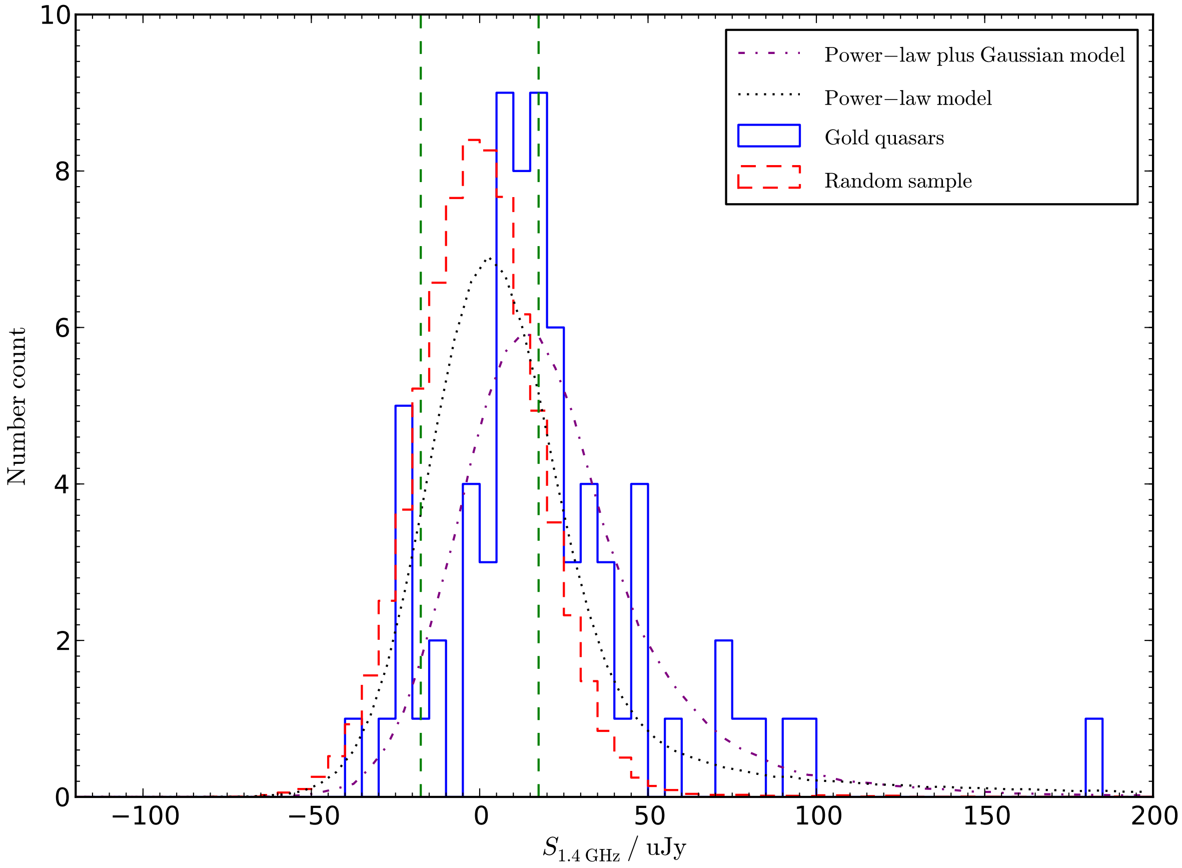

Figure 3.1: Radio flux-density distributions, with the blue (solid) histogram corresponding to the Gold QSOs. The red (dashed) histogram corresponds to the random sample, where the fluxes are extracted from pixels 17 to 42 arcsec away from the Gold QSO positions. (Their number counts have been scaled to aid comparison.) The green, dashed lines demarcate the mean noise level of the VLA map, at ±17.5 µJy. Two curves represent the distributions for simulated flux densities (see Section 3.1.3), where the radio number counts for the quasars is modelled by a power-law (black, dotted line) or a Gaussian-plus-power-law (purple, dash-dotted line). Note that there are two brighter Gold quasars that have radio flux densities outside of the plot range.

$S_\nu \propto \nu^\alpha$), this is the only quasar in the sample that is 'radio-loud', according to the definition of $L_{8.4\,\mathrm{GHz}} > 10^{25}\,\mathrm{W\,Hz^{-1}}$ [Hooper et al., 1996]. It also satisfies the criteria for radio-loudness defined by Kellermann et al. [1989] and Miller et al. [1990]. However, I reiterate that these are arbitrary boundaries, and although the emission process may be physically different, I continue to include this object in my analysis.

Lastly, although the single-point statistics presented are interesting, it must be remembered that stacking leads to a loss of information and it is far more informative to study the entire flux-density distribution [e.g. Mitchell-Wynne et al. 2014].

Table 3.1: Stacked radio flux densities for the quasar and control samples. ‘Negative fraction’ refers to the number of flux-density values that are negative, and the *p*-value is the result from a Kolmogorov–Smirnov (KS) test. This indicates the probability of the null hypothesis that the two distributions are drawn from the same underlying distribution. The second Gold sample (third row) is created by weighting the appearance of each quasar in accordance with the fraction of its probability distribution function (PDF, Section 2.4.1.1) that survives the $M_i \leq -22$ cut imposed in Section 2.4.2. The last four rows correspond to galaxy samples with stellar-mass estimates determined assuming black-hole (BH) masses of $10^8\,\mathrm{M}_\odot$ and $10^9\,\mathrm{M}_\odot$, and specifies whether or not redshift evolution in the M_{BH}-M_* relation was used (see Section 3.1.4 for details). In each case, 74 – the final number of Gold quasars – is used as the sample size for calculating the uncertainties. The error in the median flux is the median absolute deviation (MAD), which reduces the effect of outliers in the distribution. Also, the *p*-value quoted is a median, having performed 1000 KS tests with each control sample.

Sample	Median flux (μJy)	Mean flux (μJy)	Negative fraction	KS test *p*-value
Gold quasars	17.6 ± 14.6	57.9 ± 32.4	0.19	N/A
Random positions	-0.3 ± 11.9	1.2 ± 6.0	0.51	10^{-12}
Gold quasars weighted by the PDFs	17.8 ± 13.5	63.6 ± 34.4	0.18	N/A
$M_{\mathrm{BH}} = 10^8\,\mathrm{M}_\odot$ and redshift evolution	2.5 ± 12.4	7.6 ± 17.3	0.44	10^{-4}
$M_{\mathrm{BH}} = 10^9\,\mathrm{M}_\odot$ and redshift evolution	9.4 ± 14.6	25.5 ± 32.0	0.33	10^{-2}
$M_{\mathrm{BH}} = 10^8\,\mathrm{M}_\odot$ and no redshift evolution	5.0 ± 12.7	10.0 ± 11.1	0.40	10^{-3}
$M_{\mathrm{BH}} = 10^9\,\mathrm{M}_\odot$ and no redshift evolution	29.9 ± 25.4	75.3 ± 37.5	0.15	10^{-3}

3.1.2 Statistical detections of radio emission

The majority of objects from my quasar sample have radio emission that is below the 1-σ flux-density limit of the VLA map. Therefore I analyse the radio flux distribution of the quasars to determine whether or not there is a statistical detection of significant radio emission. Figure 3.1 indicates there is, but to investigate this quantitatively a two-sample Kolmogorov–Smirnov (KS) test is used. This tests the null hypothesis that the Gold quasar sample and the flux-density measurements at random positions are drawn from the same underlying distribution. I find a KS statistic of $D = 0.42$ and p-value $= 10^{-12}$. Therefore the null hypothesis can be rejected, confirming an excess of radio emission for the Gold sample.

I take the analysis a step further by investigating whether the excess radio emission from quasars persists at all redshifts. The 74 quasars in the Gold sample, from Section 2.4.2, are binned in a probabilistic manner by splitting the simulated objects (derived from the Colour-z PDFs and subjected to a $M_i = -22$ magnitude cut) into four redshift ranges. The frequency with which a quasar appears in each bin is recorded, and this is then used to weight the number count distribution for the quasars across the redshift bins. The number counts for the random flux densities, corresponding to a particular quasar as they are (again) constrained to lie between 17 and 42 arcsec away, are weighted in the same way. To create a Gold subsample for each bin, a number of simulated objects are randomly selected according to how many of the original 74 quasars are sampled within that bin. For the corresponding random subsample, 1000 random positions are selected per Gold object. A KS test is then carried out between the redshift-based subsample and the measurements at random positions, and the procedure repeated 1000 times. The results are shown in Figure 3.2 and Table 3.2 and indicate that, for each of the redshift bins, the null hypothesis can be rejected. That is, there is excess radio emission from the quasars at all redshifts.

The Gold quasars were then binned *separately* by their absolute i-band magnitude, using the same probabilistic procedure with regard to the simulated objects. As before, the ranges of these 4 bins were set so that there was roughly the same total number of simulated objects in each. The median p-values, calculated from 1000 KS tests between

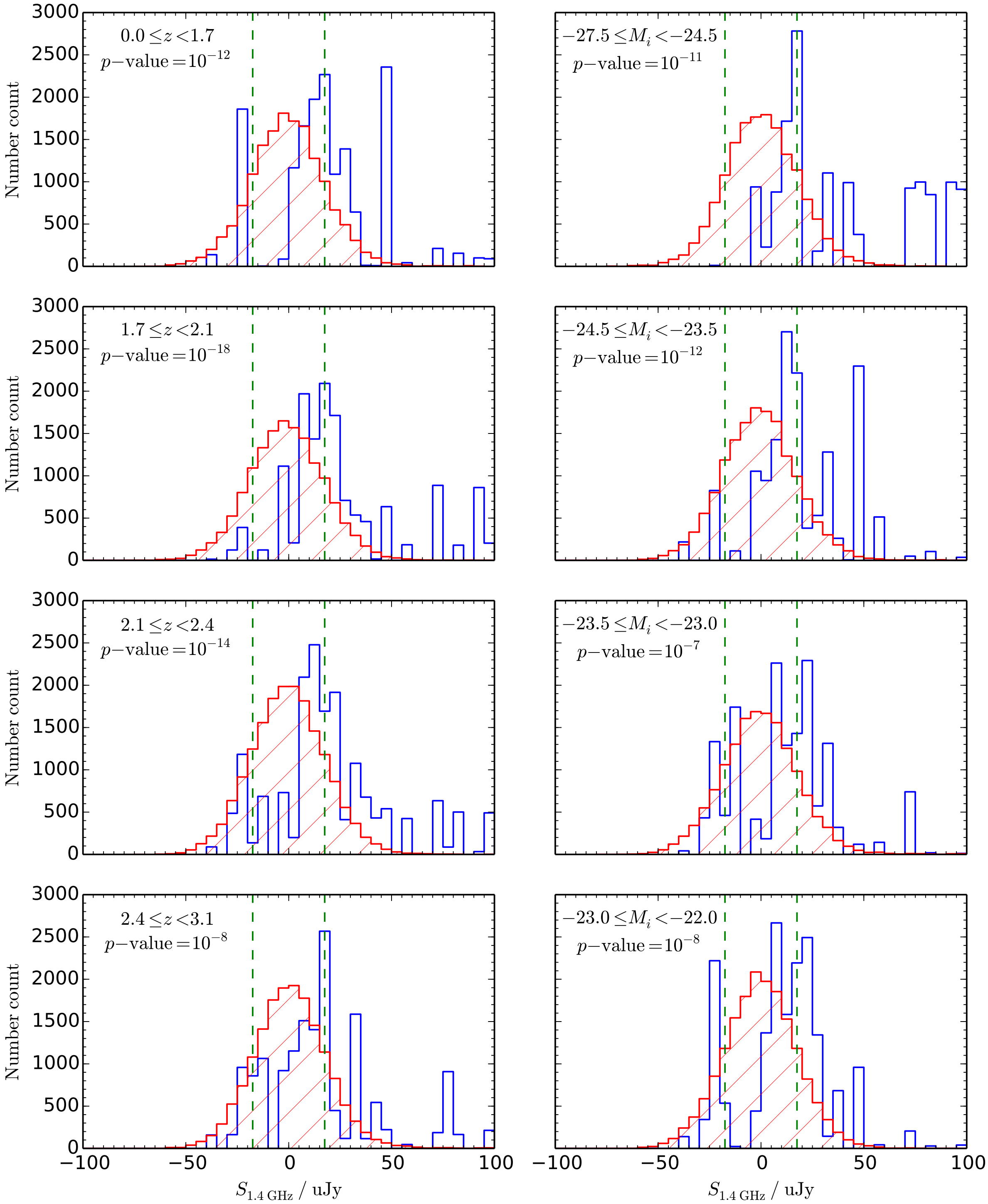

Figure 3.2: The flux-density distribution of Gold quasars (blue histograms), subject to a $M_i \leq -22$ cut, binned according to redshift (left column) and absolute i-band magnitude (right column). To compare with the intrinsic radio noise properties, the flux-density value was also measured at random positions, confined to lie between 17 and 42 arcsec away from each quasar position (red, hatched histograms, scaled to aid comparison). The dashed green lines are at ±17.5 μJy, the mean rms noise (i.e. 1σ) level of the VLA map [Bondi et al., 2003]. The positive offset of the quasar histogram from the random distribution indicates a statistical detection of faint radio emission. The median p-value, resulting from 1000 KS tests between the Gold and random subsamples, is given for each bin (Table 3.2).

Table 3.2: Mean and median radio flux densities for the quasars in the Gold sample, binned by redshift and separately by absolute i-band magnitude. The number of different quasars appearing in each bin is used to calculate the uncertainties. The error in the median flux is the median absolute deviation (MAD), which reduces the effect of outliers in the distribution. 'Negative fraction' refers to the number of flux-density values that are negative. 1000 KS tests are performed per bin, with the median of the resulting p-values quoted here.

Bin range	Median flux (μJy)	Mean flux (μJy)	Negative fraction	Median p-value
$0.0 \leq z < 1.7$	17.3 ± 9.8	22.5 ± 8.0	0.14	10^{-12}
$1.7 \leq z < 2.1$	19.9 ± 12.0	38.8 ± 10.0	0.12	10^{-18}
$2.1 \leq z < 2.4$	18.8 ± 13.9	34.2 ± 12.7	0.19	10^{-14}
$2.4 \leq z < 3.1$	15.6 ± 17.6	155.9 ± 66.7	0.25	10^{-8}
$-27.5 \leq M_i < -24.5$	40.8 ± 32.9	197.6 ± 105.5	0.06	10^{-11}
$-24.5 \leq M_i < -23.5$	19.4 ± 14.4	34.7 ± 9.9	0.14	10^{-12}
$-23.5 \leq M_i < -23.0$	13.3 ± 13.8	11.8 ± 3.2	0.29	10^{-7}
$-23.0 \leq M_i < -22.0$	14.8 ± 8.3	13.2 ± 4.2	0.21	10^{-8}

the Gold and random distributions for each M_i bin, are also shown in Figure 3.2 and in Table 3.2. I find evidence to reject the null hypothesis, at the $\gg$99.99% confidence level, for each of the bins in absolute i-band magnitude.

Using the individual flux-density measurements and the redshift probability distributions to calculate the distribution in $L_{1.4\,\mathrm{GHz}}$ and M_i, Figure 3.3 shows the radio luminosity against the absolute i-band magnitude. To perform a correlation test, I randomly select one simulated object per Gold quasar (resulting in a total of 74 simulated objects for each test) and repeat the process 1000 times. A strong correlation is found, with a median coefficient of $r = -0.4 \pm 0.0$ and median p-value $= 10^{-4}$. The trend remains when I consider only the objects that have a flux that is above the rms noise level, with $S_{1.4\,\mathrm{GHz}} > 17.5\,\mu\mathrm{Jy}$ (dark-blue triangles in Figure 3.3). The apparent 'smearing' of the data points is due to slightly different values of $L_{1.4\,\mathrm{GHz}}$ and M_i arising from the redshift probability distribution for the quasars (Section 2.4.1.1). If I only use $L_{1.4\,\mathrm{GHz}}$ and M_i as derived from the best-fit photometric redshift, Colour-z, a correlation test for the 74 quasars results in $r = -0.2$ and p-value $= 10^{-1}$. 18% of simulated objects (that survived the $M_i < -22$ cut) are missing from Figure 3.3, due to them having a negative flux value extracted from the VLA map. However, the binned median values and associated error bars (in black) *do* include quasars with negative fluxes. The resulting negative values of $L_{1.4\,\mathrm{GHz}}$ are also

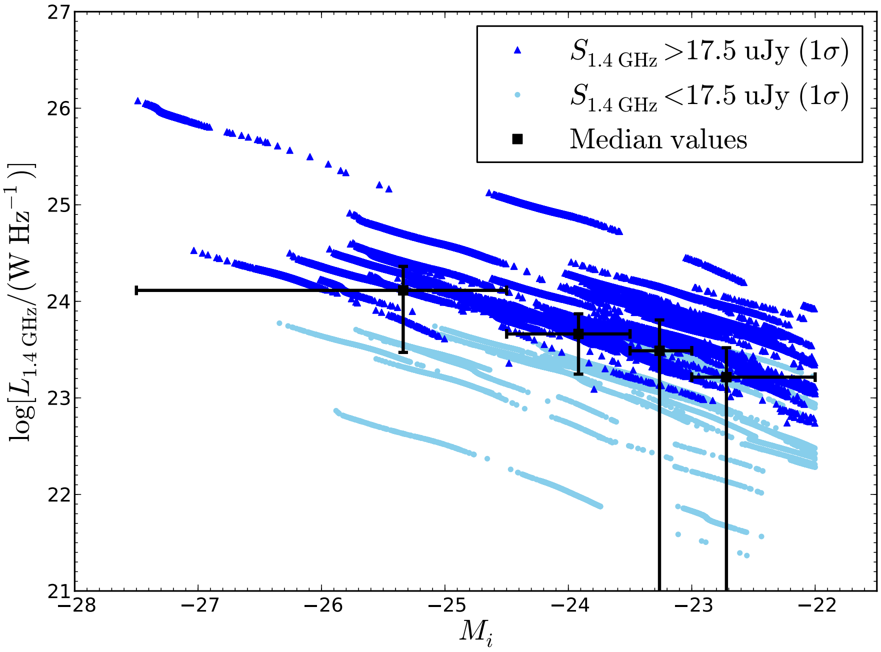

Figure 3.3: Radio luminosity against absolute i-band magnitude for my sample of quasars. Dark-blue triangles are simulated objects (based on the photometric-redshift probability distributions) with $S_{1.4\,\mathrm{GHz}} > 17.5\,\mu\mathrm{Jy}$ (i.e. $> 1\sigma$), and light-blue circles are those below this radio flux threshold. Overplotted in black are the median luminosities derived for these objects, binned in M_i. The horizontal error bars indicate the ranges of the M_i bins (Table 3.2), and the ordinate error bars represent the uncertainties on the median radio luminosities.

used for the correlation test, meaning the sample is not flux-limited in the radio and the trend seen is real.

This correlation between the optical luminosity, which is dominated by thermal emission from the accretion disc, and the non-thermal radio emission has previously been found for radio-loud quasars [e.g. Serjeant et al. 1998; Fernandes et al. 2011; Punsly and Zhang 2011], and has been used to infer that the jet-production process is related to the accretion rate, but with black-hole spin playing an important role [e.g. Punsly, 2011; Tchekhovskoy et al., 2011]. However, at the lower radio luminosities observed in this sample, I cannot rule out that such a trend is due to the various correlations between black-hole mass, stellar mass and star-formation rate [e.g. Noeske et al., 2007].

3.1.3 Quasar-related radio source counts

In this subsection I follow the work of Kimball et al. [2011] and Condon et al. [2013] and investigate the shape of the radio source counts due to quasars. To parameterise the radio background as I probe to lower flux densities, it is necessary to understand the individual contributions from various populations. For example, in the semi-empirical simulation of Wilman et al. [2008, 2010] the number counts of extragalactic objects are broken down into radio-loud and radio-quiet AGN, star-forming galaxies, and starbursts.

In Figure 3.4 I show the contribution to the radio source counts from my Gold quasar sample using the measurements discussed in Section 3.1.1. The counts are brightness-weighted so that the product, $S^2n(S)$, is proportional to the contribution by sources, within each logarithmic bin in flux density, to the sky-background temperature [Condon et al., 2012]. Below 1 mJy I find that a 'bump' appears in the number counts, as opposed to a single power-law to lower radio flux densities. Such a bump has also been found in studies based on the SDSS [Kimball et al. 2011; Condon et al. 2013] and has been attributed to star formation in the quasar host-galaxy in both cases. In this subsection I quantify the bump in terms of different parameterisations of the measured radio flux-density distribution, and then explore whether the radio emission is due to star formation or related to the accretion process in Section 3.1.4.

To fit the shape of the radio source count contribution from the Gold quasar sample, I need to impose the same survey flux-density limit as the radio data. To begin with, a simulated catalogue is created by drawing fluxes from a function of $S^2n(S)$ that follows a particular power-law (see below). Then noise, with rms = 17.5 μJy, is incorporated into the simulated fluxes by adding the flux from randomly-selected pixels of the VLA map used in Section 3.1.1. Effectively I have injected the model fluxes into the radio map and then re-extracted the resultant flux value. This accounts for any small non-uniformity in the noise distribution.

Next, for different combinations of the prescribed slope (α) and normalisation (c) of the power-law, a chi-squared (χ^2) test is performed between the data and the simulated flux distribution. For this I normalise the simulated distribution so that the total number of objects is 74, to match the size of the quasar sample. A minimum in the χ^2 value (reduced $\chi^2_{\text{min}} = 6.2$) is found for the combination of $\alpha = 0.89 \pm 0.01$ and $c = 14000 \pm 1000$, and the distribution produced by this power-law model is shown by a black, dotted line in Figure 3.1. It appears significantly different to the flux-density distribution of the quasars, and this is confirmed by a KS test of the two distributions producing a p-value of 7×10^{-5}. With no evidence that the simulated fluxes are drawn from the same distribution as the quasar fluxes, I conclude that a power-law is an inadequate description of the number counts.

I adjust my model by adding a Gaussian contribution to the power-law, and use this to create alternative simulated catalogues. The prescribed function of $S^2 n(S)$ is then given by

$$\log_{10}[S^2 n(S)] = \log_{10}[cS^\alpha] + A \exp\left(\frac{\log_{10}[S] - \mu}{2\sigma^2}\right). \tag{3.1}$$

Minimising the χ^2 value for the data and the resulting simulated flux-density catalogue (reduced $\chi^2_{\rm min} = 3.2$), the best-fit model is described by $\alpha = 1.04 \pm 0.01$, $c = 26000 \pm 2000$, $A = 0.5 \pm 0.1$, $\mu = -4.9 \pm 0.1$, and $\sigma = 0.5 \pm 0.1$. This gives p-value $= 0.3$ when a KS test is performed between the simulated distribution and the measured radio flux density of the quasars. This indicates that the distribution arising from this power-law plus Gaussian model is indistinguishable from that of the quasars, and can be seen by comparing the purple, dash-dotted line to the blue histogram in Figure 3.1. Furthermore, the corresponding contribution to the radio source counts for this model is shown in Figure 3.4 (red triangles). Note that they do not follow the purple, dash-dotted line (due to e.g. some objects having negative fluxes, and some objects being shifted between adjacent bins even at the bright end) but do overlap with the real data, thereby illustrating the effect of the noise on the shape of the number counts. This is particularly prominent below $\log_{10}[S_{1.4\,\rm GHz}] = -4.8$, where the data and the simulated fluxes are within the 1-σ noise of the VLA radio map (shaded region of Figure 3.4). In addition, the relatively small survey area that I use ($1\,\rm deg^2$) leads to only one Gold quasar in the bins at each end of the flux-density distribution, and the addition of the noise is the dominant reason why these objects are boosted into the brighter flux bins, from the more well-populated regions at fainter flux densities. Indeed, this is why I simulate the flux-distribution based on the model with the noise from the radio map included, to ensure a fair comparison between model and data.

The Gold quasars presented in this thesis exceed the SDSS quasar counts by Condon et al. [2013], as shown by the offset between my data points and their power-law fit

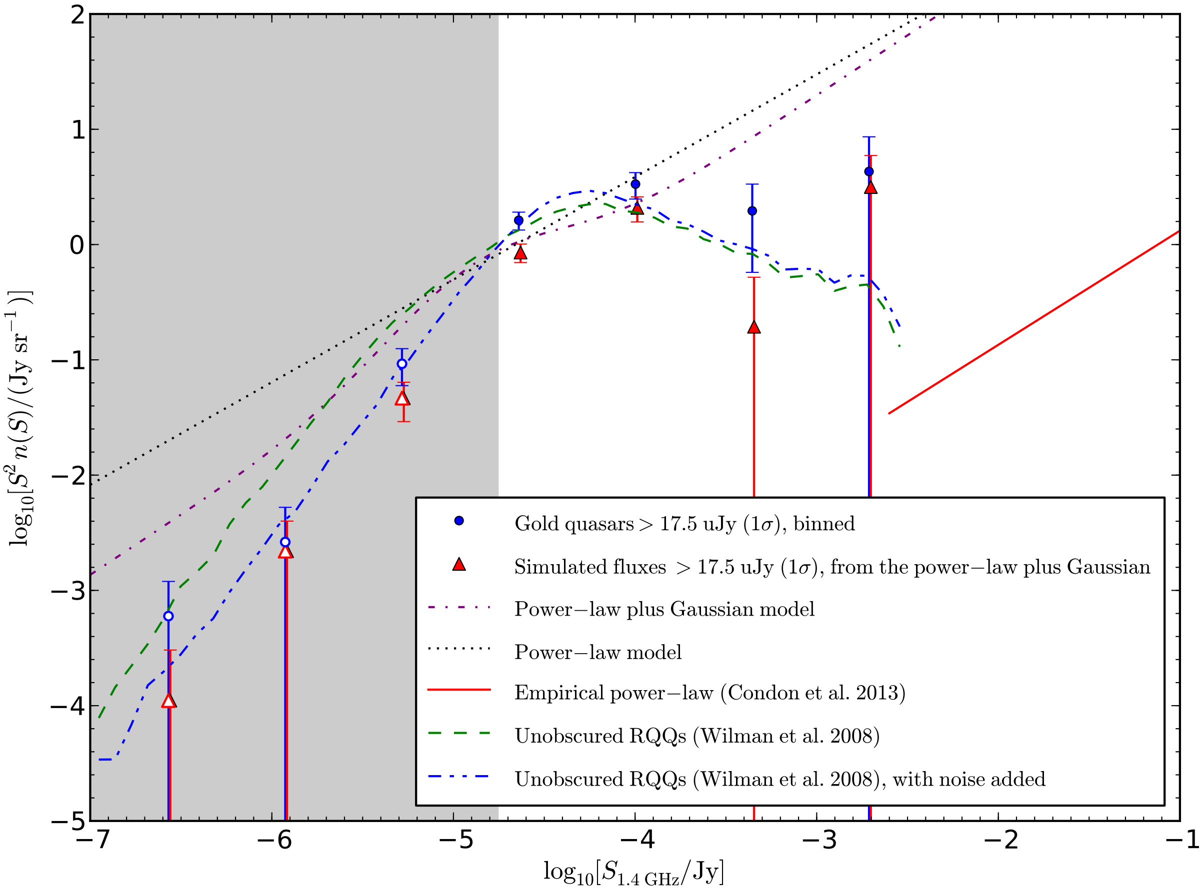

Figure 3.4: The brightness-weighted counts of the Gold quasars (blue dots with error bars), relative to the power-law fit (red, solid line) by Condon et al. [2013]. The equation of their fit is $S^2 n(S) = (12.9 \pm 1.0) \times S^{0.99 \pm 0.02}\,\mathrm{Jy\,sr}^{-1}$. The *prescribed* number counts (purple, dash-dotted line) for our simulated points is created by adding a Gaussian to a power-law, as described in Section 3.1.3. It does not include the noise contribution later added to create the simulated fluxes (red triangles, slightly offset to show the extent of the error bars). A power-law only model (dotted, black line) is also illustrated. Overplotted are the number counts for RQQs simulated by Wilman et al. [2008], with and without the addition of noise from the VLA map [Bondi et al., 2003]. The shaded region indicates the region fainter than the 1σ rms flux-density of the radio data, and so the data points corresponding to $S_{1.4\,\mathrm{GHz}} < 17.5\,\mu\mathrm{Jy}$ (unfilled symbols) should be treated with caution. Because log-log space is needed to display the data clearly, Gold quasars that have a negative flux density do not appear in the plot. The error bars are Poissonian, depending only on the number of objects appearing in a particular logarithmic bin, $\Delta \log S = 0.643$. (All points are plotted at the centres of the logarithmic bins.)

(Figure 3.4). This is because I include much fainter optically-selected sources, by 6 orders of magnitude in the r band, and do so over a redshift range of $0.5 < z < 3.1$ rather than $1.8 < z < 2.5$. Some authors have suggested that, if the radio emission is due to accretion, then the power-law used to describe the brightness-weighted number counts above 1 mJy should simply extend to lower luminosities. Therefore, any deviation away from this must indicate the presence of radio emission from an alternative process, e.g. star formation [Hopkins et al. 1998; Kimball et al. 2011]. However simulations by Wilman et al. [2008] show that, even when considering the AGN population alone, a distinct 'bump' is seen in the number counts. This is because the relation between accretion rate and radio luminosity for radio-quiet quasars may not follow the same scaling relations that are applicable to the radio-loud objects [e.g. Willott et al. 1999; Jarvis et al. 2001; Fernandes et al. 2011]. This may be further accentuated by an emergent star-forming population, and so a combination of the two should be considered.

For my quasar sample, a bump in the number counts is evident below 1 mJy, and is in agreement with the work of Condon et al. [2013]. As another check with the literature, I perform the same procedure outlined earlier in this subsection using the source counts for radio-quiet quasars as simulated by Wilman et al. [2008]. That is, their model fluxes are injected into the VLA map and then re-extracted, in order for them to have the same noise properties as the real data and simulated fluxes. Since I cannot impose the same criteria used for my quasar selection, as the simulations do not include reliable absolute magnitudes at optical wavelengths, I simply adjust the normalisation of the resulting number counts (green, dashed line and blue, dash-double-dotted line in Figure 3.4), emphasising my interest in the shape alone. Both the Gold quasars (blue dots) and the simulated fluxes (red triangles) incorporate the noise properties of the radio map, and so both datasets should be compared with the blue (dash-double-dotted) line. I find excellent agreement between my data points and the unobscured RQQs modelled by Wilman et al. [2008], indicated by their overlap within the Poissonian error-bars. Wilman et al. [2008] used the empirical relation between X-ray luminosity and radio luminosity for a sample of RQQs, coupled with the X-ray luminosity function to determine the radio luminosity function, and therefore the source counts of the RQQ population. Consequently, such a comparison does not necessarily imply that the radio emission is related to the accretion process, because more luminous AGN are more likely to be powered by more massive black holes that reside in more massive galaxies. These massive galaxies also have a larger gas reservoir from which stars can form, and so generally have higher star-formation rates. The strong correlation between stellar mass and star-formation rate is in fact observed over multiple decades in stellar mass, and is known as the star-formation main sequence [Noeske et al., 2007]. 'Normal' star-forming galaxies are found to lie along this sequence, whilst starbursts lie above the relation. Therefore, I further investigate the possibility that the radio emission from the RQQs is due to star formation.

3.1.4 Radio emission from AGN or star formation

To explore the origin of the radio emission for my sample, I use the VIDEO survey to create large samples of quiescent galaxies at similar redshifts to the quasars. This is to determine whether there is excess radio emission from the quasars compared to 'normal' galaxies of similar mass. Constructing a sample of galaxies that is matched in stellar mass to the quasars is problematic given that the quasar nucleus outshines the host galaxy, thus rendering direct measurements difficult without deep space-based imaging. I therefore adopt an approach whereby I use the observed relation between black-hole mass, $M_{\rm BH}$, and stellar mass, M_*, from Bennert et al. [2011], $M_{\rm BH} \propto M_*^{\alpha}(1+z)^{\beta}$ where $\alpha = 1.12$ and $\beta = 1.15$. This is quite a moderate evolution compared to other studies [e.g. McLure et al., 2006; Peng et al., 2006]. I also compare this to the case where I assume no redshift evolution in the relation ($\beta = 0.00$). Rather than calculating the black-hole mass for each quasar, which would require complete spectroscopy that includes either $\text{C}\textsc{iv}_{1549}$, $\text{Mg}\textsc{ii}_{2799}$ or $\text{H}\beta_{4861}$ broad lines [Wandel et al. 1999; McLure and Jarvis 2002; Vestergaard 2002], I adopt two fixed black-hole masses of 10^8 and $10^9\,\text{M}_\odot$, and calculate the stellar mass of the host according to the $M_{\rm BH}$–M_* relation.

The stellar masses of the normal galaxies are determined by the VIDEO team, using photometric redshifts from Le PHARE, in combination with stellar population synthesis models of Bruzual and Charlot [2003] (see Johnston et al. [in prep.] for more details). The galaxies are then matched to the quasars in both redshift ($z \pm 0.1$) and stellar mass

($M_* \pm 0.3\,\mathrm{dex}$) using the full probability distributions in redshift and absolute magnitude, to produce four control samples. For a fair comparison, the Gold quasars are weighted according to the same probability distributions, using the fraction of simulated objects that are brighter than $M_i = -22$. With all four control samples, 1000 KS tests are then performed, each time having randomly selected 74 galaxies that are matched to the quasars. Assuming $M_{\mathrm{BH}} = 10^8\,\mathrm{M}_\odot$, multiple KS tests show that the underlying distribution of radio flux density for the quasars and galaxy control sample is significantly different, with median $p = 10^{-4}$ and 10^{-3}, with and without evolution in the M_{BH}–M_* relation, respectively (Table 3.1 and Figure 3.5). Also, the median flux density of the galaxies is much lower than that of the Gold quasars, for both scenarios. I therefore find evidence for excess radio emission from the quasars, independent of whether or not I assume redshift evolution in the M_{BH}–M_* relation.

Next I study the control sample created using $M_{\mathrm{BH}} = 10^9\,\mathrm{M}_\odot$ and M_{BH}–M_* evolution. The median flux density is higher for these matched galaxies compared to those of the first control sample in Table 3.1, as would be expected for galaxies lying on the star-formation main sequence [Noeske et al., 2007]. As a result the p-value is also larger, indicating that the radio output from these matched galaxies is more significant relative to the quasars' emission. However, the median for this control sample is still below that of the Gold quasar sample, suggesting that emission from the quasars remains in excess. In the case of no redshift evolution in the M_{BH}–M_* relation, the p-value shows the quasar and galaxy flux distributions to be distinct, but this time the median flux from the galaxies does exceed that of the Gold quasars. This suggests that, for quasars hosted by the most massive galaxies, star formation could be the cause of the radio emission.

However, any evolution in the ratio between M_{BH} and M_* weakens the case for star formation in the quasar hosts. Furthermore, it is unlikely that the majority of the quasars have $10^9\,\mathrm{M}_\odot$ black-hole masses, given the shape of the black-hole mass function (BHMF) [e.g. McLure and Dunlop 2004; Vestergaard and Osmer 2009]. Additional BHMFs are collated in the review by Kelly and Merloni [2012], showing that $10^8\,\mathrm{M}_\odot$ black holes outnumber $10^9\,\mathrm{M}_\odot$ black holes by a factor of ∼10–20, throughout the redshift range $0 < z < 3$. Although I could use a realistic black-hole mass distribution for my analysis,

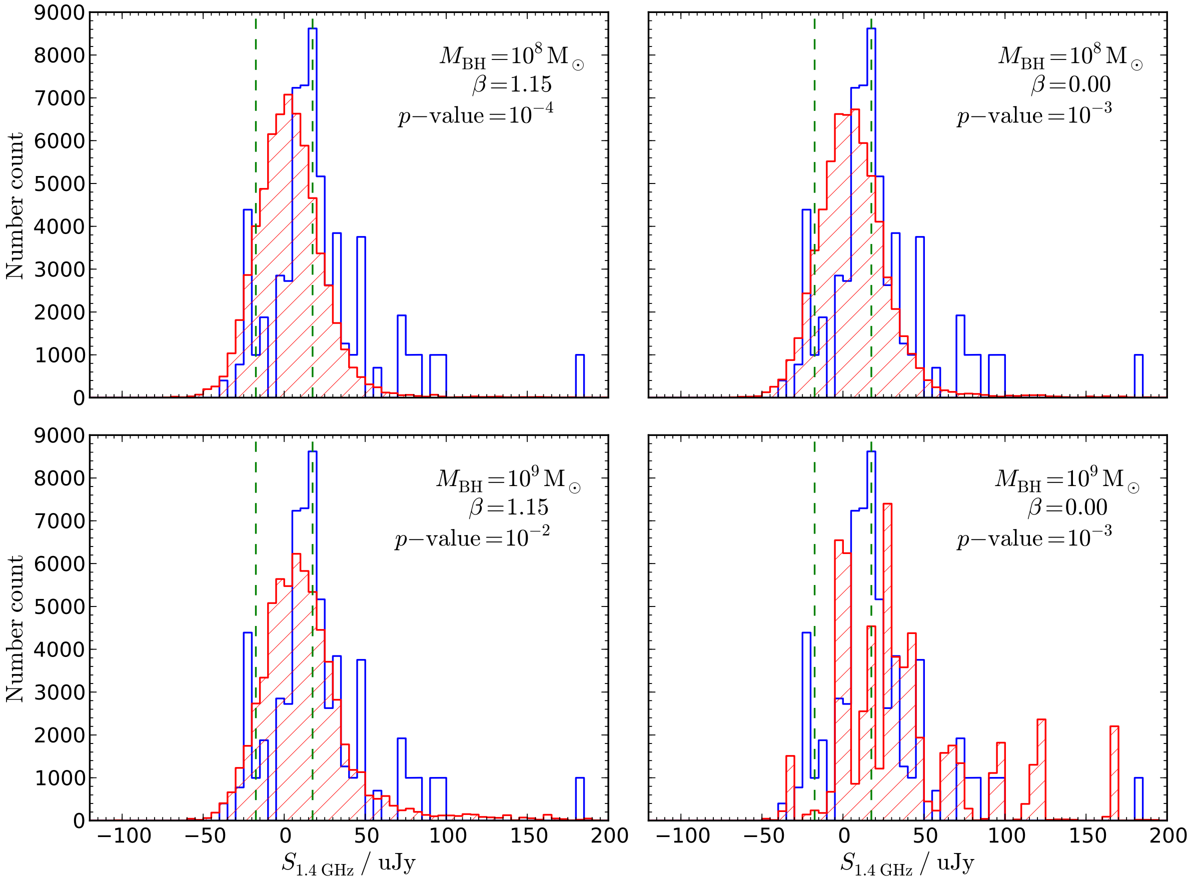

Figure 3.5: Radio flux-density distributions, with the blue histograms corresponding to the Gold quasars. These have been weighted according to the fraction of simulated objects that are brighter than $M_i = -22$. (As in Figure 3.1, two Gold quasars have radio fluxes outside of this plot range.) The red (hatched) histograms correspond to a control sample, where one galaxy has been matched in z and M_* for each simulated object, again having $M_i \leq -22$. The stellar masses are estimated assuming that the quasar has $M_{\rm BH} = 10^8\,{\rm M}_\odot$ (upper panels) or $M_{\rm BH} = 10^9\,{\rm M}_\odot$ (lower panels). Whether or not redshift evolution in the $M_{\rm BH}$–M_* relation is used for this calculation is indicated by the value of β; For evolution we use $\beta = 1.15$ (left panels), from the work of Bennert et al. [2011], whilst $\beta = 0.00$ (right panels) corresponds to zero evolution. The median p-value, from 1000 KS tests between the Gold and control galaxy samples (Table 3.1), is quoted in the top-right corner of each panel, and the green, dashed lines demarcate the mean noise level of the VLA map, at ±17.5 µJy.

rather than a single fixed black-hole mass, I choose not to do so as this would add another layer of complexity. By simply using assumed values, I can more clearly see the impact of the black-hole mass when investigating the origin of the radio emission in RQQs. In addition, most work in the literature uses data from the SDSS to study the BHMF, rather than quasars selected to the same depth as my sample. Therefore I would expect my quasars to have, on average, lower-mass black holes.

Star formation in the host galaxies of quasars has also recently been studied by several authors. Bonfield et al. [2011] used a sample of SDSS quasars and data from the *Herschel*–ATLAS [Eales et al., 2010] to show that the star formation is correlated to the quasar accretion luminosity as well as the redshift. In a similar study, Rosario et al. [2013] find that the star formation properties of quasars are consistent with a model where the host galaxy lies on the star-formation main sequence [Noeske et al. 2007; Whitaker et al. 2012]. These are both based on the assumption that the AGN emission dominates the optical light and does not make a strong contribution to the far-infrared, which is used to calculate the star-formation rate. In addition, support for radio emission from quasars being related to star formation is provided by recent results on sub-mJy radio source populations [Padovani et al., 2014], although I note that the AGN in the study of Padovani et al. are generally much fainter optically than the quasars considered here.

I therefore further investigate the origin of the radio emission in my quasar sample by comparing two independent estimates of the star-formation rate. The first estimate uses the 1.4 GHz flux extracted from the VLA map, and uses the relation between radio luminosity and SFR, as quantified by Yun et al. [2001] for a sample of IR-selected galaxies. A second estimate of the SFR is based on the assumption that the quasar host-galaxies lie on the star-formation main sequence, as found by e.g. Karouzos et al. [2014]. Of course this may not be the case for the quasars in my sample, whose radio emission may instead be due to starbursts, but it is a suitable first approximation. For this I use the redshifts (simulated from the photometric-redshift probability distributions) and typical black-hole masses for a quasar (10^8–$10^{10}\,\mathrm{M}_\odot$) to estimate the total stellar mass, as previously described. (An insufficient number of galaxies in the VIDEO catalogue could be matched to the quasars when assuming $M_{\mathrm{BH}} = 10^{10}\,\mathrm{M}_\odot$, and so this control sample was not created for the previous investigation.) These stellar-mass estimates are then combined with the finding that SFR $\propto M_*^{0.6}$ [Whitaker et al., 2012], which describes the redshift evolution of the star-formation main sequence. The distribution in the SFRs are presented in Figure 3.6, with the mean and median values for each distribution provided in Table 3.3. To further aid comparison, these SFRs are represented by contours in Figure 3.7, effectively acting as probability distribution functions for a particular black-hole mass.

There is a mismatch between the two sets of star-formation rates calculated for the simulated objects associated with the final 74 quasars (Figure 3.7), independent of whether the $M_{\rm BH}$–M_* relation is evolving or not. Quasars are most likely to have black-hole masses of $10^8 < M_{\rm BH} < 10^9\,{\rm M}_\odot$ [e.g. McLure and Dunlop, 2004], but the SFR implied by their stellar mass indicates that this is an order of magnitude lower than expected from the radio emission. Indeed, if there is evolution in the $M_{\rm BH}$–M_* relation, the quasars would need to have $M_{\rm BH} \approx 10^{10}\,{\rm M}_\odot$ in order for their SFRs to have a one-to-one correspondence (lying on the dashed line). Assuming no evolution, the black-hole mass would need to be $> 10^9\,{\rm M}_\odot$ if I am to explain the total radio emission as due to star formation alone. Note that only objects with positive radio fluxes appear in Figure 3.7. However, this is taken into account by the median and mean SFRs that are also shown, as all objects were used for their calculation.

Therefore, either the assumption that the quasar hosts lie on the SF–mass sequence is incorrect, and the quasars reside in starburst galaxies, or the AGN is contributing a significant fraction towards the radio flux. I argue that the latter is the most probable explanation because, based on work using far-infrared data [Bonfield et al., 2011; Rosario et al., 2013], it is unlikely that the quasar host-galaxies are undergoing massive starburst activity.

As mentioned earlier, the selection criteria I use to create my sample mean that I am biased towards the brightest quasars (with high accretion rates/high black-hole masses) and the faintest host galaxies (possibly with low stellar mass). Since these objects are best-fit by a Type-1 quasar template, and dust has less of an effect in the $K_{\rm S}$ band, obscuration is unlikely to be the reason for the faintness of the host galaxy in the optical

Table 3.3: Mean and median star-formation rates (SFRs) for the simulated objects, according to how their SFR was derived. The first row corresponds to the relation of Yun et al. [2001] being applied to the extracted radio fluxes. The remaining calculations of SFR involve stellar-mass estimates, for a particular assumed black-hole (BH) mass with (or without) $M_{\rm BH}$-M_* evolution (see Section 3.1.4 for details). In each case, 74 – the final number of Gold quasars – is used as the sample size for calculating the uncertainties. The error in the median SFR is the median absolute deviation (MAD), which reduces the effect of outliers in the distribution.

Estimate used to derive the SFR	Median SFR ($\rm M_\odot\ yr^{-1}$)	Mean SFR ($\rm M_\odot\ yr^{-1}$)
$L_{1.4\,\rm GHz}$	206.0 ± 187.9	1165.9 ± 758.2
M_* using $M_{\rm BH} = 10^8\,\rm M_\odot$ and redshift evolution	52.1 ± 12.5	48.7 ± 2.1
M_* using $M_{\rm BH} = 10^9\,\rm M_\odot$ and redshift evolution	124.2 ± 18.2	113.9 ± 3.6
M_* using $M_{\rm BH} = 10^{10}\,\rm M_\odot$ and redshift evolution	293.9 ± 14.0	269.9 ± 5.8
M_* using $M_{\rm BH} = 10^8\,\rm M_\odot$ and no redshift evolution	85.5 ± 19.9	78.9 ± 3.4
M_* using $M_{\rm BH} = 10^9\,\rm M_\odot$ and no redshift evolution	203.8 ± 27.2	184.5 ± 6.0
M_* using $M_{\rm BH} = 10^{10}\,\rm M_\odot$ and no redshift evolution	477.2 ± 23.5	437.1 ± 10.0

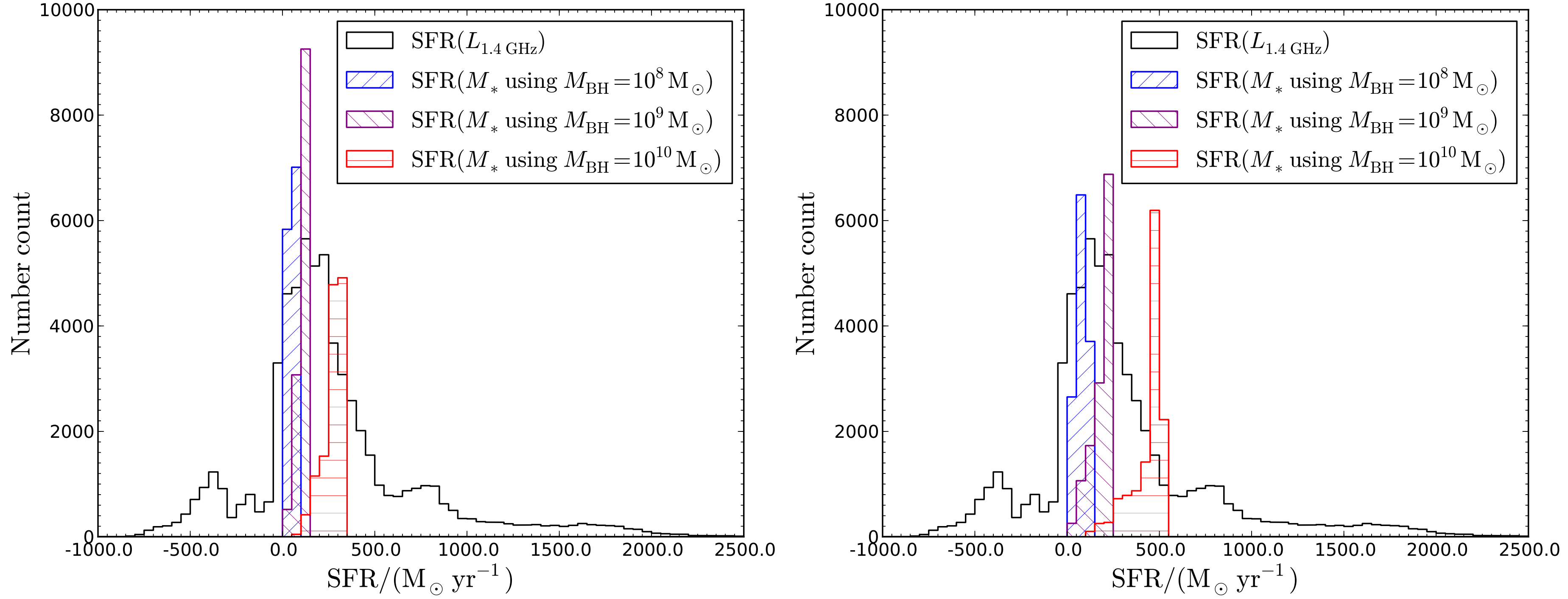

Figure 3.6: Distributions in the SFR for the quasars, as derived from either the radio luminosity (black histograms) or an estimate of the stellar mass. The latter is calculated using a combination of assumed black-hole mass – $10^8\,\mathrm{M}_\odot$ (blue histograms), $10^9\,\mathrm{M}_\odot$ (purple histograms) or $10^{10}\,\mathrm{M}_\odot$ (red histograms) – and evolution (left) or no evolution (right) in the M_{BH}–M_* relation. These hatched histograms have been scaled by a factor of 0.2 to ease comparison with the SFR($L_{1.4\,\mathrm{GHz}}$) distribution. Note that two quasars, brightest in radio luminosity, lie beyond the range of these plots.

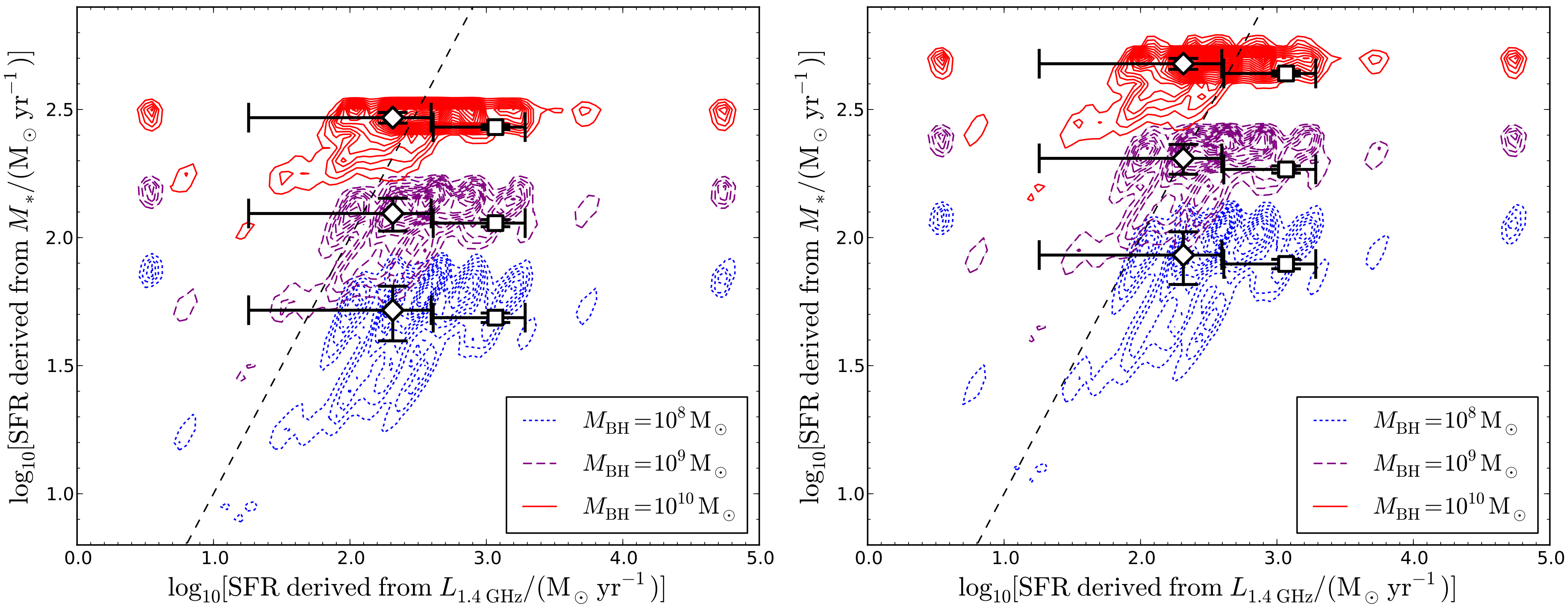

Figure 3.7: The SFR calculated from an estimate of the stellar mass, derived for different black-hole masses (see legend), against the SFR calculated from the extracted radio flux density at 1.4 GHz. The stellar masses used are calculated *with* (left) and *without* (right) evolution in the $M_{\rm BH}$–M_* relation. The simulated quasars (derived from the photometric-redshift probability distributions) are represented by blue (dotted), purple (dashed) and red (solid) contours (interval = 50), for assumed black-hole masses of $10^8\,{\rm M}_\odot$, $10^9\,{\rm M}_\odot$ and $10^{10}\,{\rm M}_\odot$, respectively. The dashed line indicates the one-to-one relation, if star formation (consistent with the SF-mass sequence) accounts for all of the radio emission. Quasars that have a measured negative radio flux are not shown, however they do contribute to the median and mean SFRs (white diamonds and squares, respectively, with error bars giving the uncertainties – see Table 3.3).

and near-infrared bands. Instead, these objects may have low stellar mass and therefore low star-formation rates, and so I would expect there to be less radio emission due to star formation as a result of my selection.

On a similar note, it may seem inappropriate to apply the standard $M_{\rm BH}$–M_* relation, given the biases described above and my selection of only 20% of the total quasar population (see end of Section 2.4). By doing so, for each assumed black-hole mass, I may in fact be overestimating the stellar mass. Consequently, the SFR of the host is also overestimated, and the true proportion of radio emission due to accretion would be even greater. Kimball et al. [2011] and Condon et al. [2013] use SDSS-selected quasars, which are also biased towards high accretion and low galaxy mass, albeit not to the same degree as my sample. (This is because my selection is strongly dependent on the $K_{\rm S}$ band, where the host galaxy and quasar emission are generally more comparable, relative to selection at optical wavelengths.) I also note however, that if the relation between optical luminosity and radio luminosity shown in Figure 3.3 is due to the accretion process then I would expect a greater degree of AGN-related radio emission in the SDSS samples. Therefore carrying out the same analysis for their quasars would also lead to an overprediction of the amount of radio emission due to star formation. Thus my conclusions, that the accretion process is the primary origin of the radio emission at $S_{1.4\,{\rm GHz}} < 1\,{\rm mJy}$, are strengthened.

3.2 Conclusions

As we probe to lower radio luminosities, it is vital that we fully appreciate the various populations contributing to the radio background. Of particular importance are star-forming galaxies and radio-quiet quasars (RQQs). These two types of sources may be confused for one another, owing to the similar amount of low-level radio emission they produce. They may even be composite, having both ongoing star-formation and black-hole accretion. To disentangle the two, and understand their roles in galaxy evolution, these objects must be better studied.

1. Using a probabilistic method to bin the Gold quasars by redshift, and separately by absolute i-band magnitude, two-sample Kolmogorov–Smirnov (KS) tests were

performed to compare the radio flux-density distribution of the quasars with that of random positions. The results show that there is an excess of radio emission, at the $\gg$99.99% confidence level, for quasars belonging to each of the redshift and luminosity bins. I also find a trend across the M_i bins, with higher radio luminosity correlating with increased optical luminosity. This provides indirect evidence for a relation between the accretion process and the source of the radio emission.

2. By comparing the radio flux-density distribution for the Gold quasars with that for control galaxies matched in redshift and stellar mass, I find that the quasars have excess radio flux when assuming the most reasonable values of black-hole mass ($\sim 10^8\,\mathrm{M}_\odot$), independent of whether I adopt an evolution in the black-hole mass – stellar mass relation. Star formation could explain the radio emission for quasars with the most massive ($\sim 10^9\,\mathrm{M}_\odot$) black holes, only if there is very little or *no* evolution in the $M_{\rm BH}$–M_* relation. This indicates that accretion is the primary origin of the quasars' total radio emission.

3. The contribution to radio source counts from quasars cannot be described by a power-law alone, due to a 'bump' appearing below 1 mJy. I find that a power-law plus Gaussian model for the source count distribution reproduces the behaviour over the range $-4.8 < \log_{10}[S_{1.4\,\mathrm{GHz}}] < -2.5$. I also find that such a source count distribution is in good agreement with the source-count model for unobscured RQQs, as simulated by Wilman et al. [2008]. The appearance of this feature is consistent with previous work in the literature [e.g. Kimball et al. 2011; Condon et al. 2013]. These authors suggest that star formation in the hosts of RQQs is the source of the radio emission. I make two independent calculations of SFR, one based on the expected stellar mass of the quasar's host galaxy, and the other using the radio luminosity. A comparison of the two indicates that the AGN in these RQQs are making the dominant contribution to the total radio emission. Although I cannot rule out the possibility that the host galaxies are undergoing starburst activity, I note that studies using far-infrared data from *Herschel* appear to rule out such prodigious star formation in quasar hosts.

4

Sample definition & JVLA data reduction for $z \sim 1$ quasars

> "With great bandwidth comes great sensitivity"
>
> – Uncle Rick, adapted from *Spider-Man*

In the previous chapter, my analysis on the origin of the radio emission was done statistically, with SFRs derived from stellar-mass estimates and directly from the radio luminosity. As discussed, the host galaxy is outshone by the AGN, making it difficult to determine the stellar mass. In the following piece of work (Chapters 4 and 5), for another sample of RQQs, I instead utilise *Herschel* photometry to calculate an independent measure of the SFR. In the far-infrared, light is dominated by thermal emission from the cool dust associated with star formation, with negligible heating from the AGN [Rowan-Robinson 1995; Genzel and Cesarsky 2000]. Further advantages of using this particular sample, described in Section 4.1, are that the RQQs are all at $z \sim 1$ (thereby minimising evolutionary effects) and have been selected to span a factor of ~ 100 in optical luminosity (enabling the luminosity-dependence of any correlations to be studied). In addition, this work exploits the improved sensitivity of the Karl G. Jansky Very Large Array (JVLA), with the reduction of these radio observations forming the basis of this chapter. For reference, I also include the theory behind radio interferometry.

4.1 Sample selection

Investigations that use samples covering a wide redshift range are subject to K-correction uncertainties and evolutionary effects. Therefore careful study of objects belonging to a single epoch is an important step towards understanding radio emission due to AGN, and that due to star formation. These findings, including the way in which properties vary as function of optical luminosity, can then be incorporated into how the underlying physical processes evolve over cosmic time.

A sample of 72 RQQs is used for the work presented in this and the next chapter. These are taken from the *Spitzer-Herschel* Active Galaxy Survey [SHAGS; Jarvis et al., in prep.], which includes quasars that are selected from the SDSS using multi-colour criteria. The quasars are restricted to a thin redshift slice of $0.9 < z < 1.1$ (Figure 4.1), so chosen because: (a) this is the minimum redshift at which there are sufficient high-luminosity quasars for comparison to bright objects at higher redshifts, and (b) the targets are still close (i.e. bright) enough that a large sample of them can be studied in a reasonable amount of time.

The quasars span nearly 5 magnitudes in optical luminosity ($1.1 \times 10^{11} < L_{\rm opt}/{\rm L}_{\odot} < 9.6 \times 10^{12}$), and the FIRST [White et al., 1997], NVSS [Condon et al., 1998], and WENSS [Westerbork Northern Sky Survey; Rengelink et al., 1997] radio catalogues are used to identify those that are radio-loud. These are divided into four bins in bolometric luminosity, and a sample is randomly selected such that there are around 20 radio-loud quasars per bin. The RQQ sample is then created, forced to match the radio-loud quasars in terms of redshift and bolometric luminosity. Being undetected in FIRST, which has a flux-density limit of 1 mJy/beam, targeted observations for the RQQs were obtained using the JVLA (Section 4.2.3), exploiting the greater sensitivity of this instrument compared to the VLA.

4.2 Data

As illustrated in Chapters 2 and 3, it is necessary to have a wealth of ancillary data available for the AGN in question, allowing various galaxy-evolution processes to be disentangled from one another. Whilst MIR data and X-ray data exist for this sample, in

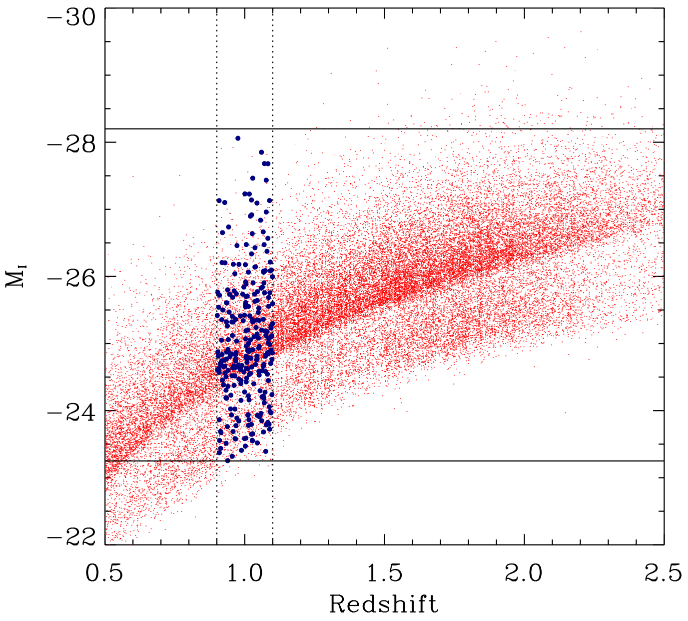

Figure 4.1: Absolute i-band magnitude against redshift for SDSS quasars (red dots), from which my sample of 72 RQQs is selected. This is done over the redshift range $0.9 < z < 1.1$, with radio-loud quasars (blue circles) removed. These are identified using NVSS, FIRST and WENSS radio surveys. (Figure from Jarvis et al., in prep.)

the form of *Spitzer* and *XMM-Newton* observations, I describe below only the datasets that I use in the current investigation.

4.2.1 Optical: SDSS

Optical photometry ($ugriz$) from the SDSS is used for the pre-selection of the quasars [Richards et al., 2002; Schneider et al., 2005], with positions accurate to within 0.2 arcsec. Follow-up spectroscopy from the fifth data release (DR5) [Adelman-McCarthy et al., 2007] provides accurate redshifts, and allows absolute magnitudes to be calculated. The band that I am most interested in for this work is the i band, as this is dominated by thermal emission from the accretion disc and is less susceptible to dust than bluer bands. The usual cut of $M_i = -22$ is used to separate quasars from Seyfert galaxies [Schneider et al., 2003], although the relatively high redshift $0.9 < z < 1.1$ means that Seyferts are already eliminated from this sample of 72 objects by the SDSS spectroscopic limit.

4.2.2 Far-infrared: *Herschel*

To estimate the level of star formation in the quasars, I use 5 far-infrared photometric bands from the *Herschel Space Observatory* [Pilbratt et al., 2010]. These are at 70 and 160 µm using the Photodetector Array Camera and Spectrometer (PACS) instrument [Poglitsch et al., 2010], and at 250, 350 and 500 µm using the Spectral and Photometric Imaging REceiver (SPIRE) instrument [Griffin et al., 2010]. The mean 1-σ photometric uncertainties for the PACS and SPIRE bands are (2.56, 5.27) mJy and (6.29, 5.38, 7.09) mJy, respectively, and the beam sizes range from 5 to 36 arcsec at full-width half-maximum. The RQQ sample was cross-matched with public data, including fields of the *Herschel* Multi-tiered Extragalactic Survey [Oliver et al., 2012], and the remaining measurements (for 53 of the 72 sources) were obtained as part of a targeted program (PI: Jason Stevens). All maps were reduced by Eleni Kalfountzou and Jose Manuel Cao Orjales [Kalfountzou et al., in prep.], using pipelines within the *Herschel* Interactive Processing Environment (HIPE).

4.2.3 Radio: JVLA

In 2012, the VLA completed the upgrade of its receivers, and began operations as the JVLA. For observations done at 1.4 GHz (‘L band’), this means a large improvement in sensitivity due to the instantaneous bandwidth increasing from 1.3–1.7 GHz to 1.0–2.0 GHz. Previously, an integration time of 8 hours would be needed to reach a depth of 30 µJy/beam [Napier et al., 1983], making targeted observations of large samples unfeasible. Using the JVLA, however, 25 minutes per quasar was chosen in order to achieve an rms noise level of 12.5 µJy/beam. In addition to this, 10 minutes per source for overheads and calibration are required, leading to 42 hours of observations in total (VLA-12B-115, PI: Jarvis). These were taken between 4th November 2012 and 9th December 2012. Visibilities are recorded every second for 16 spectral windows, each having 64 channels of 1-MHz bandwidth. The most-extended configuration of the JVLA, the ‘A’ array, is used to obtain the highest resolution. Its layout of antennae is presented in Figure 4.2, with each arm extending 21 km in length, creating a maximum baseline of 36.4 km. For the L band, this results in a synthesised beam that is 1.3 arcsec across.

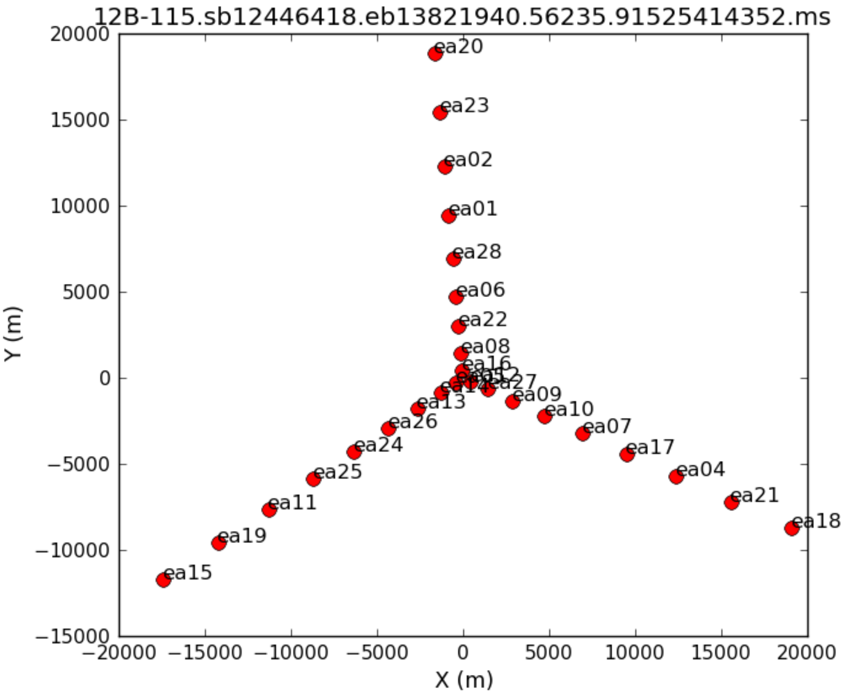

Figure 4.2: The JVLA's A-array configuration, with distances in the X and Y directions given relative to the centre of the array. The antennae at the centre are those labelled 'ea05', 'ea12' and 'ea16'.

4.3 Radio interferometry

When a circular aperture is uniformly illuminated, an Airy diffraction pattern is produced. This consists of a bright central region, known as the Airy disc, surrounded by numerous concentric rings of decreasing brightness (Figure 4.3). Two sources of light, each producing its own Airy pattern, are said to be 'just resolved' when the Rayleigh criterion is satisfied. This is where the peak intensity of one pattern overlays the first null of the other pattern, as shown in Figure 4.4. The size of the Airy disc is defined by the angle (θ, in radians) at which the first minimum occurs:

$$\sin\theta \approx 1.22\frac{\lambda}{D}, \tag{4.1}$$

where λ is the wavelength of observation and D is the diameter of the aperture. When dealing with small angles, the small-angle approximation $\sin\theta \approx \theta$ can be made, giving:

$$\theta \approx 1.22\frac{\lambda}{D}. \tag{4.2}$$

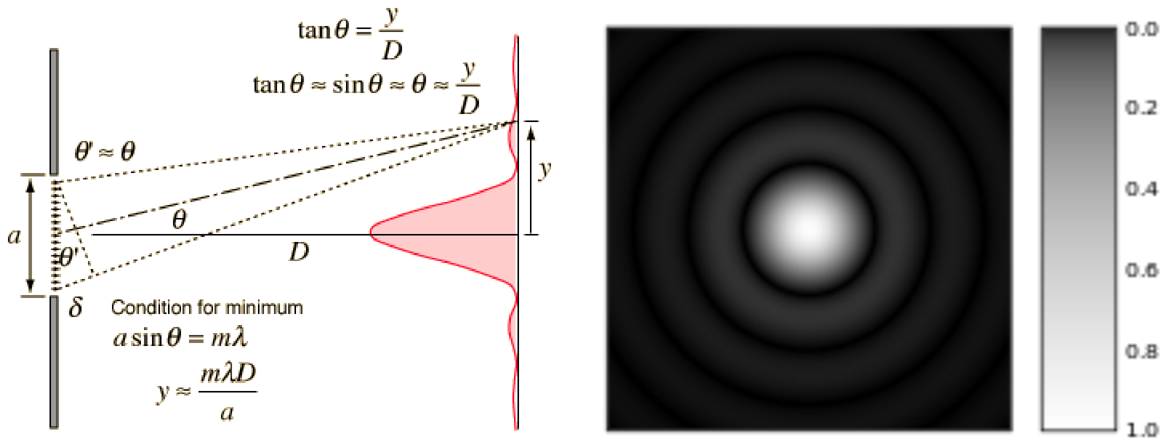

Figure 4.3: The geometric set-up, shown in cross-section (left), that leads to an Airy diffraction pattern (right) when a circular aperture is used. The intensity is indicated by the grey-scale bar, though note that the scaling has been modified to enhance the outermost rings. Credit: (left) HyperPhysics ©C.R. Nave, 2012, (right) retrieved from https://en.wikipedia.org/wiki/Airy_disk.

This angle is also referred to as the diffraction limit, and governs the angular resolution of a single-dish telescope. Due to the scaling with wavelength, larger telescopes (i.e. larger dish-diameters, D) are needed to maintain resolution at longer wavelengths. For example, single-dish radio telescopes such as the Lovell Telescope ($D = 76\,\mathrm{m}$) and the Arecibo Radio Telescope ($D = 305\,\mathrm{m}$) achieve resolutions of 50–500 arcsec. In order to go beyond this, so that we can study the sub-arcminute structure of astrophysical objects, another technique is required: radio interferometry.

4.3.1 Aperture synthesis

Radio interferometry works by using a combination of individual dishes, or antennae, to synthesise a much larger dish. Hence the term 'aperture synthesis'. Instead of the diameter of an antenna, the maximum distance *between* antennae determines the resolution. This is also called the maximum baseline, b_{max}, and so Equation 4.2 becomes $\theta \approx 1.22\lambda/b_{\mathrm{max}}$. Starting with the simplest set-up, a two-element radio interferometer operates much in the same way as Young's double-slit experiment (Figure 4.5). For a wavefront incoming at angle θ (Figure 4.6), light arrives at the second antenna after a time delay of τ_g, having traversed the extra distance $\vec{b} \cdot \vec{s}$. This is the 'geometric delay' and is corrected for by adding a delay to the voltage signal received at the first an-

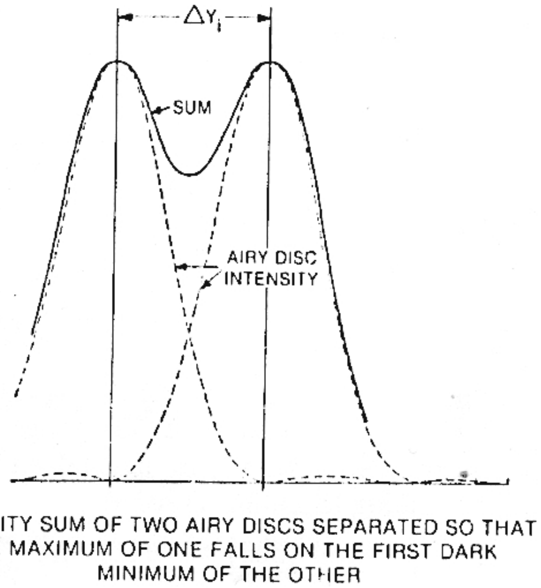

Figure 4.4: The diffraction patterns for two point sources, at the limit where they can be resolved, thereby demonstrating the Rayleigh criterion, $\Delta Y_i \approx 1.22\lambda/D$. Credit: Moller [1988].

tenna. The two signals are then brought together at the correlator, where they undergo interference via multiplication and integration. The resulting interference fringes are the telescope's response function, encoding information about the spatial distribution of the sky's brightness.

An outline of the mathematics involved is given below, where the signals received by the two antennae (V_1 and V_2) are taken to be quasi-monochromatic at frequency ν. Angled brackets represent time-averaging, which is carried out by the correlator's integrating circuit. The output is then as follows:

$$\begin{aligned}
r(\tau_g) &= \langle V_1(t)V_2(t)\rangle, && (4.3)\\
&= \int v_1\cos[2\pi\nu(t-\tau_g)]v_2\cos[2\pi\nu t]dt, && (4.4)\\
&= \int v_1v_2(\cos[2\pi\nu t]\cos[2\pi\nu\tau_g]+\sin[2\pi\nu t]\sin[2\pi\nu\tau_g])\cos[2\pi\nu t]dt, && (4.5)\\
&= \int v_1v_2\cos^2[2\pi\nu t]\cos[2\pi\nu\tau_g]dt, && (4.6)\\
&= \frac{1}{2}v_1v_2\cos[2\pi\nu\tau_g]. && (4.7)
\end{aligned}$$

Next I consider the primary-beam response function of an individual dish. This governs the field-of-view and sets the effective collecting area, $A(\vec{s})$. (I state its dependence on

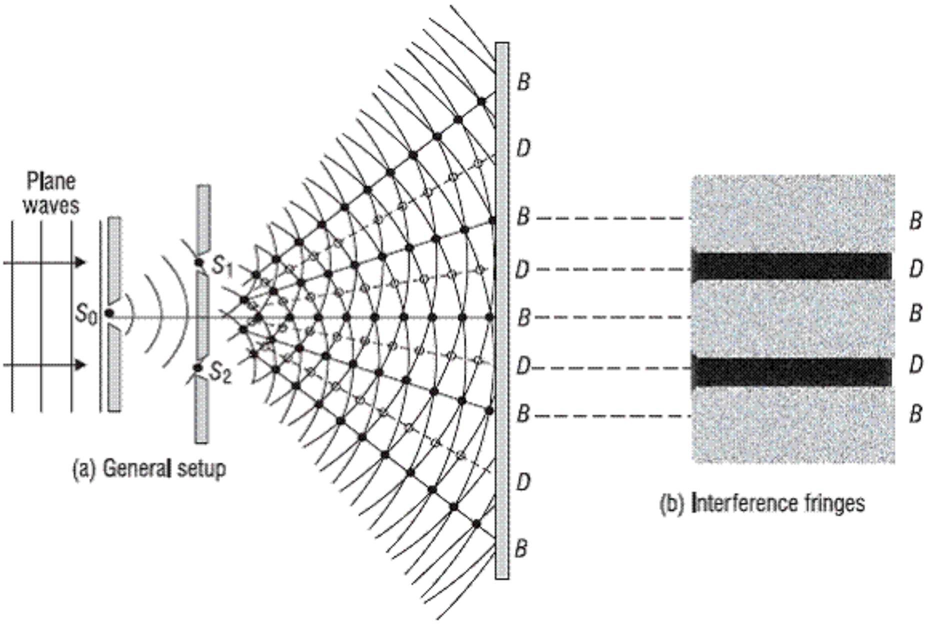

Figure 4.5: Young's double-slit experiment (a), showing the diffraction of light waves through the two slits, S_1 and S_1, and the resulting intereference pattern of bright and dark 'fringes' (b). Credit: image retrieved from https://astro.uni-bonn.de/~wucknitz/gravlens/.

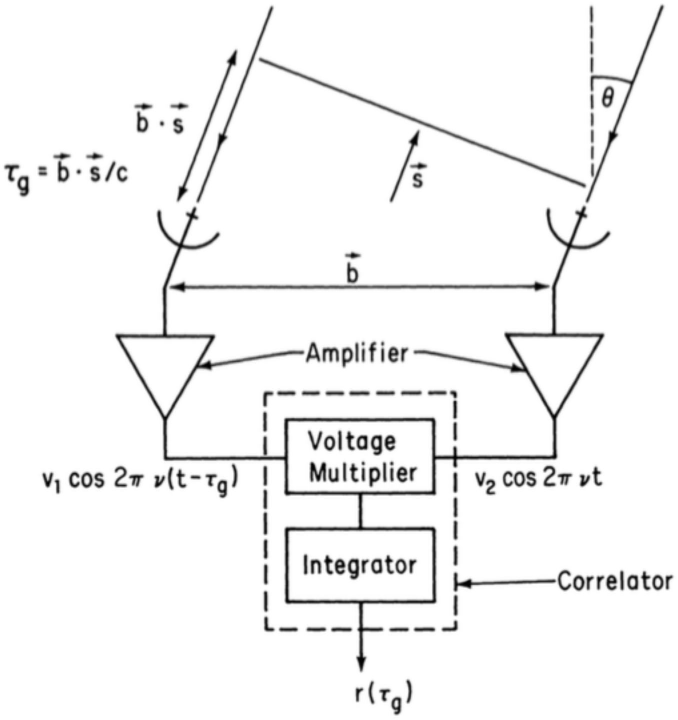

Figure 4.6: A schematic diagram of a two-element interferometer, sampling a wavefront in the direction $\vec{s}$ at angle θ from the zenith. Credit: Thompson [1999].

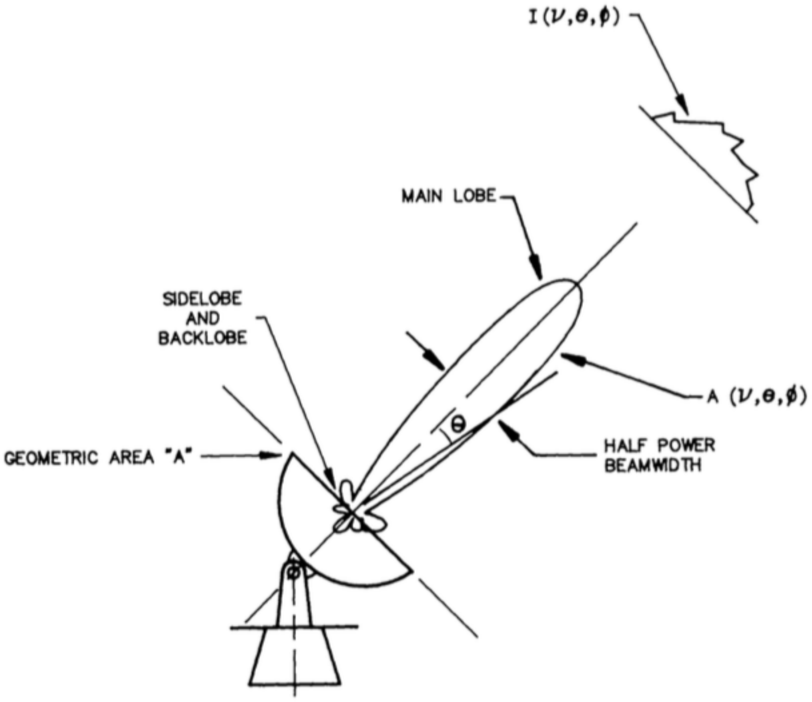

Figure 4.7: An antenna's primary-beam response, A, which varies with frequency (ν) and direction co-ordinates (θ and ϕ). The intensity distribution of the astrophysical object being observed is indicated by $I(\nu, \theta, \phi)$. Credit: Napier [1999].

$\vec{s}$ to maintain consistency with Figure 4.6, but it can also be written $A(\nu, \theta, \phi)$ as done so in Figure 4.7, which is provided for illustration.) $I(\vec{s})$ is the brightness of the radio source at frequency ν, in the direction $\vec{s}$. The total power received from the source, over bandwidth $\Delta\nu$ and solid angle $d\Omega$, is $A(\vec{s})I(\vec{s})\Delta\nu\, d\Omega$. Since $v_1 v_2$ is proportional to the received power, the output from the correlator for the signal over solid angle $d\Omega$ is

$$dr = A(\vec{s})\ I(\vec{s})\ \Delta\nu\ \ \cos[2\pi\nu\tau_g]\ d\Omega, \tag{4.8}$$

where constant gain factors have been omitted. Integrating over the celestial sphere, Ω, and remembering that τ_g is a function of the baseline and source vectors, the total output from the correlator is

$$r = \Delta\nu \int_{\Omega} A(\vec{s})\ I(\vec{s})\ \cos\left[\frac{2\pi\nu\vec{b}\cdot\vec{s}}{c}\right] d\Omega. \tag{4.9}$$

Note that the above takes the form of the real part of a Fourier transform (FT, Equation 4.11, where ξ is any real number). Hence the sky's radio-brightness distribution

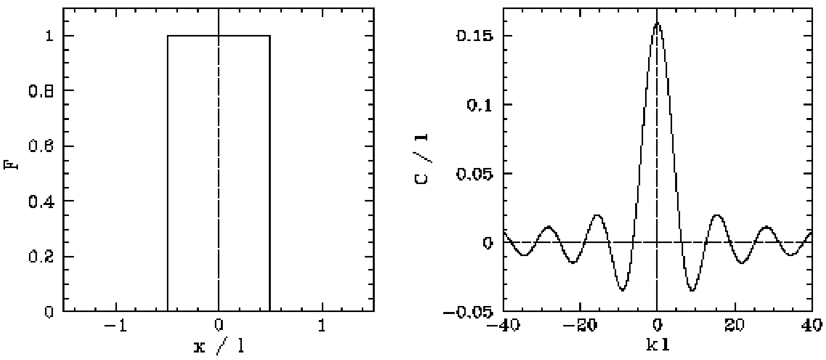

Figure 4.8: An example of a top-hat function (left) and its Fourier transform, a sinc function (right). Credit: Richard Fitzpatrick, 2013, retrieved from https://farside.ph.utexas.edu/teaching/315/Waveshtml/node57.html.

is connected to the interferometer's response (r, effectively the interference pattern) via an FT. This means that it is possible to invert the cross-correlated signal mathematically to produce an image of the sky.

$$\hat{f}(\xi) = \int_{-\infty}^{\infty} f(x)\ e^{-2\pi i x \xi}\, dx, \tag{4.10}$$

$$= \int_{-\infty}^{\infty} f(x)\ (\cos[2\pi x\xi] - i\sin[2\pi x\xi])\, dx. \tag{4.11}$$

To take the FT of a function means to convert it into a reciprocal (Fourier) space where it can be represented by a series of sinusoidal functions. This is based on the assumption that the original function is incoherent and so obeys the superposition principle. In the case of an interferometer this means that the signal over a patch of sky, $d\Omega$, is uncorrelated with that from another. This then allows the 'total' interferometer response to be written as a linear superposition of the individual responses to each patch of sky. In the case of a true point-source, its intensity distribution on the sky is a δ-function, which then becomes a constant in Fourier space. Alternatively, a source may have its brightness distribution described as a top-hat function. The FT of this is a sinc function, as shown in Figure 4.8. Further examples of FT pairs, or 'reciprocity relations', are presented in Figure 4.9. It is also useful to note that a broad feature/function in real space corresponds to a narrow feature/function in Fourier space, and vice versa.

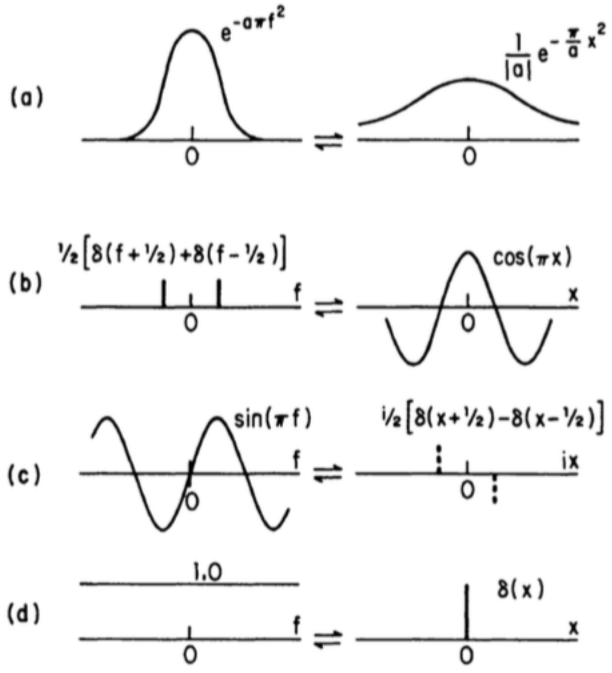

Figure 4.9: Examples of what a function in real space looks like in Fourier space when it has undergone an FT. Note that the asymmetry of the sine wave means that its FT is in the imaginary domain, as indicated by the dashed lines. Credit: Ekers [1999].

4.3.1.1 Measuring visibilities

The cosine function in the response, r (Equation 4.9), leads to the interferometer being sensitive to only the even (symmetric) part of the source-brightness distribution, $I(\vec{s})$. Therefore a second correlator is implemented to detect the odd (anti-symmetric) part. This is done by inserting a 90° phase delay into the output of one of the antennae, and the resulting response is

$$R_{\text{sin}} = \Delta\nu \int_S A(\vec{s})\ I(\vec{s})\ \sin\left[\frac{2\pi\nu\vec{b}\cdot\vec{s}}{c}\right] d\Omega. \tag{4.12}$$

The final measurement, the 'visibility', is therefore a combination of cosines and sines, which means that we can make use of the identity,

$$e^{i\psi} = \cos(\psi) + i\sin(\psi), \tag{4.13}$$

to write it more conveniently as a complex quantity:

$$V = R_{\text{cos}} - iR_{\text{sin}} = Ae^{-i\psi}, \tag{4.14}$$

where the visibility amplitude (A) and phase (ψ) are given by Equations 4.15 and 4.16:

$$A = \sqrt{R_{\mathrm{cos}}^2 + R_{\mathrm{sin}}^2}, \tag{4.15}$$

$$\psi = \arctan(R_{\mathrm{sin}}/R_{\mathrm{cos}}). \tag{4.16}$$

As such, Equation 4.9 can be written in its complex form:

$$V = \Delta\nu \int_S A(\vec{s})\ I(\vec{s})\ \exp\left[\frac{-i2\pi\nu\vec{b}\cdot\vec{s}}{c}\right] d\Omega. \tag{4.17}$$

The Fourier space of the sky-brightness distribution, described by co-ordinates θ and ϕ, is referred to as the u-v plane. The position of each visibility measurement is given by the co-ordinates, u and v, where u is in the East-West direction and v in the North-South direction. u and v are usually quoted in units of wavelength. However, so far I have described the response of the most-basic radio interferometer, which consists of two antennae. Since the antennae are arranged in a one-dimensional fashion, their sensitivity to the sky (and hence the apparent sky brightness) is also one-dimensional.

The Westerbork Synthesis Radio Telescope (WSRT) is a linear array of 14 antennae, lying in an East-West direction. A short integration time produces the one-dimensional fringes seen in (a) of Figure 4.10, whilst longer integration times leads to more extended coverage of the u-v plane (b), and so a better synthesised-beam. (The synthesised beam is produced by averaging the point-source responses that are output by all possible pairs of antennae in the array. It is analogous to a point-spread function but, because it is calculated from the distribution and sizes of the antennae in the array, its response function is known precisely.) The better u-v coverage over time is a consequence of the Earth's rotation, causing the source's elevation to change. As this happens, the *projected* baseline between a pair of antennae varies (i.e. $\vec{b}\cdot\vec{s}$ changes), and so more u-v space is 'swept out'. As a result, the object is measured with more baselines and therefore a greater number of Fourier components. These enable the interferometer's response to a point source to be better constrained.

The arrangement of the antennae in an array determines the number and range of independent baselines with which visibilities can be measured. So that there is instantaneous two-dimensional coverage of the u-v plane, without the need for very long integration times, the Very Large Array (VLA) uses a Y-shaped configuration. This leads to a synthesised beam with order-6 symmetry, illustrated in (c) of Figure 4.10. Although the shape of the synthesised beam is taken into account during imaging (Section 4.3.1.3), artefacts may still remain. Hence, as shown by Figure 4.10 (d), observing the source at numerous elevations leads to an improvement. Furthermore, whilst baseline lengths determine the resolution, sensitivity is calculated in the same way as for single-dish telescopes, with larger collecting areas being favoured. The difference is that, because an interferometric technique is used, this sensitivity is not uniform across all angular scales.

Radio observations can be done from the ground as they are not affected by phase perturbations introduced by the atmosphere. This is because of a concept called ‘closure phase’, which applies for an array with at least three antennae [Jennison, 1958]. The phase of the visibility measured on baseline ‘1,2’ is $\Phi(12) = \phi(12) + \varepsilon(1) - \varepsilon(2)$, where $\phi(12)$ is the true source visibility on that baseline and ϵ values are the phase offsets caused by atmospheric turbulence above each antenna (Figure 4.11). Writing equivalent expressions for the other two baselines and adding them together gives the closure phase. Note that the atmospheric offsets (and, similarly, all other *antenna*-based phase errors) cancel out, leaving a dependence on only the source’s true brightness-distribution.

However, atmospheric effects do limit the frequency range of the radio window. Towards the high-frequency end ($\nu > 30\,\mathrm{GHz}$, Wilson et al. 2009), the vibrational energies of atmospheric molecules (namely H_2O, O_2 and CO_2) are comparable to the energies of mid-infrared photons, and so most of this extraterrestrial radiation is absorbed. The limit at the lower end ($\nu < 10\,\mathrm{MHz}$, Burke and Graham-Smith 2009) is a consequence of photons reflecting off the ionosphere, which is a part of the upper atmosphere that is partially ionised by solar ultraviolet radiation.

Finally, for any observation, there are in fact two sets of visibilities that are created independently, doubling the data rate. This is due to the receiver on each antenna detecting the electric vector, E, of the incoming electromagnetic wave in two orthogonal

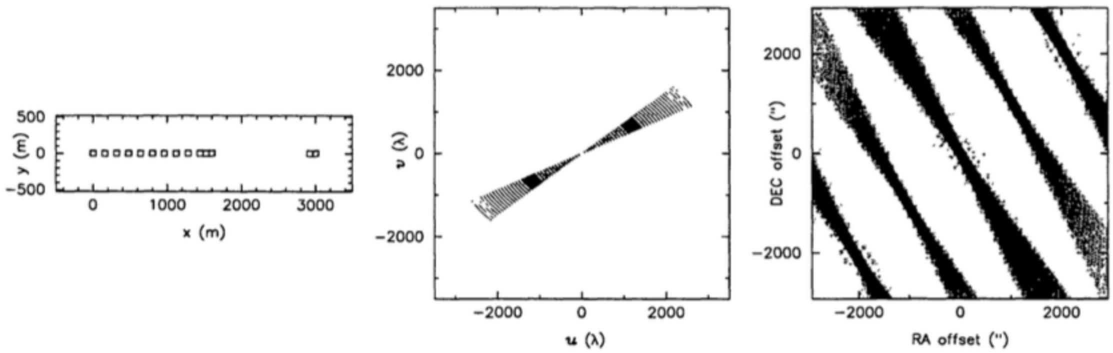

(a) Snapshot u-v coverage using the WSRT

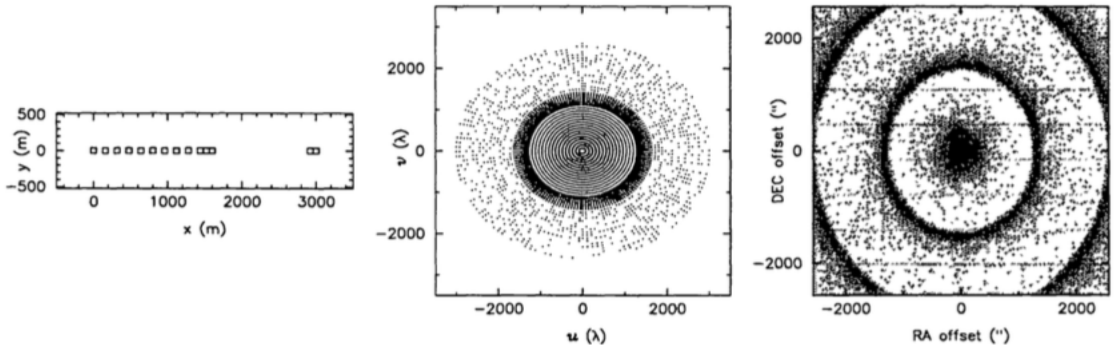

(b) Integrated u-v coverage using the WSRT

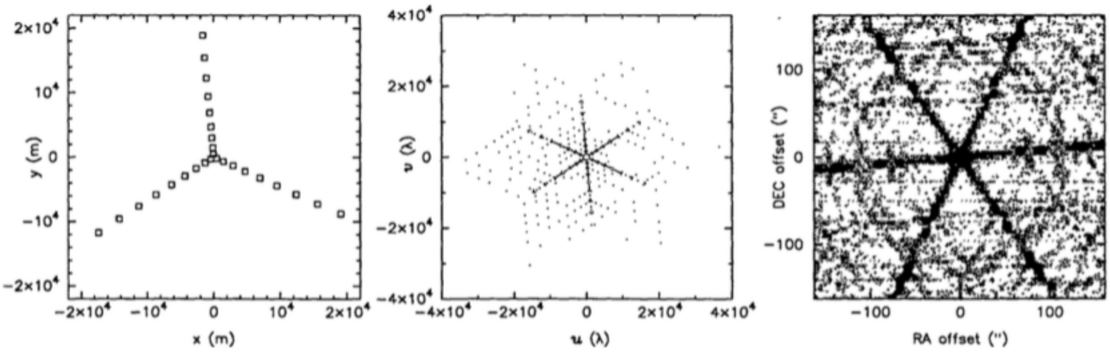

(c) Snapshot u-v coverage using the VLA

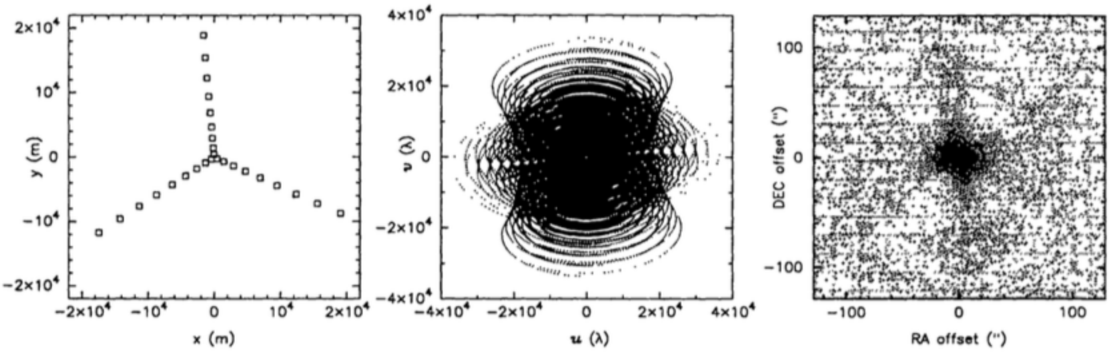

(d) Integrated u-v coverage using the VLA

Figure 4.10: The antenna layout (left column), u-v coverage (middle column), and the resulting synthesised beam (right column) for the Westerbork Synthesis Radio Telescope (WSRT) and the Very Large Array (VLA). The integration time for each observation is: (a) 1 hour, (b) 12 hours, (c) 1 minute, (d) 12 hours. Credit: Holdaway and Helfer [1999].

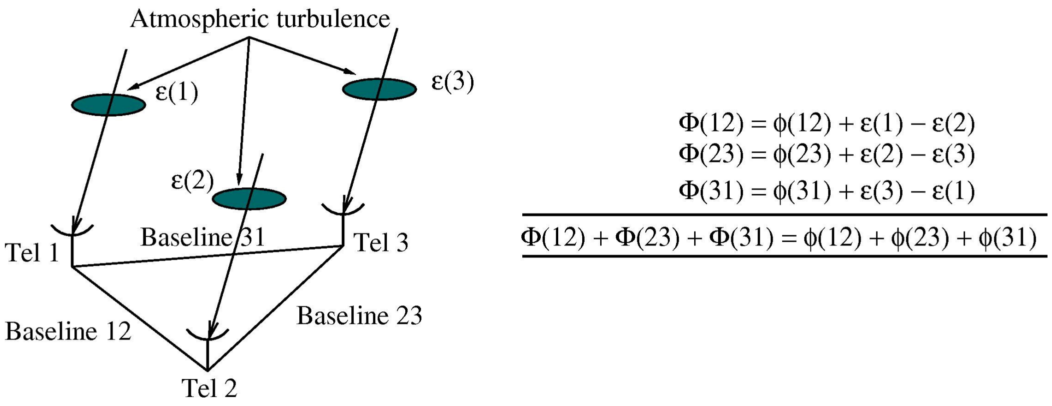

Figure 4.11: An illustration of closure phase, which depends on the source structure (ϕ) and not any phase perturbation (ε) introduced by the atmosphere. Cross-correlations along different baselines mean that the latter cancels out, if at least three antennae are used. Credit: Haniff [2007].

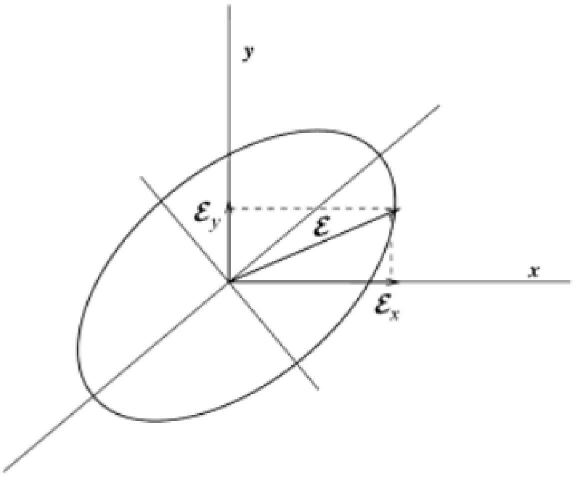

Figure 4.12: A monochromatic wave that is elliptically polarised. As the electric vector, E, traces an ellipse, the two components E_x and E_y oscillate along their orthogonal directions with phases ϕ_1 and ϕ_2, respectively. Credit: Burke and Graham-Smith [2009].

directions, E_x and E_y (Figure 4.12). These are complex amplitudes, each having their own phase associated with them:

$$E = (\hat{x}E_x e^{i\phi_1} + \hat{y}E_y e^{i\phi_2})e^{i\omega t}. \tag{4.18}$$

The E_x signals from all the antennae are cross-correlated separately from the E_y signals. With these visibilities it is possible to determine the polarisation of the radiation, which could be a single wave or the sum of a number of waves. The net polarisation is then stated in terms of the Stokes parameters, defined as follows:

$$I \equiv E_x^2 + E_y^2, \tag{4.19}$$

$$Q \equiv E_x^2 - E_y^2, \tag{4.20}$$

$$U \equiv 2E_xE_y\cos[\Delta\phi], \tag{4.21}$$

$$V \equiv 2E_xE_y\sin[\Delta\phi], \tag{4.22}$$

where the relative phase between the E_x and E_y components is $\Delta\phi = \phi_1 - \phi_2$. The most commonly-used Stokes parameter for imaging is I, as this is proportional to the total power of the wave, i.e. the intensity. Q and U parametrise linear polarisation, and circular polarisation is described via the V parameter.

In the case of a fully-polarised wave, $I^2 = \sqrt{Q^2 + U^2 + V^2}$. For describing partially-polarised radiation, $P = \sqrt{Q^2 + U^2 + V^2}$ and the degree of polarisation is given by P/I. If the radiation is completely unpolarised, I is equal to the intensity and $Q = U = V = 0$.

4.3.1.2 Calibration

A consequence of the multiplication step during cross-correlation is that slight fluctuations in the amplifier gains do not matter too much, as they are generally uncorrelated with the amplifier of the second antenna. This is another great advantage over single-dish observations. Having said this, if there *are* correlations in the fluctuations, then the visibilities of a source with known output need to be measured at regular intervals. Doing so allows the gains to be tracked over time and corrected for, which is one of the calibration steps that are required before the visibilities can be used for imaging.

Dependent on the path differences introduced by the electronics, or proximity of the antenna to the correlator, an *instrumental* delay needs to be included in addition to the geometric delay (Figure 4.6). This is referred to as delay calibration, and necessarily takes into account the relative positions of the antennae in each cross-correlation pair.

There are a variety of different effects within the system that, like those explained above, modify the measured visibilities once the wavefronts are received and processed by the instrument. If we represent the true visibilities by the vector V_{ij} then each process corrupting the visibilities can be written as a Jones matrix acting on this vector. (The ij subscript refers to the baseline between antenna i and antenna j.) Combining multiple processes (described below), we then obtain the Measurement Equation [Hamaker et al., 1996]:

$$V'_{ij} = M_{ij}\, B_{ij}\, G_{ij}\, D_{ij}\, O_{ij}\, T_{ij}\, F_{ij}\, P_{ij}\, V_{ij}. \tag{4.23}$$

By linearising this expression and solving via χ^2 minimisation, the true visibilities can be inferred from the data (V'_{ij}) algebraically. The various processes that need to be corrected for are:

- P_{ij} - The transformation that may be needed, to go between the co-ordinate system of the rotating sky and the co-ordinate system of the antenna receiver's rotating mount (if it is not equatorial). This involves a rotation over the parallactic angle.

- F_{ij} - The Faraday rotation of the electric-field vector, caused by the ionosphere.

- T_{ij} - Any tropospheric effects, which are not dependent on polarisation. These are multiplicative and include the atmosphere's opacity and variation of the light's path length.

- O_{ij} - The collecting area's dependence on elevation, and other effects as a result of the telescope's optical components.

- D_{ij} - The 'D-term', describing the instrument's response to polarisation. There may be leakage between the feeds, such as left-polarised emission being picked up by the right-polarised detector.

- G_{ij} - The complex gain response, which is a consequence of the electronic components encountered along the signal path from the feed to the correlator. It includes the scale factor for calibrating the absolute flux density, and depends on the polarisation.

- B_{ij} - The bandpass response, which depends on the frequency and the spectral filters in the electronic transmission system.

- M_{ij} - Any baseline-based correlator errors. These are non-closing (see discussion of closure phase in Section 4.3.1.1), unlike the errors represented by the previous matrices, which are antenna-based.

For each set of observations, a standard flux-calibrator and phase calibrator are required. Measuring the visibilities for these sources then provides information about the response of the radio instrument, allowing calibration solutions (for both amplitude and phase) to be derived via Equation 4.23. These solutions, which correct for the corruption of the visibilities outlined above, are then applied to the science targets. To achieve good calibration, the order of observations is important, and can influence the choice of calibrators. For example, it is necessary to alternate scans between the science target and the phase calibrator so that there is good interpolation of amplitudes and phases over time. Therefore it is advantageous to choose a phase calibrator that is close to the science target, to reduce slewing time and minimise any differences caused by atmospheric turbulence. The flux calibrator is used to calibrate the bandpass and bootstrap the flux densities, but because it does not have any time variation (relative to the timescale of the observations), only a single scan is required.

4.3.1.3 Imaging

In order to produce an image of the sky-brightness distribution $[I(\theta,\phi)]$, an *inverse* Fourier transform (IFT) needs to be performed on the visibilities. This would be straightforward if we had complete information, with a visibility measurement at every position on the u-v plane. In reality, the u-v plane has only been sampled, and this sampling function $[S(u,v)]$ relates the true visibility $[V(u,v)]$ to the sampled visibility $[V'(u,v)]$ as follows:

$$V'(u,v) = S(u,v)\,V(u,v). \tag{4.24}$$

As already described, the visibility is the related to the sky brightness via

$$V(u,v) = \mathrm{FT}[I(\theta,\phi)]. \tag{4.25}$$

In accordance with the convolution theorem, a point-wise multiplication in one domain (e.g. Fourier space) is equal to a convolution (defined by Equation 4.26) in the reciprocal domain (e.g. real space). Hence, taking the IFT of $V'(u, v)$ gives Equation 4.28:

$$(f * g)(t) \equiv \int_{-\infty}^{\infty} f(\tau)\, g(t - \tau)\, d\tau, \tag{4.26}$$

and

$$\begin{aligned} \mathrm{IFT}[V'(u, v)] &= \mathrm{IFT}[S(u, v)] * \mathrm{IFT}[V(u, v)], && (4.27) \\ &= \mathrm{IFT}[S(u, v)] * I(\theta, \phi). && (4.28) \end{aligned}$$

The ‘dirty beam’ is $B(\theta, \phi) = \mathrm{IFT}[S(u, v)]$, and so the image produced from the sampled visibilities is the true-sky image convolved with the dirty beam. This is called the ‘dirty image’. As the synthesised beam is well-characterised, it can be accurately deconvolved from the dirty image, thereby producing a ‘cleaned’ image.

As the effect of the beam is iteratively deconvolved, the image’s residuals are regularly updated. It it therefore possible to see an improvement in the noise level as the imaging progresses. This is a good indication of image quality, as it dictates the depth to which radio sources may be detected. An indication that imaging is close to completion is the noise level asymptoting to the theoretical-noise value. This limit is set by the sensitivity equation:

$$\Delta I = \frac{\mathit{SEFD}}{\eta_{\mathrm{c}} \sqrt{n_{\mathrm{pol}}\, N(N-1)\, t_{\mathrm{int}}\, \Delta\nu}}, \tag{4.29}$$

where *SEFD* stands for the ‘system equivalent flux density’, measured in Jansky units ($1\,\mathrm{Jy} = 10^{-26}\,\mathrm{W\,m^{-2}\,Hz^{-1}}$). This is defined as the flux density a source must have to double the system temperature, T_{sys}, which is the summation of the noise temperatures of the receiver, the antenna and the sky. Lower values of *SEFD* correspond to better sensitivity, and for the VLA’s antennae, $\mathit{SEFD} = 5.62\, T_{\mathrm{sys}}/\eta_{\mathrm{A}}$ where η_{A} is the (frequency-dependent) antenna-aperture efficiency. The remaining quantities are: η_{c} - the correlator efficiency; η_{pol} - the number of polarisation products in the image; N - the number of antennae; t_{int} - the total on-source integration in seconds; and $\Delta\nu$ - the bandwidth in Hz.

Throughout Section 4.3.1 I have assumed that the radiation is quasi-monochromatic.

This means that visibilities, that are actually measured over a finite bandwidth ($\Delta\nu$), have values of u and v that are incorrect. (Remember that these Fourier-space co-ordinates are measured in units of wavelength.) Clearly the effect is greatest at the extreme ends of the band, away from the central frequency (ν_0) that had been assumed. The result in the image plane is smearing in the radial direction, which worsens with distance from the pointing centre. The effect is known as bandwidth smearing (B_{S}, c.f. chromatic aberration), and can be parametrised as in Equation 4.30, where θ is the angular offset of the source from the centre and θ_{HPBW} is the half-power beamwidth of the synthesised beam. It is deemed to be significant when the value of B_{S} is of order unity [Fomalont and Perley, 1999].

$$B_{\mathrm{S}} = \left(\frac{\Delta\nu}{\nu_0}\right)\left(\frac{\theta}{\theta_{\mathrm{HPBW}}}\right). \tag{4.30}$$

Time-averaging may be implemented to reduce the large volume of radio interferometric data, but this also leads to smearing in the image plane. It arises because the averaged visibilities are assigned (u, v) values that correspond to the mid-points of the averaging intervals (Δt_{int}). Bearing in mind that the u-v plane is swept out over time as the Earth rotates, this means that averaged visibilities have been rotated away from their original positions. Since rotation in the u-v plane is reflected by rotation on the image plane, sources appear to be smeared in a tangential direction. However, this is strictly only true for the combination of a polar source and East-West baselines. For other set-ups the direction of the smearing is complicated by the array distribution and the elevation of the source. Furthermore, the motion of a source through the interferometer's fringe pattern leads to losses in amplitude when time-averaging is done. Again, the effect gets worst with increasing offset from the pointing centre, scaling as shown in Equation 4.31,

$$\Delta A \propto (\theta\,\Delta t_{\mathrm{int}})^2. \tag{4.31}$$

4.4 JVLA data reduction

A key consideration, before reducing JVLA data (unlike VLA data), is to set up a platform with sufficient memory. This particular program consists of 11 scheduling blocks, each (typically) containing data for one flux calibrator, three phase calibrators, and seven science targets. These were defined by Martin Hardcastle in scheduling of the observations. Each block amounts to ~170 GB in its raw form, but then expands to 2–3 times in size during the numerous processing steps, described below. These were carried out using the Common Astronomy Software Applications (CASA) package [McMullin et al., 2007]. As CASA requires the data to be input as a visibility file (or 'measurement set'), it must first be converted from its original archival science data model (ASDM) format. Also, to avoid long processing times, averaging needs to be done strategically so that important information is not lost.

4.4.1 Calibration of the visibilities

As described in Section 4.3.1, each visibility measurement consists of two parts: the amplitude and the phase. It is these values that, when Fourier transformed, produce an image of the radio sky brightness. As various environmental and instrumental effects lead to deviations of amplitude and phase from their true values (Section 4.3.1.2), calibration is required to correct these, and to scale the radio fluxes appropriately.

4.4.1.1 Hanning smoothing

The first step in the reduction process was to Hanning smooth the data, which is done to remove artefacts caused by Gibbs ringing. This is a phenomenon seen in the Fourier transform when the particular function it is describing (in this case, the sky brightness distribution) encounters a discontinuity. The result is repeated overshooting and undershooting of the true function, as recreated by the Fourier transform. The effect is illustrated in Figure 4.13 by a Fourier series, which still uses a combination of sine and cosine terms but to describe a periodic (rather than non-periodic) function.

4.4.1.2 Initial RFI-flagging

The most time-consuming step was flagging, which involves masking visibilities that are deemed to be unreliable (e.g. due to radio-frequency interference, RFI). Whilst automatic flagging can achieve an rms of 50 μJy/beam for my data, additional manual flagging is

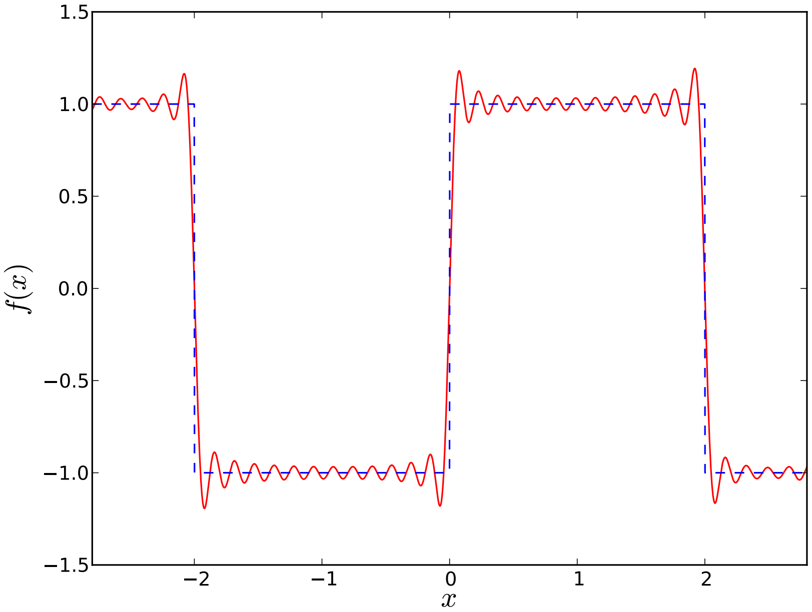

Figure 4.13: Fourier synthesis (red, solid line) of a square wave function (blue, dashed line), using N=40 harmonics. The Gibbs phenomenon can be seen at each discontinuity in the original function.

necessary to approach the theoretical noise of $\sim 12\,\mu$Jy/beam.

Even with averaging done over time and frequency, a simple diagnostic plot could take up to an hour to load and display. Therefore I developed a strategy where I inspected multiple scheduling blocks at a time, one per workstation, and rotated between them. An initial flagging step was carried out to remove particularly strong RFI, identified by plotting visibility amplitudes against frequency, over all of the objects in a scheduling block. Doing so showed spectral windows 0–1, 3 and 8–9 to be the worst affected, which correspond to frequency ranges 994–1122 MHz, 1186–1250 MHz and 1494–1622 MHz, respectively. The origins of this interference include terrestrial transmissions, aircraft, and satellites. For example, there is intermittent RFI from the Radar Target Scatter (RATSCAT) Division, a radar system located at the nearby White Sands Missile Range in New Mexico, and used to detect low observable weapon systems. Also, the JVLA's modem produces continuous RFI at 1200 MHz, whilst Global Position System (GPS) satellites use 1575 MHz ('L1') and 1228 MHz ('L2') as their carrier frequencies.

4.4.1.3 The JVLA pipeline

For Stokes I continuum observations (such as the present dataset), the National Radio Astronomy Observatory (NRAO) has designed a JVLA calibration pipeline, consisting of multiple Python scripts for running in CASA. Since Semester 2013A, it is run automatically when a scheduling block has been completed, with the user downloading the calibrated data from the archive.

In order for the pipeline to function correctly, over one scheduling block at a time, each object must be labelled with the correct 'scan intent'. This dictates whether those visibilities should be used for the phase calibration, the amplitude and bandpass calibration, or whether they are the science targets over which the calibrations are applied. It took about 36 hours (per block) for the pipeline to complete all of the different stages, listed below.

1. **Hanning smoothing of the data.** This is an optional step, if it hasn't previously been done. (The data needs to be Hanning smoothed before any preliminary flagging.)

2. **Application of deterministic flags.** This includes flagging visibilities where an antenna is not online yet, those for which a subreflector or focus error is recorded (Figure 4.14), and any visibilities whose amplitude is exactly zero, as output by the correlator. Another consideration is where the target is at such a low elevation that antennae cast 'shadows' over one another. (Remember from Section 4.3.1.1 that it is the *projected* baseline that is important for interferometry.) However, this is not a problem for the current dataset, given the extended configuration of the A array.

3. **Preparing models for the primary flux-calibrator.** For 10 of the 11 scheduling blocks the flux calibrator is J1331+3030 (a.k.a. 3C 286), and J0137+331 (3C 48) is used for the remaining block. Both are quasars identified in the Third Cambridge Catalogue of Radio Sources [3C; Edge et al., 1959], whose flux densities have been carefully monitored using the JVLA. Being the most compact of the bright radio sources studied by Perley and Butler [2013], and having the flattest spectral index, 3C 286 is the preferred calibrator for providing an accurate flux-density scale. Any

variability is of only a few percent per century, unlike 3C 48, which varies over a timescale of several years. However, Perley and Butler [2013] fit a cubic polynomial to the changing spectrum, allowing it to be used as a reference source. This is necessary for four of the science targets (those circled in Figure 4.15), as 3C 48 is the only flux calibrator that is above the horizon for the appropriate time period of observation. The model visibilities for 3C 286 and 3C 48 are shown in Figure 4.16, with the higher amplitudes on the shorter spacings (i.e. lower values of u-v distance) corresponding to extended emission on arcsecond scales. This structure is confirmed by higher-resolution imaging [An et al., 2004; Wilkinson et al., 1991], but would only cause problems for the calibration if it was *not* well modelled.

4. **Deriving pre-determined calibrations.** The first calibration involves antenna position corrections, which is vital if the correct phase delays are to be applied to the raw data. Such discrepancies in positions may be due to an antenna recently being moved to its current pad, as a result of maintenance or the array acquiring a different configuration for the next semester of observation. Other calibrations include the 'known' behaviour of the receivers, via the application of elevation-dependent gain curves, and making corrections for atmospheric opacity. However, at frequencies of 1–2 GHz, the atmosphere's opacity is typically less than 0.01, and really becomes more important for the JVLA's higher-frequency bands. For example, the K band sits over the 22 GHz emission line for water vapour, and so atmospheric opacity strongly depends on the time of day and the season.

5. **Determining the initial delay-calibration.** This is completed iteratively, and leads on directly from corrections to antenna positions. As explained in Section 4.3.1.2, for each baseline a certain time delay must be added to the signals, to take into account the extra distance travelled between the first antenna and the correlator, compared to that baseline's second antenna. This is in addition to the delay caused by the wavefront reaching one antenna before the other. These delays are all calculated relative to a reference antenna, chosen to be one of those at the centre of the array (Figure 4.17). Following the initial delay-calibration, the cross-correlated phases should be roughly the same, corresponding to the same part of the radiation's

wavefront being sampled by each baseline.

6. **Identifying problems within the system.** This is done during steps such as the previous one, and includes the identification of poor signal-processing components, such as bad 'deformatters'. A deformatter takes the optical-fibre signal that arrives from the antenna and converts this into an electronic signal, which is then sent to the correlator. (The original conversion of the electronic signal from an antenna receiver, so that it can be transported along an optical fibre, is completed by a 'formatter'.)

7. **Flagging of RFI.** Flagging is included in the pipeline, as each calibration process highlights any visibilities that lead to particularly anomalous calibration solutions. However, having eliminated only the worst RFI by hand, little improvement is seen in the output dataset, suggesting that the algorithm could be improved.

8. **Determining the initial bandpass-calibration.** This is required to correct for the slightly different bandpasses of all the antennae, which vary as a function of frequency. (The bandpass is analogous to the transmission curve of an optical/infrared filter.) Ideally the bandpasses for the individual spectral windows would have the shape of a top-hat function, but instead there is undulation and end-channels that do not fall away as steeply as others (Figure 4.18). As such, solutions are found iteratively for each spectral window, on a channel-by-channel basis. This is done using the flux calibrator observations, as its well-known spectrum allows it to double as a bandpass calibrator. The spectral index of 3C 286 (or 3C 48) is therefore also derived during this process.

9. **Deriving the initial gain-calibration.** This step makes use of the bandpass calibration table. Here the relative gain variations of the system are solved for as a function of time, rather than frequency. These 'relative' gains are found for the target by observing a nearby phase calibrator, close enough that atmospheric differences (due to the different lines of sight for the target and the phase calibrator) can be minimised. 'Absolute' gains are then found by bootstrapping the solutions to the absolute flux density of the flux calibrator.

10. **Deriving final calibrations.** These are for the delays, bandpasses, and gains, which are subsequently applied to the data. These solutions may have changed slightly, from those in the initial-calibration tables, due to the RFI flagging done by the pipeline (though minimal) and identification of bad deformatters.

11. **Running an RFI-flagging algorithm on the target data.** If the visibility of a calibrator is flagged by the pipeline, then a calibration solution will not be calculated for that particular time and frequency of observation. As such, interpolating the calibration over the science targets will lead to some of the target data being flagged by association. However, due to the intermittent nature of RFI, further flagging of the target data is required, to be sure that corrupt visibilities do not affect the imaging process.

12. **Calculation of the data weights.** This is done empirically, based on the standard deviation of corrected visibilities within each spectral window. Such a calculation is sufficient because the imaging process is only affected by errors in the relative weights between visibilities, rather than the absolute scale error of the weights.

4.4.1.4 Further flagging

The pipeline outputs a large set of diagnostic plots, and from these it was obvious that additional flagging was required to eliminate corrupted visibilities. For this I averaged over 2 channels (i.e. 2 MHz) and 10 s, even though Equations 4.30 and 4.31 suggest that I can average over 100 MHz in frequency, and the entire observation time per quasar, and still recover a peak response of more than 95%. However, this would risk throwing away a significant amount of good data if there is only a confined amount of RFI over the specified bin of visibilities.

Each scheduling block is accompanied by a VLA Operator Log, and for two blocks it was noted that a binary data file (BDF) was missing for a particular scan. These scans therefore needed to be flagged, which I did so manually. However, bearing in mind that other automatically-generated notes may be recorded due to oversensitivity, I compared them to the pipeline's diagnostic plots. Issues such as warming of a receiver, or stowing

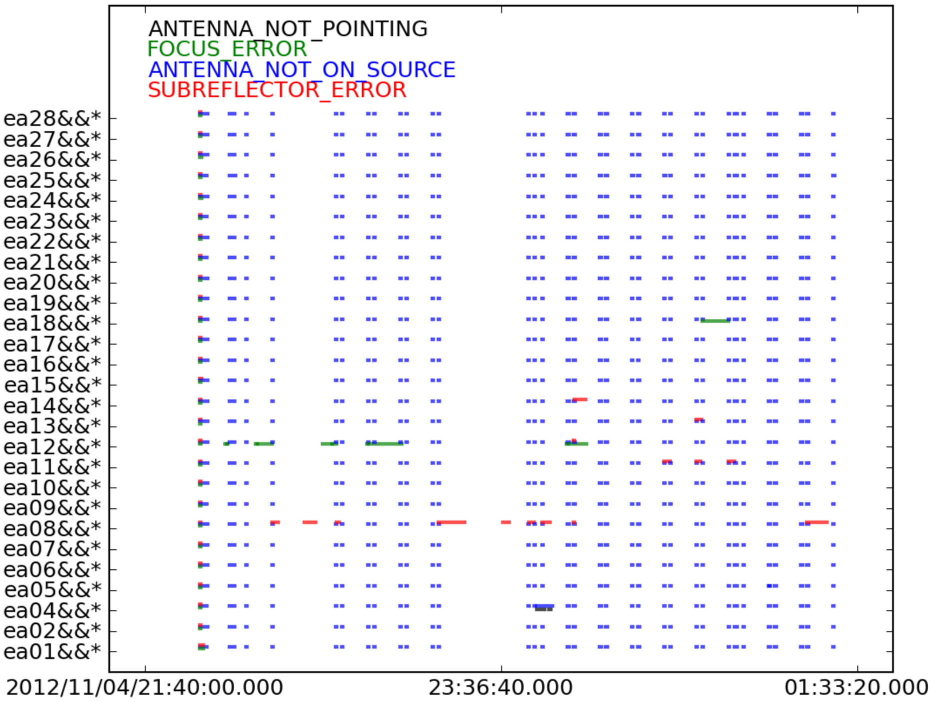

Figure 4.14: An example set of four types of deterministic flags that are applied to a block of observations, as indicated via the colour of the text in the top-left corner. The time is given along the x axis, and the y axis lists the individual antennae. ('&&*' is CASA syntax, indicating a selection of cross- and auto-correlation baselines between the specified antenna and all other available antennae.)

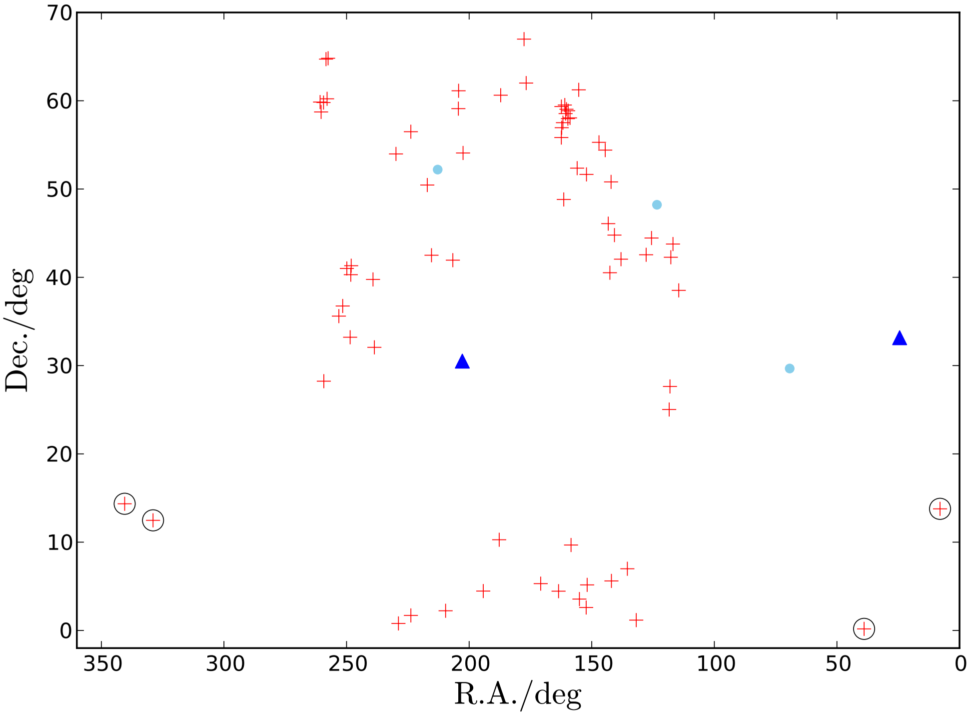

Figure 4.15: Positions of the science targets (red plusses) and the flux calibrators used (dark-blue triangles). The targets circled in black are flux-calibrated using 3C 48 rather than 3C 286. Positions of alternative flux calibrators are indicated by light-blue circles.

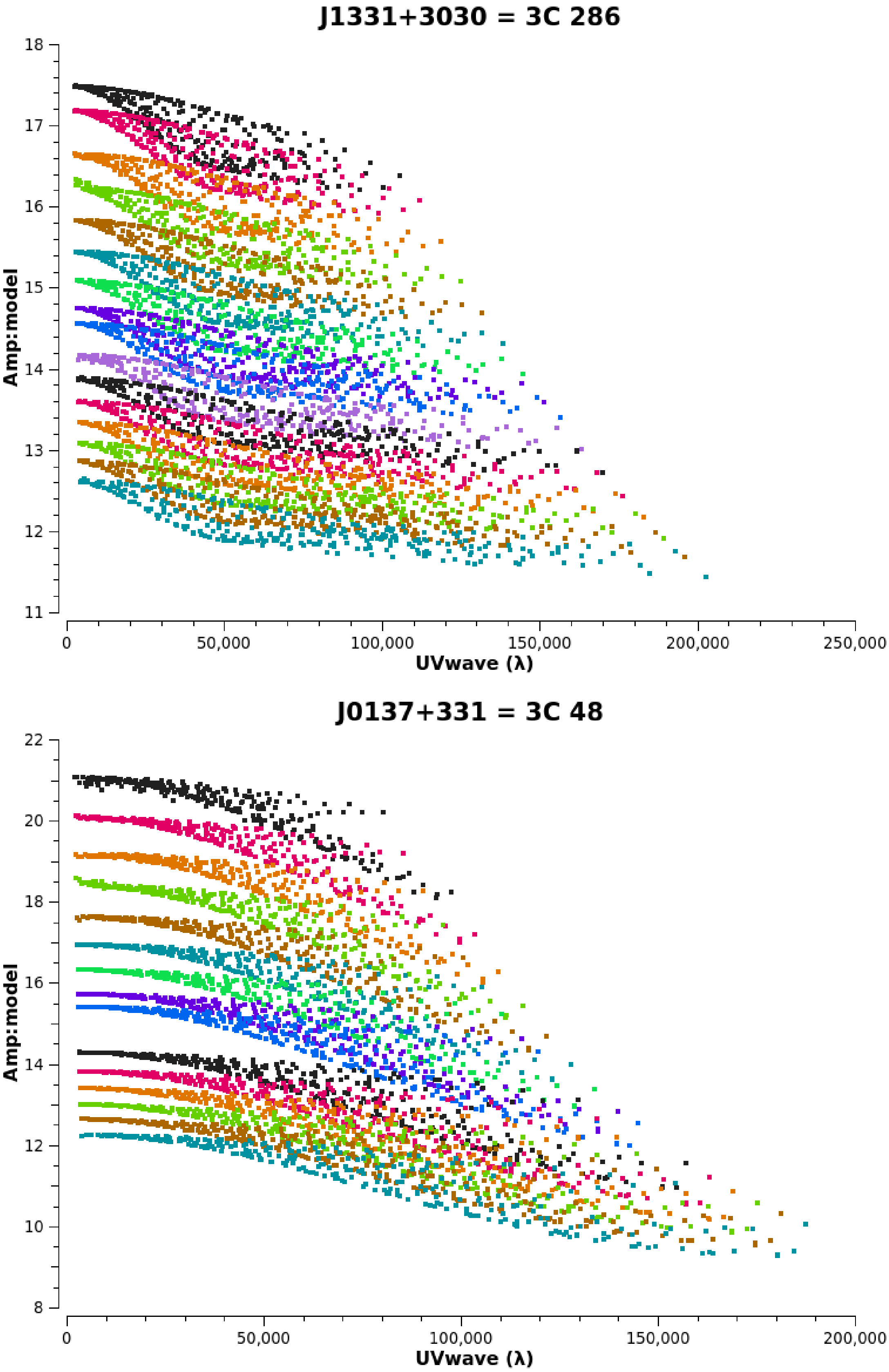

Figure 4.16: The model visibilities for 3C 286 (upper panel) and 3C 48 (lower panel), when observed in the L band with the A-array configuration of antennae. Note that the u-v distance (x axis) is given in wavelengths, with amplitudes colour-coded by spectral window. Spectral window 9 (lilac points) was flagged completely for 3C 48, hence its absence from the lower panel. For this figure, the visibilities have been averaged over each spectral window (i.e. 64 channels) and over the total integration time.

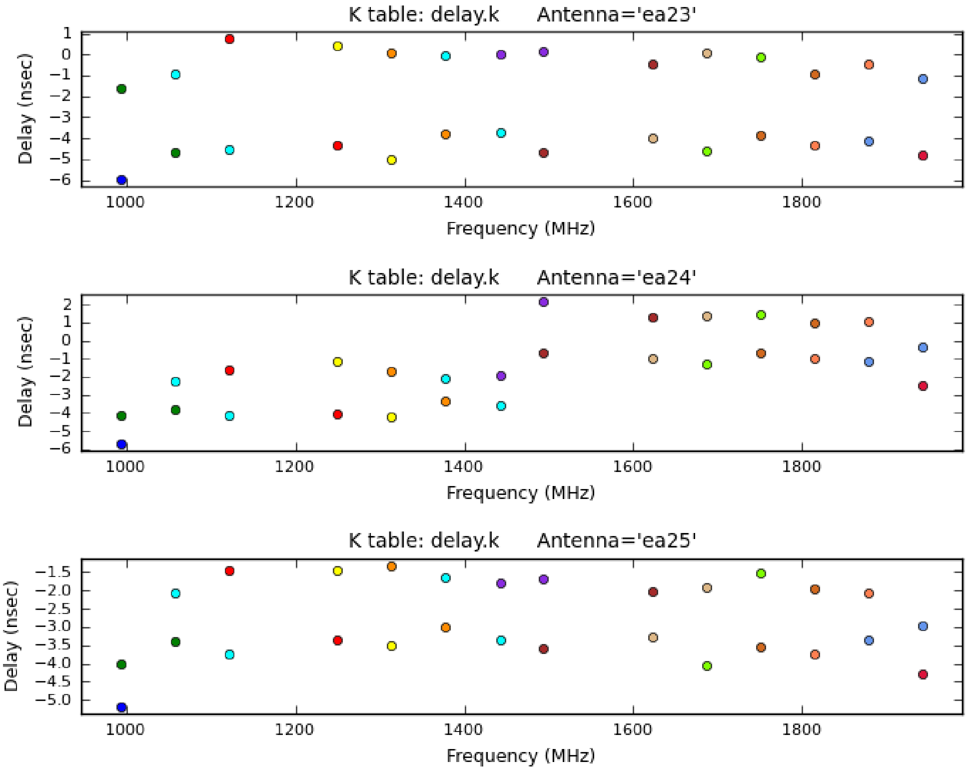

Figure 4.17: The initial delays determined for three of the 27 antennae, all relative to the reference antenna. The two datapoints per spectral window correspond to the right ('R') and left ('L') polarisations. Given the dimensions of the A array, the *range* in delays is not expected to be higher than 8 ns.

of an antenna due to bad weather conditions, were clearly identifiable within the plots, leading me to flag the corresponding data. (Such problems are not picked up by the pipeline's flagging algorithm.)

As mentioned in the previous section, bandpass calibration was carried out by the pipeline, to correct for frequency-dependence effects on the measured amplitudes. However, given that the signal-to-noise ratio (SNR) of a particular channel needs to be at least 5 for a solution to be calculated, the response of the end channels of the spectral window was not reproduced very well. This led to corrected amplitudes that were constant as a function of frequency for the central channels, but appeared as 'spikes' at either end of the spectral window. Therefore I also flagged these end channels.

Next I inspected the corrected amplitude versus u-v distance for each of the calibrators. The flux calibrator had visibilities that were in line with the model (Figure 4.16), but differing shapes were seen for the phase calibrators. The latter were chosen on the assumption that they appear as point sources in the L band, and so have visibilities (both

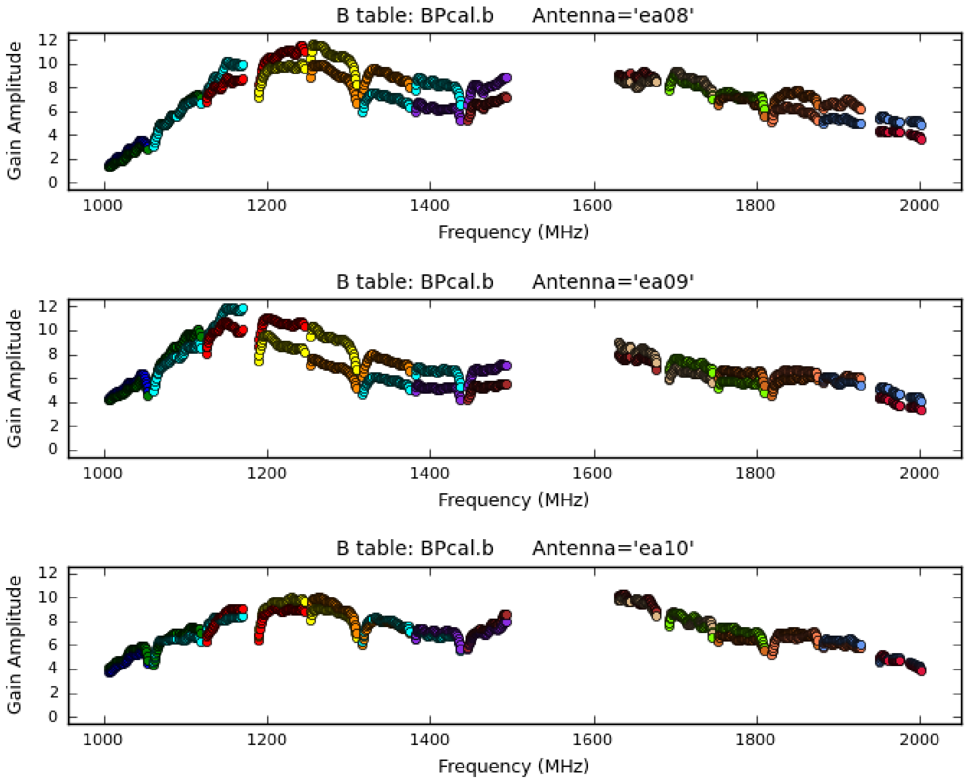

(a) Amplitude solutions

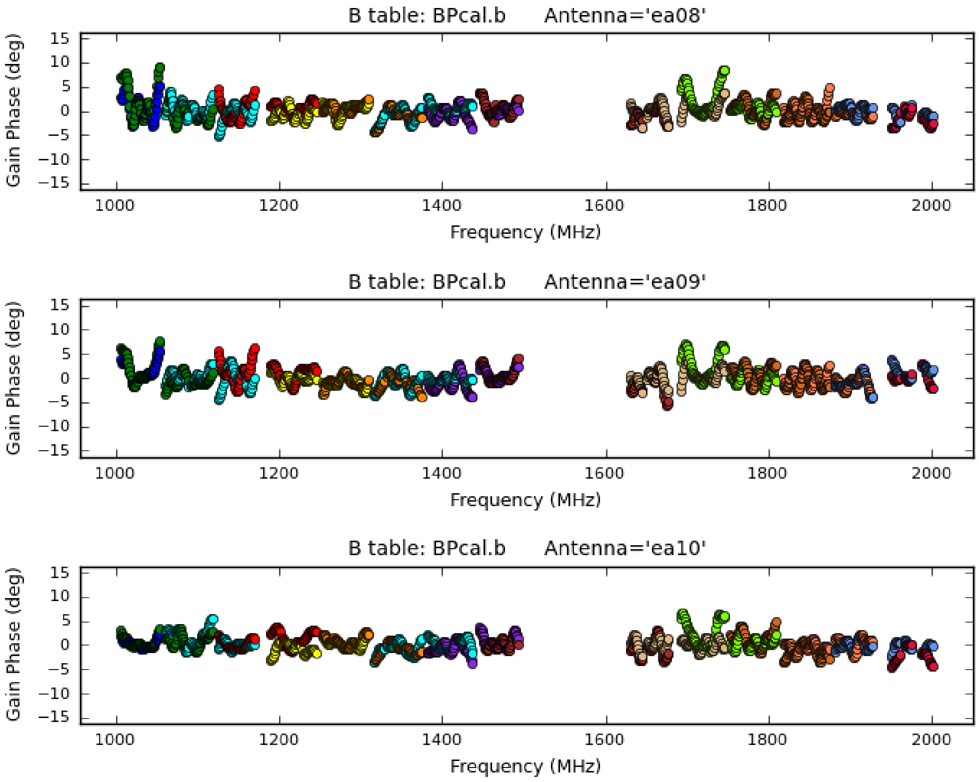

(b) Phase solutions

Figure 4.18: The (a) amplitude and (b) phase solutions resulting from bandpass calibration, for scheduling block sb12435448. For each spectral window the two colours represent the left and right polarisations.

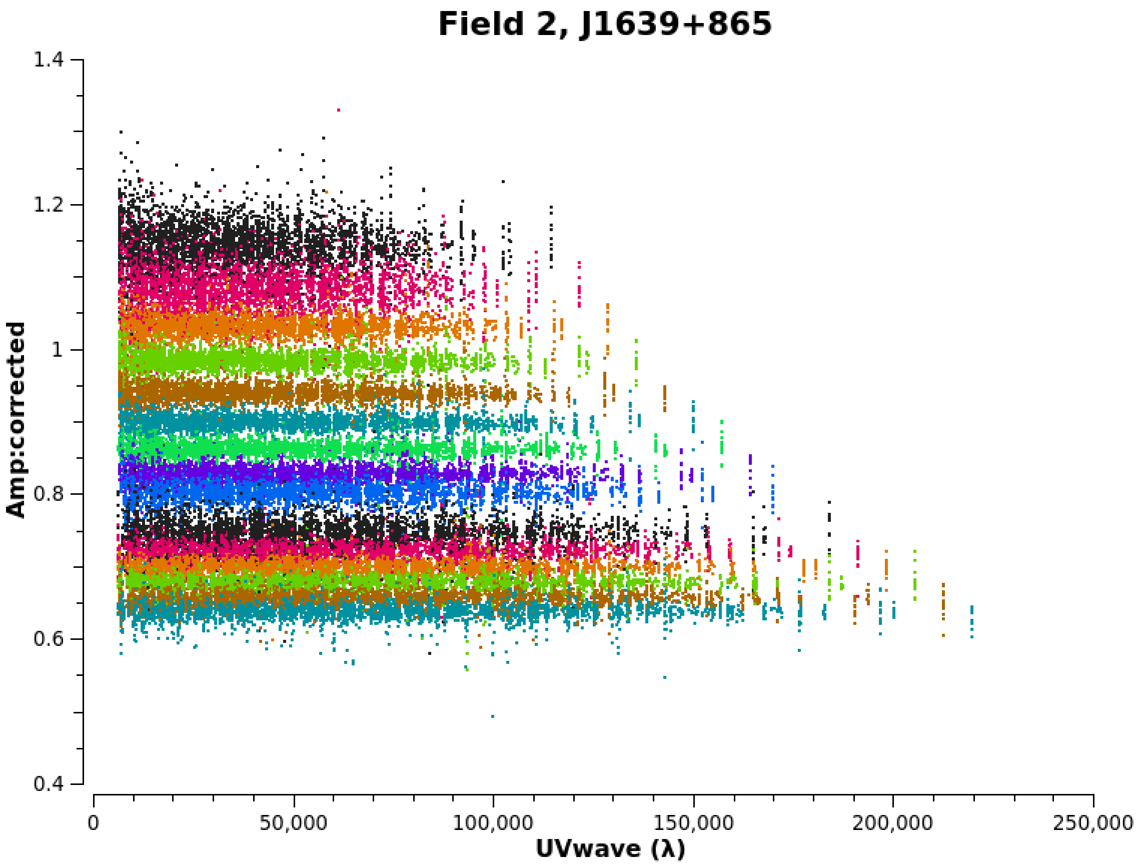

Figure 4.19: Amplitudes as a function of *u*-*v* distance for the phase calibrator, J1639+865, used in the sb12447081 scheduling block. The datapoints are colour-coded by spectral window, and averaged over 64 frequency channels and over the total integration time.

amplitude and phase) that do not depend on the baseline over which they are measured (Section 4.3.1). Figure 4.19 is an example of their expected flat appearance over *u*-*v* distance (given here in units of wavelength). I also inspected the phases as a function of *u*-*v* distance for each of the calibrators, to check that these were also independent of the baseline, and to aid identification of faulty antennae.

For one of the phase calibrators, J1024-008 (Figure 4.20), strange undulation in the amplitudes was observed. (Note that a combination of noise and having a flat spectral index is the reason that the differently-coloured spectral windows appear to be interspersed.) Further investigation revealed that these 'bumps' were due to faulty antennae, which I then flagged. The improvement is seen in the lower panel of Figure 4.20, which was produced following a second run of the pipeline (Section 4.4.1.5).

Another stage, when investigating the (corrected) response of the interferometer to the phase calibrators, was to consult the VLA Calibrator Manual. This gives quality flags for each of the calibrators, dependent on which band is being used for the observation.

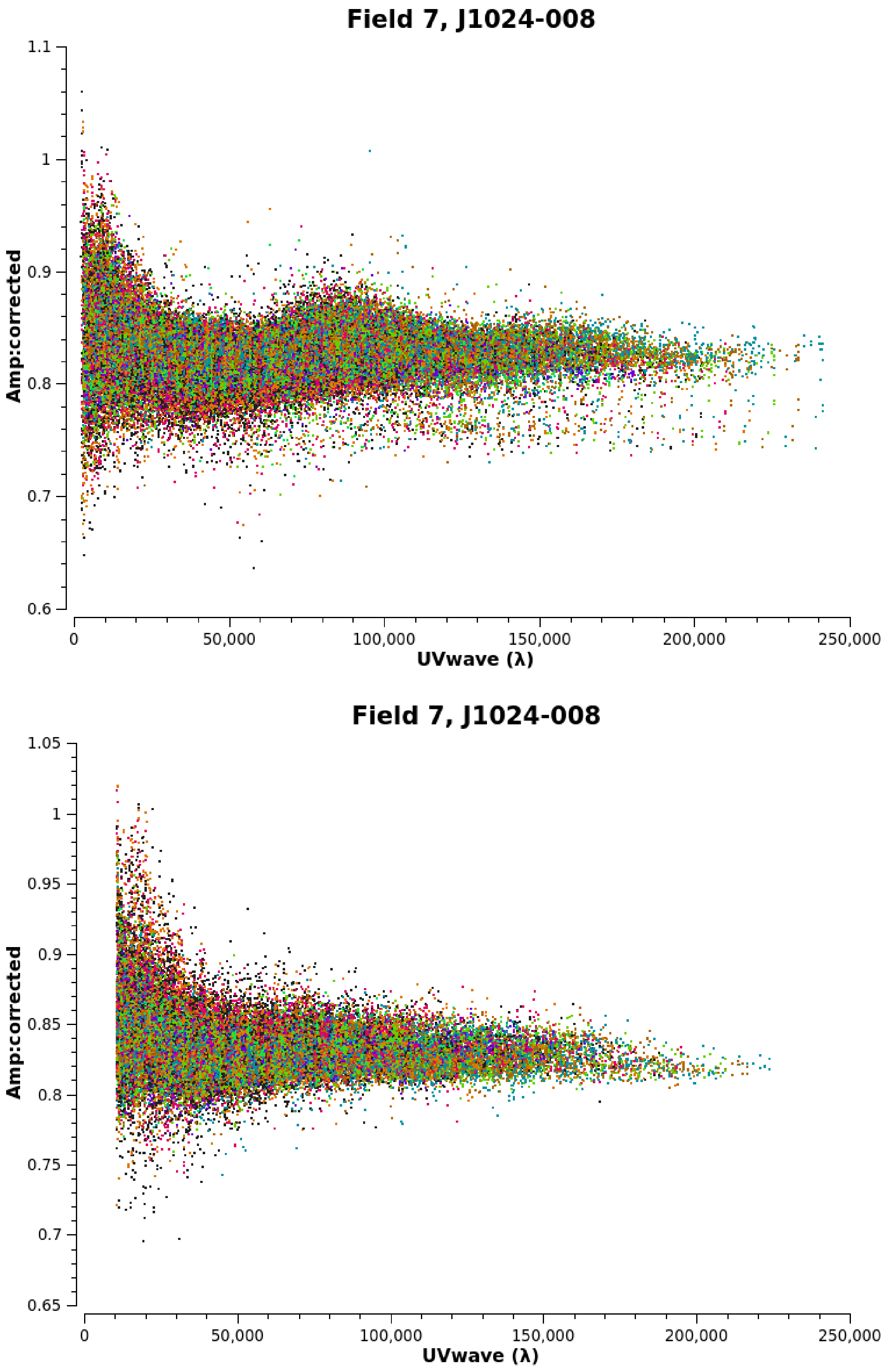

Figure 4.20: Amplitudes as a function of u-v distance for the phase calibrator, J1024-008, as calibrated by the first pipeline run (upper panel) and by the second pipeline run (lower panel). This refers to the sb12435448 scheduling block, and the datapoints are colour-coded by spectral window. The visibilities are averaged over 64 frequency channels and over the total integration time.

However, these are largely out-of-date, with such notes relevant to the old VLA rather than the JVLA. Nevertheless, they offer additional information to help understand amplitudes such as those shown in Figure 4.21. The upturn in amplitudes for short baselines is indicative of large-scale structure in the calibrator's emission, which was confirmed when I imaged the field (Figure 4.22). According to the VLA Calibrator Manual, J0818+423 is a high-quality calibrator, but is only reliable when its u-v range is restricted to $\geq$ 10 kilo-wavelengths. However, I saw evidence of structure for baselines up to 50 kilo-wavelengths, so I flagged visibilities with UVwave $< 50\,\mathrm{k}\lambda$ before running the pipeline again. I emphasise that such a restriction was applied to the calibrator *only*. Flagging the associated targets in the same way would mean that sensitivity to extended structure is lost, and so a radio jet (if present) would not be imaged. Similarly, for other phase calibrators, I used the output of the first pipeline run to inform what u-v cut should be made so that the remaining amplitudes are a flat function of u-v distance. This is a legitimate thing to do because the gain-calibration solutions are antenna-based rather than baseline-based, meaning that the restriction is in place for the calibration itself but does not affect which baselines are present once applied over the target data.

Plots of amplitude versus u-v distance also proved useful for identifying anomalous visibilities for the targets themselves. For example, I found that the high amplitudes evident in Figure 4.23, following the first pipeline run, were due to a subset of baselines that needed to be flagged. Although clipping above a certain threshold may appear to achieve the same result, doing so could lead to artificial features in the final imaging.

4.4.1.5 Re-calibration using the JVLA pipeline

Having completed additional flagging, as detailed in the previous section, the pipeline was run a second time so that the visibilites could be re-calibrated. For this a new measurement set was created, where the *corrected* data from the original file was copied across and existing calibration tables were cleared. The updated set of flags was also applied. As calibration solutions are *offsets* to be applied to the input data, the majority of those produced by the second run were incremental in size.

Figures 4.24 to 4.29 are presented to illustrate the improvement that is made between

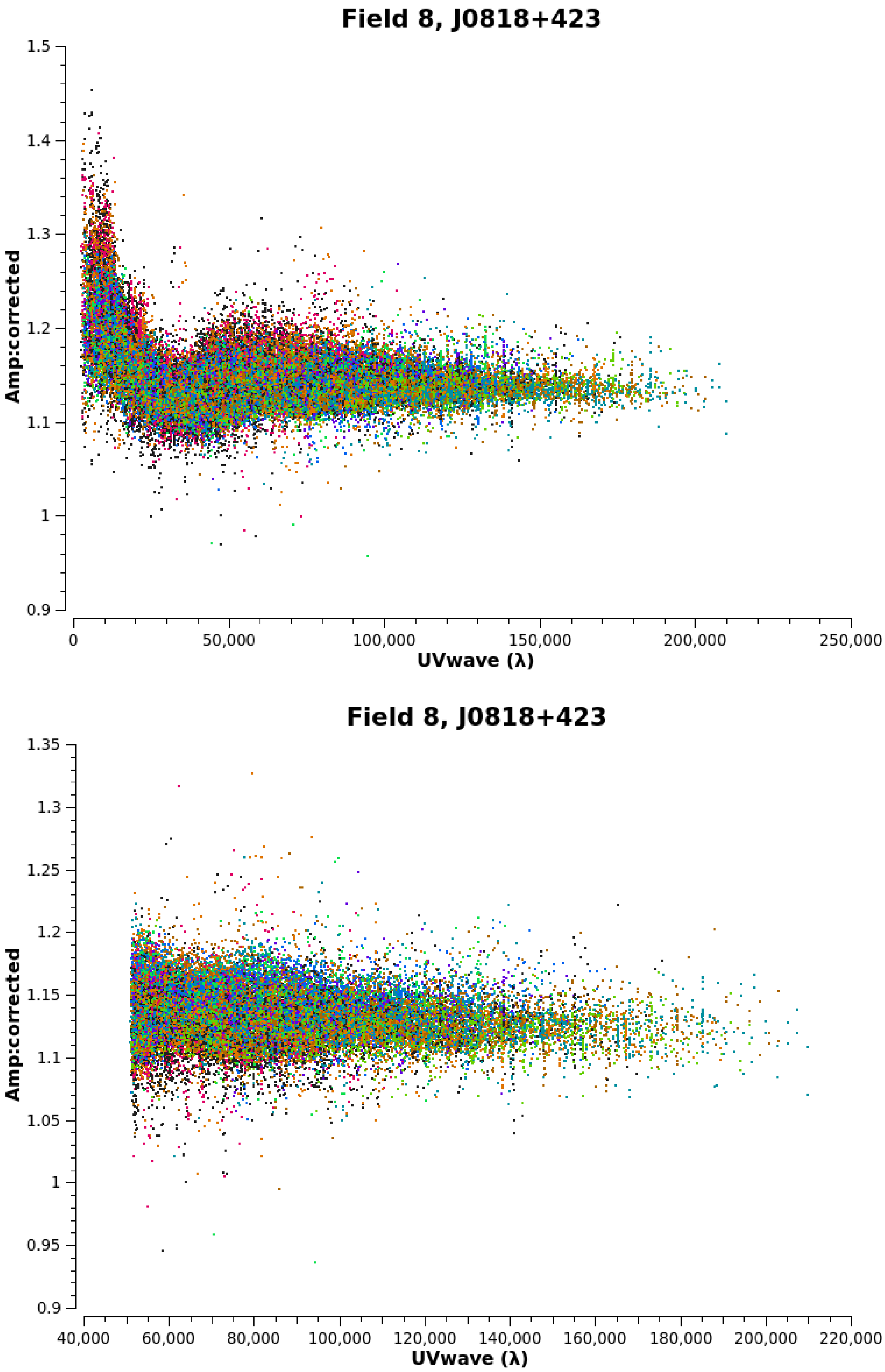

Figure 4.21: Amplitudes as a function of *u*-*v* distance for a phase calibrator in the sb12434705 block. The output of the first pipeline run (upper panel) is used to inform what *u*-*v* cut should be applied for the second pipeline run (lower panel). Doing so removes the non-linear shape seen in the upper panel, which is the result of the calibrator's extended structure. The datapoints are colour-coded by spectral window, and the visibilities are averaged over 64 frequency channels and over the total integration time.

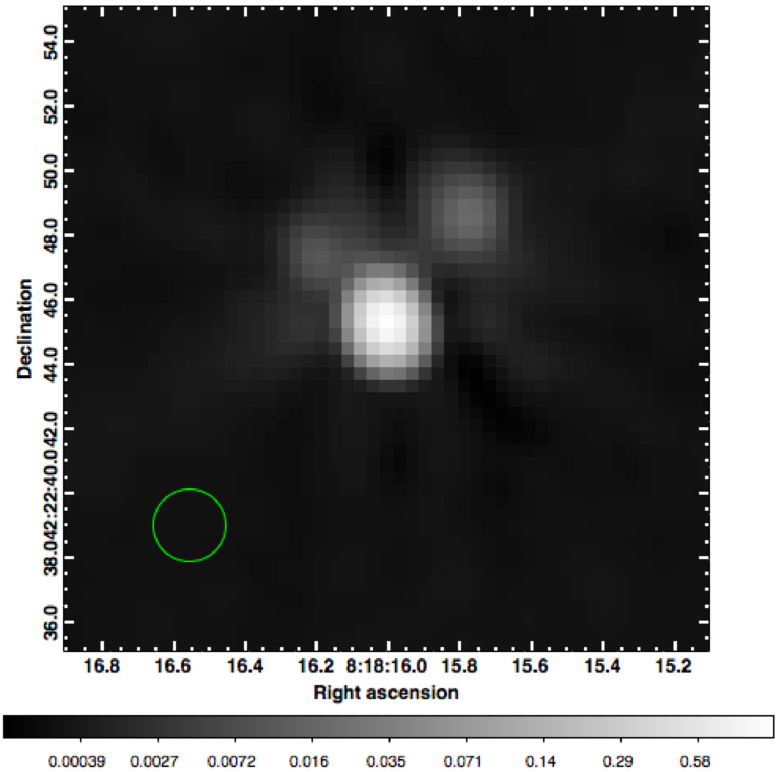

Figure 4.22: Imaging the phase calibrator J0818+423, which is used in the sb12434705 block. The beamsize is illustrated by the green ellipse in the bottom left-hand corner, and the greyscale bar represents the intensity on a logarithmic scale (units of Jy/beam).

the first and second pipeline runs. The first of these, Figure 4.24, shows the large amount of RFI that was not identified by the pipeline's flagging algorithm. The amplitude variation that remains is largely due to noise, and the different amplitudes sampled by the antennae on account of their positions within the array.

Figure 4.25 is an example of the phase solutions calculated during the initial gain-calibration, using 'ea14' as the reference antenna. These should be a steady function of time, representing phase stability, but a sudden change could be seen for antenna ea15 in the upper panel. (Note that datapoints moving between the two extremes of the y axis are just a consequence of plotting the phases on a linear scale of -180 to 180 deg, rather than using polar axes.) This was accompanied by a shift in the amplitude solutions (Figure 4.26). The explanation behind this was clearly revealed during the final gain-calibration (Figure 4.27), where the upper baseband – spectral windows 8 to 15 – appeared to be problematic, and so was flagged before the second pipeline run.

From the same scheduling block, in Figure 4.28, are the amplitude solutions for another

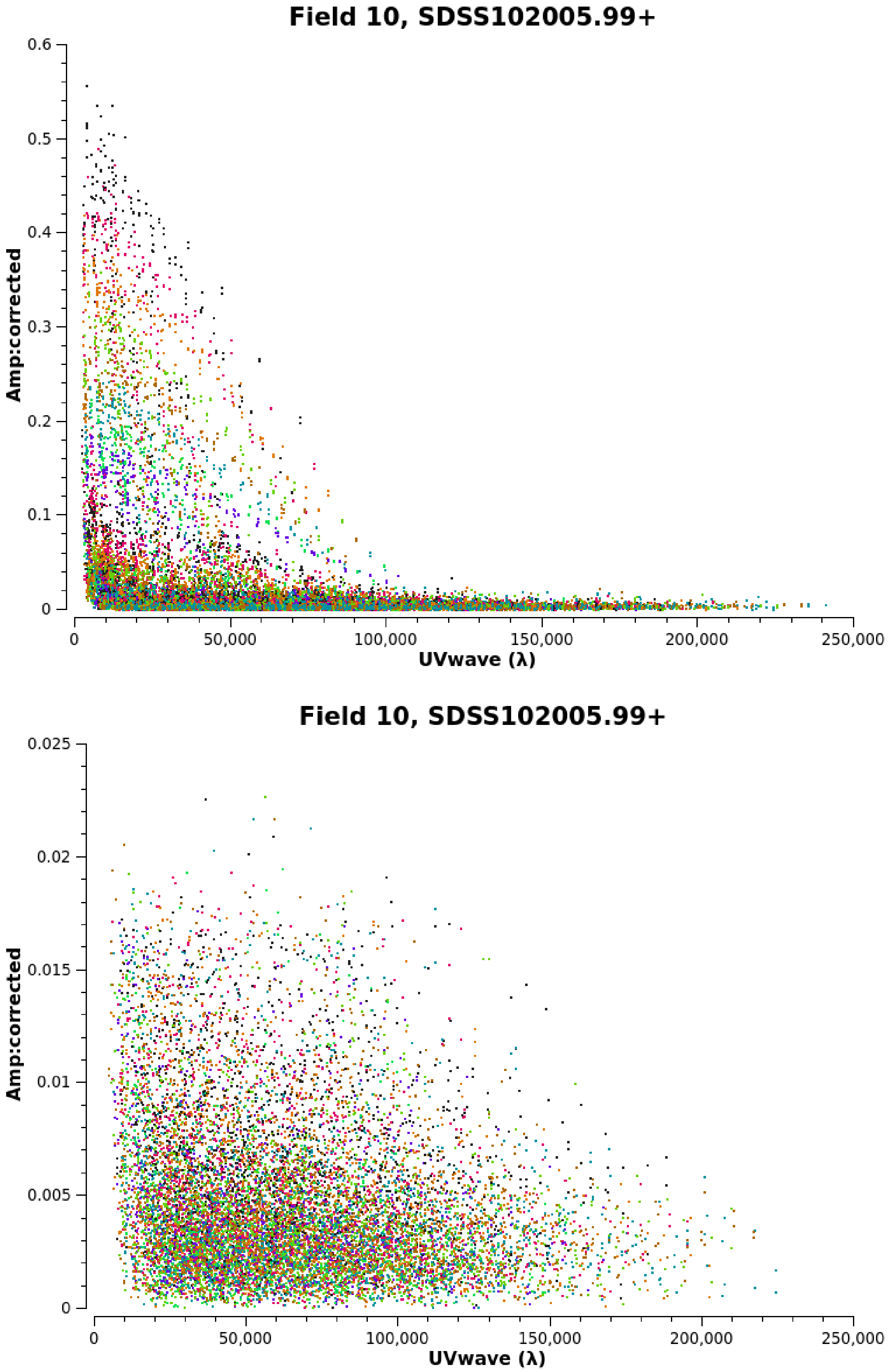

Figure 4.23: Amplitudes as a function of u-v distance for a target in the sb12435448 block, as calibrated by the first pipeline run (upper panel) and by the second pipeline run (lower panel). The datapoints are colour-coded by spectral window, and the visibilities are averaged over 64 frequency channels and over the total integration time.

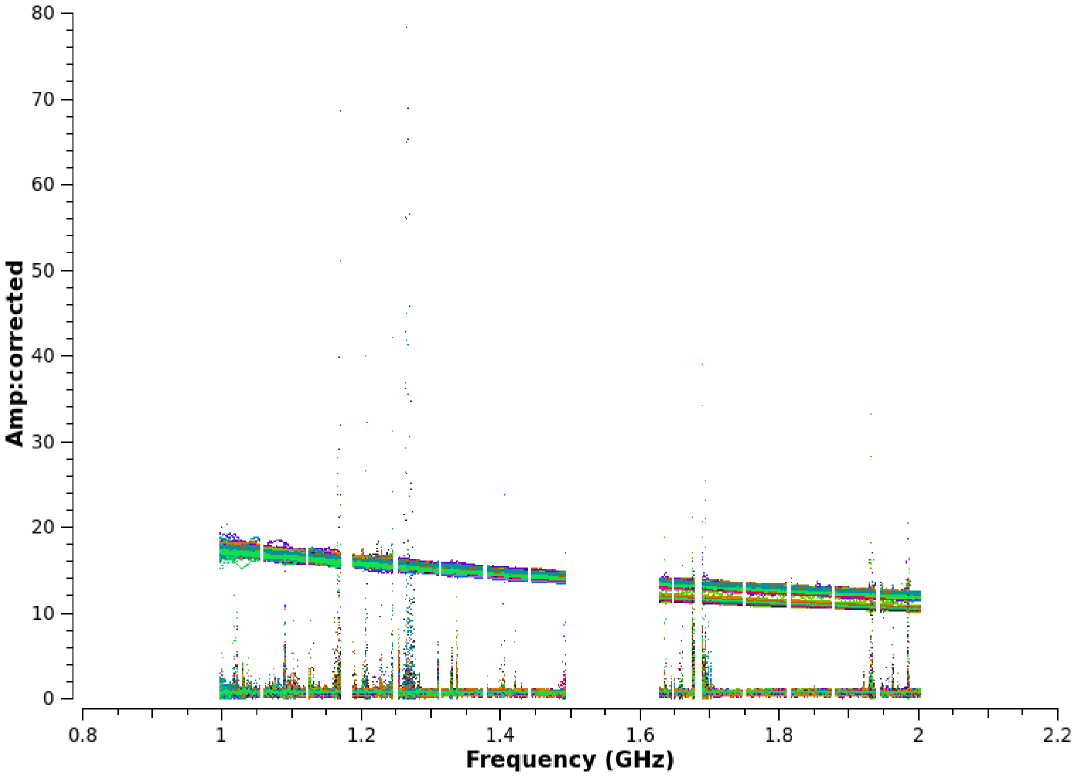

(a) First pipeline run

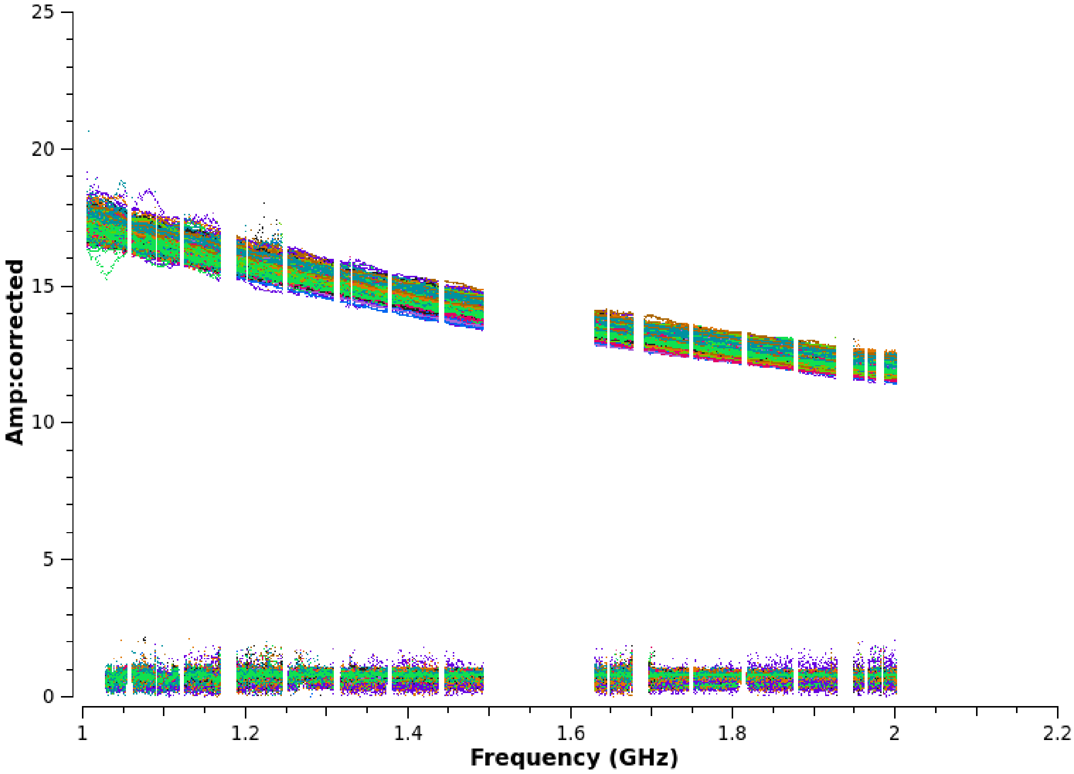

(b) Second pipeline run

Figure 4.24: Corrected amplitudes as a function of frequency, partway through the calibration conducted by the (a) first and (b) second pipeline runs. Only the calibrators in scheduling block sb12435448 are plotted here; the object around amp = 15 is the flux calibrator, and the lower amplitudes (0–1) correspond to the phase calibrators. The vertical streaks seen in the upper panel are due to RFI in the spectrum, and the improvement brought about by manual flagging of this RFI is evident in the lower panel. Colour is used to denote the different baselines, with averaging over all time only.

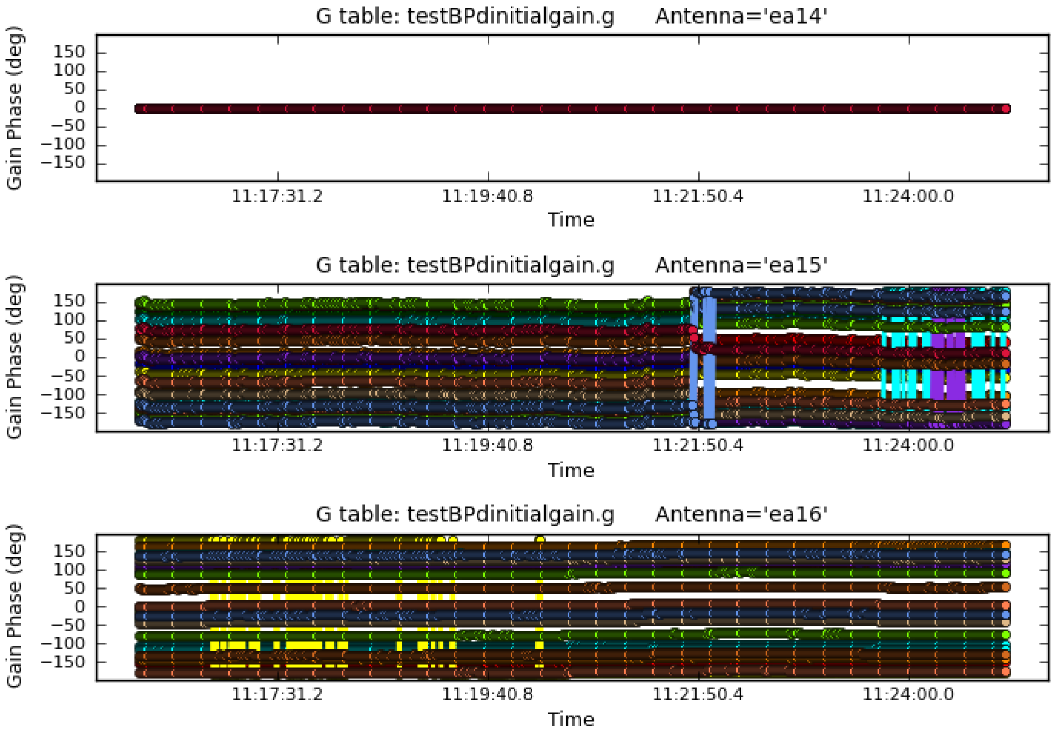

(a) First pipeline run

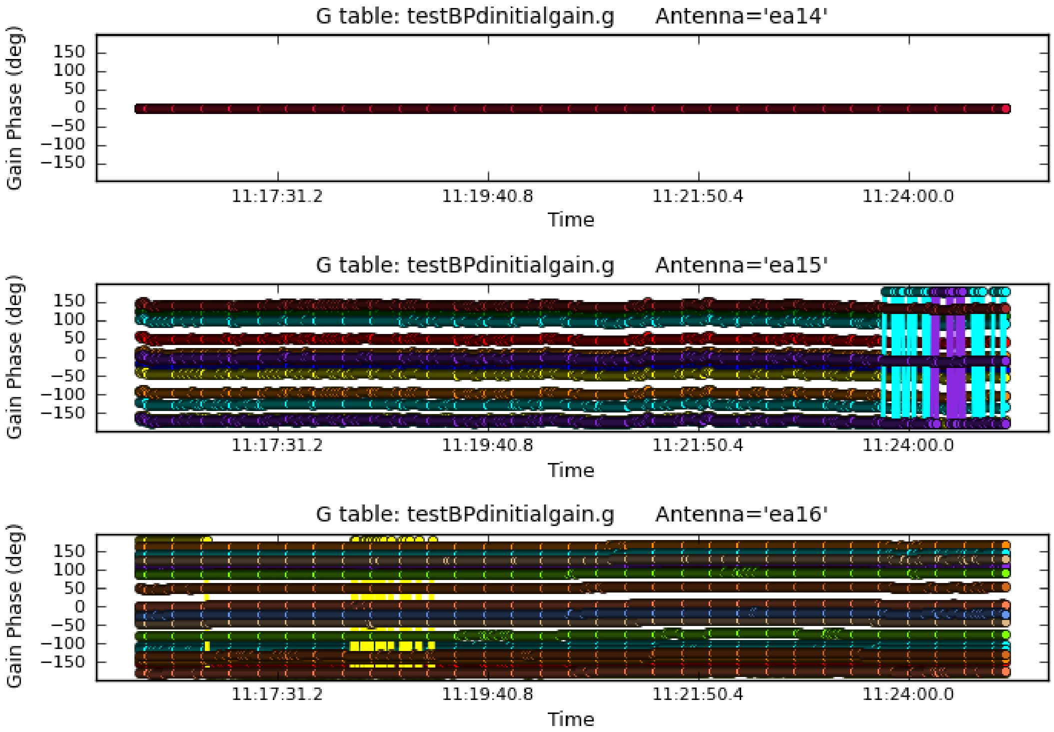

(b) Second pipeline run

Figure 4.25: Phase solutions following the initial gain-calibration during (a) the first pipeline run and (b) the second pipeline run for scheduling block sb12435448. The datapoints are colour-coded by spectral window (0–15). In the first run, the solutions for antenna ea15 became 'displaced' at time 11:21:50.4. Flagging was completed so that the remaining solutions, re-calculated during the second run, were smoothly-varying and approximately constant over time.

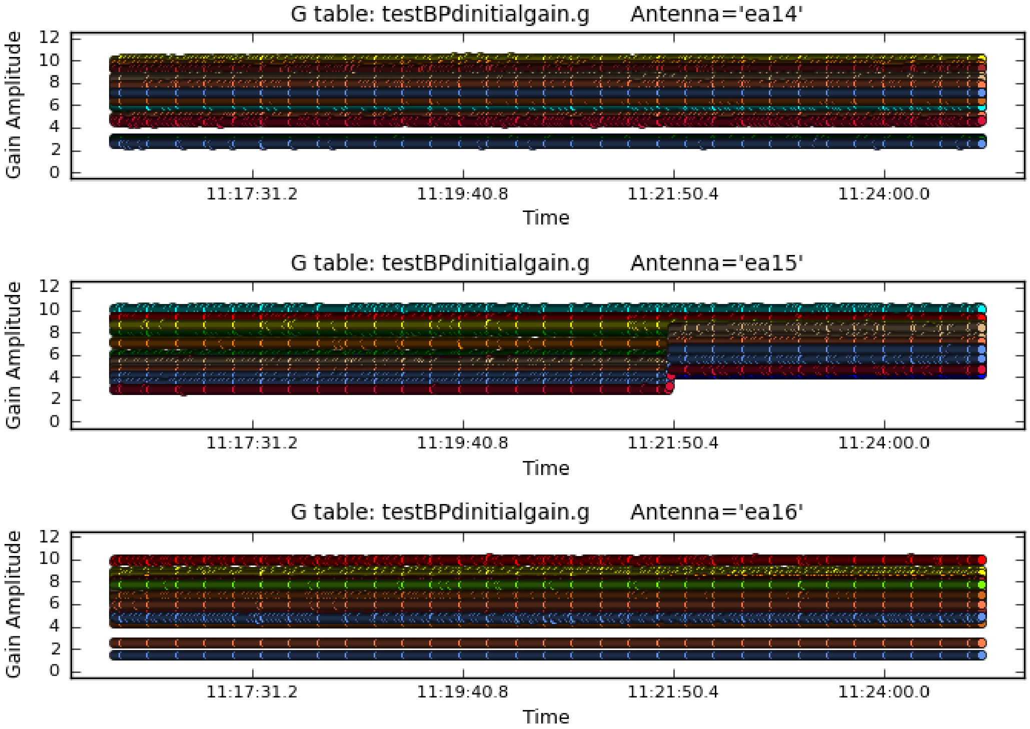

(a) First pipeline run

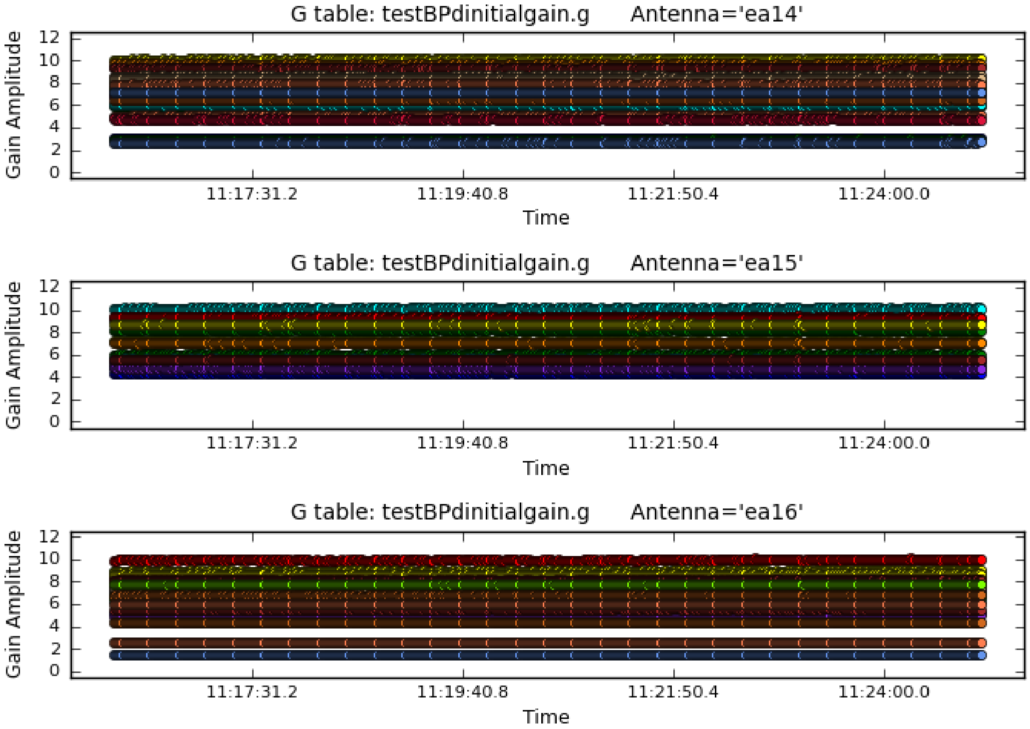

(b) Second pipeline run

Figure 4.26: Amplitude solutions following the initial gain-calibration during (a) the first pipeline run and (b) the second pipeline run for scheduling block sb12435448. The datapoints are colour-coded by spectral window (0–15). As in Figure 4.25, the solutions for antenna ea15 became displaced at time 11:21:50.4. Flagging the affected spectral windows left only those with reliable, smoothly-varying solutions for the second run.

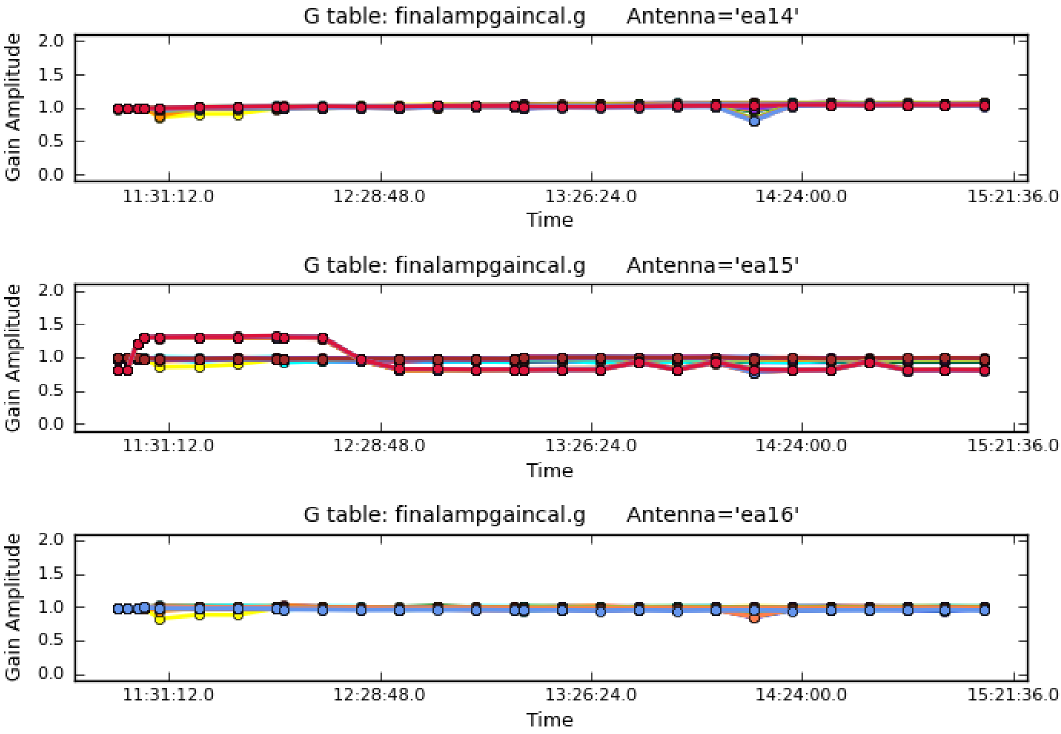

(a) First pipeline run

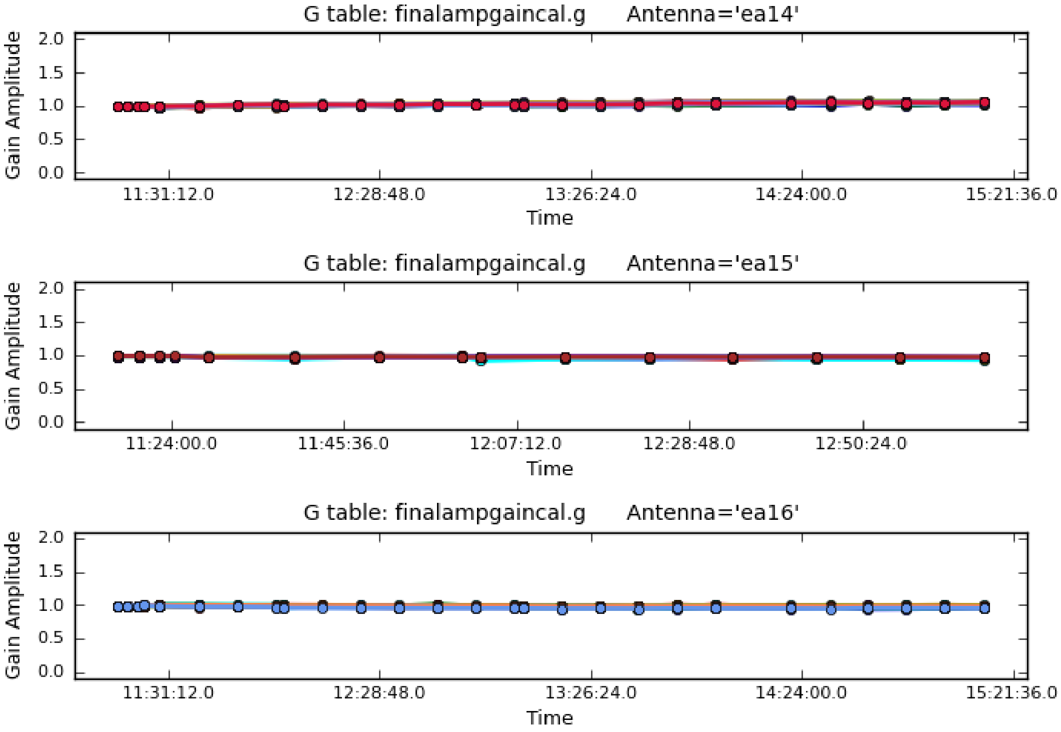

(b) Second pipeline run

Figure 4.27: Gain amplitudes as a function of time. These are the result of applying the final gain-calibration during the (a) first and (b) second pipeline runs for scheduling block sb12435448. The datapoints refer to individual scans, which are colour-coded by spectral window (0–15). Deviations away from an amplitude value of 1.0 (a) suggested that there was a problem with those scans or, as in the case of ea15, an entire spectral window. These were therefore flagged before running the pipeline a second time (b).

three antennae. Note how one of the spectral windows, coloured in red, does not vary smoothly with time in the first pipeline run. This is important as these solutions needed to be interpolated over the targets. Through more-careful flagging, however, the fluctuating visibilities were removed before re-calibrating.

Shown in parallel with Figure 4.27 are the gain amplitudes as a function of frequency, rather than a function of time (Figure 4.29). These allowed me to identify particular scans that were offset from an amplitude value of 1.0, and which spectral windows needed to be inspected more carefully for RFI. In this case, for each of the antennae displayed, improved calibrations were attained after further flagging.

4.4.1.6 Problematic scheduling blocks

Unfortunately, not all of the scheduling blocks could be reduced by the pipeline on the first attempt. As mentioned in Section 4.4.1.3, the numerous steps are heavily reliant on the objects within the block having the correct scan intent. For sb11472787, the pipeline failed as there appeared to be no flux/bandpass calibrator present. However this was simply the result of an incorrectly-labelled scan, which I corrected in a raw meta-data file, and the absence of a ‘dummy scan’. (The first scan of every scheduling block is usually a scan of less than 1 minute long, whilst the electronics settle, and is automatically deleted.)

In the case of sb12434705, the second pipeline run showed there to be no gain calibration solutions associated with the phase calibrator shown in Figure 4.21. Realising that this was due to the cut made in u-v distance (Section 4.4.1.4), I relaxed the calibration requirements. This meant reducing the minimum number of baselines per antenna from 13 to 5, and changing the minimum SNR from 5 to 3. The expected number of solutions per antenna was then calculated.

4.4.2 Imaging JVLA data

4.4.2.1 Final flagging

Before the targets’ calibrated visibilities could be used for imaging, another round of flagging was required. Previous manual flagging of any residual RFI (Sections 4.4.1.2 and 4.4.1.4) involved viewing the visibilities of each scheduling block at once, to speed up

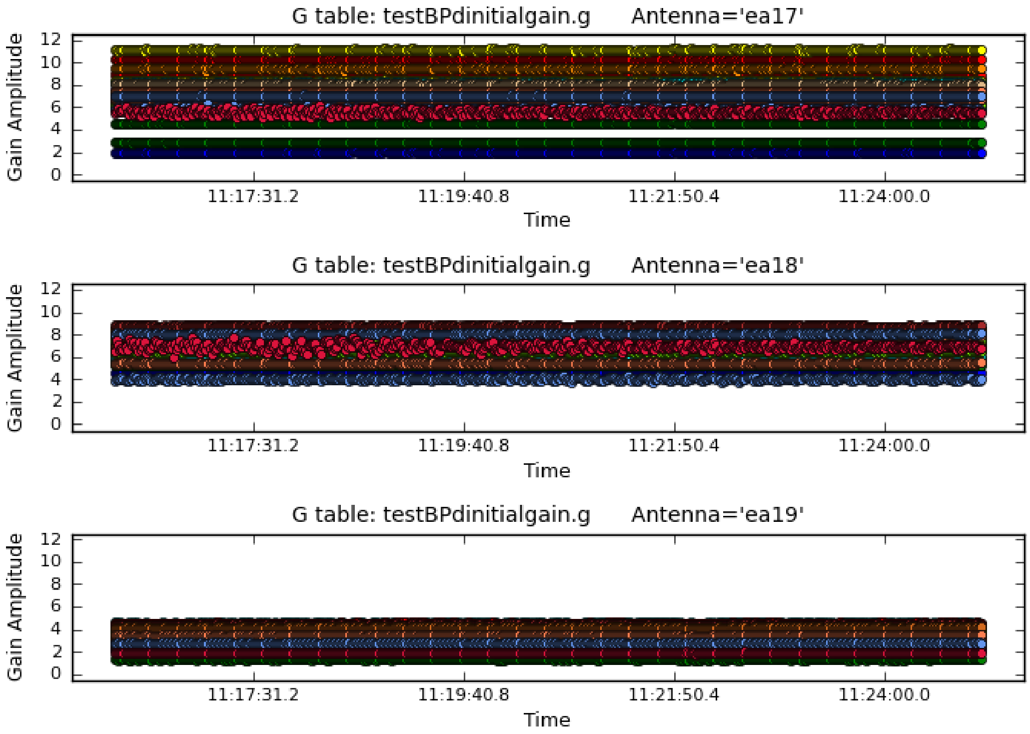

(a) First pipeline run

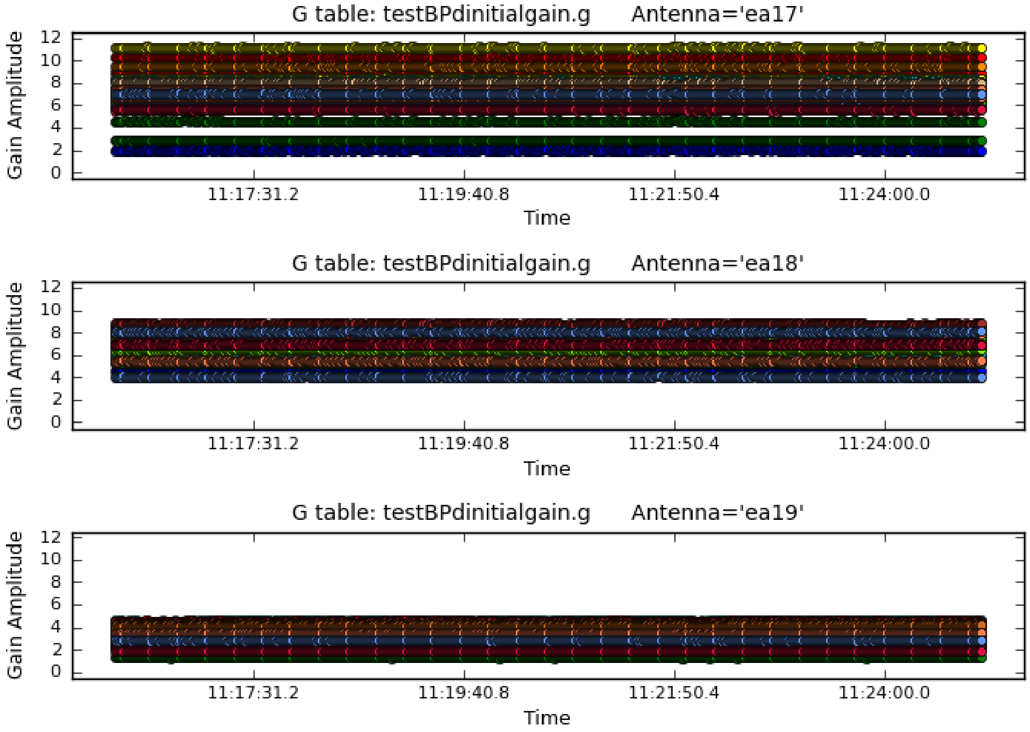

(b) Second pipeline run

Figure 4.28: Additional amplitude solutions following the initial gain-calibration during (a) the first pipeline run and (b) the second pipeline run for scheduling block sb12435448. The datapoints are colour-coded by spectral window (0–15). The bright-red datapoints in the upper panel, for both the ea17 and ea18 antennae, show a great degree of oscillation over time. Consequently, the corresponding spectral window was flagged, and so is absent from the lower panel.

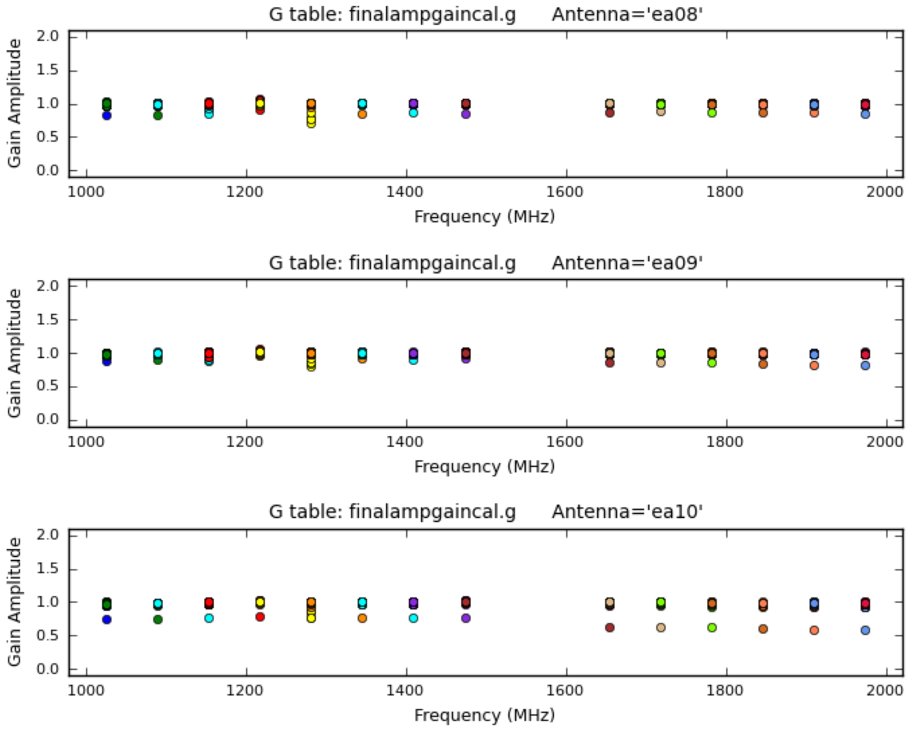

(a) First pipeline run

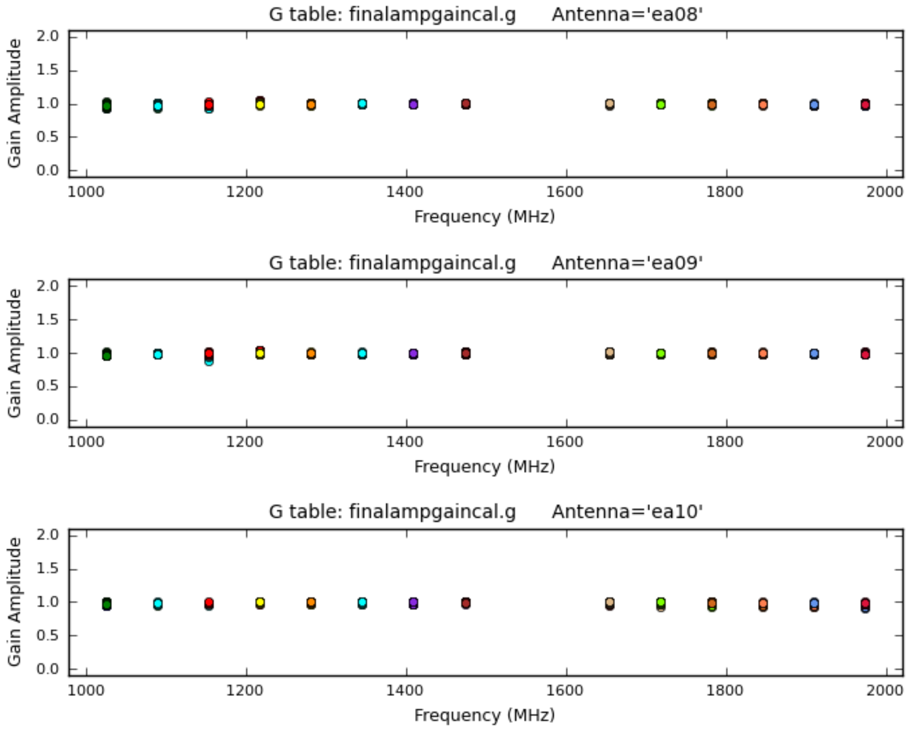

(b) Second pipeline run

Figure 4.29: Gain amplitudes as a function of frequency. These are a result of the final gain-calibration during the (a) first and (b) second pipeline runs for scheduling block sb12435448. The datapoints refer to individual scans, but for each spectral window, the two colours used correspond to the left and right polarisation. Deviations away from an amplitude value of 1.0 (a) suggested that there was a problem with that spectral window or, as in the case of ea10, a particular scan across the whole frequency range. These were therefore flagged before running the pipeline a second time (b).

the process, rather than on an object-by-object basis. As a result, the flagging mainly involved data corresponding to the calibrators. This is because their amplitudes are larger than those of the targets, creating an artificially-high threshold against which to compare rogue RFI amplitudes. Further inspection was therefore required over the individual targets themselves. They were first plotted scan-by-scan (still with averaging of 10 s and 2 channels) as a function of frequency, which indeed helped to identify weaker RFI. This was followed by inspecting the calibrated data as a function of time, allowing me to carefully flag start and end intervals for scans – the antennae and electronics being disrupted during a slew – in addition to checking for RFI. Doing this for each spectral window *individually* meant that I avoided needlessly reducing the number of visibility measurements for the targets. I then checked what proportion of the total bandwidth had been flagged, and used this value in conjunction with Equation 4.29 to estimate the theoretical rms for each image (Table 4.1).

4.4.2.2 Preliminary imaging

Next I created an image using CASA's standard CLEAN algorithm. This involves Fourier transforming the visibilities to produce an image of the sky-brightness distribution (the 'dirty image'), and then deconvolving the synthesised beam to better reproduce the 'true' distribution (Section 4.3.1.3). The deconvolution is done on an iterative basis, with CLEAN searching for the peak flux in the current (residual) image, subtracting off the beam pattern, and storing these 'CLEAN components' so that they can be used to create the final image. For this process to be most effective, the synthesised beam needs to be well-sampled, with 3 to 5 pixels covering its diameter. I used a pixel size of 0.25 arcsec, which provided just over 5 pixels across the full-width half-maximum of the beam. If the beam is under-sampled then aliasing effects may manifest themselves, where the sampling rate is not sufficient to distinguish between two different underlying distributions. (This is usually discussed in the context of frequencies but is equally valid for 'spatial' functions.)

In order for CLEAN to work correctly, CLEAN boxes need to be set for the image. These act as a mask, defining the region over which we already know there to be genuine emission. This avoids artefacts in the dirty image being misinterpreted as real emission,

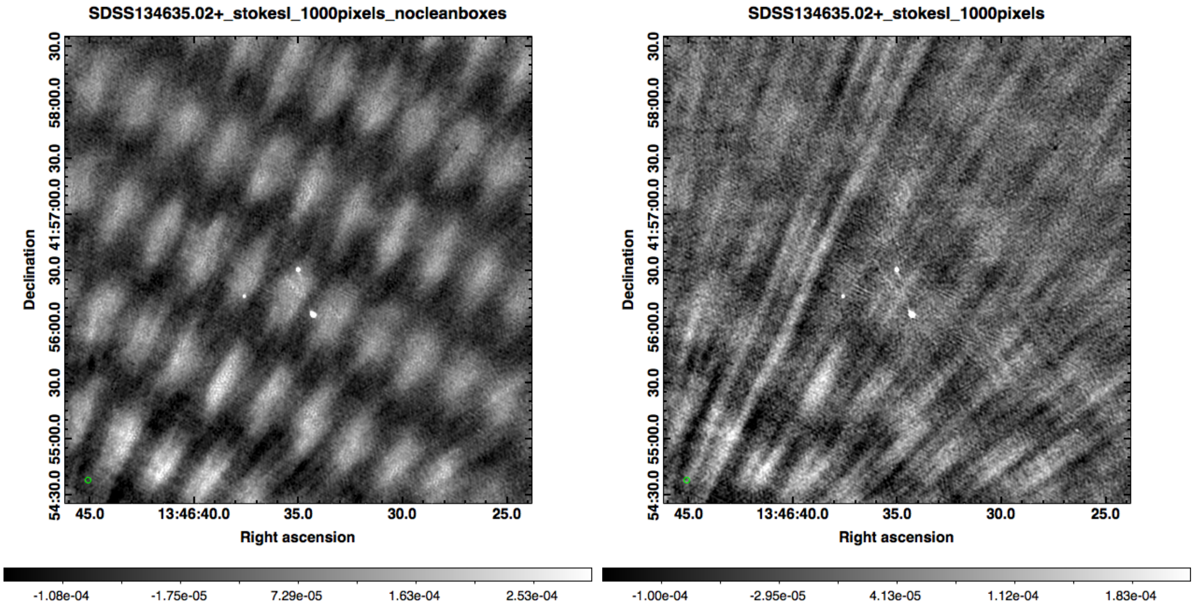

Figure 4.30: JVLA imaging of target SDSS134635.02+415630.9, with (left) and without (right) CLEAN boxes being set during the deconvolution algorithm. This highlights the need for CLEAN boxes, to eliminate artefacts such as the artificial pattern seen in the left-hand image. The beamsize is illustrated by the green ellipse in the bottom left-hand corner of each image, and the greyscale bar represents the flux in units of Jy/beam.

which would then result in unwanted CLEAN components being recorded. The absence of CLEAN masks can also result in a patterned effect, as demonstrated in the left-hand plot of Figure 4.30. (Section 4.4.2.3 explains how the residual streaks, emanating from the bottom left-hand corner of the right-hand plot, were removed.) To judge whether emission in the field was real or not, I used existing radio cutouts from FIRST, but this restricted such decisions to only the brighter objects. Using the interactive mode, however, I could add additional CLEAN boxes as fainter emisson became apparent (the brighter CLEAN components having already been removed).

For CLEANing I also used Briggs weighting of the visibilities, with a ‘robust’ parameter of 0.5. This setting gives the best compromise between natural weighting and uniform weighting of the data. The former involves assigning equal weights to each of the visibilities, but doing so tends to overemphasise the shorter baselines (as there are more of them), leading to better sensitivity but at the expense of angular resolution. Meanwhile, an extra factor is used for uniform weighting, so that the density of the data is the same across the u-v plane of visibilities. As a result, longer baselines are upweighted and shorter baselines are downweighted, giving the reverse scenario of improved angular resolution but reduced sensitivity.

Due to the large-bandwidth upgrades of the JVLA, one of the CLEAN modes that needs to be implemented is multi-frequency synthesis imaging. As the co-ordinates in u-v space are measured in units of wavelength, they will be slightly different from one frequency channel to another. Therefore separately gridding the visibilities in the u-v plane leads to improved u-v coverage. Also part of CLEAN is the option of using a multi-scale mode, in which I can specify different angular scales for carrying out the deconvolution. However, given that all of my targets are quasars, and that any large-scale extended emission would have led to detections in FIRST or NVSS, I proceeded with the default setting. This entailed deconvolving the dirty image using the synthesised-beam response to a point source. (In other words, the final image of the sky-brightness distribution was generated from a superposition of point sources.)

Note that with each extra computation, the CLEAN algorithm took longer to complete. There was also the restriction in processing due to limited random-access memory. As a result, I found that 1000 × 1000 pixel images were of sufficient quality in most cases, taking about 1 hour to produce. This means that 4.2 arcmin is covered by each image, which is only a fraction of the primary-beam size (30 arcmin at L band). Therefore, any bright objects that are external to this field-of-view, either present in the primary beam or the sidelobes of the beam response function, may make a non-negligible contribution to the flux measured for the target at the pointing centre (Figure 4.31). To get around this, the sidelobe objects needed to be imaged so that CLEAN boxes could be placed around them, allowing their brightness to be correctly modelled by CLEAN components. The methods I used for this are described in the next subsection.

4.4.2.3 Advanced imaging

To help decide whether further work would lead to an improved final image, I checked whether there was any striping or radial patterns indicative of sidelobe artefacts (Figure 4.32). Two sets of stripes may also be overlapping, giving the image a ‘patchy’ appearance. However I bore in mind that such patchiness could also be due to phase errors (i.e. poor calibration or there still being some RFI). Of these, I also noted the

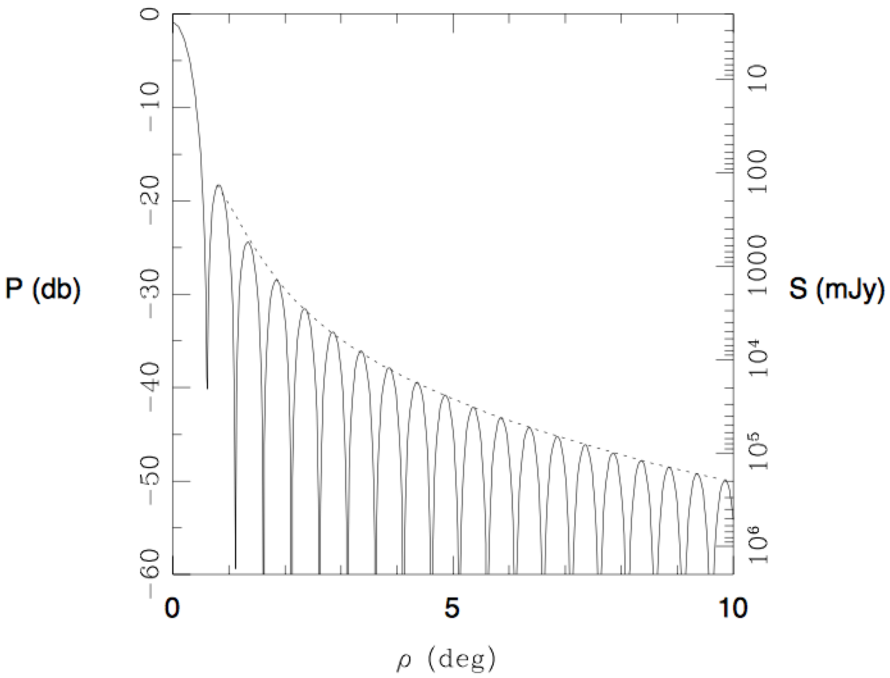

Figure 4.31: The power attenuation of the primary-beam response (in units of decibels), as a function of angular distance from the pointing centre, ρ. This has been calculated for the VLA at 1.4 GHz, each antenna being a circular aperture of diameter 24.5 m. The curve indicates the distance at which a source of flux density S could be detected above a threshold of 2 mJy, and therefore would need to be CLEANed separately. Image credit: Condon et al. [1998].

current SNR, and focused my attention on those objects that were undetected (SNR ≤ 3) in a standard 1000 × 1000 pixel image. For RSDSS171145.53+601318.4 in Figure 4.32, the artefacts were not sufficiently strong to affect the rms around the centre of the image. For SDSS114700.39+620008.1, the SNR was sufficiently high that the impact of objects detected via the sidelobes was negligible. Therefore, of the four examples shown, I carried out further work on SDSS092753.52+053637.0 and SDSS164617.17+364509.4.

The first step was to generate images with a field-of-view that covers 75 arcmin × 75 arcmin, this being 2.5 times the primary beam. I found that CASA struggled to produce images beyond 3000 × 3000 pixels without crashing, and so I used this as my maximum image size. This limited my resolution, as a single pixel was about the same size as the synthesised beam, at 1.5 arcsec. However, the purpose of this larger image was purely to get an idea of what emission lay outside of the central 250 arcsec × 250 arcsec. As such, it was deemed acceptable to leave the imaging to run non-interactively (i.e. no CLEAN boxes) because the poor recovery of any faint emission – due to CLEAN bias – was

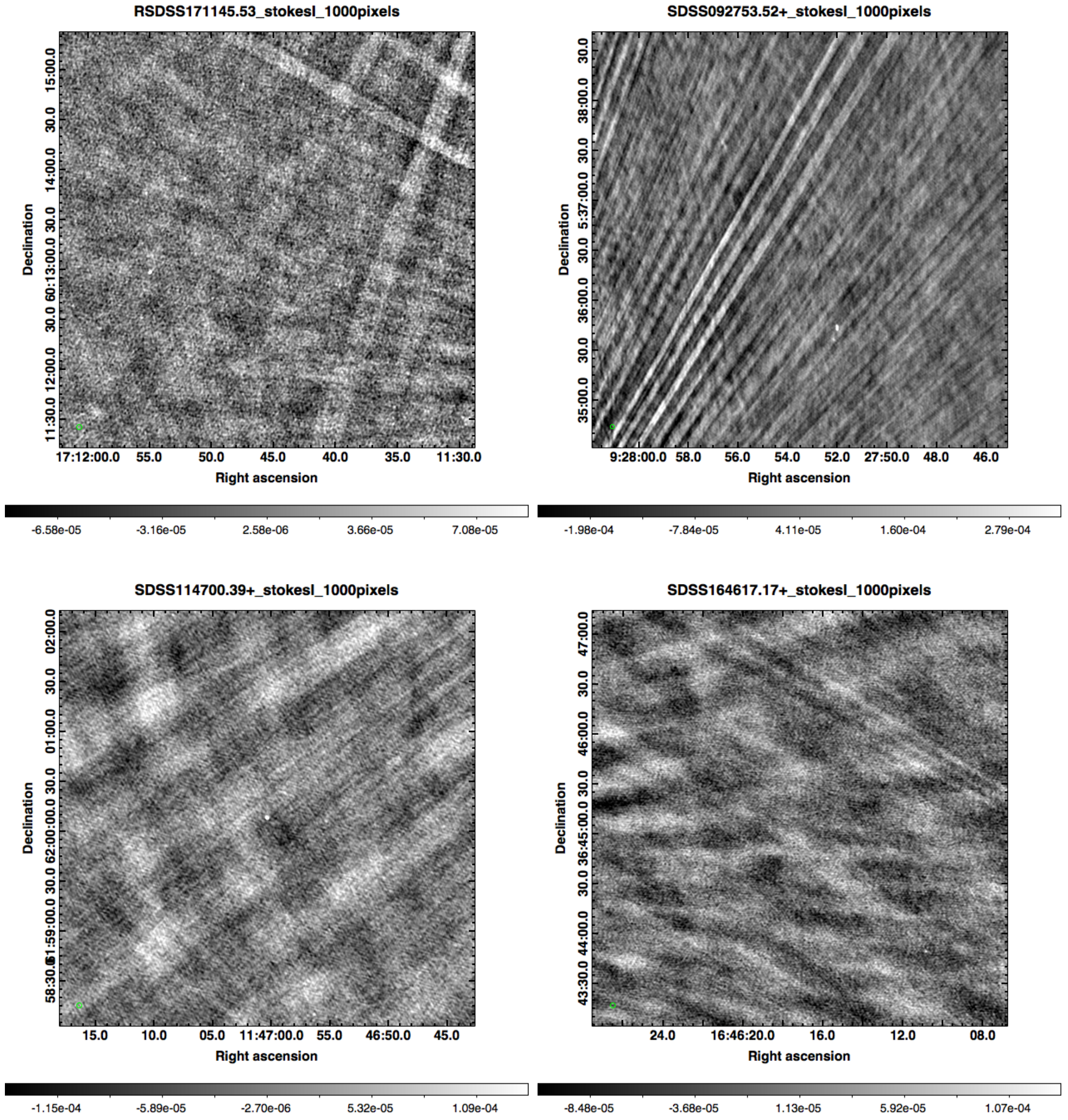

Figure 4.32: JVLA imaging of 4 RQQs, with each target at the pointing centre. For the objects in the left-hand column (RSDSS171145.53+601318.4 and SDSS114700.39+620008.1) it was deemed that neither using outlier fields nor imaging beyond 1000 pixels (i.e. 4.2 arcmin) would improve the level of detection. However, such techniques were implemented to improve the imaging of SDSS092753.52+053637.0 and SDSS164617.17+364509.4 (right-hand column). The beamsize is illustrated by the green ellipse in the bottom left-hand corner of each image, and the greyscale bar represents the flux in units of Jy/beam.

outweighed by the reduction in processing time (to $\sim$3 hours per image). In any case, faint objects would likely make a negligible contribution to flux at the pointing centre.

Another CLEAN algorithm I employed was w-projection, which is a vital correction for creating wide-field images. If the array's antennae were truly coplanar, then u and v co-ordinates are enough to describe the visibilities in Fourier space. However, as this is not the case, the baselines introduce a third component, w, in a direction orthogonal to u and v. Whilst no correction needs to be applied at the phase (i.e. pointing) centre, this effect becomes more pronounced with increasing distance from the centre. Thus, without the consideration of w-projection, any emission would become more and more 'defocused' towards the image's edges.

With these large-image 'maps', I identified any strong sources in the primary beam and sidelobes, making a note of their position and the extent of the emission. These details were kept in an 'outlier file' for each target, which I specified via the parameters of CLEAN. This time during the imaging process, the outliers were imaged separately, in addition to the 1000×1000 pixel main image. Within the outlier file I specified rectangular CLEAN boxes as a starting point for the mask, then edited these interactively as the dirty image was deconvolved.

In some cases it was clear that the artefacts originated from a source just beyond the 250 arcsec covered by the original, preliminary image (Section 4.4.2.2). Rather than spending time creating a map and an outlier file based on this, I simply extended the main imaging-region to include the outlier emission. Another scenario was where there was no real emission (or that which could be believed, on account of the noise) to set a CLEAN box in the main image. This was problematic as CLEAN's interactive window does not allow the user to progress to the outlier-field images until at least one CLEAN box has been defined. To get around this, I forced CLEAN to run with zero iterations, created a dummy mask for the main image, and edited the outlier masks appropriately via the interactive mode. I then saved the latter masks, directing the outlier file to use these instead of the default rectangular boxes, and deleted all other output associated with the zero-iteration run. Next I re-ran CLEAN non-interactively until definite emission appeared in the main image. I could then return to setting a CLEAN region for the main image, and continue the CLEAN as normal.

Figure 4.33 shows the substantial improvement in imaging quality that can be attained when sources detected outside the central region are corrected for by using outlier fields. In the case of SDSS092753.52+053637.0, although the measured peak flux remains about the same (57.7 μJy/beam instead of 54.9 μJy/beam), the noise level has halved, leading to an updated SNR of 2. For the target in the middle row of Figure 4.33, SDSS122832.94+603735.1, the pointing-centre flux is still at the level of the noise, but the field being clearly much smoother lends greater credance to this. Lastly, the SNR for SDSS142817.30+502712.6 is 3.1, which may seem surprising given the rms noise surrounding the target. (See Figure 4.36 for a zoomed-in image.) This could throw into doubt whether the emission is real or not. However, given that there is such a radio flux at the position where a quasar is known to be (the SDSS providing *a priori* information), I can be more confident of the measurements that are made.

4.4.2.4 Final measurements

For each image I measure the peak flux of the target and note the rms value over the entirety of the main image. These are provided in Table 4.1. However, this rms value will be skewed if there are other sources present in the field. I therefore also record the noise level over a manually-defined region, avoiding all sources, and use this value in my calculation of the SNR. The 32 targets that are detected with SNR ≥ 3 are presented in Figures 4.34 to 4.36, and the remaining zoomed-in images for the SHAGS sample (with SNR < 3) are shown in Figures 4.37 to 4.40.

4.5 Conclusions

As demonstrated in this chapter, the reduction of radio data is very involved, requiring a good understanding of the technique of interferometry and the algorithms used for imaging. With the recent upgrade to the JVLA, this is further complicated by much larger bandwidths for a given receiver. For example, it is necessary to obtain good bandpass calibrations and image using a multi-frequency technique. Furthermore, the improved sensitivity means that a greater number of sources need to be properly CLEANed. This

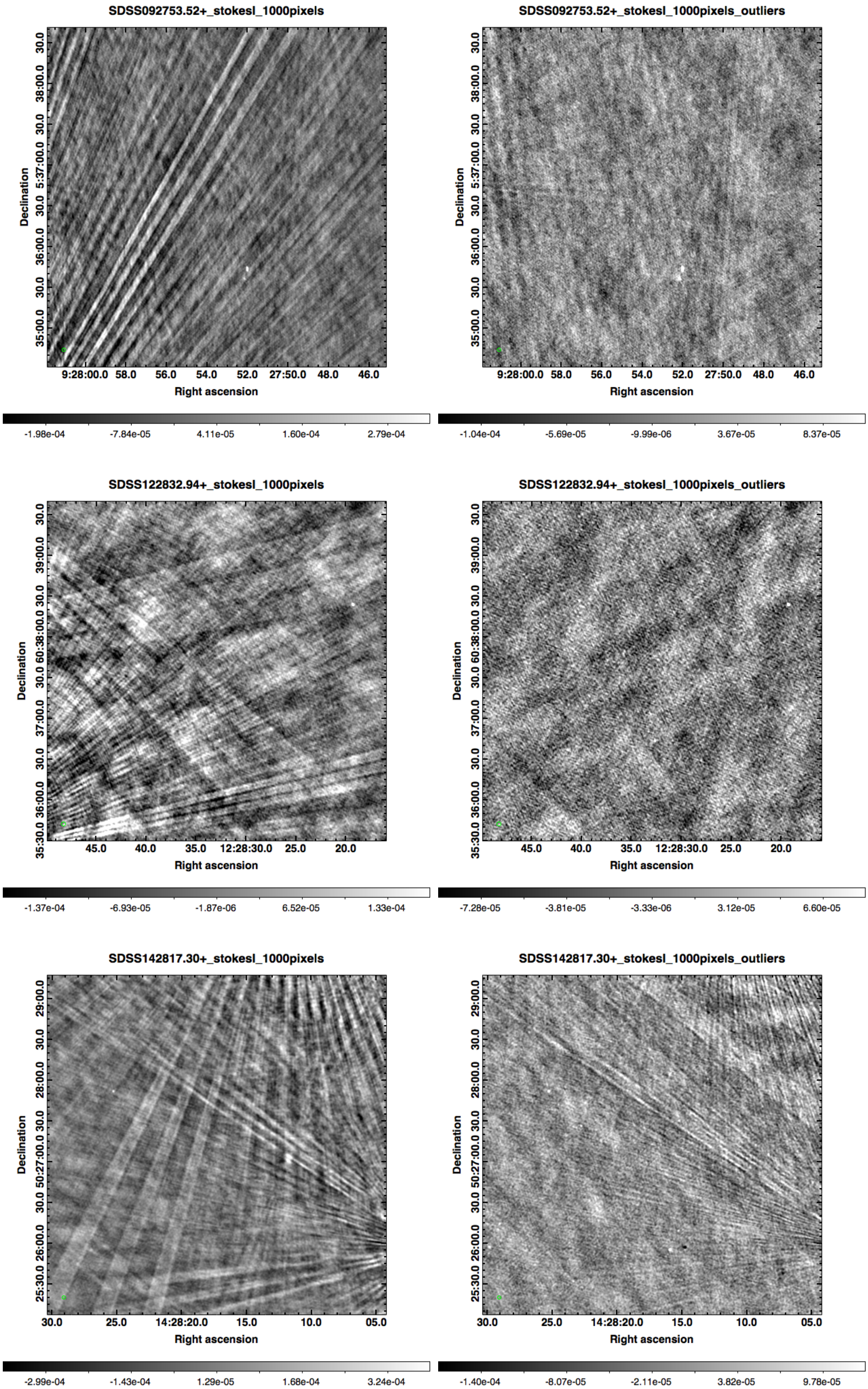
SDSS092753.52+_stokesI_1000pixels

SDSS092753.52+_stokesI_1000pixels_outliers

SDSS122832.94+_stokesI_1000pixels

SDSS122832.94+_stokesI_1000pixels_outliers

SDSS142817.30+_stokesI_1000pixels

SDSS142817.30+_stokesI_1000pixels_outliers

Figure 4.33: JVLA images for three targets, one per row, before (left column) and after (right column) outlier fields are used as part of the CLEAN process. The beamsize is illustrated by the green ellipse in the bottom left-hand corner of each image, and the greyscale bar represents the flux in units of Jy/beam.

Table 4.1: Radio measurements for the SHAGS sample of 72 radio-quiet quasars, taken from JVLA imaging. The theoretical noise is calculated according to the sensitivity equation (Equation 4.29). ‘Whole-image rms’ refers to the noise as calculated over the whole image, whilst for the ‘defined-region rms’, any sources in the field are excluded. Note that SNR = peak flux / defined-region rms.

Target’s full name	R.A. (hms)	Dec. (dms)	Theoretical rms (µJy/beam)	Whole-image rms (µJy/beam)	Defined-region rms (µJy/beam)	Peak flux (µJy/beam)	SNR
RSDSS103525.05+580335.6	10:35:25.05	+58:03:35.6	17.3	57.9	79.6	158.5	2.0
RSDSS103829.74+585204.1	10:38:29.73	+58:52:04.1	17.6	29.0	28.8	303.6	10.5
RSDSS103855.33+575814.7	10:38:55.32	+57:58:14.7	17.3	62.1	60.8	84.4	1.4
RSDSS104114.18+590219.4	10:41:14.18	+59:02:19.5	20.2	55.1	46.8	3.1	0.1
RSDSS104239.66+583231.0	10:42:39.64	+58:32:31.0	20.0	147.0	41.4	-50.4	-1.2
RSDSS104355.47+593054.0	10:43:55.46	+59:30:54.0	16.7	25.0	25.0	21.1	0.8
RSDSS104659.37+573055.6	10:46:59.37	+57:30:55.8	16.8	28.0	26.9	74.7	2.8
RSDSS104859.67+565648.6	10:48:59.66	+56:56:48.6	21.3	31.0	30.5	147.4	4.8
RSDSS104930.46+592032.6	10:49:30.45	+59:20:32.7	17.4	27.0	26.9	663.5	24.7
RSDSS163225.56+411852.0	16:32:25.56	+41:18:52.4	18.6	28.1	25.6	47.1	1.8
RSDSS163306.12+401747.0	16:33:06.12	+40:17:47.5	17.7	28.7	26.7	11.6	0.4
RSDSS163930.82+410013.2	16:39:30.81	+41:00:13.6	17.2	26.7	26.5	20.3	0.8
RSDSS171145.53+601318.4	17:11:45.52	+60:13:18.6	14.1	27.3	27.0	30.3	1.1
RSDSS171732.94+594747.7	17:17:32.92	+59:47:47.5	14.2	21.0	20.8	97.1	4.7
RSDSS172130.96+584404.1	17:21:30.96	+58:44:04.7	14.4	53.1	45.1	45.1	1.0
RSDSS172310.35+595105.6	17:23:10.34	+59:51:05.7	17.7	30.4	28.8	100.5	3.5
SDSS003146.07+134629.6	00:31:46.07	+13:46:30.0	14.8	22.4	21.9	-13.0	-0.6
SDSS023540.90+001038.9	02:35:40.90	+00:10:39.2	15.6	31.6	29.4	143.2	4.9
SDSS073802.37+383116.3	07:38:02.35	+38:31:16.5	20.0	30.1	31.3	422.8	13.5
SDSS074729.24+434607.5	07:47:29.16	+43:46:07.8	22.1	27.8	26.9	5.0	0.2
SDSS075058.21+421617.0	07:50:58.20	+42:16:16.9	19.8	30.4	29.0	-8.3	-0.3
SDSS075222.91+273823.2	07:52:22.89	+27:38:23.0	19.7	39.7	38.2	141.4	3.7
SDSS075339.84+250137.9	07:53:39.81	+25:01:37.8	19.4	51.1	46.7	56.5	1.2
SDSS082229.78+442705.2	08:22:29.76	+44:27:05.2	19.5	47.2	40.5	99.1	2.4

Table 4.1: *continued*

Target's full name	R.A. (hms)	Dec. (dms)	Theoretical rms (µJy/beam)	Whole-image rms (µJy/beam)	Defined-region rms (µJy/beam)	Peak flux (µJy/beam)	SNR
SDSS083115.89+423316.6	08:31:15.86	+42:33:16.5	19.2	52.1	45.7	185.5	4.1
SDSS084723.67+011010.4	08:47:23.64	+01:10:10.3	15.1	56.8	46.5	42.9	0.9
SDSS090153.42+065915.6	09:01:53.42	+06:59:15.3	14.8	26.0	25.6	313.3	12.3
SDSS091216.88+420314.2	09:12:16.87	+42:03:14.3	21.2	46.9	48.6	-43.2	-0.9
SDSS092257.86+444651.8	09:22:57.86	+44:46:52.1	20.5	88.7	83.2	136.2	1.6
SDSS092753.52+053637.0	09:27:53.52	+05:36:36.8	14.6	30.6	28.7	57.7	2.0
SDSS092829.86+504836.6	09:28:29.78	+50:48:36.3	22.4	32.3	31.1	346.2	11.1
SDSS093023.28+403111.0	09:30:23.28	+40:31:11.1	22.1	351.0	35.4	90.3	2.6
SDSS093303.50+460440.2	09:33:03.48	+46:04:39.8	19.5	26.7	27.0	86.5	3.2
SDSS093759.44+542427.3	09:37:59.35	+54:24:27.2	22.6	158.0	43.3	68.0	1.6
SDSS094811.89+551726.5	09:48:11.85	+55:17:26.4	24.8	49.5	51.5	-10.7	-0.2
SDSS100730.47+050942.3	10:07:30.48	+05:09:42.0	17.1	39.1	35.4	218.0	6.2
SDSS100835.81+513927.8	10:08:35.83	+51:39:27.9	16.9	22.8	22.4	36.4	1.6
SDSS100906.35+023555.3	10:09:06.33	+02:35:55.4	17.4	68.5	59.2	256.3	4.3
SDSS102005.99+033308.5	10:20:05.97	+03:33:08.4	19.9	64.2	48.7	201.7	4.1
SDSS102111.57+611415.0	10:21:11.56	+61:14:15.2	21.5	33.6	32.9	40.6	1.2
SDSS102349.40+522151.2	10:23:49.39	+52:21:51.2	20.2	58.5	39.1	107.1	2.7
SDSS103347.32+094039.0	10:33:47.30	+09:40:39.0	17.5	37.7	33.4	268.1	8.0
SDSS104537.69+484914.6	10:45:37.68	+48:49:14.6	21.8	56.7	54.2	-27.8	-0.5
SDSS104935.76+554950.6	10:49:35.76	+55:49:50.5	22.6	42.7	40.1	-8.6	-0.2
SDSS105408.88+042650.4	10:54:08.88	+04:26:50.4	17.9	38.0	36.6	29.8	0.8
SDSS112317.52+051804.0	11:23:17.49	+05:18:03.9	15.6	445.0	342.0	-875.6	-2.6
SDSS114700.39+620008.1	11:47:00.36	+62:00:08.1	19.1	43.6	41.2	1310.0	31.8
SDSS115027.25+665848.0	11:50:27.21	+66:58:48.1	18.9	28.6	28.7	143.0	5.0

Table 4.1: *continued*

Target's full name	R.A. (hms)	Dec. (dms)	Theoretical rms (µJy/beam)	Whole-image rms (µJy/beam)	Defined-region rms (µJy/beam)	Peak flux (µJy/beam)	SNR
SDSS122832.94+603735.1	12:28:32.92	+60:37:35.1	18.0	29.6	28.5	26.5	0.9
SDSS123059.71+101624.8	12:30:59.71	+10:16:24.5	15.5	27.5	26.1	85.6	3.3
SDSS125659.93+042734.4	12:56:59.90	+04:27:34.6	15.2	24.6	24.1	931.8	38.7
SDSS132957.15+540505.9	13:29:57.14	+54:05:06.0	18.4	36.2	39.7	326.0	8.2
SDSS133713.06+610749.0	13:37:13.00	+61:07:49.0	18.1	31.2	30.1	36.8	1.2
SDSS133733.30+590622.6	13:37:33.28	+59:06:22.8	18.4	31.9	30.9	186.0	6.0
SDSS134635.02+415630.9	13:46:35.01	+41:56:31.0	19.3	43.9	28.5	3677.3	129.1
SDSS135823.99+021343.8	13:58:23.97	+02:13:44.0	14.7	54.9	51.2	3.5	0.1
SDSS142124.65+423003.2	14:21:24.67	+42:30:03.1	14.1	21.2	21.5	196.0	9.1
SDSS142817.30+502712.6	14:28:17.30	+50:27:12.7	14.9	39.9	33.8	106.5	3.1
SDSS145503.47+014209.0	14:55:03.45	+01:42:09.2	16.0	33.6	24.1	35.6	1.5
SDSS145506.12+562935.6	14:55:06.09	+56:29:35.6	14.6	23.3	23.2	86.9	3.7
SDSS151520.56+004739.3	15:15:20.54	+00:47:39.4	19.0	46.1	42.7	416.8	9.8
SDSS151921.85+535842.3	15:19:21.84	+53:58:42.2	13.9	33.9	25.4	24.6	1.0
SDSS155436.25+320408.4	15:54:36.24	+32:04:08.5	14.6	25.5	25.7	14.5	0.6
SDSS155650.41+394542.8	15:56:50.40	+39:45:42.8	14.7	33.2	32.0	100.6	3.1
SDSS163408.64+331242.1	16:34:08.64	+33:12:42.1	15.3	28.9	27.6	116.4	4.2
SDSS164617.17+364509.4	16:46:17.16	+36:45:09.6	17.1	29.1	27.9	-9.0	-0.3
SDSS165231.30+353615.9	16:52:31.29	+35:36:15.9	17.9	26.9	26.1	30.1	1.2
SDSS171005.53+644843.0	17:10:05.52	+64:48:42.9	14.6	22.8	23.0	293.2	12.7
SDSS171330.21+644253.0	17:13:30.24	+64:42:53.0	17.8	27.5	26.0	1104.9	42.4
SDSS171704.69+281400.6	17:17:04.68	+28:14:00.7	16.5	40.7	34.7	263.5	7.6
SDSS215541.74+122818.8	21:55:41.73	+12:28:18.9	16.2	88.8	65.3	-40.7	-0.6
SDSS224159.43+142055.2	22:41:59.42	+14:20:55.0	16.2	23.7	23.8	27.6	1.2

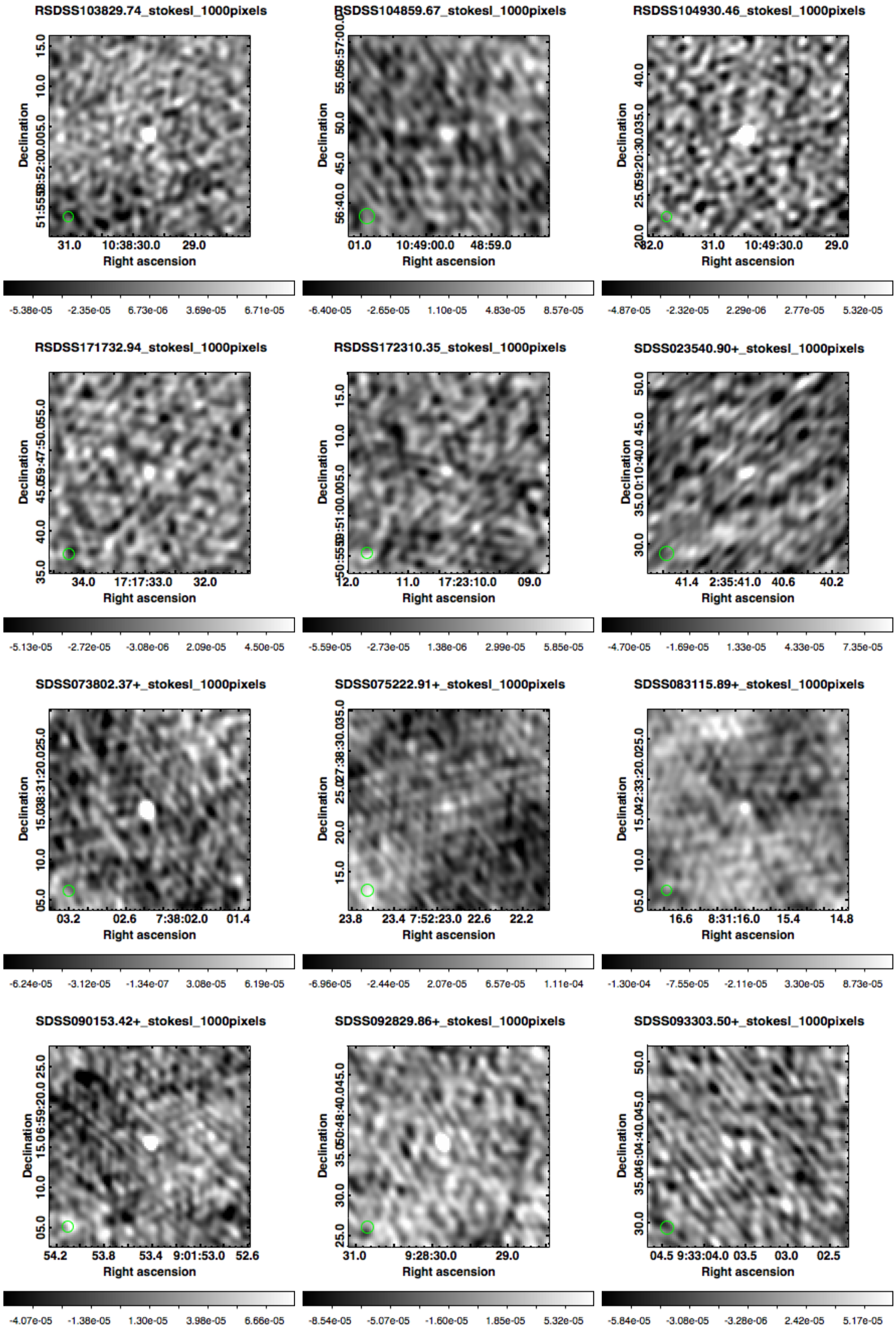

Figure 4.34: JVLA imaging of the SHAGS sample of RQQs, with each target at the pointing centre. Each of the objects in this figure are deemed 'detections', having SNR ≥ 3. The beamsize is illustrated by the green ellipse in the bottom left-hand corner of each image, and the greyscale bar represents the flux in units of Jy/beam.

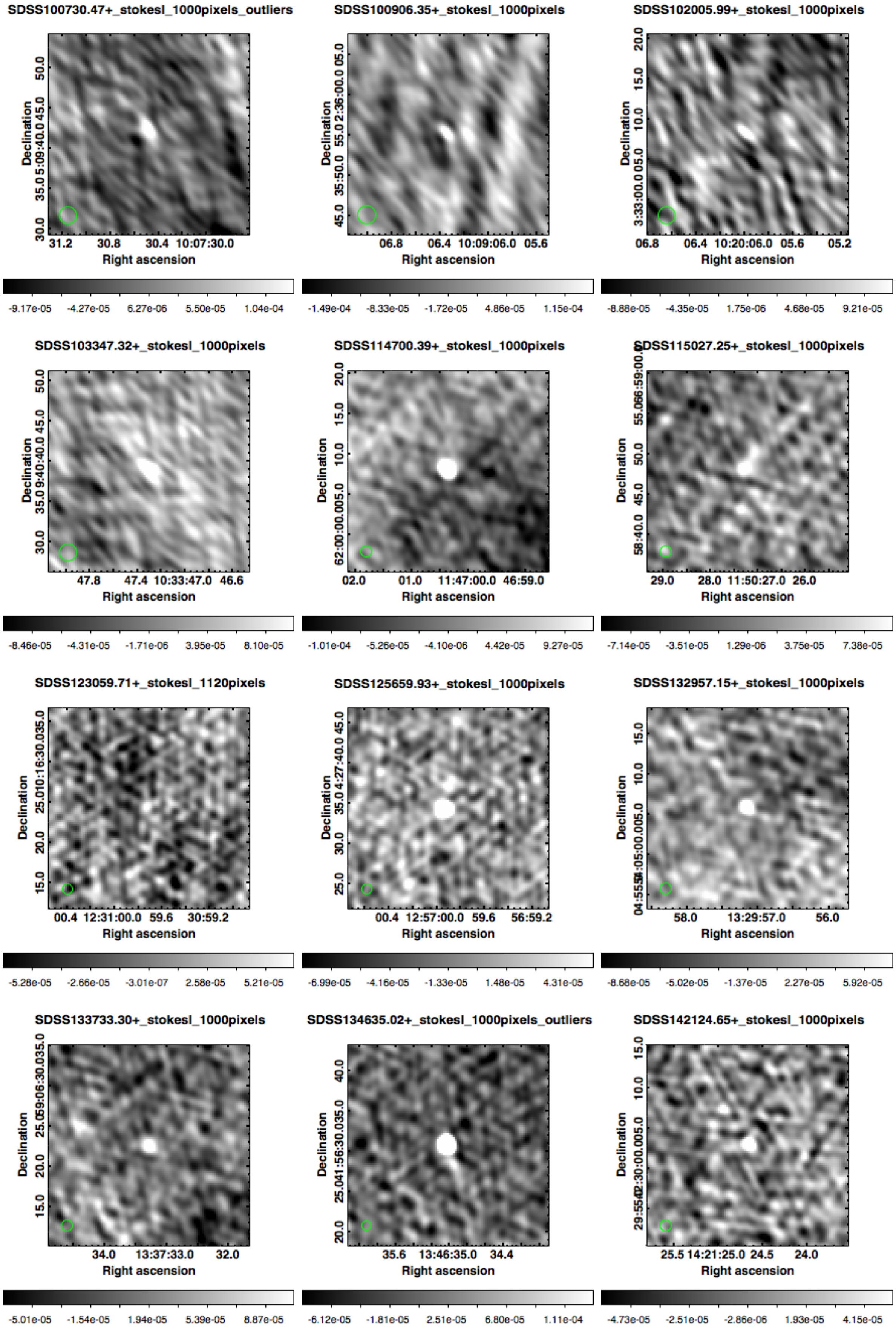

Figure 4.35: JVLA imaging of the SHAGS sample of RQQs, with each target at the pointing centre. Each of the objects in this figure are deemed ‘detections’, having SNR ≥ 3. The beamsize is illustrated by the green ellipse in the bottom left-hand corner of each image, and the greyscale bar represents the flux in units of Jy/beam.

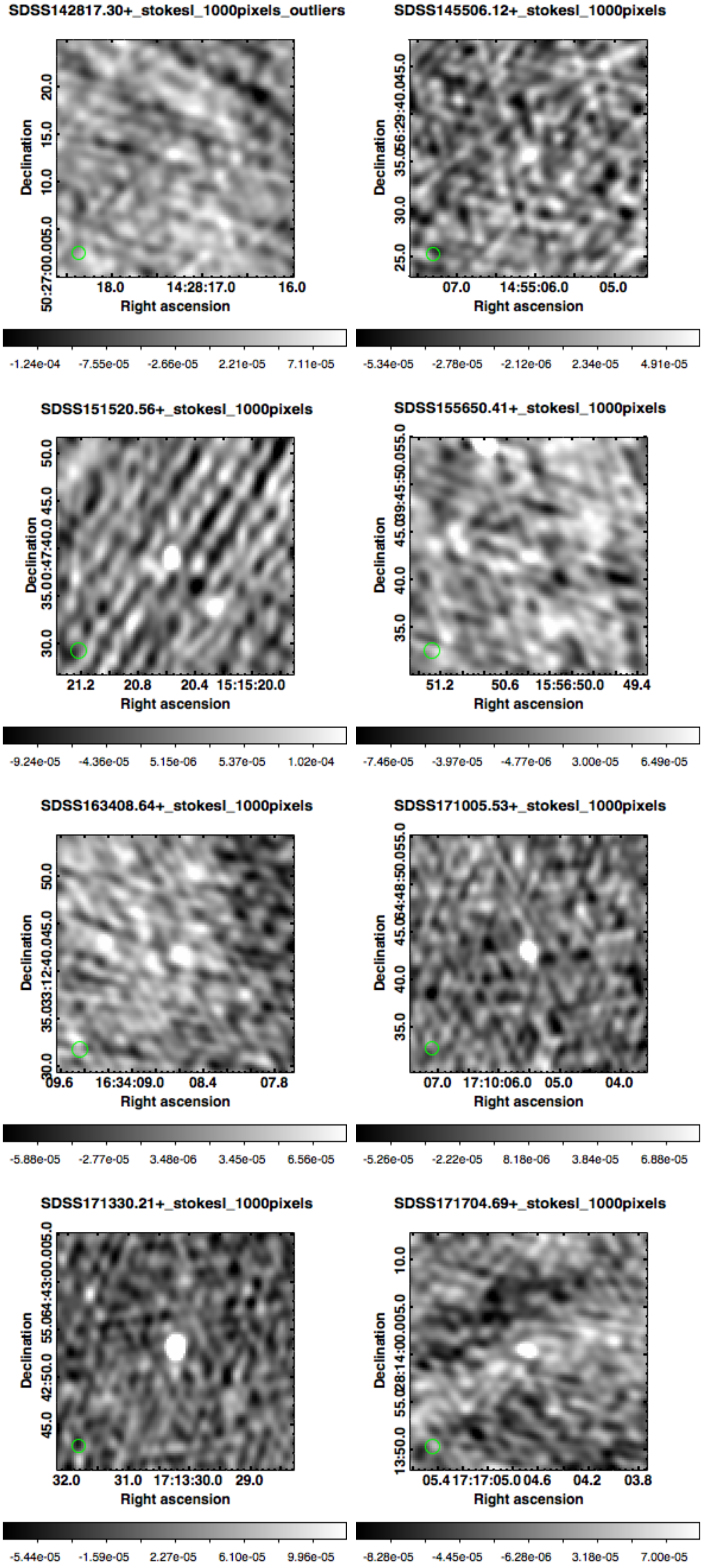

Figure 4.36: JVLA imaging of the SHAGS sample of RQQs, with each target at the pointing centre. Each of the objects in this figure are deemed 'detections', having SNR ≥ 3. The beamsize is illustrated by the green ellipse in the bottom left-hand corner of each image, and the greyscale bar represents the flux in units of Jy/beam.

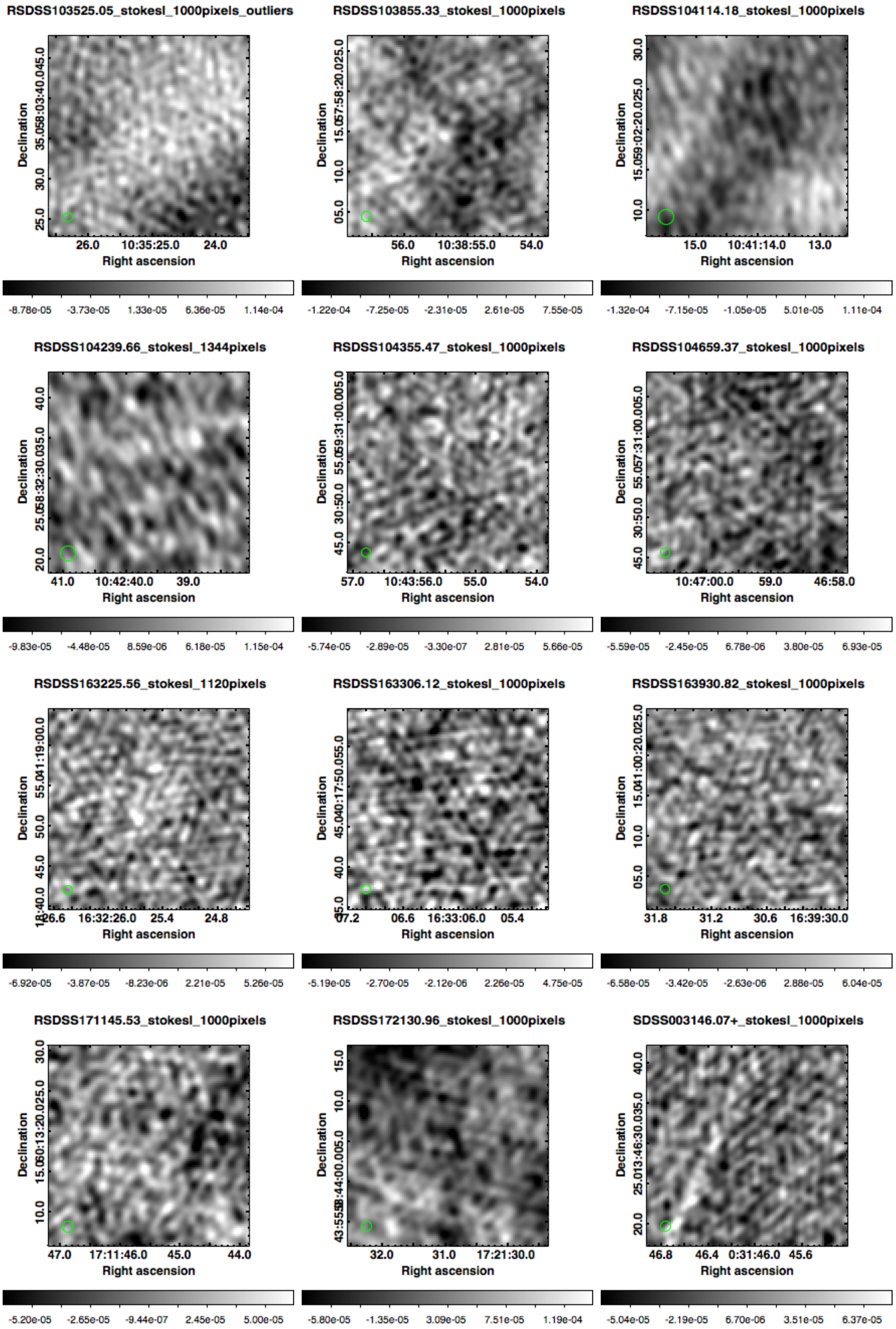

Figure 4.37: JVLA imaging of the SHAGS sample of RQQs, with each target at the pointing centre. Each of the objects in this figure are 'non-detections', having SNR < 3. The beamsize is illustrated by the green ellipse in the bottom left-hand corner of each image, and the greyscale bar represents the flux in units of Jy/beam.

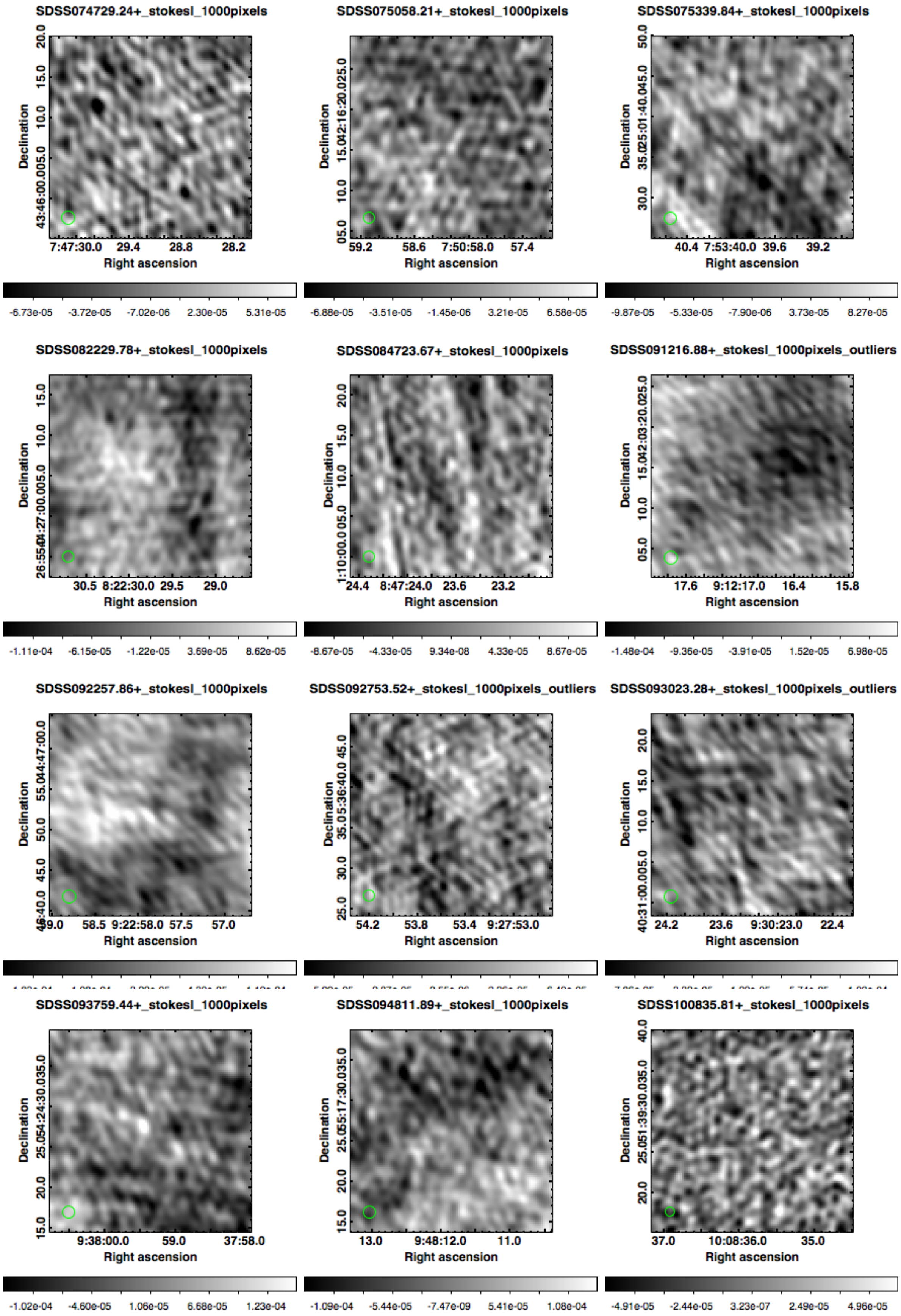

Figure 4.38: JVLA imaging of the SHAGS sample of RQQs, with each target at the pointing centre. Each of the objects in this figure are ‘non-detections’, having SNR < 3. The beamsize is illustrated by the green ellipse in the bottom left-hand corner of each image, and the greyscale bar represents the flux in units of Jy/beam.

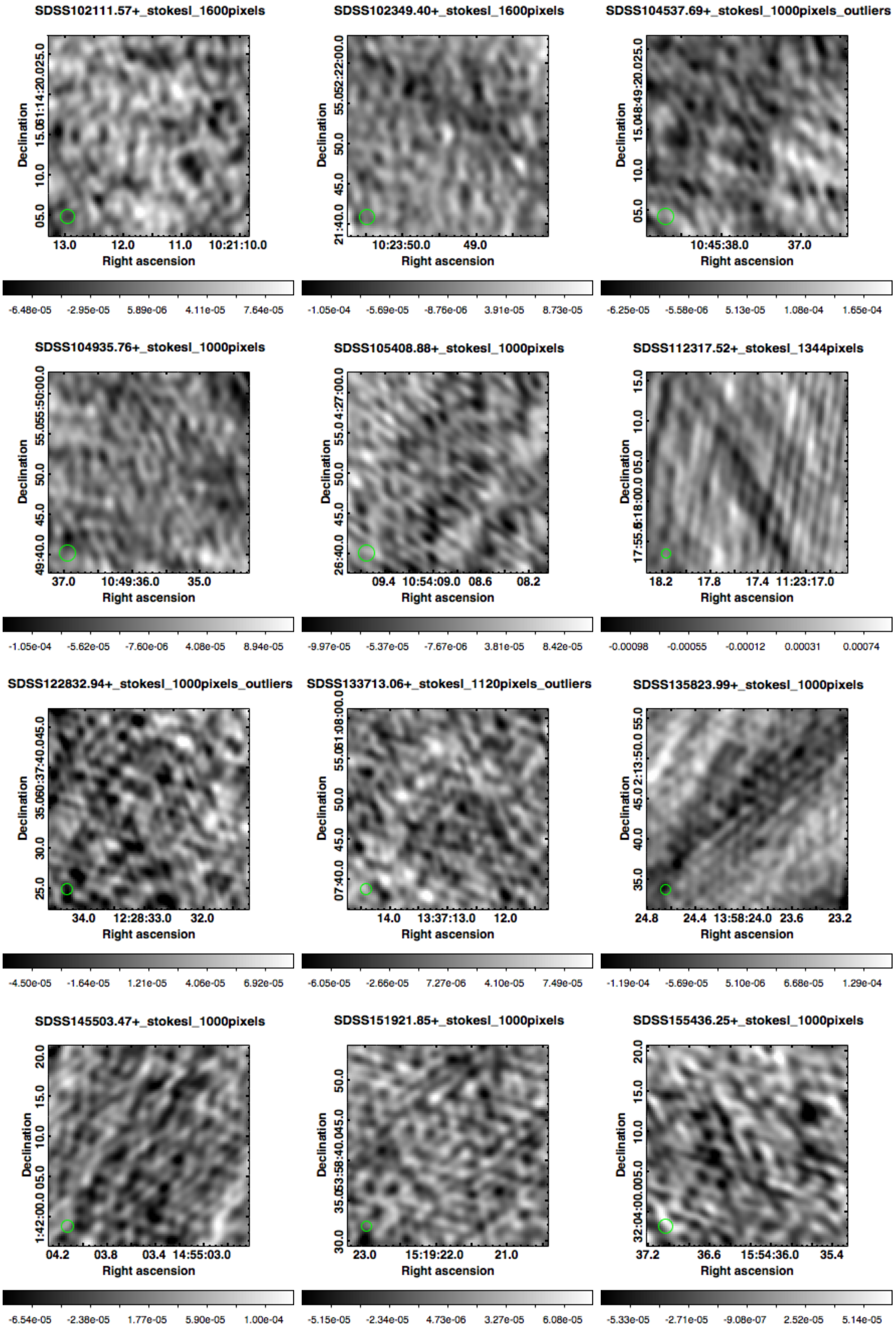

Figure 4.39: JVLA imaging of the SHAGS sample of RQQs, with each target at the pointing centre. Each of the objects in this figure are ‘non-detections’, having SNR < 3. The beamsize is illustrated by the green ellipse in the bottom left-hand corner of each image, and the greyscale bar represents the flux in units of Jy/beam.

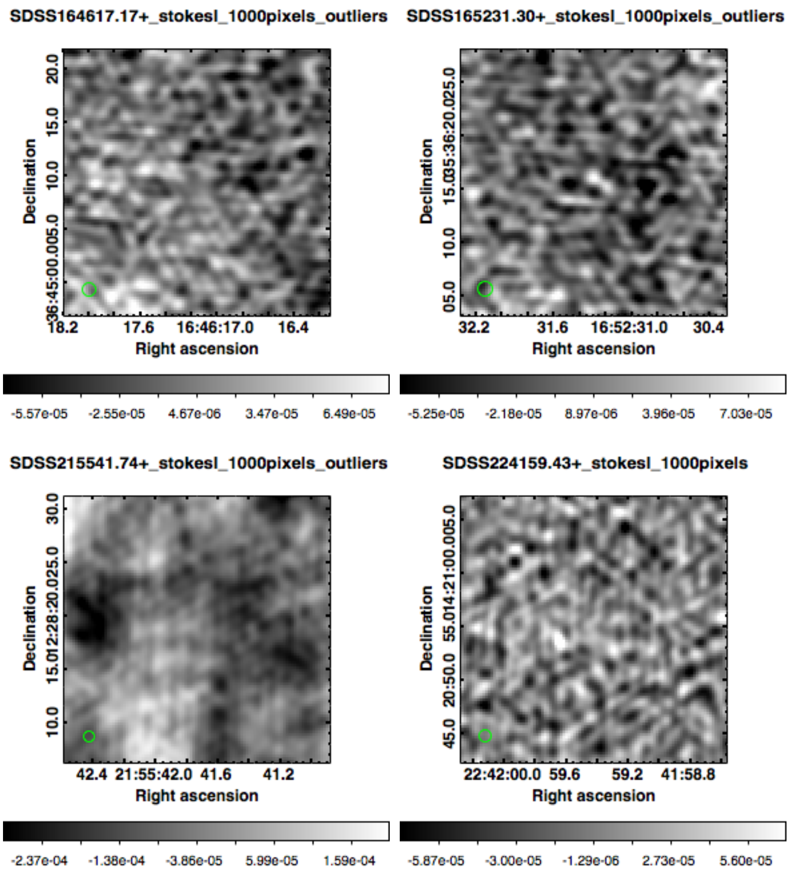

Figure 4.40: JVLA imaging of the SHAGS sample of RQQs, with each target at the pointing centre. Each of the objects in this figure are 'non-detections', having SNR < 3. The beamsize is illustrated by the green ellipse in the bottom left-hand corner of each image, and the greyscale bar represents the flux in units of Jy/beam.

requires a wider field to be imaged, and so several factors (bandwidth-smearing, time-averaging loss, and w-projection) become increasingly important. However, despite the automated systems in place, the flagging of RFI remains reliant on visual inspection of numerous diagnostic plots. Due to the reduction in sensitivity caused by flagged data, it is expected that the final images have a noise level that is 2–3 times the theoretical rms value. Such is the case for 67 of the 72 RQQs (Table 4.1), and of these, 32 objects have a $\geq$3-σ detection.

5

Analysis of $z \sim 1$ quasars

“Go ask the dust for any answers”

– Red Hot Chili Peppers, *Can’t Stop*

Using the newly-reduced JVLA images (Chapter 4), and FIR photometry already in hand, this chapter describes the analysis performed on the SHAGS sample of radio-quiet quasars. As in Chapter 3, the aim is to determine the relative contributions of black-hole accretion and star-formation processes to the total radio emission. However, rather than inferring the SFR from estimates of the stellar mass, I fit a grey-body spectrum to the FIR emission to obtain a more-direct SFR measure. Also, given that this is a complete sample over a narrow redshift range, I am able to investigate any trends with regard to the optical luminosity of the quasar, without the added complication of possible evolutionary effects and K-correction uncertainties.

5.1 Analysis of the radio emission

In the work of Falder et al. [2010], the relationship between AGN activity and environmental density is investigated at $z \sim 1$, using both the radio-loud and radio-quiet quasars in SHAGS. From the stacking analysis performed for the same sample of RQQs that I use here, they find the average flux density at 1.4 GHz to be 0.10 ± 0.02 mJy. This result was used in the JVLA proposal to inform what depth the observations should achieve, bearing in mind that the likely flux-density distribution was unknown. With the resulting JVLA imaging (Section 4.4.2.4), this distribution is revealed in the following subsection.

5.1.1 Radio flux-density measurement

Firstly, for the remainder of this chapter, when I refer to the radio flux-density or luminosity at 1.4 GHz, this is in fact the new L-band measurement (which covers 1–2 GHz). This is different to the work presented in Chapters 2 and 3, where observations with the VLA's traditional L-band was used in conjunction with VIDEO data.

To investigate the radio flux-density distribution of the SHAGS sample of RQQs, I carry out a similar analysis to that described in Section 3.1. Single-pixel flux densities are extracted from the JVLA images at the pointing centre. For detected objects, this value is superseded by the flux density extracted where the target's radio emission *peaks*. A tolerance of 1 arcsec from the pointing centre is used to account for any pointing error in the observations, although such an offset is seen for only one of the targets. In each case, the radio emission from well-detected objects appears as an unresolved point-source, with none of the RQQs showing any extended emission. Resolution better than the present 1.3 arcsec, easily achieved with the Square Kilometre Array (SKA), would be needed to distinguish between unresolved emission from the central engine and any small radio jets.

Average flux-densities for the sample are given in Table 5.1, with the mean flux-density found to be 189.1 ± 58.5 μJy/beam. This is within 1.1-σ error of the finding by Falder et al. [2010], but my measurement is more accurate due to the better sensitivity of the JVLA images compared to the typical 0.15 mJy rms of FIRST. Also presented in Table 5.1 are the average fluxes extracted at random positions. The latter refer to the 1000 pixel values that are extracted from each JVLA image, lying between 3 and 9 arcsec from the pointing centre. This is done so that the different noise properties of each of the radio images can be taken into consideration. The effect of noise is particularly evident through the fractions of flux densities that are negative, with the fraction for the random positions (0.52) far exceeding that for the quasar sample (0.14).

Figure 5.1 shows the distributions of the flux densities, with the long positive tail of the quasars clearly demonstrating that they are detected above the level of the noise. This is quantitatively confirmed by 1000 Kolmogorov–Smirnov (KS) tests, which test the null

Table 5.1: Stacked radio flux densities for the quasars, random sample, and when binned in absolute i-band magnitude. The number of flux-density values that are negative is given by the ‘negative fraction’, and the p-value is the median result from 1000 Kolmogorov–Smirnov (KS) tests being performed per sample. This calculates the probability of the null hypothesis that the two distributions are drawn from the same underlying distribution. The error in the median flux is the median absolute deviation (MAD), which reduces the effect of outliers in the distribution.

Sample	Median flux (µJy/beam)	Mean flux (µJy/beam)	Negative fraction	KS test p-value
$z = 1$ quasars	86.1 ± 68.7	189.1 ± 58.5	0.14	N/A
Random positions	-2.1 ± 23.8	-4.1 ± 6.7	0.52	10^{-21}
$-28.0 \leq M_i < -26.7$	193.9±125.8	221.9±51.0	0.11	10^{-8}
$-26.7 \leq M_i < -25.4$	88.6±46.7	150.8±29.4	0.06	10^{-10}
$-25.4 \leq M_i < -24.3$	91.4±58.5	338.1±100.3	0.06	10^{-9}
$-24.3 \leq M_i < -23.0$	22.9±31.5	45.7±10.6	0.33	10^{-2}

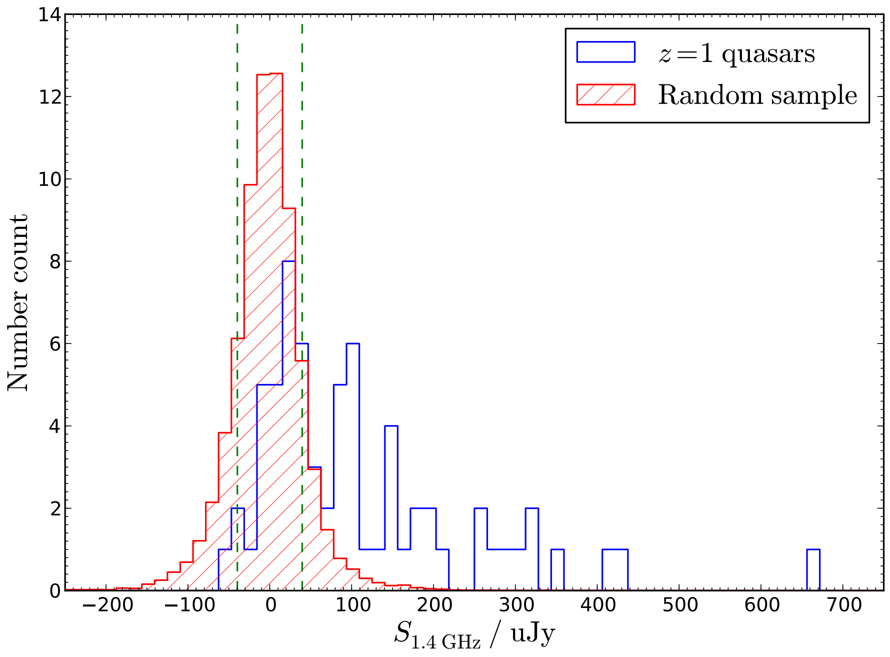

Figure 5.1: The radio flux-density distribution for the SHAGS sample of RQQs (blue histogram). The red (hatched) histogram corresponds to the random sample, where the fluxes are extracted from pixels 3 to 9 arcsec away from the quasar positions. (Their number counts have been scaled to aid comparison.) The green, dashed lines demarcate the mean rms noise level (±39.6 µJy/beam), found by averaging over all 72 JVLA images. Note that four brighter quasars lie beyond the radio flux-density range shown.

hypothesis that the quasars' flux densities and those extracted from random positions are drawn from the same underlying population. 1000 tests are done in order to account for the differing noise properties of the images, and the median p-value produced by these tests is 10^{-21}. This means that the null hypothesis can be strongly rejected, and that the excess in radio emission from the quasars (compared to the random sample) is real.

5.1.2 Radio properties as a function of optical luminosity

To investigate the sample's radio flux-density distribution further, I bin the quasars in absolute i-band magnitude (M_i) and bin the radio flux-densities at the random positions according to the M_i range of the associated quasar (Figure 5.2). For every bin in M_i I perform several KS tests in order to derive a median p-value. Doing so enables the random-position flux-densities to be well-sampled, as there are 1000 of these per quasar. They are therefore selected at random, so that each test is between the flux densities of the quasars within that bin and an equal number of random-position flux-densities. The resulting p-values are quoted in Table 5.1 and Figure 5.2. For each of the M_i bins there is evidence to confidently reject the null hypothesis that the quasars are drawn from the same underlying flux distribution as the random positions. However, note that the level of confidence with which I can reject the null hypothesis for the faintest bin ($-24.3 \leq M_i < -23.0$) is 99.0%. Looking at the corresponding flux-density distribution (bottom right-hand panel of Figure 5.2), there are three objects that clearly lie beyond the histogram for the random flux-densities, but the remaining quasars are at the level of the noise. In fact, 6 of the 18 quasars present in this bin have negative flux densities, as measured from the JVLA images. Whilst this is a higher proportion than for the other M_i ranges, it is still not as high as the fraction expected for flux densities extracted from pure noise (i.e 0.5). This means that the radio emission at the positions of the quasars is real.

Next I determine whether there is a correlation between the radio luminosity and the absolute i-band magnitude. As explained in Section 3.1.2, this may be expected for RQQs if they exhibit the same accretion processes as radio-loud quasars [e.g. Serjeant et al. 1998; Punsly and Zhang 2011]. That is, the amount of radio emission due to

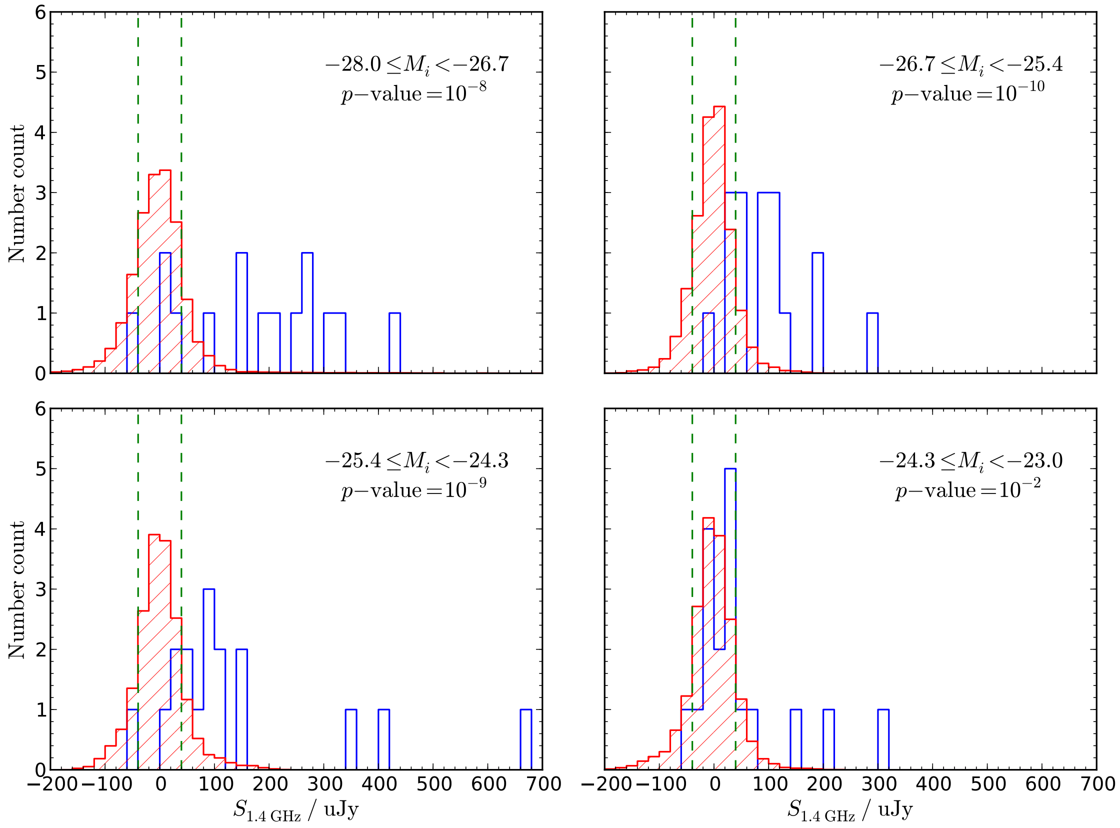

Figure 5.2: The flux-density distribution of the RQQs taken from SHAGS (blue histograms), binned in absolute i-band magnitude. The flux-density value was also measured at random positions, confined to lie between 3 and 9 arcsec away from each quasar position (red, hatched histograms, scaled), to allow comparison with the intrinsic radio noise properties. The dashed green lines are at ±39.6 µJy, which is the mean rms noise (i.e. 1σ) level of the JVLA images. A statistical detection of faint radio emission is indicated by the positive offset of the quasar histogram from the random distribution. The median p-value, resulting from 1000 KS tests between the Gold and random subsamples, is given for each bin (Table 5.1). Note that four brighter quasars lie beyond the radio flux-density range shown.

accretion is strongly-coupled to the optical luminosity of the accretion disc, due to the thermal emission that is produced as material is transported inwards. However a different mechanism may exist for RQQs, as suggested by Hardcastle et al. [2006]. A similar conclusion is drawn from the stacking analysis by Fernandes et al. [2011] for optically-selected quasars (Section 1.4.1.2), which include the RQQs presented here. The result lies well above the minimum accretion-rate envelope dictated by the radio-loud sources (Figure 1.13), but this could be skewed by a few quasars. (The radio data they use is not deep enough to study the distribution on an individual basis.) Here I carry out a linear regression analysis between the radio luminosity and the absolute i-band magnitude, for each of the 72 RQQs (upper panel of Figure 5.3). The coefficient of determination, R^2, indicates how good the fit is on a scale from 0 to 1. The value of 0.02 shows that the one-to-one relation between the two intrinsic properties is poor, but a trend can still be seen by eye, where increasing radio luminosity is accompanied by increasing brightness in the optical.

The translation of this best-fit line into logarithmic space is presented in the lower panel of Figure 5.3, and overplotted are the median values for each M_i bin. Note that these median luminosities include the negative values derived for RQQs that had a negative flux-density extracted from the radio image. Finally, a Pearson correlation test gives $r = -0.1$ and p-value=0.3, which indicates that the radio luminosity and the absolute i-band magnitude are not strongly correlated. The reason for the weaker trend compared to the VIDEO sample (Section 3.1.2) may in part be due to observational effects that are not present in the SHAGS sample, such as the higher accretion rates observed at redshifts beyond $z \sim 1$ [Richards et al. 2006b; Croom et al. 2009]. To explore this further, deeper radio data on optically-selected quasars is needed so that the correlation between radio and optical luminosity can be studied as a function of redshift.

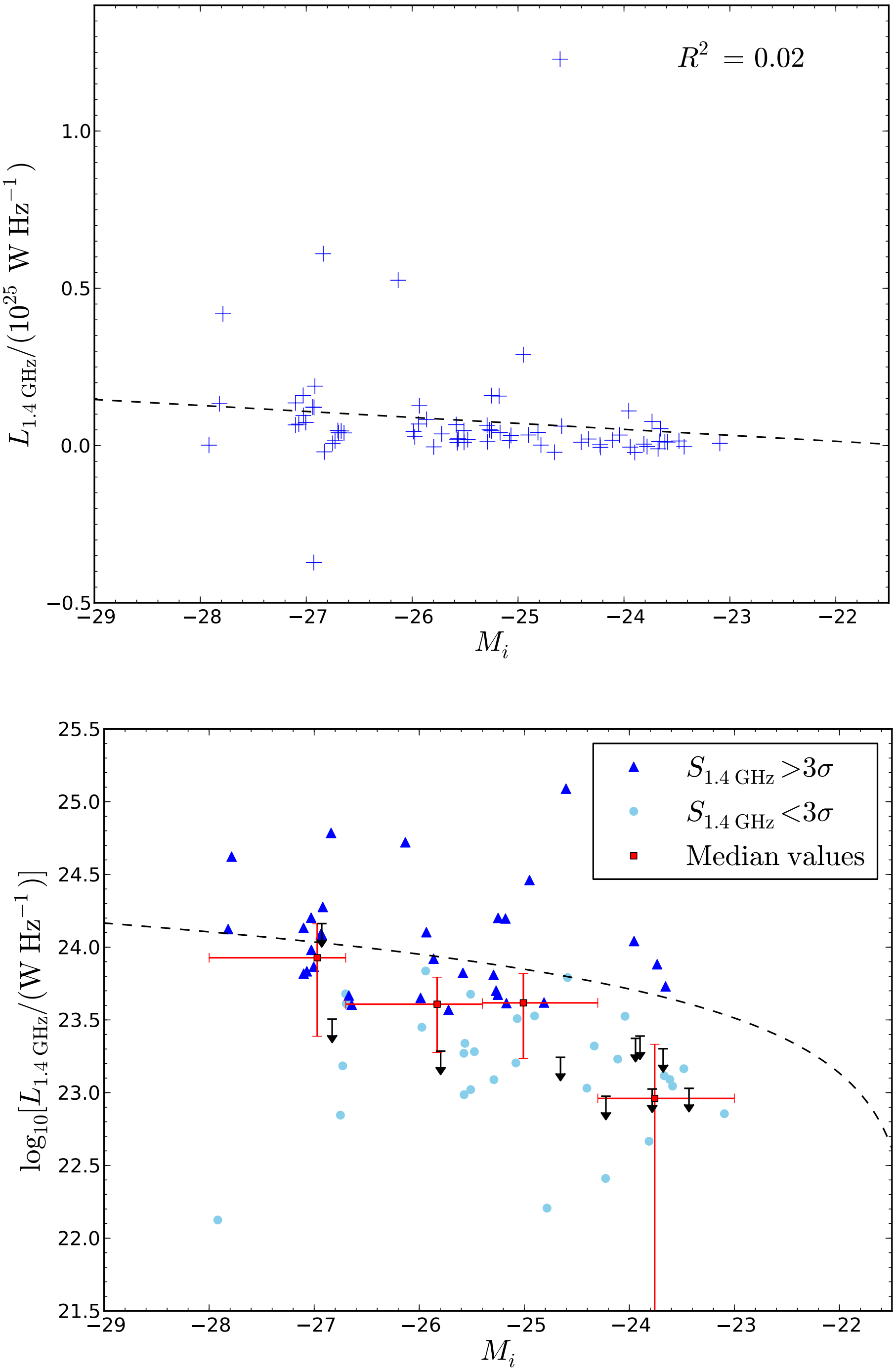

Figure 5.3: The top panel shows the linear regression analysis performed between the radio luminosity ($L_{1.4\,\mathrm{GHz}}$) and the absolute i-band magnitude (M_i) for the SHAGS sample of RQQs. This is in linear space to show negative radio luminosities. The coefficient of determination (R^2) is given in the top-right corner, and the same dashed line, $L_{1.4\,\mathrm{GHz}} = -1.90 \times 10^{23} M_i - 4.04 \times 10^{24}$, appears in both plots. In the lower panel is $L_{1.4\,\mathrm{GHz}}$ against the absolute i-band magnitude, M_i. Dark-blue triangles correspond to objects detected with a signal-to-noise ratio of over 3 ($S_{1.4\,\mathrm{GHz}} > 3\sigma$), and light-blue circles are those below this detection threshold. The black arrows represent 1-σ upper limits for objects with negative radio fluxes, as measured from the JVLA images. Overplotted in red are the median luminosities for these objects, derived from the measured flux-densities, binned in M_i. They are offset from the dashed line because the latter is determined via mean luminosities. The horizontal error bars indicate the ranges of the M_i bins (Table 5.1), and uncertainties on the median radio luminosities are given by the ordinate error bars.

5.2 Analysis of the far-infrared emission

5.2.1 Multi-band fitting in the far-infrared

Far-infrared emission is produced by the cool dust associated with star formation, and therefore acts as a good tracer of the SFR. This emission is typically approximated by a grey-body spectrum, which is the usual black-body function given by Planck's law,

$$B_\nu(\nu, T) = \frac{2h\nu^3}{c^2}\frac{1}{e^{\frac{h\nu}{k_\mathrm{B}T}} - 1}, \tag{5.1}$$

multiplied by a frequency-dependent emissivity term, $Q_\nu = Q_0(\nu/\nu_0)^\beta$ [Hildebrand, 1983]. B_ν is the object's brightness at frequency ν; T is the dust temperature; h is Planck's constant; c is the speed of light; k_B is Boltzmann's constant; and β is the dust emissivity. The emissivity is usually in the range $1.0 < \beta < 2.0$, and encodes details about the dust grains, such as the absorption of radiation, their size, and their chemical composition. As this leads to a degeneracy with temperature, I simplify the fitting by using a fixed value: $\beta = 1.8$. This is the weighted-mean β used by Hardcastle et al. [2013] and Smith et al. [2013], whose samples consist of galaxies selected from *Herschel*-ATLAS (Astrophysical Terahertz Large Area Survey) at $z < 1$.

With the advent of data from the Infrared Astronomical Satellite (IRAS), studies such as Chini et al. [1986] and de Jong and Brink [1987] appear to provide a realistic description of the far-infrared emission by using a two-component model. That is, a cold-dust population and a warm-dust population are fitted simultaneously by independent grey-body spectra. The true dust population is likely to have a continuous distribution of temperatures, however, and Bothun et al. [1989] point out that the dust mass derived from the far-infrared measurements is highly dependent on the dust temperature that is assumed, since $10^2\,\mathrm{M}_\odot$ of warm dust ($T = 50\,\mathrm{K}$) has the same luminosity as $10^5\,\mathrm{M}_\odot$ of cold dust ($T = 20\,\mathrm{K}$). Given this degeneracy, a simple single-component isothermal model should perform equally well, and this is confirmed by Smith et al. [2013]. Kalfountzou et al. [2014] reach the same conclusion when they compare fits using an isothermal model with those using a two-temperature model. The exceptions are where the warm-dust component is better-described by a temperature that is significantly different from the value assumed for the two-temperature model. In these cases the single-temperature model is a better description. An added advantage is that this method allows the work to be compared to a greater number of studies in the literature, as the single-component model is more widely used. Thus, with β fixed and the (single) temperature allowed to vary between 10 and 60 K, the only other free parameter I use in the grey-body fitting code is the normalisation.

I begin by using all of the available far-infrared photometry, that being the fluxes and their errors as measured from PACS and SPIRE maps at 70, 160, 250, 350 and 500 µm (Section 4.2.2). However, if I am to determine the SFR from the far-infrared luminosity (through integration of the fitted spectrum, over 8–1000 µm; Sanders and Mirabel 1996), then I need to be sure that this emission is not contaminated by dust-heating of AGN origin. Such a contribution is a concern for only the 70 µm band as, at $z \sim 1$, this corresponds to 35 µm in the rest frame. Here the AGN is heating its (putative) dusty torus, and this energy is re-radiated in the mid-infrared. As the AGN component of the mid- to far-infrared emission appears to become negligible beyond rest-frame 60 µm [e.g. Hatziminaoglou et al. 2010; Ivison et al. 2010a; Feltre et al. 2014; Leipski et al. 2014], the longer-wavelength bands should be a reliable measure of the cooler dust, heated by star-formation processes. The old stellar population may also contribute to the far-infrared emission, via heating of the dust in the diffuse interstellar medium (ISM). This is naturally less dense than the molecular birth clouds that host newly-forming stars [Charlot and Fall, 2000], and therefore at cooler temperatures with emission at longer wavelengths.

As shown in Figure 5.4, the contribution of mid-infrared emission to the 70 µm flux biases the fit of the far-infrared to high temperatures. Without the constraint imposed by this band, the grey-body spectrum moves to longer wavelengths, where it is better able to describe the photometry (accompanied by a lower χ^2 value). Therefore I continue my fitting of the far-infrared emission using only the 160, 250, 350 and 500 µm data, and demonstrate in Figure 5.5 the improvement that this makes to the resulting χ^2 values. The integrated-FIR luminosities calculated using these four bands are presented in Table 5.2.

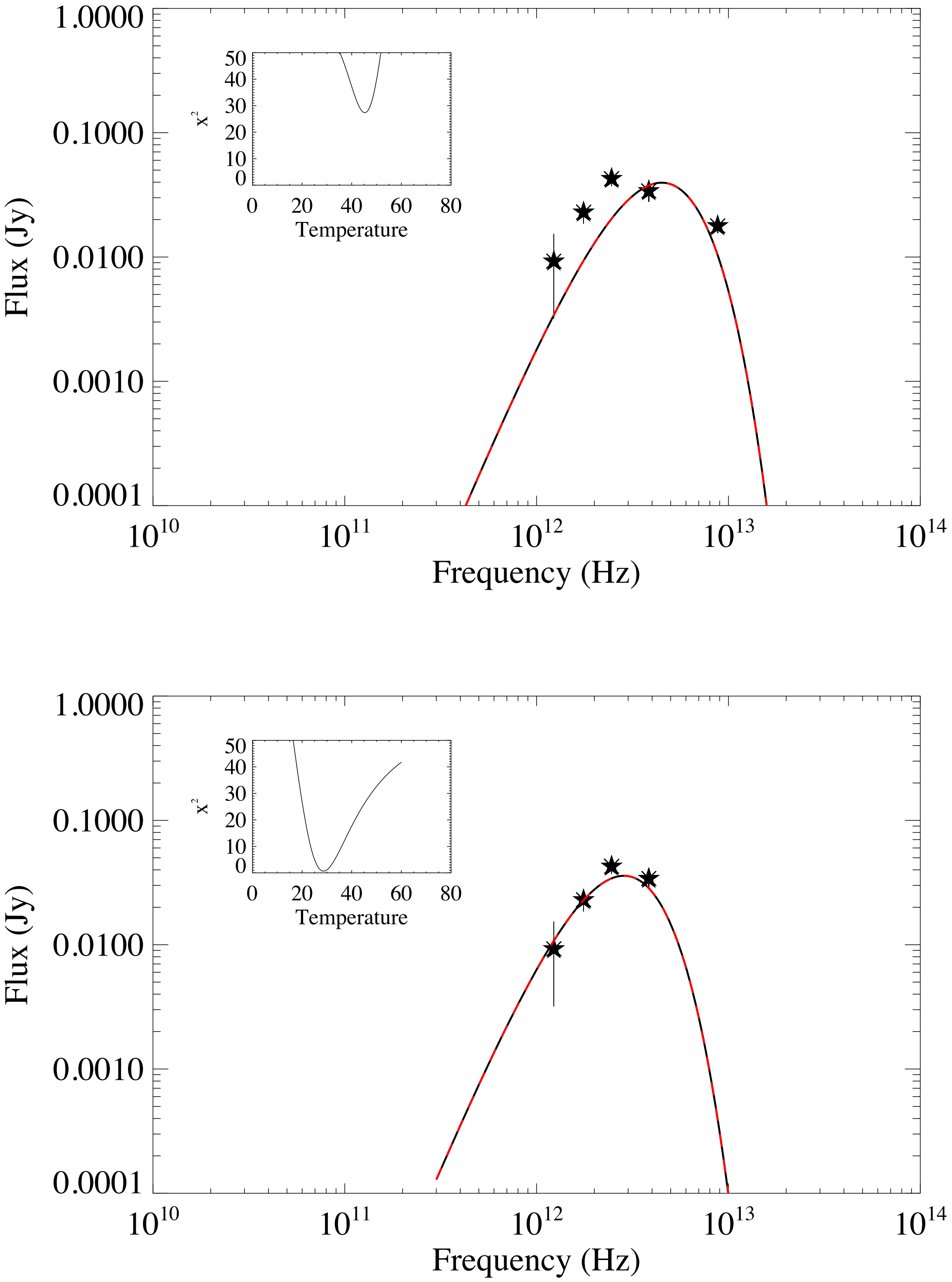

Figure 5.4: An example of fitting the far-infrared emission where all five PACS/SPIRE bands are used (upper plot). When the 70 μm flux is not included (lower plot), there is an improvement in the fit, judged by the lower χ^2 value (inset plot) and better overlap of the grey-body spectrum (curved line) with the photometry (black datapoints).

Table 5.2: Far-infrared measurements, and derived luminosities, for the SHAGS sample of 72 radio-quiet quasars. The confusion limits for the 160, 250, 350 and 500 µm bands are 0.68 [Magnelli et al., 2013], 5.8, 6.3 and 6.8 mJy/beam [Nguyen et al., 2010], respectively. The resolution of the 70 µm band is such that the observations are well above the predicted confusion level of 2.26 µmJy/beam [Lagache et al., 2003]. The integrated-FIR luminosities presented, L_{FIR}, are determined using the measurements at 160, 250, 350 and 500 µm.

R.A. (hms)	Dec. (dms)	S_{70} (mJy)	σ_{70} (mJy)	S_{160} (mJy)	σ_{160} (mJy)	S_{250} (mJy)	σ_{250} (mJy)	S_{350} (mJy)	σ_{350} (mJy)	S_{500} (mJy)	σ_{500} (mJy)	z	L_{FIR} (W)	$L_{125\,\mu\mathrm{m}}$ (W Hz^{-1})
00:31:46.07	+13:46:30.0	2.20	2.63	7.85	4.09	8.45	5.95	3.82	4.98	-0.53	7.38	1.01	6.88e37	2.24e25
02:35:40.90	+00:10:39.2	4.81	2.34	18.20	4.93	6.97	7.01	-5.50	5.70	0.31	9.06	0.95	2.87e38	1.64e25
07:38:02.40	+38:31:16.7	35.02	2.46	64.91	4.67	104.45	6.32	70.82	5.15	32.79	7.39	1.02	6.97e38	2.85e26
07:47:29.04	+43:46:07.7	3.46	2.56	8.21	4.76	-1.70	6.36	10.25	5.11	6.73	6.26	1.09	3.96e37	-5.22e24
07:50:58.32	+42:16:17.0	2.84	2.28	5.62	4.98	3.24	6.45	16.42	4.90	15.45	6.46	0.94	5.69e37	7.44e24
07:52:22.80	+27:38:22.9	20.85	2.65	14.18	5.32	8.92	6.17	1.09	4.97	3.79	7.17	1.06	1.81e38	2.60e25
07:53:39.84	+25:01:37.9	6.87	2.34	11.16	5.18	6.36	8.84	15.31	7.30	3.41	8.58	0.94	7.54e37	1.48e25
08:22:29.76	+44:27:05.4	8.99	2.39	4.73	5.81	0.93	7.02	-7.16	8.04	4.60	8.30	1.06	3.56e37	2.71e24
08:31:15.84	+42:33:16.6	16.87	2.54	48.53	5.45	58.69	5.52	39.14	5.66	10.96	6.96	0.93	3.66e38	1.33e26
08:47:23.52	+01:10:10.3	3.75	2.30	13.86	5.74	17.24	7.69	18.07	5.11	5.80	7.17	1.08	1.53e38	5.25e25
09:01:53.52	+06:59:15.3	7.61	2.49	15.07	4.77	25.98	6.50	31.90	5.55	25.57	7.58	1.08	2.23e38	7.92e25
09:12:16.80	+42:03:14.4	2.82	2.65	14.20	4.67	10.48	6.95	16.83	5.32	-0.70	7.25	1.08	1.32e38	3.17e25
09:22:57.84	+44:46:52.0	12.29	2.74	29.01	5.75	32.54	5.75	33.80	5.36	12.81	7.30	1.08	3.04e38	9.83e25
09:27:53.52	+05:36:36.8	8.83	2.31	21.11	5.67	12.90	7.69	9.53	6.29	16.33	9.04	1.06	1.97e38	3.79e25
09:28:29.76	+50:48:36.4	2.42	2.73	8.72	5.31	-5.27	6.54	5.71	5.22	0.72	7.48	1.03	7.98e37	-1.47e25
09:30:23.28	+40:31:10.9	6.05	2.49	19.05	5.20	21.71	6.58	11.73	5.27	9.06	6.59	1.10	2.08e38	6.80e25
09:33:03.36	+46:04:39.7	6.26	2.33	15.88	4.86	22.10	6.16	19.78	5.43	14.35	7.75	1.09	1.93e38	6.83e25
09:37:59.28	+54:24:27.4	6.48	2.51	19.99	5.29	62.29	6.18	80.68	5.31	70.17	8.41	1.07	4.82e38	1.85e26
09:48:11.76	+55:17:26.5	3.62	3.14	7.10	5.26	14.23	6.01	14.44	5.09	1.56	6.79	1.03	9.40e37	3.97e25
10:07:30.48	+05:09:42.0	13.32	2.19	56.86	5.37	68.67	6.36	40.09	5.40	8.79	5.13	0.92	4.19e38	1.52e26
10:08:35.76	+51:39:27.7	5.60	2.50	12.09	5.13	11.92	5.95	7.95	4.88	8.23	7.01	1.08	1.24e38	3.65e25
10:09:06.24	+02:35:55.4	2.72	2.71	4.24	2.65	21.46	6.24	9.63	4.04	5.42	7.89	1.10	1.11e38	6.76e25
10:20:06.00	+03:33:08.4	8.33	2.70	13.11	5.09	19.08	6.16	19.84	4.98	16.93	6.59	0.94	1.17e38	4.37e25
10:21:11.52	+61:14:15.0	2.94	2.42	5.48	5.05	10.44	6.02	-1.69	5.75	3.01	6.70	0.93	4.73e37	2.37e25

Table 5.2: *continued*

R.A. (hms)	Dec. (dms)	S_{70} (mJy)	σ_{70} (mJy)	S_{160} (mJy)	σ_{160} (mJy)	S_{250} (mJy)	σ_{250} (mJy)	S_{350} (mJy)	σ_{350} (mJy)	S_{500} (mJy)	σ_{500} (mJy)	z	$L_{\rm FIR}$ (W)	$L_{125\,\mu\rm m}$ ($\rm W\,Hz^{-1}$)
10:23:49.44	+52:21:51.1	9.41	5.63	21.14	5.63	42.85	6.52	36.92	5.74	13.39	6.61	0.96	2.31e38	1.02e26
10:33:47.28	+09:40:39.0	13.46	2.71	19.63	5.01	31.29	5.98	25.15	5.21	19.31	7.58	1.03	2.22e38	8.63e25
10:35:24.96	+58:03:35.6	2.78	2.28	11.10	5.12	22.24	5.89	15.64	5.22	6.54	7.17	0.96	1.20e38	5.41e25
10:38:29.76	+58:52:04.1	6.99	2.85	17.26	5.83	32.41	6.17	22.88	5.21	16.10	6.88	0.93	1.68e38	7.41e25
10:38:55.20	+57:58:14.5	4.77	2.49	11.32	5.06	14.15	5.04	12.82	4.88	9.87	7.01	0.96	9.48e37	3.38e25
10:41:14.16	+59:02:19.3	4.17	2.72	5.99	5.44	10.06	5.95	4.77	5.75	2.85	8.24	1.09	7.58e37	3.13e25
10:42:39.60	+58:32:31.2	3.46	2.51	8.95	5.63	14.02	6.16	10.87	5.40	10.09	7.48	1.00	9.33e37	3.65e25
10:43:55.44	+59:30:54.0	4.22	2.38	19.64	5.42	15.55	6.24	13.50	4.18	8.73	7.58	0.91	1.22e38	3.36e25
10:45:37.68	+48:49:14.5	2.20	2.47	18.13	5.46	19.36	5.93	29.38	4.95	12.71	5.95	0.94	1.40e38	4.50e25
10:46:59.28	+57:30:55.8	3.22	2.46	5.43	5.60	5.75	6.84	9.47	5.74	11.47	6.46	1.03	5.18e37	1.58e25
10:48:59.76	+56:56:48.5	6.24	2.99	17.40	5.49	13.01	6.27	25.35	5.09	14.18	6.26	1.01	1.39e38	3.49e25
10:49:30.48	+59:20:32.6	8.92	3.43	12.72	4.65	10.05	6.21	6.16	5.09	4.69	7.38	1.01	1.08e38	2.68e25
10:49:35.76	+55:49:50.5	6.06	2.56	9.72	5.22	14.35	6.24	19.98	5.43	25.09	6.88	1.06	1.24e38	4.17e25
10:54:08.88	+04:26:50.4	9.20	2.14	35.22	5.62	38.59	5.44	34.75	4.78	17.26	6.21	1.08	3.69e38	1.18e26
11:23:17.52	+05:18:03.9	20.88	2.60	16.75	5.01	18.04	6.32	4.87	5.91	2.25	8.24	1.00	1.47e38	4.72e25
11:47:00.24	+62:00:08.3	22.19	2.32	47.16	5.08	68.20	6.85	43.16	5.80	18.97	7.53	1.04	5.00e38	1.93e26
11:50:27.12	+66:58:48.0	11.34	2.37	9.22	4.76	15.84	5.04	13.73	4.18	4.91	5.13	1.04	1.09e38	4.43e25
12:28:32.88	+60:37:35.0	2.48	2.51	6.13	5.84	6.62	5.34	9.46	4.87	5.73	6.88	1.04	5.84e37	1.87e25
12:30:59.76	+10:16:24.6	1.72	2.31	3.94	4.76	18.87	6.32	7.82	6.31	6.15	5.13	1.06	9.44e37	5.49e25
12:57:00.00	+04:27:34.6	53.24	2.51	57.65	5.86	65.53	6.46	42.30	5.40	21.01	7.01	1.03	5.35e38	1.80e26
13:29:57.12	+54:05:06.0	27.86	2.78	19.38	5.11	21.14	6.27	1.71	5.41	3.26	7.00	0.95	1.58e38	4.98e25
13:37:12.96	+61:07:49.1	3.07	2.33	6.44	6.01	7.20	6.54	7.40	5.14	6.86	8.04	0.93	4.80e37	1.62e25
13:37:33.36	+59:06:22.7	16.15	2.23	14.01	6.31	25.71	5.81	22.39	5.00	18.97	6.72	1.09	1.99e38	7.91e25
13:46:35.04	+41:56:30.8	2.53	2.71	34.53	5.87	22.18	5.97	53.14	4.90	24.57	7.89	0.90	1.91e38	4.72e25

Table 5.2: *continued*

R.A. (hms)	Dec. (dms)	S_{70} (mJy)	σ_{70} (mJy)	S_{160} (mJy)	σ_{160} (mJy)	S_{250} (mJy)	σ_{250} (mJy)	S_{350} (mJy)	σ_{350} (mJy)	S_{500} (mJy)	σ_{500} (mJy)	z	L_{FIR} (W)	$L_{125\,\mu\mathrm{m}}$ ($\mathrm{W\,Hz^{-1}}$)
13:58:24.00	+02:13:44.0	8.16	2.49	8.46	5.02	6.67	6.02	-0.39	5.21	-1.09	6.63	0.96	9.03e37	1.60e25
14:21:24.72	+42:30:03.2	9.86	2.43	21.44	5.99	31.63	6.17	38.37	5.02	31.02	7.24	1.00	2.28e38	8.27e25
14:28:17.28	+50:27:12.6	11.72	2.43	10.58	5.46	7.86	6.24	12.87	4.99	3.70	7.71	1.01	8.30e37	2.11e25
14:55:03.36	+01:42:09.2	4.36	2.42	21.94	5.40	40.95	6.08	56.54	5.61	21.51	7.84	1.05	3.18e38	1.18e26
14:55:06.00	+56:29:35.5	9.66	2.76	25.06	5.97	19.20	5.89	24.28	4.99	7.83	5.55	1.04	2.10e38	5.40e25
15:15:20.64	+00:47:39.4	14.47	2.39	36.68	5.46	52.51	6.84	39.97	6.24	25.63	8.90	0.95	3.19e38	1.24e26
15:19:21.84	+53:58:42.2	2.91	2.63	4.91	4.44	2.98	6.50	0.86	5.88	-2.00	6.36	1.03	4.76e37	8.20e24
15:54:36.24	+32:04:08.4	5.58	2.37	11.47	5.87	23.63	6.06	24.20	5.04	13.01	7.59	1.06	1.68e38	6.89e25
15:56:50.40	+39:45:42.8	16.32	2.63	70.04	5.07	70.57	6.21	64.89	5.62	23.46	7.05	0.94	5.16e38	1.64e26
16:32:25.68	+41:18:52.2	6.04	2.63	12.29	5.58	12.62	6.54	16.48	4.88	8.54	7.53	0.91	8.38e37	2.73e25
16:33:06.00	+40:17:47.4	5.10	2.49	9.30	5.69	19.34	5.87	28.82	6.24	15.34	6.21	0.97	1.28e38	4.80e25
16:34:08.64	+33:12:42.1	4.19	2.59	5.39	5.18	11.83	6.36	11.02	5.52	-3.61	6.90	1.01	6.75e37	3.13e25
16:39:30.72	+41:00:13.7	2.67	2.44	8.79	5.71	13.36	6.52	10.93	6.25	3.52	5.95	1.05	9.99e37	3.85e25
16:46:17.28	+36:45:09.7	3.54	2.29	9.45	5.31	19.12	6.23	29.14	4.94	14.10	6.96	0.96	1.22e38	4.59e25
16:52:31.20	+35:36:15.8	4.46	2.46	22.62	5.74	32.60	6.32	26.42	5.74	6.55	7.01	0.93	1.85e38	7.35e25
17:10:05.52	+64:48:42.8	21.71	2.52	65.92	5.41	94.70	6.11	76.58	4.97	46.75	7.21	1.01	6.59e38	2.51e26
17:11:45.60	+60:13:18.5	3.72	2.44	5.45	5.59	8.07	6.32	12.25	6.31	15.06	7.58	0.98	6.16e37	2.03e25
17:13:30.24	+64:42:52.9	17.80	2.25	34.04	6.02	42.70	5.60	22.93	4.39	9.25	6.06	1.05	3.50e38	1.23e26
17:17:04.80	+28:14:00.6	36.59	2.57	44.26	4.02	42.86	7.38	35.24	6.31	25.47	7.24	1.08	4.47e38	1.30e26
17:17:32.88	+59:47:47.4	7.39	2.55	17.06	5.12	27.74	6.24	25.23	5.22	9.22	6.61	1.06	2.09e38	8.12e25
17:21:30.96	+58:44:04.6	2.58	2.57	22.47	5.13	15.31	5.44	15.24	5.02	15.40	6.70	1.00	1.75e38	4.00e25
17:23:10.32	+59:51:05.8	7.41	2.64	22.65	5.29	30.38	6.17	20.15	5.22	12.11	7.01	0.99	2.07e38	7.78e25
21:55:41.76	+12:28:18.8	8.49	2.47	16.42	5.54	15.40	7.34	3.75	6.25	-1.47	7.63	1.06	1.74e38	4.55e25
22:41:59.52	+14:20:55.0	5.88	2.35	9.44	4.95	15.76	5.87	14.30	5.22	8.04	5.80	0.95	9.21e37	3.75e25

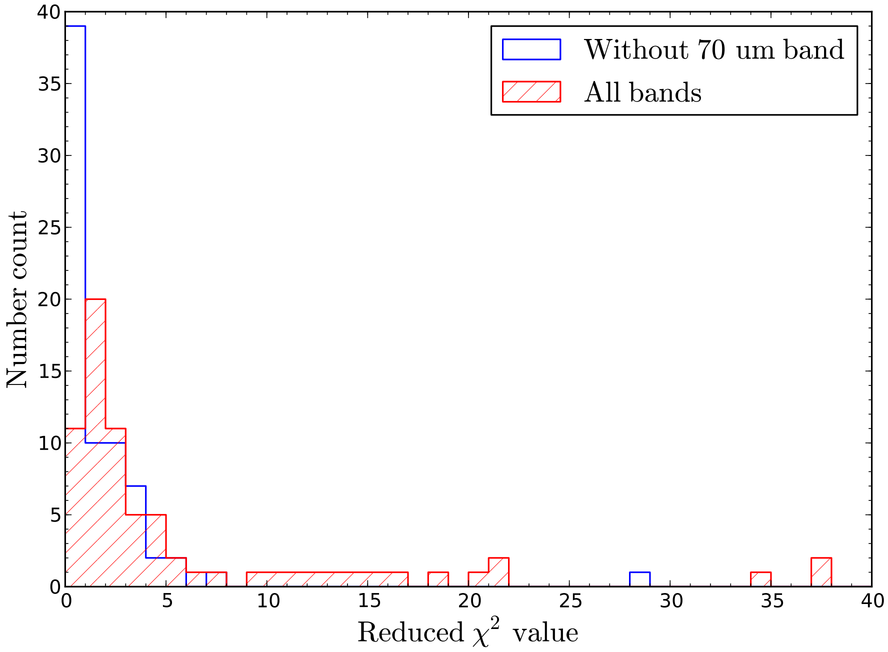

Figure 5.5: The distribution in reduced χ^2 values, with and without the use of the 70 µm band during the fitting of the far-infrared emission (red, hatched histogram and blue histogram, respectively). The outlier at $28 < \chi^2 < 29$ for the blue histogram corresponds to an object for which a single grey-body spectrum is a particularly poor description of the data.

5.2.2 Single-band fitting in the far-infrared

Due to some RQQs not having good detections in each of the 4 PACS/SPIRE bands, I also fit the grey-body constrained by a single band: 250 µm. This band is chosen because, for this sample, it measures the emission close to the grey body's peak, which is expected to be at ~100 µm in the rest frame [Guiderdoni et al., 1998]. Near the peak, any temperature variations lead to a minimal difference in the measured 250 µm flux, and so this can be a good indicator of the bolometric luminosity if the temperatures are similar. Technically the 160 µm band measures flux even closer to the peak, but this is on the shorter-wavelength side of the peak and so is more likely to suffer from AGN contamination. The 250 µm therefore offers the best compromise.

With only one band constraining the fit, the same χ^2 value would be produced by all possible combinations of temperature and normalisation (α), these being the two free parameters. If I fix the temperature to a sensible value, the best fit can be determined by the normalisation alone. To decide the most appropriate temperature to use for the subsequent single-band fitting, I inspect the current distribution for the sample (attained

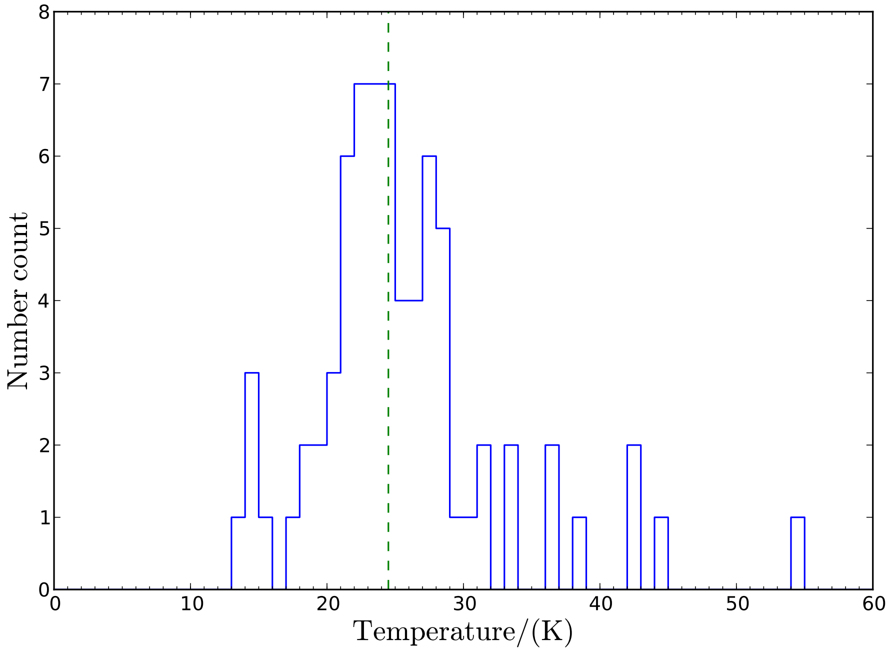

Figure 5.6: The distribution in temperatures when multiple bands (160, 250, 350 and 500 µm) are used to constrain the fit of the far-infrared emission, with emissivity fixed via $\beta = 1.8$. The dashed line indicates the median temperature for the sample, at 24.5 K.

through multi-band fitting, Figure 5.6) and calculate the median temperature. This is 24.5 K. For comparison, Hardcastle et al. [2013] use a fixed temperature of 20 K whilst Smith et al. [2013] find that 23.5 K is the best-fitting global temperature for their sample. This suggests that the temperature of the dust present in this sample is similar to the general low-redshift galaxy population and also obscured radio galaxies. By using the median instead of the mean value, my results are less affected by outliers amongst the RQQs.

5.2.3 Determining the far-infrared luminosity

For both the multi-band and single-fitting cases, the far-infrared luminosity for each RQQ is calculated using the following integral:

$$L_{\mathrm{FIR}} = \frac{4\pi D_L^2}{1+z} \int \alpha Q_\nu B_\nu d\nu, \tag{5.2}$$

where D_L is the luminosity distance, and the integration is done over wavelengths $8 < \lambda/\mu\mathrm{m} < 1000$ [Sanders and Mirabel 1996; Bell 2003].

5.3 Investigating the level of star formation

Regarding the origin of the far-infrared continuum in quasars, Sanders et al. [1989] concluded that the emission over 2–1000 µm was mainly due to re-radiation from a warped disc, heated by the AGN. However today the general consensus agrees with Rowan-Robinson [1995] and Haas et al. [1999], who argued that it is star formation in the quasar hosts that results in the far-infrared emission. To investigate whether star-formation activity is sufficient to explain the total radio emission for my sample, I compare two estimates of the SFR in the subsection below.

5.3.1 Comparison of star-formation rates

As in Section 3.1.4, I calculate one estimate of the SFR directly from the radio luminosity, following the relation of Yun et al. [2001]. This assumes that the total flux in the radio is due to star formation alone. The second SFR estimate comes from the far-infrared luminosity, $L_{\rm FIR}$, as determined in the previous section through fitting a grey-body spectrum to PACS/SPIRE photometry. For this I use Equation 5.3, taken from Kennicutt [1998], which applies to starbursts. This is most relevant for my purposes, as the SFRs in such objects is at a maximum, limited only by the volume of gas that is available. In other words, I am assuming that the conversion of gas into stars is at its most efficient, and so the derived SFR values are themselves upper limits. Bell [2003] suggests a two-power law relation between far-infrared and radio emission, however, this second power-law is only warranted at very low SFRs, which are well below the SFR that could explain any of the radio emission in my RQQ sample.

$$\mathrm{SFR}/(\mathrm{M}_{\odot}\ \mathrm{yr}^{-1}) = 4.5 \times 10^{-44} L_{\rm FIR}/(\mathrm{erg\ s}^{-1}). \tag{5.3}$$

In Figure 5.7 I show the two SFR estimates against one another, for both the multi-band and single-band fitting cases. There are three single-band datapoints that have particularly low SFRs derived from $L_{\rm FIR}$, prompting me to double-check the fitting. Two of them have negative fluxes extracted from the 250 µm maps, whilst the third is forced to a low $L_{\rm FIR}$ on account of the 250 µm flux being significantly lower than for the adjacent bands. Other than these three anomalous points, the results are very similar for the two types of fitting. This provides further support that sampling close to the peak emission provides a good indication of the integrated far-infrared luminosity.

If the total radio emission from the RQQs in the SHAGS sample can be explained entirely by star formation, then the datapoints should lie along a one-to-one relation (dashed lines in Figure 5.7). As seen in Figure 3.7, the majority of the RQQs have values of SFR($L_{1.4\,\mathrm{GHz}}$) that exceed this relation, suggesting that the radio emission is above that expected from star formation alone.

With reference to Figure 3.7, I present the same comparisons of SFR estimates but this time colour-coded by black-hole mass for each of the 72 RQQs in this sample (Figure 5.8). These masses were calculated by Falder et al. [2010], who use the virial-mass estimate technique of McLure and Jarvis [2002] with Mg$\textsc{ii}_{2799}$ broad lines from SDSS DR5 spectroscopy (Section 4.2.1). It may be expected that, because of the larger gas reservoirs associated with more-massive galaxies (and, implicitly, more-massive black holes), the amount of star formation would increase with black-hole mass. However, no such trend is seen between black-hole mass and SFR in Figure 5.8. As a further check, I investigate more directly whether any correlation exists between black-hole mass and SFR in Figure 5.9, and confirm that the two properties are not clearly correlated for these objects. What is apparent, however, is the higher radio-detection rate for higher black-hole masses.

Figures 5.8 and 5.9 illustrate the difficulty of using sample properties to determine how various galaxy-evolution processes interact. One explanation for the lack of correlation between black-hole mass and SFR is that, being from the same epoch at $z \sim 1$, the typical gas density is similar for each of the RQQs, independent of how massive the galaxy is. With larger stellar mass not necessarily being connected to higher SFR, this may seem to contradict the star-formation mass sequence studied by numerous authors [e.g. Noeske et al. 2007; Whitaker et al. 2012; Johnston et al. 2015]. However, note that such a relation is studied with samples of ∼20,000 star-forming galaxies, hence poor number statistics may be behind the lack of an observable trend for this sample of RQQs. This is assuming that the host galaxies of RQQs do behave in the same way as normal star-forming galaxies, as suggested by Rosario et al. [2013]. Another consideration is that a larger black-hole

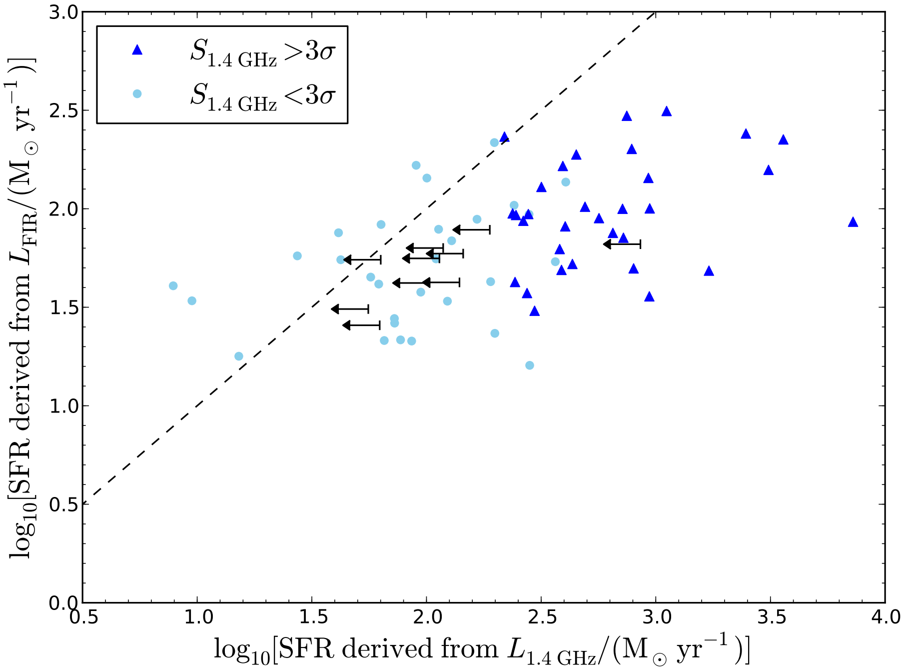

(a) Multi-band fitting in the FIR

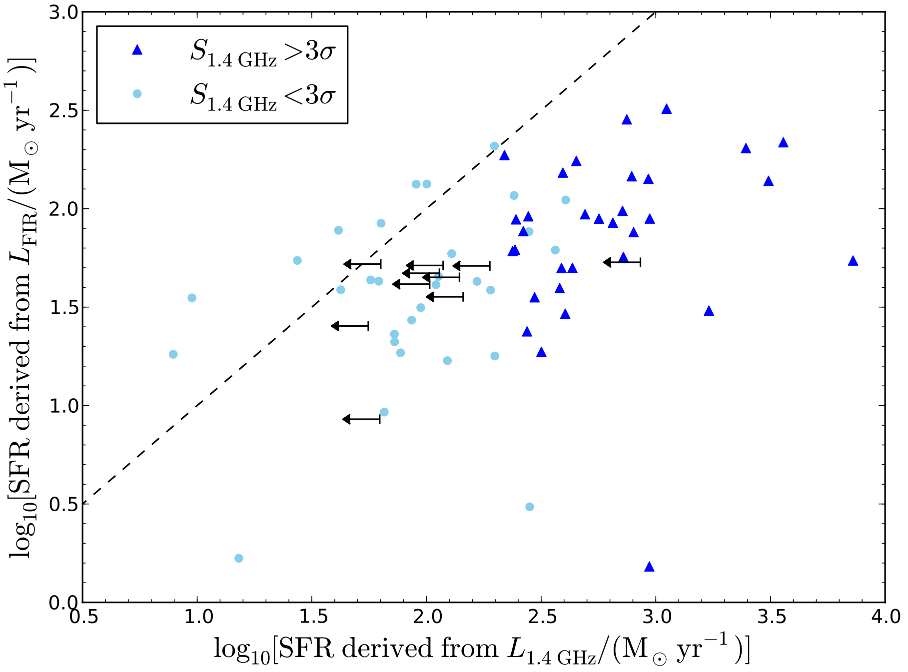

(b) Single-band fitting band in the FIR

Figure 5.7: The SFR calculated from the integrated-FIR luminosity (L_{FIR}, Section 5.2) against the SFR calculated from the extracted radio flux density at 1.4 GHz. L_{FIR} is determined by using either (a) 4 bands to fit the grey-body spectrum, or (b) the 250 µm measurement only. Dark-blue triangles correspond to objects detected with a radio signal-to-noise ratio of over 3 ($S_{1.4\,\mathrm{GHz}} > 3\sigma$), and light-blue circles are those below this detection threshold. Black arrows represent 1-σ upper limits in the radio-derived SFR for quasars having a negative flux density measured from the JVLA images. The dashed line indicates the one-to-one relation, if star formation accounts for all of the radio emission.

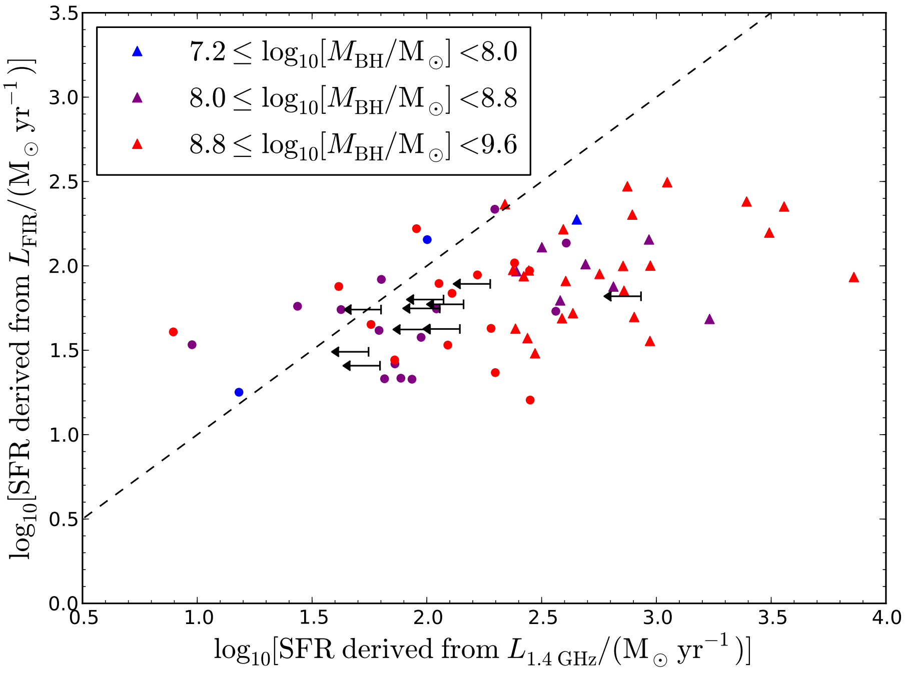

(a) Multi-band fitting in the FIR

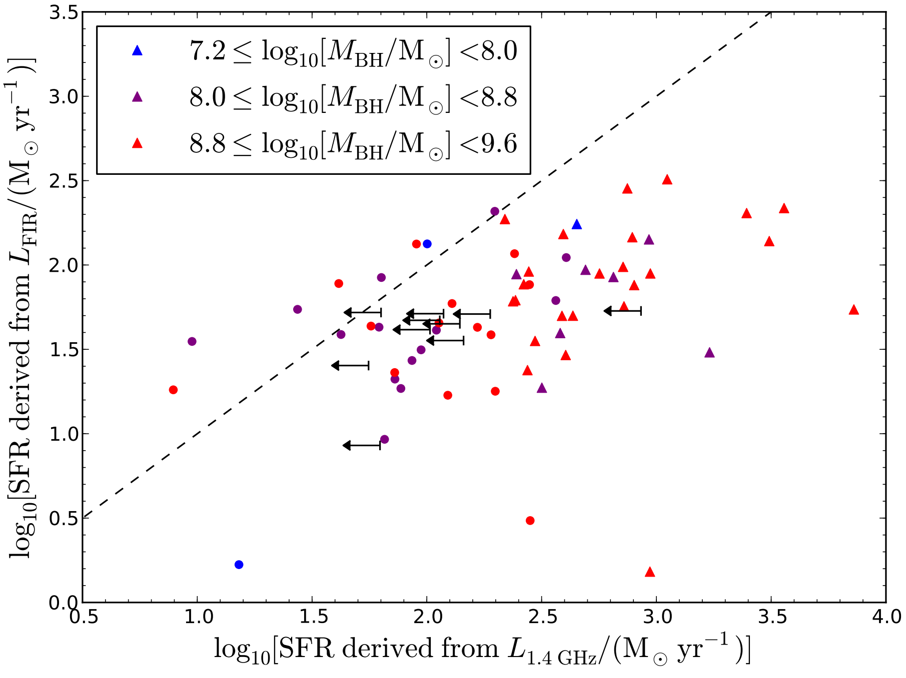

(b) Single-band fitting band in the FIR

Figure 5.8: The same as Figure 5.7 but colour-coded according to the black-hole mass, $M_{\rm BH}$, as shown in the legend. Triangles are still used to represent objects detected with a radio signal-to-noise ratio of over 3 ($S_{1.4\,{\rm GHz}} > 3\sigma$), and circles for those below this detection threshold.

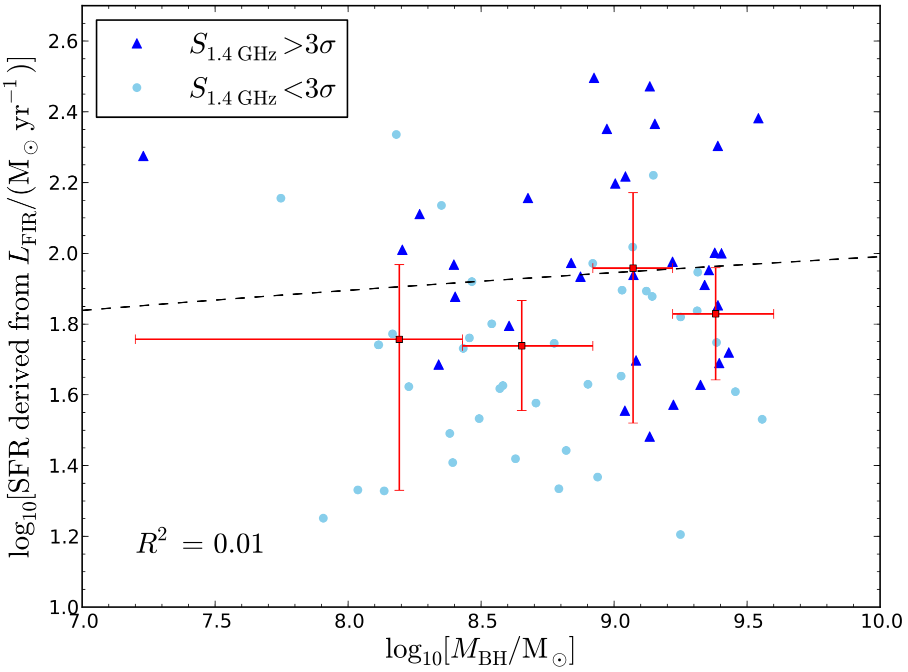

(a) Multi-band fitting in the FIR

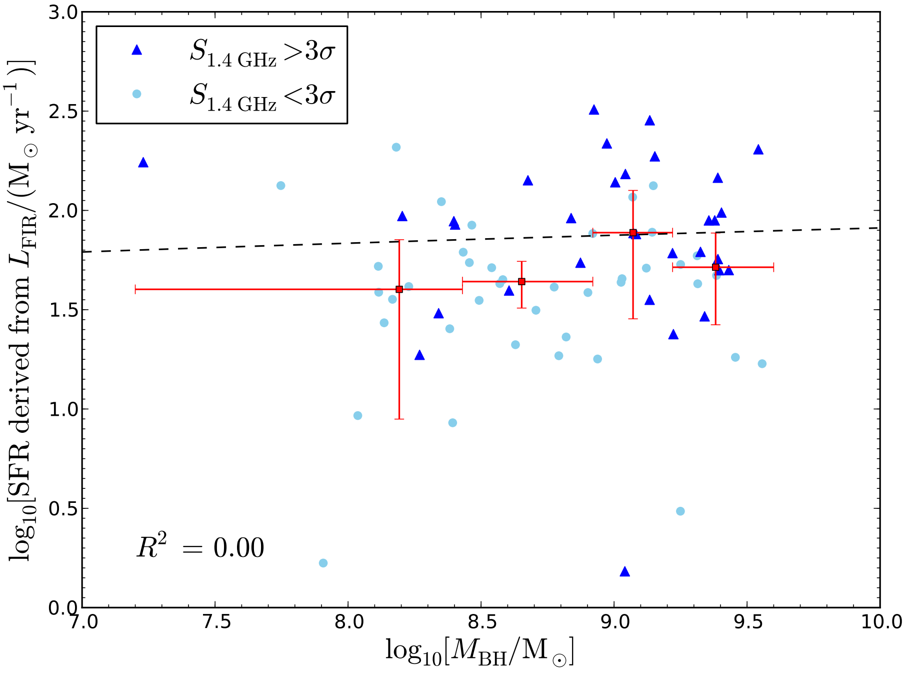

(b) Single-band fitting band in the FIR

Figure 5.9: The SFR calculated from the integrated-FIR luminosity (L_{FIR}, Section 5.2) against the black-hole mass, M_{BH}. L_{FIR} is determined by using either (a) 4 bands to fit the grey-body spectrum, or (b) the 250 µm measurement only. Dark-blue triangles correspond to objects detected with a radio signal-to-noise ratio of over 3 ($S_{1.4\,\mathrm{GHz}} > 3\sigma$), and light-blue circles are those below this detection threshold. The lines of best-fit are given by $\mathrm{SFR}(L_{\mathrm{FIR}}) = 9.62\log_{10}[M_{\mathrm{BH}}] + 1.63$ and $\mathrm{SFR}(L_{\mathrm{FIR}}) = 6.61\log_{10}[M_{\mathrm{BH}}] + 15.5$, and the associated coefficient of determination is shown in the bottom left-hand corner of each plot. Overplotted in red are the median SFRs derived for these objects, binned in M_{BH}. The horizontal error bars indicate the ranges of the M_{BH} bins, and uncertainties on the median SFRs are given by the ordinate error bars.

accretion rate may restrict how much gas is available for star formation, but similarly, star-formation activity may place a limit on the volume of gas that can be accreted [cf. Bouché et al. 2010]. Unfortunately I do not have any CO observations to directly determine the abundance of gas, and so will simply study the relative contributions of star formation and accretion to the total radio emission in Section 5.4.

5.3.2 The far-infrared–radio correlation

Star formation makes a contribution to the total radio emission and, as shown in the previous subsection, can be measured using far-infrared data. Therefore, as part of my analysis of the RQQs in SHAGS, I will use the well-established far-infrared to radio correlation (FIRC, Section 1.4.2). A temperature-dependence in this relation has been identified by Smith et al. [2014], and so I use a measurement of the far-infrared that minimises any bias with respect to temperature. As already explained (Section 5.2.2), for this sample, the 250 µm band meets this criterion and is a reliable tracer of the far-infrared emission. I therefore use this to construct a FIRC that is appropriate for these RQQs. The reason why I do not use the integrated far-infrared luminosity instead is that the relevant FIRCs in the literature, for comparing with, are not determined using objects all at the same redshift. As a result, they are less suitable for extrapolation to my sample.

For $z \sim 1$ objects, 250 µm fluxes provide the monochromatic luminosity at 125 µm in the rest-frame (Equation 5.4). In order to accurately measure the intrinsic emission, it is necessary to apply a luminosity K-correction [Schneider, 2014], the derivation of which is presented below.

$$L_{125} = \frac{4\pi D_L^2 S_{250}}{1+z}. \tag{5.4}$$

Rearranging the above and writing with generalised observed and emitted frequencies, ν and ν', respectively:

$$\begin{aligned} S_\nu &= \frac{(1+z)L_{\nu'}}{4\pi D_L^2} && (5.5)\\ &= \frac{(1+z)L_{\nu'}}{4\pi D_L^2}\frac{L_\nu}{L_\nu} && (5.6)\\ &= \frac{L_\nu}{4\pi D_L^2}\left[\frac{L_{\nu'}}{L_\nu}(1+z)\right]. && (5.7) \end{aligned}$$

Now the contents of the square brackets is the total K-correction that is made, consisting of a bandwidth term, $(1+z)$, and a spectral term, $L_{\nu'}/L_{\nu}$. The latter takes into account the changing shape of the SED, comparing the spectrum at the observed frequency to that at the rest-frame frequency. If I wanted to use the 250 µm flux to get the monochromatic luminosity at 250 µm in the rest-frame, then I would use the entire expression. As I am probing the 125 µm emission directly with the 250 µm band, there is no need for the spectral term, due to the narrow redshift range of the quasars in my sample. The necessary calculation then reverts to Equation 5.4. However, to show consistency between the luminosity K-correction above and the magnitude K-correction (Equation 2.7, repeated as Equation 5.10), I take the logarithm of the contents in square brackets:

$$K(z) \propto \log_{10}\left[1+z\right] + \log_{10}\left[\frac{L_{\nu'}}{L_{\nu}}\right] \tag{5.8}$$

$$= \log_{10}[1+z] + \log_{10}\left[\frac{\int F(\nu')S(\nu)d\nu}{\int F(\nu)S(\nu)d\nu}\right]. \tag{5.9}$$

$$K(z) = 2.5\log_{10}[1+z] + 2.5\log_{10}\left[\frac{\int F(\lambda')S(\lambda)\mathrm{d}\lambda}{\int F(\lambda'/(1+z))S(\lambda)\mathrm{d}\lambda}\right]. \tag{5.10}$$

Since $F(\nu) \propto \lambda^2 F(\lambda)$, Equations 5.9 and 5.10 are equivalent.

Following Smith et al. [2014], I use a dimensionless parameter, q_{λ}, to describe the FIRC (Equation 5.11), where λ is the rest-frame wavelength. Since I use the 250 µm band, and my RQQs are all at $z \sim 1$, the FIRC parameter is as defined in Equation 5.12. The work of Smith et al. [2014] included investigation into the temperature dependence of q_{100} and q_{160} (which use 100 µm and 160 µm, respectively, for Equation 5.11). They present stacked values for these q parameters – their $z < 0.5$ sample binned in dust temperature – and I use the extremes of these values ($q_{160} = 2.4$ and $q_{100} = 2.9$) as a guide for what I can expect my q_{125} values to be. (As the 125 µm rest-frame emission lies between emission at 100 µm and emission at 160 µm, I expect the behaviour of q_{125} to be bounded by the behaviour of q_{100} and q_{160}.) Note that the values 2.4 and 2.9 are read from Fig. 9 of Smith et al. [2014], and I simply use the midpoint value for the definition below:

$$q_{\lambda} = \log_{10}\left[\frac{L_{\lambda}}{L_{1.4\,\mathrm{GHz}}}\right], \tag{5.11}$$

$$q_{125} = \log_{10}\left[\frac{L_{125\,\mu\mathrm{m}}/(\mathrm{W\,Hz^{-1}})}{L_{1.4\,\mathrm{GHz}}/(\mathrm{W\,Hz^{-1}})}\right] = 2.65. \tag{5.12}$$

The positions of the RQQs with respect to the FIRC can be seen in Figure 5.10. Purely star-forming galaxies are expected to lie between the dashed lines, but the majority of the sample are towards the right-hand side of the FIRC. This means that the total radio emission exceeds that expected from star formation. This plot is effectively the same as Figure 5.7 but without the conversion from observable quantities to SFRs. In this plane the interpretation, that accretion-connected radio emission is significant in RQQs, is clear. Hence, I have additional evidence (Section 3.1.4) that this process makes a significant contribution to the radio observations of RQQs, with the current work being complementary to that for the VIDEO sample, having different selection effects and biases. It also benefits from using individual measurements of $L_{125\,\mu\mathrm{m}}$ for each quasar, rather than relying on probability contours derived from assumed black-hole masses and empirical scaling relations.

For comparison, Seymour et al. [2009] find that their stacked values of q_{70} are at least 0.5 dex lower for AGN than for the star-forming galaxies in their sample of sub-mJy radio sources, which extends to $z \sim 3$. This means that there is more radio emission from the AGN, and this excess can be explained by the accretion process. However, note that they use the definition $q_{70} = \log_{10}[S_{70}/S_{1.4\,\mathrm{GHz}}]$, i.e. *observed* rather than rest-frame measurements. Care then needs to be taken as the 70 µm band is subject to emission from AGN heating of the torus, and the degree of this contamination will vary with redshift.

To appreciate the level of the contribution by the accretion process to the total radio luminosity, I use the FIRC ($q_{125} = 2.65$) to calculate the radio luminosity based on the value of $L_{125\,\mu\mathrm{m}}$ for each object. This gives me the radio luminosity expected due to star-formation processes, $L_{1.4\,\mathrm{GHz,\,SF}}$. Subtracting this from the total radio luminosity then determines the radio luminosity that is connected to accretion (Equation 5.13). I do this for all of the RQQs, including those lying to the left-hand side of the solid line in Figure 5.10. Although they are likely to have a negligible contribution from accretion to the radio emission, and (by the definition below) have unphysical values of $L_{1.4\,\mathrm{GHz,\,acc}}$, it

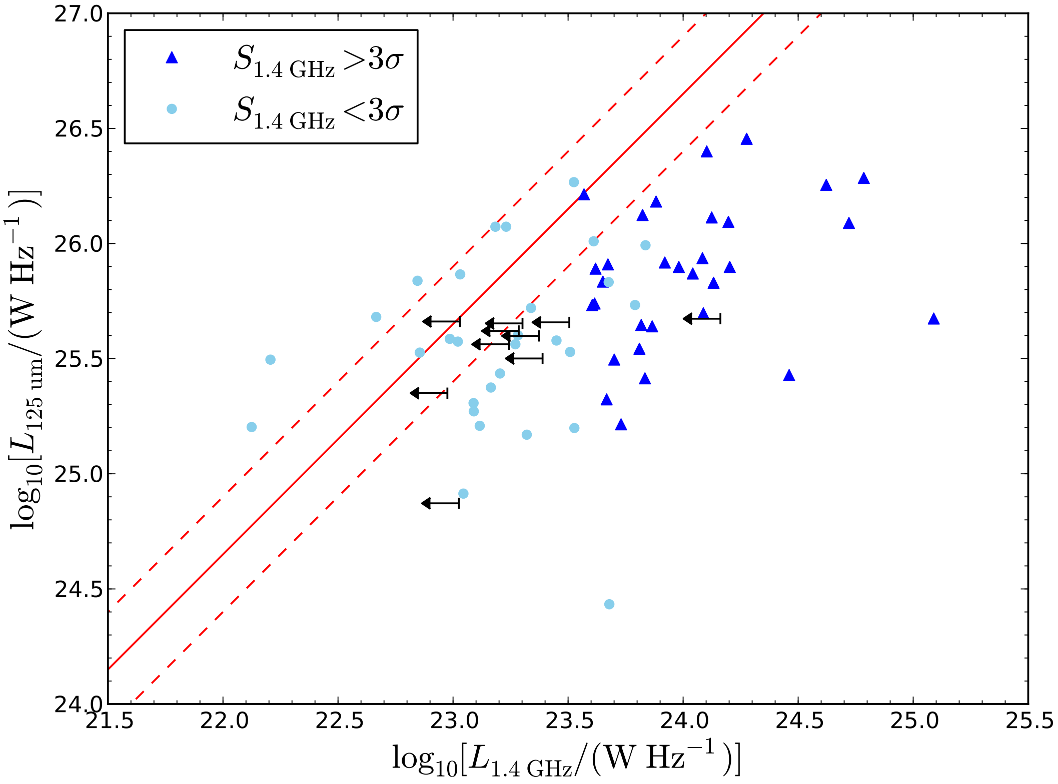

Figure 5.10: The monochromatic luminosity at rest-frame 125 µm, $L_{125\,\mu\mathrm{m}}$, versus the radio luminosity, $L_{1.4\,\mathrm{GHz}}$. Dark-blue triangles correspond to objects detected with a radio signal-to-noise ratio of over 3 ($S_{1.4\,\mathrm{GHz}} > 3\sigma$), and light-blue circles are those below this detection threshold. Black arrows represent 1-σ upper limits in $L_{1.4\,\mathrm{GHz}}$ for quasars having a negative flux density measured from the JVLA images. Note that objects with $\log_{10}[L_{125\,\mu\mathrm{m}}] \lesssim 25.6$ have FIR fluxes that are detected below $3\,\sigma$. The dashed lines are the lower and upper bounds on q_{125}, 2.4 and 2.9, respectively. The solid line corresponds to the midpoint value, $q_{125} = 2.65$ (Equation 5.12).

is statistically correct to use the full sample.

$$L_{1.4\,\mathrm{GHz}} = L_{1.4\,\mathrm{GHz,\,SF}} + L_{1.4\,\mathrm{GHz,\,acc}}. \tag{5.13}$$

I then use these $L_{1.4\,\mathrm{GHz,\,acc}}$ values to calculate what fraction of the sample has AGN-dominated radio emission, and the total accretion-related radio luminosity for all of the objects (Table 5.3). This is repeated using upper-limit radio luminosities and 1-σ detected RQQs, to avoid using negative values of $L_{1.4\,\mathrm{GHz}}$ (derived for 10 sources by virtue of their flux-density measurement). In each of these cases I find that ≥65% of the RQQs have a significant amount of radio emission due to accretion. Moreover, this process accounts for ≥82% of the total radio luminosity, summed across the full sample. Taking this a step further, I separately study the RQQs for which the total radio luminosity is in excess of $q_{125} = 2.15$. This corresponds to lying over $2\,\sigma$ away from the FIRC, where I have approximated the error in q_{125} via the relative positions of the lower and upper bounds ($\Delta q_{125} = 0.25$, see Figure 5.10). For these 31 RQQs, all of which are AGN-dominated and make up 43% of the SHAGS sample, the accretion-related contribution to the total radio emission is at a level of 92%.

For completeness, as several studies in the literature use the integrated far-infrared emission to describe the FIRC [e.g. Murphy 2009; Ivison et al. 2010b], I convert the q_{125} relation into L_{FIR}-$L_{1.4\,\mathrm{GHz}}$ space. To do this I first determine the best-fit line that maps my monochromatic luminosities, $L_{125\,\mu\mathrm{m}}$, onto the correlated far-infrared luminosity, L_{FIR} (upper plot of Figure 5.11). I then apply the same transformation to the lines of constant q_{125} (q_{125}=2.4, 2.65 and 2.9), which leads to the curved lines shown in the lower plot of Figure 5.11. They appear to approach an asymptote at $\log_{10}[L_{\mathrm{FIR}}] = 37.55$, but this is non-physical and just a consequence of the best-fit relation between $L_{125\,\mu\mathrm{m}}$ and L_{FIR} having a non-zero y intercept.

5.4 Trends between radio and optical luminosities

In this section I investigate how star formation and black-hole accretion, quantified by their contribution to the total radio luminosity, correlate with the optical luminosity.

Table 5.3: The accretion-related contribution to the radio luminosity, across the SHAGS sample of RQQs. An object with $L_{1.4\,\mathrm{GHz,\,acc}}/L_{1.4\,\mathrm{GHz}} > 0.6$ is described as being 'AGN-dominated'. 'Summed radio luminosity' refers to the summation of the total radio luminosity for each object ($\Sigma\, L_{1.4\,\mathrm{GHz}}$), and the 'fraction that is accretion-related' is given by $\Sigma\, L_{1.4\,\mathrm{GHz,\,acc}}/\Sigma\, L_{1.4\,\mathrm{GHz}}$.

Description of values used	Number of objects	Fraction that are AGN-dominated	Summed radio luminosity ($\mathrm{W\,Hz^{-1}}$)	Fraction that is accretion-related
Derived values of $L_{1.4\,\mathrm{GHz}}$	72	0.72	5.66e25	0.82
Using upper limits of $L_{1.4\,\mathrm{GHz}}$ for objects with $S_{1.4\,\mathrm{GHz}} < 0$	72	0.65	6.44e25	0.84
Derived values of $L_{1.4\,\mathrm{GHz}}$ for objects with $S_{1.4\,\mathrm{GHz}} > 1\,\sigma$	50	0.78	6.01e25	0.86
Derived values of $L_{1.4\,\mathrm{GHz}}$ for objects right-wards of $q = 2.15$	31	1.00	4.94e25	0.92

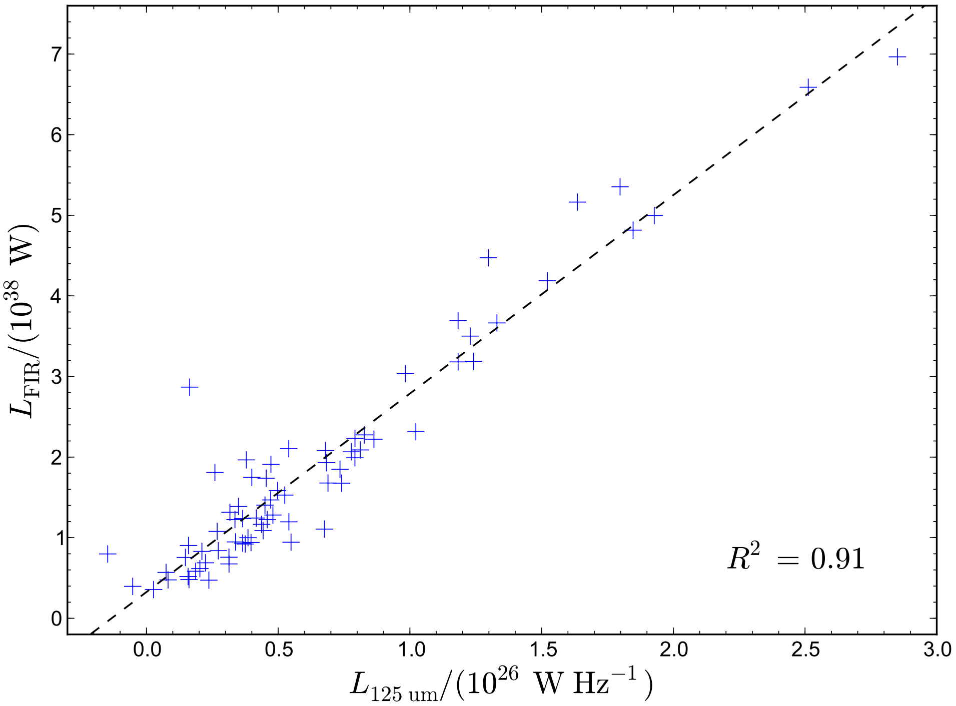

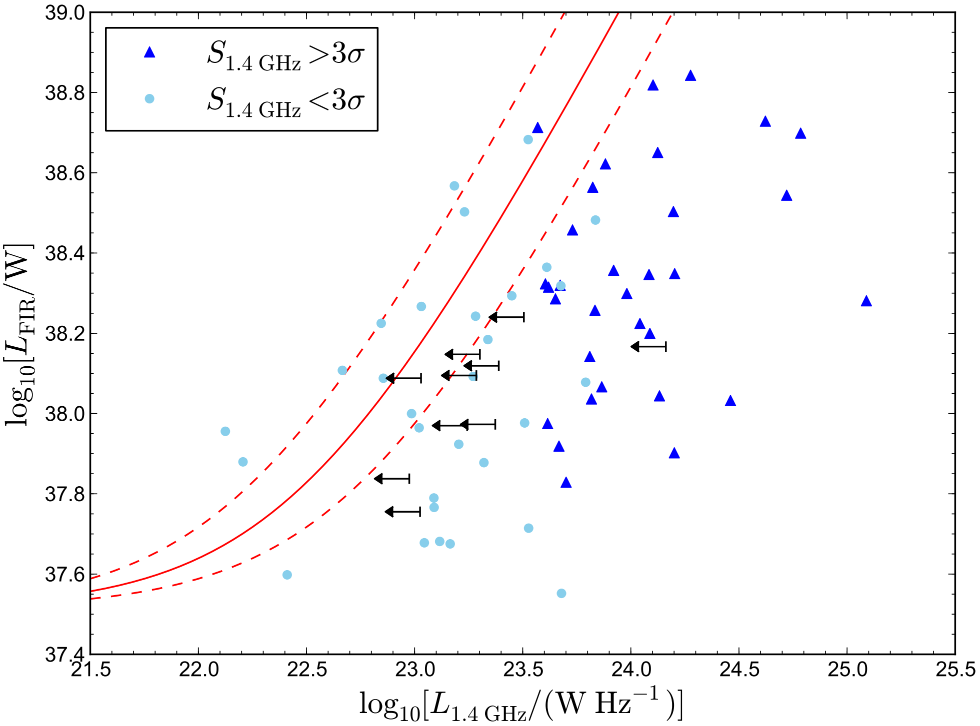

Figure 5.11: The integrated-FIR luminosity, L_{FIR}, using multi-band fitting, against the monochromatic luminosity at rest-frame 125 µm, $L_{125\,\mu\mathrm{m}}$ (upper plot). The coefficient of determination, R^2, is given in the bottom right-hand corner. The line of best-fit, $L_{\mathrm{FIR}} = 2.46 \times 10^{12}\, L_{125\,\mu\mathrm{m}} + 3.26 \times 10^{37}$, is used to convert the lines of constant q_{125} (Figure 5.10) into FIR-luminosity versus radio-luminosity space (lower plot). As before, the solid line corresponds to the midpoint value, $q_{125} = 2.65$. Dark-blue triangles correspond to objects detected with a radio signal-to-noise ratio of over 3 ($S_{1.4\,\mathrm{GHz}} > 3\sigma$), and light-blue circles are those below this detection threshold. Black arrows represent 1-σ upper limits in $L_{1.4\,\mathrm{GHz}}$ for quasars having a negative flux density measured from the JVLA images.

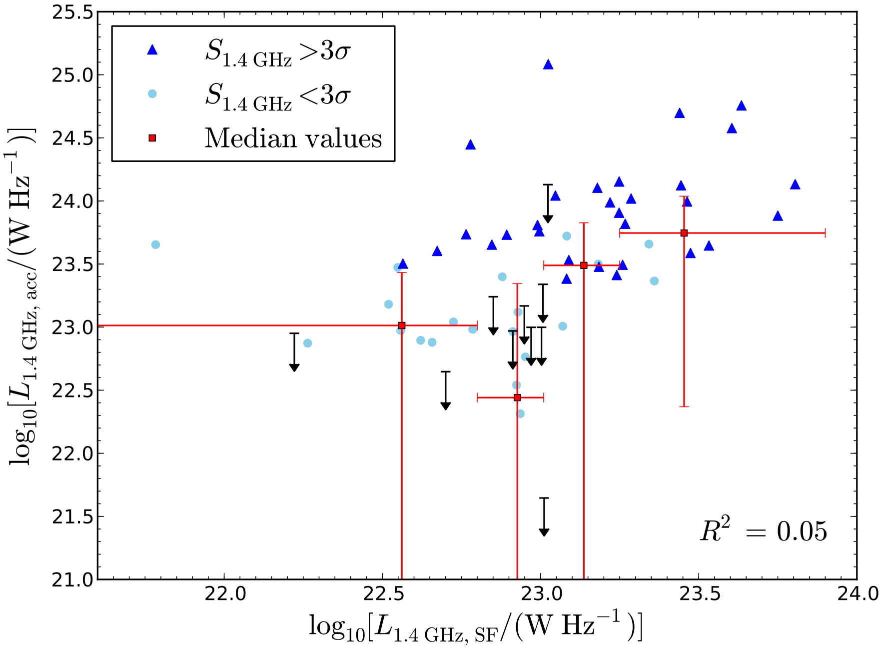

Figure 5.12: The accretion luminosity, $L_{1.4\,\mathrm{GHz,\,acc}}$, against the SF luminosity, $L_{1.4\,\mathrm{GHz,\,SF}}$. Dark-blue triangles correspond to objects detected with a radio signal-to-noise ratio of over 3 ($S_{1.4\,\mathrm{GHz}} > 3\sigma$), and light-blue circles are those below this detection threshold. Black arrows represent 1-σ upper limits in $L_{1.4\,\mathrm{GHz}}$ for quasars having a negative flux density measured from the JVLA images. A linear regression analysis gives the coefficient of determination shown in the bottom right-hand corner. Overplotted in red are the median luminosities derived for these objects, binned in $L_{1.4\,\mathrm{GHz,\,SF}}$. Horizontal error bars indicate the ranges of the $L_{1.4\,\mathrm{GHz,\,SF}}$ bins, and uncertainties on the median accretion luminosities are given by the ordinate error bars.

Firstly, I present the accretion-related radio luminosity against the star formation-related radio luminosity in Figure 5.12. A linear regression analysis gives the coefficient of determination, $R^2 = 0.05$, which indicates that the correlation between accretion and star formation is weak. However, a positive trend can be seen by eye. This suggests that the two processes may be connected via feedback mechanisms, although the correlation could also be explained by a common factor, such as the amount of gas that is available (fuelling both star formation and the AGN).

The star-formation radio luminosity is shown against the absolute i-band magnitude, M_i, in the upper panel of Figure 5.13. Although the correlation appears to be poor, linear regression analysis indicates (via $R^2 = 0.09$) that the trend is in fact stronger than that seen between the *total* radio luminosity and M_i (Figure 5.3). The reason could be that the greater scatter introduced by the accretion-related radio emission, as evident in the lower panel of Figure 5.13, has been removed. The coefficient of determination for $L_{1.4\,\mathrm{GHz,\,acc}}$ against M_i is only $R^2 = 0.01$. As a check, I use an alternative method for calculating $L_{1.4\,\mathrm{GHz,\,SF}}$, and thereby $L_{1.4\,\mathrm{GHz,\,acc}}$. This involves the one-to-one relation shown in Figure 5.7, where the SFR derived from L_{FIR} is used to set $L_{1.4\,\mathrm{GHz,\,SF}}$. The resulting values of $L_{1.4\,\mathrm{GHz,\,acc}}$ are shown in Figure 5.14, and are very similar to those in Figure 5.13.

It is puzzling that these two observables ($L_{1.4\,\mathrm{GHz,\,acc}}$ and M_i) are not more closely correlated, given that it may be expected for both to be directly associated with the accretion disc. A common gas-reservoir can explain the trend between $L_{1.4\,\mathrm{GHz,\,SF}}$ and M_i, since this gas can fuel both star formation and accretion. Therefore, with M_i acting as a proxy for accretion rate, another factor must be at work to explain the scatter in $L_{1.4\,\mathrm{GHz,\,acc}}$. For example, magnetic fields may play a role, leading to radio jets that boost the value of $L_{1.4\,\mathrm{GHz,\,acc}}$ but are too small to be resolved in the JVLA images. Furthermore, the environmental density will dictate how much radio emission results from such jets. The reason is that denser material will interact more strongly with the jet, thus rapidly decelerating electrons and producing more radio emission. This is substantiated by the hydrodynamical numerical modelling of radio-galaxy lobes by Hardcastle and Krause [2013], although their analysis does not take into account radiative losses. They also focus on FRII objects (Section 1.4.1), and simply scaling down the interaction between jets and the environment may be inappropriate for RQQs. Along these lines, Yee and Green [1984] and Falder et al. [2010] find that RQQs occupy less-dense environments compared to their radio-loud counterparts. In addition, regarding Figure 5.14, note that the faintest M_i bin contains numerous objects with negative radio flux-densities, and so the median $L_{1.4\,\mathrm{GHz,\,acc}}$ value is itself negative. With deeper radio data the detection rate should improve, allowing for better investigation into trends between the radio and the optical at the faint end.

Next I calculate $L_{1.4\,\mathrm{GHz,\,SF}}/L_{1.4\,\mathrm{GHz,\,acc}}$, and study how this varies with M_i (Figure 5.15). This ratio gives the relative contributions of the star-formation and accretion processes to the total emission. No trend can be seen with optical luminosity, although it is interesting that the brightest bin in M_i is the one that contains the greatest proportion of $3\,\sigma$-detected RQQs. In order for the quasars to be this optically-bright it is

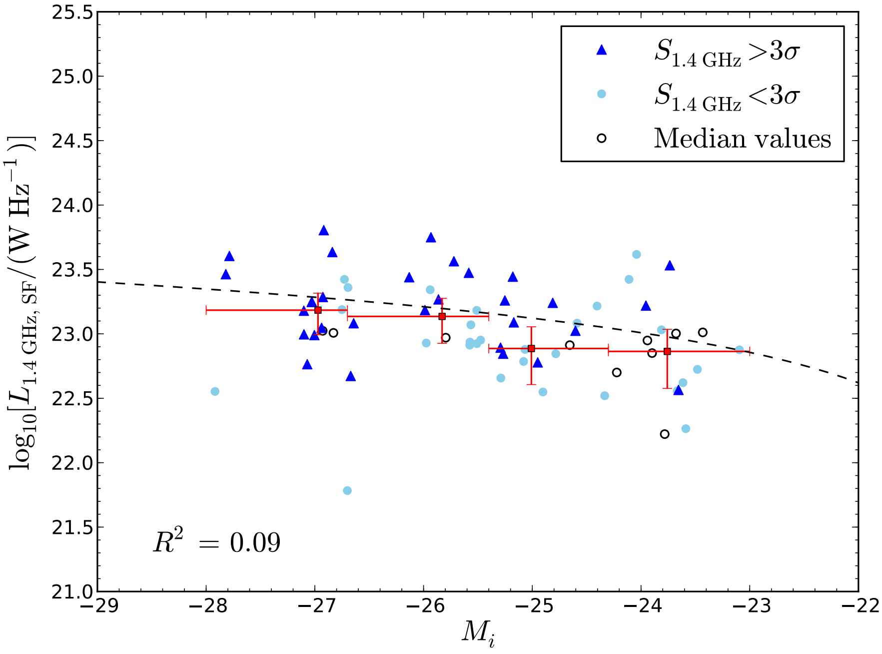

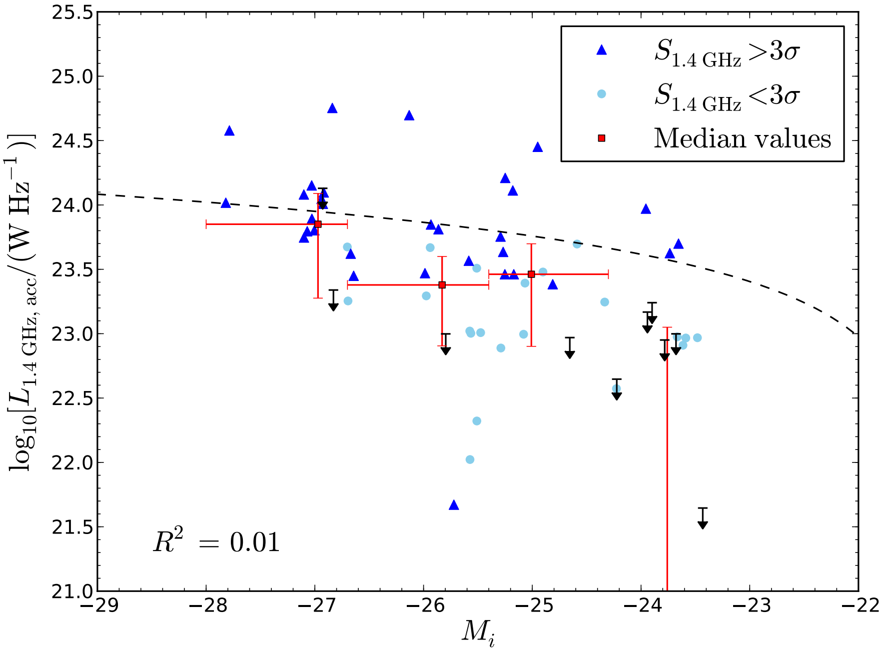

Figure 5.13: The SF luminosity, $L_{1.4\,\mathrm{GHz,\,SF}}$ (upper plot), and the accretion luminosity, $L_{1.4\,\mathrm{GHz,\,acc}}$ (lower plot), against the absolute i-band magnitude, M_i. Dark-blue triangles correspond to objects detected with a radio signal-to-noise ratio of over 3 ($S_{1.4\,\mathrm{GHz}} > 3\sigma$), and light-blue circles are those below this detection threshold. Quasars having a negative flux density measured from the JVLA images are represented by black circles in the upper plot, and by 1-σ upper-limit arrows in the lower plot. The lines of best-fit are given by $L_{1.4\,\mathrm{GHz,\,SF}} = -3.02 \times 10^{22} M_i - 6.23 \times 10^{23}$ and $L_{1.4\,\mathrm{GHz,\,acc}} = -1.60 \times 10^{23} M_i - 3.42 \times 10^{24}$, and the associated coefficient of determination is shown in the bottom left-hand corner of each plot. Overplotted in red are the median luminosities derived for these objects, binned in M_i. The horizontal error bars indicate the ranges of the M_i bins (Table 5.1), and uncertainties on the median radio luminosities are given by the ordinate error bars.

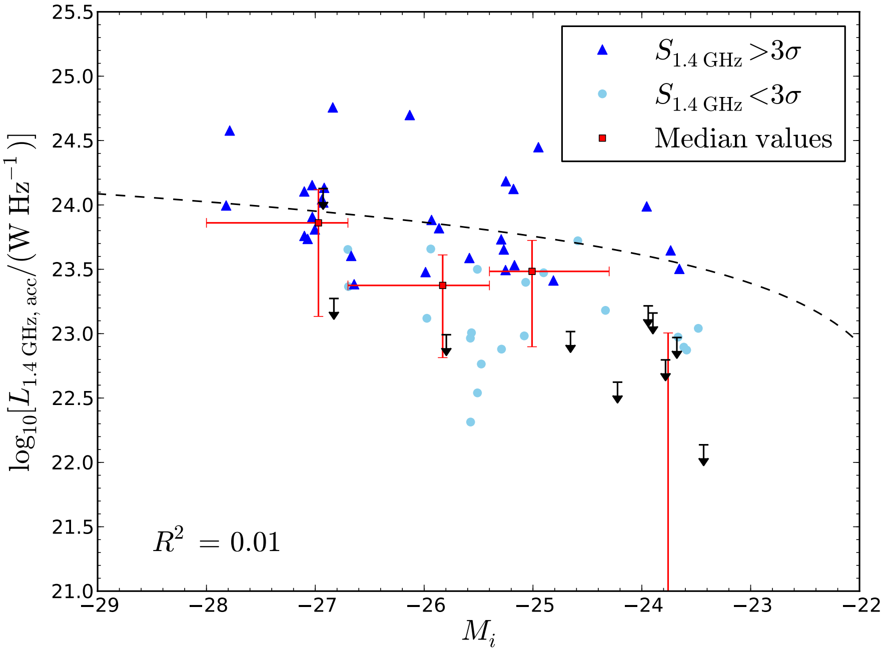

Figure 5.14: The accretion luminosity, $L_{1.4\,\mathrm{GHz,\,acc}}$ (calculated via an alternative method to that for Figure 5.13, see text), against the absolute i-band magnitude, M_i. Dark-blue triangles correspond to objects detected with a radio signal-to-noise ratio of over 3 ($S_{1.4\,\mathrm{GHz}} > 3\sigma$), and light-blue circles are those below this detection threshold. Black arrows represent 1-σ upper limits in $L_{1.4\,\mathrm{GHz}}$ for quasars having a negative flux density measured from the JVLA images. The line of best-fit is given by $L_{1.4\,\mathrm{GHz,\,acc}} = -1.62 \times 10^{23} M_i - 3.49 \times 10^{24}$, and the associated coefficient of determination is shown in the bottom left-hand corner. Overplotted in red are the median luminosities derived for these objects, binned in M_i. The horizontal error bars indicate the ranges of the M_i bins (Table 5.1), and uncertainties on the median radio luminosities are given by the ordinate error bars.

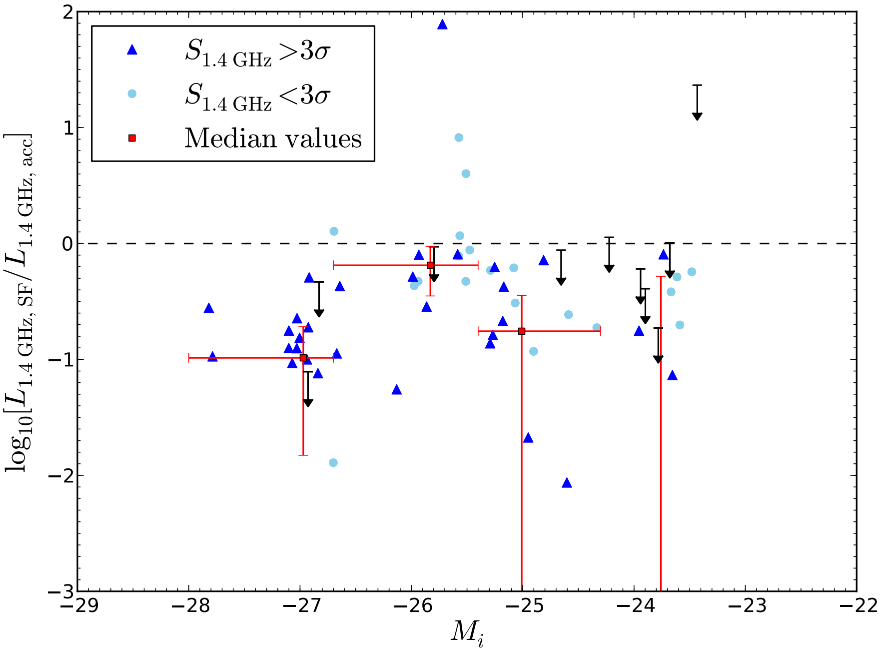

Figure 5.15: The ratio of the SF-related radio luminosity, $L_{1.4\,\mathrm{GHz,\,SF}}$, to the accretion-related radio luminosity, $L_{1.4\,\mathrm{GHz,\,acc}}$, as a function of the absolute i-band magnitude, M_i. Dark-blue triangles correspond to objects detected with a radio signal-to-noise ratio of over 3 ($S_{1.4\,\mathrm{GHz}} > 3\sigma$), and light-blue circles are those below this detection threshold. Quasars having a negative flux density measured from the JVLA images are represented by 1-σ upper-limit arrows. The dashed line is to guide the eye where $L_{1.4\,\mathrm{GHz,\,SF}} = L_{1.4\,\mathrm{GHz,\,acc}}$. Overplotted in red are the median ratios for these objects, binned in M_i. The horizontal error bars indicate the ranges of the M_i bins (Table 5.1), and uncertainties on the median ratios are given by the ordinate error bars.

necessary for them to be accreting efficiently, since this leads to greater thermal emission from the accretion disc, which dominates the i band. Also associated with higher accretion rates is the larger amount of electrons being accelerated by magnetic fields in the disc and around the black hole. This produces synchrotron emission, resulting in higher values of $L_{1.4\,\mathrm{GHz,\,acc}}$. It is therefore reasonable to suggest that the median ratio of $L_{1.4\,\mathrm{GHz,\,SF}}/L_{1.4\,\mathrm{GHz,\,acc}}$ in this bin is lower than the others because some mechanism is leading to more-efficient accretion. Also, if accretion efficiency *is* larger, then (depending on the exact location of the gas with respect to the black hole and the host galaxy) star formation will be suppressed due to a lack of fuel. This could be further compounded by the thermal energy from the accreting black hole, preventing gas from cooling enough to collapse and form stars.

5.5 Conclusions

Using a sample selected over a single epoch ($0.9 < z < 1.1$) and spanning two orders of magnitude in optical luminosity, I investigate the star-formation and accretion properties of RQQs in the *Spitzer-Herschel* Active Galaxy Survey (SHAGS). The narrow redshift range allows any evolutionary effects to be decoupled from my findings, breaking the degeneracy between luminosity and redshift that is inherent in most samples. Previous studies that used the same sample needed to invoke stacking analyses, as the radio data was not of sufficient sensitivity. The current work uses new JVLA images, whose reduction is described in the previous chapter, to uncover the following results:

1. 32 of the 72 objects are detected a 3-σ level in the 1.4 GHz radio images, with the median flux-density for the whole sample determined to be 86.1 ± 73.3 μJy/beam.

2. A Kolmogorov–Smirnov (KS) test between the quasar sample and fluxes extracted at random positions leads to a p-value of 10^{-21}, confirming that they are drawn from distinct populations, as indicated by the significant positive tail in the flux-density distribution. This means that the quasars have a statistical detection of radio emission.

3. The sample is binned in absolute i-band magnitude, M_i, and additional KS tests are performed to compare the radio flux-density distribution of the quasars with that of random positions for each bin. For the three brightest bins there is evidence at the $\gg$99.99% confidence level for excess radio emission from the quasars. However for the faintest bin, the confidence level falls to 99.0%. Even deeper radio data is required to properly investigate the properties of these quasars.

4. A linear regression analysis between the radio luminosity and M_i indicates that correlation between the two is poor, although a weak trend can be seen by eye, with the optically-bright quasars having the highest radio luminosities.

5. Far-infrared luminosities are used to estimate individual star-formation rates (SFRs) for the quasars, which are then compared against SFRs derived from the radio luminosity. The latter are based on the assumption that all of the radio emission is a consequence of star-formation processes.

6. The inclusion of black-hole masses in the analysis indicates that quasars harbouring more-massive black holes do not necessarily have higher SFRs. This may be expected from more-massive black holes residing in galaxies with larger stellar mass, which in turn are more likely to host larger reservoirs of gas. One explanation for the lack of correlation is the role of AGN feedback, with star formation being suppressed as a result of accretion-related heating of the gas. Another is simply that black-hole mass and SFR are not related.

7. The monochromatic luminosity at rest-frame 125 µm, $L_{125\,\mu\mathrm{m}}$, is a reliable tracer of the far-infrared emission for this sample. It is therefore used to describe the far-infrared to radio correlation (FIRC), via the dimensionless parameter q_{125}. As was found for the VIDEO sample (Section 3.1.4), emission from star formation alone cannot explain the total radio emission for the majority of RQQs, suggesting that accretion still makes an important contribution.

8. Exploiting the FIRC, I divide the total radio emission ($L_{1.4\,\mathrm{GHz}}$) into its constituent components: that related to star formation, $L_{1.4\,\mathrm{GHz,\,SF}}$, and that related to accretion, $L_{1.4\,\mathrm{GHz,\,acc}}$. The latter is used to quantify the contribution of the AGN to the

total radio luminosity. Given a 1-σ detection level in the radio, 78% of the RQQs are AGN-dominated (having $L_{1.4\,\mathrm{GHz,\,acc}} > 0.6\,L_{1.4\,\mathrm{GHz}}$), and the accretion process accounts for 86% of the radio luminosity when summed across the objects. This proportion increases to 92% for objects lying over $2\,\sigma$ away from the FIRC.

9. The radio emission connected with star formation is found to vary with M_i, which could be explained by the common reservoir of gas, although regression analysis indicates that the trend is a weak one. Meanwhile, $L_{1.4\,\mathrm{GHz,\,acc}}$ shows large scatter when plotted against M_i, and no trend with optical luminosity is observed for the relative contribution of the two processes ($L_{1.4\,\mathrm{GHz,\,SF}}/L_{1.4\,\mathrm{GHz,\,acc}}$). Deeper radio data, a larger sample size, and additional multi-wavelength data may help to disentangle the various feedback mechanisms at work, if they are indeed playing a significant role. It is unclear whether this would strengthen or dilute the trends currently observed.

6

Summary and future work

“Even the smallest person can change the course of the future”

– Galadriel, *The Lord of the Rings: The Fellowship of the Ring*

6.1 Summary

Black-hole accretion and star formation are crucial to galaxy evolution, with several studies citing their interaction as the reason for the suggested co-evolution of black-hole mass with bulge mass [Croton et al., 2006; Silk and Mamon, 2012]. Another indication that the two processes are connected is that they both peak in activity over the epoch $z \sim 1$–3 [Madau et al., 1996; Ueda et al., 2003]. However, recent work [e.g. Rosario et al. 2012; Feltre et al. 2014] suggests that there is actually little dependence of SFR on the luminosity of the AGN. In addition, the impact of AGN feedback is dependent on the environment, with the possibility of triggered star formation occurring on nuclear [Davies et al., 2006], galactic [Ishibashi and Fabian, 2012], and intracluster [Croft et al., 2006] scales. Other sources of feedback include supernovae, which expel material that may otherwise accrete onto the central black hole. The remnants left behind by supernovae in star-forming regions accelerate relativistic electrons, resulting in synchrotron radiation that emits at radio frequencies. Therefore, since accretion also produces synchrotron emission, radio observations can provide an unbiased view of both AGN and star-forming populations.

As part of disentangling accretion and star-formation processes, we need to develop a better understanding of how the various populations contribute to the total radio emission. This is particularly important at low radio luminosities, where the relative proportions of star-forming galaxies and RQQs is debated. Kimball et al. [2011] and Condon et al.

[2012] suggest that the radio emission from RQQs is dominated by star formation, whilst Simpson et al. [2006], Smolčić et al. [2008] and Wilman et al. [2008] show that RQQs are making an important contribution in the sub-mJy regime. However, the level of star formation that occurs *within* RQQs is not very well understood.

To investigate further, I examine the origin of the radio emission in a sample of 74 RQQs, selected using the VIDEO Survey (Chapter 2). Using VLA imaging to study their faint radio emission, I find evidence that it is predominantly accretion-powered rather than due to star formation (Chapter 3). This is through a comparison of two independent estimates of the SFR, one based on the radio flux-density and the other on the stellar mass of the host galaxy. Additional evidence comes from comparing the radio flux-density distribution of the RQQs to that of control samples of galaxies, matched in both redshift and stellar mass.

In an extension of the work done by Condon et al. [2013], I carry out an improved stacking analysis by properly accounting for the varying noise level in the radio data, and using deeper data that allows me to probe lower black-hole masses and/or accretion rates. I find very good agreement between source counts derived using this technique and the number of RQQs predicted by Wilman et al. [2008], and demonstrate that a power-law function is an inadequate description for AGN at low radio luminosities. Instead, a power-law plus Gaussian model enables the behaviour in the number counts (notably the 'bump' below 1 mJy, Figure 1.14) to be reproduced.

I then carry out a similar analysis (with regard to a comparison of SFRs) for another sample of RQQs, previously constructed as part of the *Spitzer-Herschel* Active Galaxy Survey (SHAGS). For these I have reduced new JVLA data (Chapter 4), leading to a $\geq$3-σ detection for 32 of the 72 objects. Again I calculate the SFR based on the radio luminosity, but this time use far-infrared luminosities (from photometric fitting of *Herschel* data) to obtain an alternative SFR estimate. As before, the majority of the sample have excess radio emission that cannot be accounted for by star formation alone, thus indicating that emission from an AGN is making an important contribution (Chapter 5). The same conclusion is drawn when I use the appropriate FIRC for this sample, defined via the ratio of the luminosity at rest-frame 125 μm to that at 1.4 GHz. Using this relation I am able to demonstrate that the bulk of the radio emission originates from the AGN.

For both samples of RQQs I also investigate whether there is a correlation between the radio luminosity and the optical luminosity. Such a trend would be expected for objects in which accretion dominates the radio emission, as this process also manifests itself via thermal emission from the accretion disc in the i band. In the case of the quasars selected using VIDEO, there is good evidence of a correlation between the two properties, which is hypothesised to be largely redshift-driven. This is then tested using the complementary SHAGS sample, where the RQQs span a narrow redshift range ($0.9 < z < 1.1$), allowing the degeneracy with possible evolutionary and K-correction effects to be broken. I find that there is only a weak trend between radio luminosity and optical luminosity for the $z \sim 1$ quasars, confirming the influence of redshift-dependence for the VIDEO sample. Next I use the FIRC to calculate the radio luminosity due to star formation and that due to accretion for the SHAGS sample. The former shows a weak correlation with optical luminosity, possibly explained by the common gas-reservoir that fuels both star formation and the AGN. Blandford and Payne [1982] and Reynolds et al. [2006] argue for the power of radio jets to scale with accretion rate, given that the accretion of magnetic flux onto the black hole may factor into whether or not a radio jet is produced. However, no trend is seen between the accretion-connected radio-luminosity and the optical luminosity for these RQQs. I suggest that this could be due to the magnetic field in or surrounding the accretion disc to not be of sufficient strength to produce a large amount of synchrotron radiation, and not simply related to the accretion rate. This points towards a different mechanism, to that in radio-loud quasars, producing radio emission.

Through the work described in this thesis I have shown that, for the RQQ population, the bulk of the emission below 1 mJy (at 1.4 GHz) emanates from the AGN, in contention with current ideas that it is star-formation dominated. Although such emission may be in the form of jets [e.g. Blundell and Rawlings, 2001], it is possible that synchrotron radiation from shock fronts, associated with outflows driven by the quasar, is also contributing to the total radio emission [Zakamska and Greene, 2014]. In addition, I have found evidence that the level of star formation is only weakly correlated with the level of accretion. This could be due to the different timescales associated with AGN activity and star formation, leading to a delay between the two [Wild et al., 2010] that may be particularly pronounced for radio-quiet objects.

Furthermore, the latter result is in contrast with radio-loud quasars, which exhibit a stronger correlation [Kalfountzou et al., 2012, 2014] that could be brought about by the compression of molecular clouds by radio jets [e.g. Croft et al., 2006]. The reason for the coupling between AGN activity and star formation being weaker in RQQs may (again) be due to these objects having a different accretion mechanism to that in radio-loud quasars. Although jets may still be present, AGN-related feedback could instead be dominated by disc winds from the outermost regions of the accretion disc [as observed in microquasars, e.g. Blundell et al. 2001]. Alternatively, Laor and Behar [2008] suggest that synchrotron emission in RQQs could be due to magnetic reconnection events accelerating electrons in the corona above the disc.

6.2 Future work

Galaxy evolution studies will benefit from even deeper radio data, leading to larger sample sizes of individually-detected objects. The combination with deep multi-wavelength is also needed, enabling the radio emission to be separated accurately into accretion-connected and star formation-connected components. In this section I describe what further work can be done, based on the investigations outlined above, and highlight related gaps in our understanding that require further research.

6.2.1 The obscured population

A limitation of many AGN studies reliant on optical data, such as the quasar luminosity function of Croom et al. [2009], is that the obscured population is not well-accounted for. Using X-ray data, Gilli et al. [2007] suggest that the obscured fraction is as high as 80%, accompanied by an anticorrelation with bolometric luminosity [Treister et al., 2008]. Their inclusion, therefore, will teach us more about the quasar population as a whole, including what underlying physics govern the different accretion modes that are observed. Furthermore, by investigating the way in which obscuration varies with redshift, it may be possible to discern orientation effects from evolutionary effects that are due to the quasar expelling its dusty envelope [Hopkins et al., 2008].

Re-radiation from the torus emits in the mid-infrared and so, following Lacy et al. [2004] and Stern et al. [2005], I could use mid-infrared criteria to reliably select both obscured and unobscured AGN. This selection is orientation independent [Martínez-Sansigre et al., 2006], and I would need optical/near-infrared imaging or spectroscopy to classify the objects as Type 1 or Type 2 (Section 1.2). I would then use the radio emission to see if there is an excess from the obscured population, as may be expected from the evolution scenario. Following on from this, I could instead select for star-forming objects using a far-infrared selection, which is also orientation independent with regard to the AGN. As before, I would use optical/near-infrared data to distinguish between Type-1 and Type-2 AGN, and then investigate whether I find excess radio emission from the obscured population. However, a key element for such studies is matching the obscured and unobscured populations in redshift and bolometric luminosity, which is difficult without full SEDs.

Furthermore, while creating my sample of quasars from the VIDEO survey (Chapter 2), I noticed several objects that didn't satisfy the gJK selection cuts but did lie within the Stern and Lacy wedges (Figure 2.4). Many of them are fitted by LE PHARE's 'torus' quasar template [Polletta et al., 2006], and it would be interesting to investigate their radio properties, in terms of the contributions made by accretion and star formation to the total radio emission. Recent studies [e.g. Chen et al., 2015] suggest that the SFRs in obscured quasars are higher than in their unobscured counterparts, but care must be taken due to possible contamination from the AGN.

6.2.2 Extension of luminosity functions

In order to better constrain how various populations contribute to the total radio source counts [e.g. Wilman et al., 2008], we need to probe to lower radio luminosities. From these measurements, luminosity functions can be constructed, allowing the evolution of RQQs to be studied.

The lower limit of a radio luminosity function is naturally limited by the depth of the observations, although stacking analyses enable sources below this threshold to be extracted. The simplest method is to overlay multiple images to increase the SNR, but this discards information about the individual sources and gives only a single, mean measurement. In Chapter 3 I employed a more-advanced analysis, in that I used the individual measurements (whether detected above the rms noise or not) to model the flux-density distribution of the RQQs. However, information is still lost via the binning process. Mitchell-Wynne et al. [2014] improve upon this by using a maximum-likelihood method to model the flux-density distribution, whilst Zwart et al. [2015] extend the analysis to a Bayesian framework, where model selection is implemented based on the Bayesian evidence. The resulting number counts, in terms of flux, can then be converted into a radio-luminosity function, ideal for specific populations identified at other wavelengths. I could take this a step further by modelling the luminosity function itself, generating a catalogue of simulated flux-densities from this, and then using the methods of Mitchell-Wynne et al. [2014] and Zwart et al. [2015] to determine whether the original luminosity function is reproduced. This study could also include the redshift dependence of the luminosity function by incorporating redshift information from multi-wavelength surveys [e.g. Roseboom and Best 2014].

Note that the techniques described above are suitable for data in which the rms is dominated by instrumental noise. For those that are confusion-limited, where sources are unresolved and ‘blur’ into the overall radio background, a probability of deflection, $P(D)$, analysis should be applied to find additional objects [Scheuer 1957; Patanchon et al. 2009; Glenn et al. 2010; Vernstrom et al. 2014].

6.2.3 Exploiting VLBI resolution

In this thesis I have separated accretion-related radio emission from star formation-related radio emission in two samples of RQQs (Chapters 3 and 5), using stellar-mass estimates and far-infrared luminosities in combination with radio data. Another method I could use is to spatially resolve the two components, resulting in a possibly cleaner separation that is less dependent on empirical relations and their associated caveats. This requires sub-arcsec resolution, which is achievable through very-long-baseline interferometry (VLBI).

Using baselines of length ≥100 km, it is possible to resolve the core emission of the

AGN, and any small radio jets that may be present in RQQs [Ulvestad et al., 2005]. For this I plan to use data, already in hand, from the extended Multi-Element Radio Linked Interferometer Network (e–MERLIN) to study a sample selected in the far-infrared ($S_{250\,\mu\mathrm{m}} > 38\,\mathrm{mJy}$) from the *Herschel*-ATLAS [Eales et al. 2010] and having a measurement of $S_{1.4\,\mathrm{GHz}} > 1\,\mathrm{mJy}$ in the FIRST radio survey [White et al. 1997]. These flux limits are used to ensure that the objects have a good SNR. Each of these targets are at $z < 0.5$ but unresolved in FIRST (the resolution there being ~5 arcsec), and so have no obvious jets. By subtracting the radio emission that can be confidently attributed to black-hole accretion, using the high-resolution e–MERLIN data, from the total emission as detected in FIRST, the contribution from star formation in the host galaxy can be calculated. The latter will be a lower limit due to (possible) nuclear star-formation being confused with radio emission from the accretion disc. Then, using the far-infrared data from Herschel, a FIRC can be determined that is free from AGN contamination.

Another project is already underway using e–MERLIN: the e–MERlin Galaxy Evolution Survey [eMERGE; Guidetti et al. 2013]. This is a deep observation, down to sub-μJy levels, over the GOODS–N (Great Observatories Origins Deep Survey–North) field. The aim is to study the formation and evolution of AGN and star-forming galaxies out to $z \sim 5$, with resolutions of 50–200 milliarcsec probing scales of 0.5–1.5 kpc at $z > 1$. The result will be the first detailed view of how star-forming regions are distributed *within* galaxies, over the peak in star-formation activity, and unaffected by dust obscuration. In parallel, accretion-connected radio emission will be resolved over the epoch of peak AGN-activity.

6.2.4 The Square Kilometre Array and its precursors

Although VLBI is excellent for producing high-resolution images, such instruments have sensitivity only on specific spatial scales. Arrays generally have a larger collecting area, and for a point-source, radio-continuum sensitivity of 1 μJy ($1\,\sigma$), a 48 hr integration is required using the JVLA's S band (its most-sensitive band, at 2–4 GHz). However with the SKA, the world's largest next-generation radio telescope, a 2.8 μJy rms can be achieved at 2.35 GHz in only 1 hr [Prandoni and Seymour, 2015]. Over the next decade, studies of the radio properties of radio-quiet AGN will therefore move from the statistical work described in Chapters 3 and 5 to direct detections with precursors of the SKA. For example, the MeerKAT–MIGHTEE continuum survey [Jarvis, 2012] will survey 35 $\deg^2$ to 1 μJy rms, and ASKAP–EMU [Norris et al., 2011] will image the whole sky to 10 μJy rms, thus providing direct measurements of the contribution of radio-quiet quasars to the total radio source counts.

Also in preparation for the SKA is the Murchison Widefield Array (MWA), which operates over the frequency range 70–230 MHz. In my next position as a Postdoctoral Research Associate I will be using the GaLactic and Extragalactic All-sky MWA (GLEAM) survey [Wayth et al., 2015] to study the different populations that contribute to the total radio number counts, and how they evolve with redshift over a wide frequency range. Due to the 130-arcsec resolution of the GLEAM mosaic, this will require careful statistical analysis based on multi-wavelength data, with *ugriz* photometry from the VLT Survey Telescope ATLAS survey [Shanks et al., 2015] and YJK photometry from VISTA Hemisphere Survey [VHS; McMahon et al. 2013]. The results will be particularly exciting, as the Southern sky has never been explored at such low frequencies.

As reviewed by McAlpine et al. [2015], Jarvis et al. [2015], and Smolčić et al. [2015], the SKA will play a pivotal role in determining the accretion history and star-formation history of objects throughout the Universe. One key technical concern, however, is the unparalleled volumes of data that will be produced. As shown in this thesis, even dealing with JVLA data requires large processing effort and careful visual inspection that is very time-consuming. The current capabilities of the JVLA lead to data rates of up to 140 $\mathrm{MB\,s^{-1}}$, whilst for SKA Phase 1 the data rates are expected to reach 20 $\mathrm{PB\,s^{-1}}$ [Dewdney et al., 2013]. Therefore a substantial amount of effort will be invested over the coming years, to improve the pipelines for processing data and outputting final data products. Doing so will encourage more members of the scientific community to use the SKA, and not just those with a background in radio astronomy. However, this takes us towards the realm of search algorithms and other automatic procedures, where there are not the same opportunities for serendipitous discoveries. To counter this, one of the six key science projects of the SKA will be exploration of new parameter space [Huynh and

Lazio, 2013; Wilkinson, 2014]. Whilst challenging, this means that this ground-breaking facility will be kept as flexible as possible.

Bibliography

J. K. Adelman-McCarthy, M. A. Agüeros, S. S. Allam, K. S. J. Anderson, S. F. Anderson, J. Annis, N. A. Bahcall, C. A. L. Bailer-Jones, I. K. Baldry, J. C. Barentine, T. C. Beers, V. Belokurov, A. Berlind, M. Bernardi, M. R. Blanton, J. J. Bochanski, W. N. Boroski, D. M. Bramich, H. J. Brewington, J. Brinchmann, J. Brinkmann, R. J. Brunner, T. Budavári, L. N. Carey, S. Carliles, M. A. Carr, F. J. Castander, A. J. Connolly, R. J. Cool, C. E. Cunha, I. Csabai, J. J. Dalcanton, M. Doi, D. J. Eisenstein, M. L. Evans, N. W. Evans, X. Fan, D. P. Finkbeiner, S. D. Friedman, J. A. Frieman, M. Fukugita, B. Gillespie, G. Gilmore, K. Glazebrook, J. Gray, E. K. Grebel, J. E. Gunn, E. de Haas, P. B. Hall, M. Harvanek, S. L. Hawley, J. Hayes, T. M. Heckman, J. S. Hendry, G. S. Hennessy, R. B. Hindsley, C. M. Hirata, C. J. Hogan, D. W. Hogg, J. A. Holtzman, S.-i. Ichikawa, T. Ichikawa, Ž. Ivezić, S. Jester, D. E. Johnston, A. M. Jorgensen, M. Jurić, G. Kauffmann, S. M. Kent, S. J. Kleinman, G. R. Knapp, A. Y. Kniazev, R. G. Kron, J. Krzesinski, N. Kuropatkin, D. Q. Lamb, H. Lampeitl, B. C. Lee, R. F. Leger, M. Lima, H. Lin, D. C. Long, J. Loveday, R. H. Lupton, R. Mandelbaum, B. Margon, D. Martínez-Delgado, T. Matsubara, P. M. McGehee, T. A. McKay, A. Meiksin, J. A. Munn, R. Nakajima, T. Nash, E. H. Neilsen, Jr., H. J. Newberg, R. C. Nichol, M. Nieto-Santisteban, A. Nitta, H. Oyaizu, S. Okamura, J. P. Ostriker, N. Padmanabhan, C. Park, J. Peoples, Jr., J. R. Pier, A. C. Pope, D. Pourbaix, T. R. Quinn, M. J. Raddick, P. Re Fiorentin, G. T. Richards, M. W. Richmond, H.-W. Rix, C. M. Rockosi, D. J. Schlegel, D. P. Schneider, R. Scranton, U. Seljak, E. Sheldon, K. Shimasaku, N. M. Silvestri, J. A. Smith, V. Smolčić, S. A. Snedden, A. Stebbins, C. Stoughton, M. A. Strauss, M. SubbaRao, Y. Suto, A. S. Szalay, I. Szapudi, P. Szkody, M. Tegmark, A. R. Thakar, C. A. Tremonti, D. L. Tucker, A. Uomoto, D. E. Vanden Berk, J. Vandenberg, S. Vidrih, M. S. Vogeley, W. Voges, N. P. Vogt, D. H. Weinberg,

A. A. West, S. D. M. White, B. Wilhite, B. Yanny, D. R. Yocum, D. G. York, I. Zehavi, S. Zibetti, and D. B. Zucker. The Fifth Data Release of the Sloan Digital Sky Survey. *ApJS*, 172:634–644, October 2007. doi: 10.1086/518864. 85

J. Aird, K. Nandra, E. S. Laird, A. Georgakakis, M. L. N. Ashby, P. Barmby, A. L. Coil, J.-S. Huang, A. M. Koekemoer, C. C. Steidel, and C. N. A. Willmer. The evolution of the hard X-ray luminosity function of AGN. *MNRAS*, 401:2531–2551, February 2010. doi: 10.1111/j.1365-2966.2009.15829.x. 26

A. Alonso-Herrero, C. Ramos Almeida, R. Mason, A. Asensio Ramos, P. F. Roche, N. A. Levenson, M. Elitzur, C. Packham, J. M. Rodríguez Espinosa, S. Young, T. Díaz-Santos, and A. M. Pérez-García. Torus and Active Galactic Nucleus Properties of Nearby Seyfert Galaxies: Results from Fitting Infrared Spectral Energy Distributions and Spectroscopy. *ApJ*, 736:82, August 2011. doi: 10.1088/0004-637X/736/2/82. 9

T. An, X.-Y. Hong, and W.-H. Wang. The Kiloparsec-scale Structure of 3C 286. *CJAA*, 4:28–36, February 2004. 106

R. Antonucci. Unified models for active galactic nuclei and quasars. *ARA&A*, 31:473–521, 1993. doi: 10.1146/annurev.aa.31.090193.002353. 12

A. Babić, L. Miller, M. J. Jarvis, T. J. Turner, D. M. Alexander, and S. M. Croom. Low accretion rates at the AGN cosmic downsizing epoch. *A&A*, 474:755–762, November 2007. doi: 10.1051/0004-6361:20078286. 6

S. A. Balbus and J. F. Hawley. A powerful local shear instability in weakly magnetized disks. I - Linear analysis. II - Nonlinear evolution. *ApJ*, 376:214–233, July 1991. doi: 10.1086/170270. 8

I. K. Baldry, A. S. G. Robotham, D. T. Hill, S. P. Driver, J. Liske, P. Norberg, S. P. Bamford, A. M. Hopkins, J. Loveday, J. A. Peacock, E. Cameron, S. M. Croom, N. J. G. Cross, I. F. Doyle, S. Dye, C. S. Frenk, D. H. Jones, E. van Kampen, L. S. Kelvin, R. C. Nichol, H. R. Parkinson, C. C. Popescu, M. Prescott, R. G. Sharp, W. J. Sutherland, D. Thomas, and R. J. Tuffs. Galaxy And Mass Assembly (GAMA): the input catalogue and star-galaxy separation. *MNRAS*, 404:86–100, May 2010. doi: 10.1111/j.1365-2966.2010.16282.x. 35, 45

I. K. Baldry, S. P. Driver, J. Loveday, E. N. Taylor, L. S. Kelvin, J. Liske, P. Norberg, A. S. G. Robotham, S. Brough, A. M. Hopkins, S. P. Bamford, J. A. Peacock, J. Bland-Hawthorn, C. J. Conselice, S. M. Croom, D. H. Jones, H. R. Parkinson, C. C. Popescu, M. Prescott, R. G. Sharp, and R. J. Tuffs. Galaxy And Mass Assembly (GAMA): the galaxy stellar mass function at z < 0.06. *MNRAS*, 421:621–634, March 2012. doi: 10.1111/j.1365-2966.2012.20340.x. 8

J. A. Baldwin, M. M. Phillips, and R. Terlevich. Classification parameters for the emission-line spectra of extragalactic objects. *PASP*, 93:5–19, February 1981. doi: 10.1086/130766. 26, 28

M. Baloković, V. Smolčić, Ž. Ivezić, G. Zamorani, E. Schinnerer, and B. C. Kelly. Disclosing the Radio Loudness Distribution Dichotomy in Quasars: An Unbiased Monte Carlo Approach Applied to the SDSS-FIRST Quasar Sample. *ApJ*, 759:30, November 2012. doi: 10.1088/0004-637X/759/1/30. 20

E. F. Bell. Estimating Star Formation Rates from Infrared and Radio Luminosities: The Origin of the Radio-Infrared Correlation. *ApJ*, 586:794–813, April 2003. doi: 10.1086/367829. 159, 160

V. N. Bennert, M. W. Auger, T. Treu, J.-H. Woo, and M. A. Malkan. The Relation between Black Hole Mass and Host Spheroid Stellar Mass Out to z ˜ 2. *ApJ*, 742:107, December 2011. doi: 10.1088/0004-637X/742/2/107. 73, 75

A. J. Benson. G ALACTICUS: A semi-analytic model of galaxy formation. *New Astron.*, 17:175–197, February 2012. doi: 10.1016/j.newast.2011.07.004. 4

A. J. Benson, R. G. Bower, C. S. Frenk, C. G. Lacey, C. M. Baugh, and S. Cole. What Shapes the Luminosity Function of Galaxies? *ApJ*, 599:38–49, December 2003. doi: 10.1086/379160. 15

E. Bertin and S. Arnouts. SExtractor: Software for source extraction. *A&AS*, 117:393–404, June 1996. 35

P. N. Best. Radio-Loud AGN Feedback in Elliptical Galaxies. In N. Metcalfe and T. Shanks, editors, *Cosmic Frontiers*, volume 379 of *Astronomical Society of the Pacific Conference Series*, page 213, December 2007. 14

P. N. Best and T. M. Heckman. On the fundamental dichotomy in the local radio-AGN population: accretion, evolution and host galaxy properties. *MNRAS*, 421:1569–1582, April 2012. doi: 10.1111/j.1365-2966.2012.20414.x. 19, 22

L. Bîrzan, D. A. Rafferty, B. R. McNamara, M. W. Wise, and P. E. J. Nulsen. A Systematic Study of Radio-induced X-Ray Cavities in Clusters, Groups, and Galaxies. *ApJ*, 607:800–809, June 2004. doi: 10.1086/383519. 14

R. D. Blandford. Physical processes in active galactic nuclei. In R. D. Blandford, H. Netzer, L. Woltjer, T. J.-L. Courvoisier, and M. Mayor, editors, *Active Galactic Nuclei*, pages 161–275, 1990. 10

R. D. Blandford and D. G. Payne. Hydromagnetic flows from accretion discs and the production of radio jets. *MNRAS*, 199:883–903, June 1982. 183

R. D. Blandford and R. L. Znajek. Electromagnetic extraction of energy from Kerr black holes. *MNRAS*, 179:433–456, May 1977. 18, 20

K. M. Blundell and S. Rawlings. The Optically Powerful Quasar E1821+643 is Associated with a 300 Kiloparsec-Scale FR I Radio Structure. *ApJL*, 562:L5–L8, November 2001. doi: 10.1086/337970. 183

K. M. Blundell, A. J. Mioduszewski, T. W. B. Muxlow, P. Podsiadlowski, and M. P. Rupen. Images of an Equatorial Outflow in SS 433. *ApJL*, 562:L79–L82, November 2001. doi: 10.1086/324573. 184

K. M. Blundell, A. J. Beasley, and G. V. Bicknell. A Relativistic Jet in the Radio-quiet Quasar PG 1407+263. *ApJL*, 591:L103–L106, July 2003. doi: 10.1086/377295. 10

M. Bondi, P. Ciliegi, G. Zamorani, L. Gregorini, G. Vettolani, P. Parma, H. de Ruiter, O. Le Fevre, M. Arnaboldi, L. Guzzo, D. Maccagni, R. Scaramella, C. Adami, S. Bardelli, M. Bolzonella, D. Bottini, A. Cappi, S. Foucaud, P. Franzetti, B. Garilli,

S. Gwyn, O. Ilbert, A. Iovino, V. Le Brun, B. Marano, C. Marinoni, H. J. McCracken, B. Meneux, A. Pollo, L. Pozzetti, M. Radovich, V. Ripepi, D. Rizzo, M. Scodeggio, L. Tresse, A. Zanichelli, and E. Zucca. The VLA-VIRMOS Deep Field. I. Radio observations probing the mu Jy source population. *A&A*, 403:857–867, June 2003. doi: 10.1051/0004-6361:20030382. 33, 62, 66, 71

D. G. Bonfield, M. J. Jarvis, M. J. Hardcastle, A. Cooray, E. Hatziminaoglou, R. J. Ivison, M. J. Page, J. A. Stevens, G. de Zotti, R. Auld, M. Baes, S. Buttiglione, A. Cava, A. Dariush, J. S. Dunlop, L. Dunne, S. Dye, S. Eales, J. Fritz, R. Hopwood, E. Ibar, S. J. Maddox, M. J. Michałowski, E. Pascale, M. Pohlen, E. E. Rigby, G. Rodighiero, S. Serjeant, D. J. B. Smith, P. Temi, and P. van der Werf. Herschel-ATLAS: the link between accretion luminosity and star formation in quasar host galaxies. *MNRAS*, 416:13–21, September 2011. doi: 10.1111/j.1365-2966.2011.18826.x. 16, 25, 27, 76, 77

G. D. Bothun, C. J. Lonsdale, and W. Rice. IRAS observations of optically selected galaxies. I - The properties of the UGC redshift sample. *ApJ*, 341:129–150, June 1989. doi: 10.1086/167478. 152

N. Bouché, A. Dekel, R. Genzel, S. Genel, G. Cresci, N. M. Förster Schreiber, K. L. Shapiro, R. I. Davies, and L. Tacconi. The Impact of Cold Gas Accretion Above a Mass Floor on Galaxy Scaling Relations. *ApJ*, 718:1001–1018, August 2010. doi: 10.1088/0004-637X/718/2/1001. 165

R. G. Bower, A. J. Benson, R. Malbon, J. C. Helly, C. S. Frenk, C. M. Baugh, S. Cole, and C. G. Lacey. Breaking the hierarchy of galaxy formation. *MNRAS*, 370:645–655, August 2006. doi: 10.1111/j.1365-2966.2006.10519.x. 15

G. Bruzual and S. Charlot. Stellar population synthesis at the resolution of 2003. *MNRAS*, 344:1000–1028, October 2003. doi: 10.1046/j.1365-8711.2003.06897.x. 73

D. A. H. Buckley, G. P. Swart, and J. G. Meiring. Completion and commissioning of the Southern African Large Telescope. In *Society of Photo-Optical Instrumentation Engineers (SPIE) Conference Series*, volume 6267 of *Society of Photo-Optical Instrumenta-*

tion Engineers (SPIE) Conference Series, page 0, June 2006. doi: 10.1117/12.673750. 45

B. F. Burke and F. Graham-Smith. *An Introduction to Radio Astronomy.* September 2009. 95, 97

G. Canalizo and A. Stockton. Quasi-Stellar Objects, Ultraluminous Infrared Galaxies, and Mergers. *ApJ*, 555:719–743, July 2001. doi: 10.1086/321520. 27

C. L. Carilli and F. Walter. Cool Gas in High-Redshift Galaxies. *ARA&A*, 51:105–161, August 2013. doi: 10.1146/annurev-astro-082812-140953. 24

S. Charlot and S. M. Fall. A Simple Model for the Absorption of Starlight by Dust in Galaxies. *ApJ*, 539:718–731, August 2000. doi: 10.1086/309250. 153

C.-T. J. Chen, R. C. Hickox, S. Alberts, M. Brodwin, C. Jones, S. S. Murray, D. M. Alexander, R. J. Assef, M. J. I. Brown, A. Dey, W. R. Forman, V. Gorjian, A. D. Goulding, E. Le Floc'h, B. T. Jannuzi, J. R. Mullaney, and A. Pope. A Correlation between Star Formation Rate and Average Black Hole Accretion in Star-forming Galaxies. *ApJ*, 773:3, August 2013. doi: 10.1088/0004-637X/773/1/3. 16

C.-T. J. Chen, R. C. Hickox, S. Alberts, C. M. Harrison, D. M. Alexander, R. Assef, M. Brodwin, M. J. I. Brown, A. Del Moro, W. R. Forman, V. Gorjian, A. D. Goulding, K. N. Hainline, C. Jones, C. S. Kochanek, S. S. Murray, A. Pope, E. Rovilos, and D. Stern. A Connection between Obscuration and Star Formation in Luminous Quasars. *ApJ*, 802:50, March 2015. doi: 10.1088/0004-637X/802/1/50. 185

R. Chini, E. Kreysa, E. Kruegel, and P. G. Mezger. Sub-mm observations of IRAS galaxies. *A&A*, 166:L8–L10, September 1986. 152

R. Cid Fernandes, G. Stasińska, M. S. Schlickmann, A. Mateus, N. Vale Asari, W. Schoenell, and L. Sodré. Alternative diagnostic diagrams and the 'forgotten' population of weak line galaxies in the SDSS. *MNRAS*, 403:1036–1053, April 2010. doi: 10.1111/j.1365-2966.2009.16185.x. 28

M. Cirasuolo, M. Magliocchetti, A. Celotti, and L. Danese. The radio-loud/radio-quiet dichotomy: news from the 2dF QSO Redshift Survey. *MNRAS*, 341:993–1004, May 2003. doi: 10.1046/j.1365-8711.2003.06485.x. 20

G. D. Coleman, C.-C. Wu, and D. W. Weedman. Colors and magnitudes predicted for high redshift galaxies. *ApJS*, 43:393–416, July 1980. doi: 10.1086/190674. 38

F. Combes, S. García-Burillo, V. Casasola, L. Hunt, M. Krips, A. J. Baker, F. Boone, A. Eckart, I. Marquez, R. Neri, E. Schinnerer, and L. J. Tacconi. ALMA observations of feeding and feedback in nearby Seyfert galaxies: an AGN-driven outflow in NGC 1433. *A&A*, 558:A124, October 2013. doi: 10.1051/0004-6361/201322288. 14

J. J. Condon. Cosmological evolution of radio sources. *ApJ*, 287:461–474, December 1984. doi: 10.1086/162705. 23

J. J. Condon. Radio emission from normal galaxies. *ARA&A*, 30:575–611, 1992. doi: 10.1146/annurev.aa.30.090192.003043. 19, 27

J. J. Condon, M. L. Anderson, and G. Helou. Correlations between the far-infrared, radio, and blue luminosities of spiral galaxies. *ApJ*, 376:95–103, July 1991. doi: 10.1086/170258. 24, 25

J. J. Condon, W. D. Cotton, E. W. Greisen, Q. F. Yin, R. A. Perley, G. B. Taylor, and J. J. Broderick. The NRAO VLA Sky Survey. *AJ*, 115:1693–1716, May 1998. doi: 10.1086/300337. 62, 84, 129

J. J. Condon, W. D. Cotton, and J. J. Broderick. Radio Sources and Star Formation in the Local Universe. *AJ*, 124:675–689, August 2002. doi: 10.1086/341650. 22

J. J. Condon, W. D. Cotton, E. B. Fomalont, K. I. Kellermann, N. Miller, R. A. Perley, D. Scott, T. Vernstrom, and J. V. Wall. Resolving the Radio Source Background: Deeper Understanding through Confusion. *ApJ*, 758:23, October 2012. doi: 10.1088/0004-637X/758/1/23. 22, 23, 27, 69, 181

J. J. Condon, K. I. Kellermann, A. E. Kimball, Ž. Ivezić, and R. A. Perley. Active Galactic Nucleus and Starburst Radio Emission from Optically Selected Quasi-stellar Objects.

ApJ, 768:37, May 2013. doi: 10.1088/0004-637X/768/1/37. 23, 27, 61, 68, 69, 70, 71, 72, 81, 82, 182

L. L. Cowie, A. Songaila, E. M. Hu, and J. G. Cohen. New Insight on Galaxy Formation and Evolution From Keck Spectroscopy of the Hawaii Deep Fields. *AJ*, 112:839, September 1996. doi: 10.1086/118058. 6

S. M. Crawford, M. Still, P. Schellart, L. Balona, D. A. H. Buckley, G. Dugmore, A. A. S. Gulbis, A. Kniazev, M. Kotze, N. Loaring, K. H. Nordsieck, T. E. Pickering, S. Potter, E. Romero Colmenero, P. Vaisanen, T. Williams, and E. Zietsman. PySALT: the SALT science pipeline. In *Society of Photo-Optical Instrumentation Engineers (SPIE) Conference Series*, volume 7737 of *Society of Photo-Optical Instrumentation Engineers (SPIE) Conference Series*, page 25, July 2010. doi: 10.1117/12.857000. 46

S. Croft, W. van Breugel, W. de Vries, M. Dopita, C. Martin, R. Morganti, S. Neff, T. Oosterloo, D. Schiminovich, S. A. Stanford, and J. van Gorkom. Minkowski's Object: A Starburst Triggered by a Radio Jet, Revisited. *ApJ*, 647:1040–1055, August 2006. doi: 10.1086/505526. 14, 15, 181, 184

S. M. Croom, G. T. Richards, T. Shanks, B. J. Boyle, M. A. Strauss, A. D. Myers, R. C. Nichol, K. A. Pimbblet, N. P. Ross, D. P. Schneider, R. G. Sharp, and D. A. Wake. The 2dF-SDSS LRG and QSO survey: the QSO luminosity function at $0.4 < z < 2.6$. *MNRAS*, 399:1755–1772, November 2009. doi: 10.1111/j.1365-2966.2009.15398.x. 54, 150, 184

J. H. Croston, R. P. Kraft, and M. J. Hardcastle. Shock Heating in the Nearby Radio Galaxy NGC 3801. *ApJ*, 660:191–199, May 2007. doi: 10.1086/513500. 14

D. J. Croton, V. Springel, S. D. M. White, G. De Lucia, C. S. Frenk, L. Gao, A. Jenkins, G. Kauffmann, J. F. Navarro, and N. Yoshida. The many lives of active galactic nuclei: cooling flows, black holes and the luminosities and colours of galaxies. *MNRAS*, 365: 11–28, January 2006. doi: 10.1111/j.1365-2966.2005.09675.x. 15, 16, 181

R. I. Davies, J. Thomas, R. Genzel, F. Müller Sánchez, L. J. Tacconi, A. Sternberg, F. Eisenhauer, R. Abuter, R. Saglia, and R. Bender. The Star-forming Torus and

Stellar Dynamical Black Hole Mass in the Seyfert 1 Nucleus of NGC 3227. *ApJ*, 646: 754–773, August 2006. doi: 10.1086/504963. 181

R. I. Davies, W. Maciejewski, E. K. S. Hicks, E. Emsellem, P. Erwin, L. Burtscher, G. Dumas, M. Lin, M. A. Malkan, F. Müller-Sánchez, G. Orban de Xivry, D. J. Rosario, A. Schnorr-Müller, and A. Tran. Fueling Active Galactic Nuclei. II. Spatially Resolved Molecular Inflows and Outflows. *ApJ*, 792:101, September 2014. doi: 10.1088/0004-637X/792/2/101. 10

T. de Jong and K. Brink. A simple two-component model for the far-infrared emission from galaxies. In C. J. Lonsdale Persson, editor, *NASA Conference Publication*, volume 2466 of *NASA Conference Publication*, pages 323–328, May 1987. 152

T. de Jong, U. Klein, R. Wielebinski, and E. Wunderlich. Radio continuum and far-infrared emission from spiral galaxies - A close correlation. *A&A*, 147:L6–L9, June 1985. 27

I. Delvecchio, C. Gruppioni, F. Pozzi, S. Berta, G. Zamorani, A. Cimatti, D. Lutz, D. Scott, C. Vignali, G. Cresci, A. Feltre, A. Cooray, M. Vaccari, J. Fritz, E. Le Floc'h, B. Magnelli, P. Popesso, S. Oliver, J. Bock, M. Carollo, T. Contini, O. Le Févre, S. Lilly, V. Mainieri, A. Renzini, and M. Scodeggio. Tracing the cosmic growth of supermassive black holes to z $\sim$ 3 with Herschel. *MNRAS*, 439:2736–2754, April 2014. doi: 10.1093/mnras/stu130. 26

P.E. Dewdney, W. Turner, R. Millenaar, R. McCool, J. Lazio, and T. J. Cornwell. *SKA1 System Baseline Design, SKA-TEL-SKO-DD-001*. The SKA Office, March 2013. 188

Y. Dubois, J. Devriendt, R. Teyssier, and A. Slyz. How active galactic nucleus feedback and metal cooling shape cluster entropy profiles. *MNRAS*, 417:1853–1870, November 2011. doi: 10.1111/j.1365-2966.2011.19381.x. 15

J. S. Dunlop, R. J. McLure, M. J. Kukula, S. A. Baum, C. P. O'Dea, and D. H. Hughes. Quasars, their host galaxies and their central black holes. *MNRAS*, 340:1095–1135, April 2003. doi: 10.1046/j.1365-8711.2003.06333.x. 22

S. Eales, L. Dunne, D. Clements, A. Cooray, G. de Zotti, S. Dye, R. Ivison, M. Jarvis, G. Lagache, S. Maddox, M. Negrello, S. Serjeant, M. A. Thompson, E. van Kampen, A. Amblard, P. Andreani, M. Baes, A. Beelen, G. J. Bendo, D. Benford, F. Bertoldi, J. Bock, D. Bonfield, A. Boselli, C. Bridge, V. Buat, D. Burgarella, R. Carlberg, A. Cava, P. Chanial, S. Charlot, N. Christopher, P. Coles, L. Cortese, A. Dariush, E. da Cunha, G. Dalton, L. Danese, H. Dannerbauer, S. Driver, J. Dunlop, L. Fan, D. Farrah, D. Frayer, C. Frenk, J. Geach, J. Gardner, H. Gomez, J. González-Nuevo, E. González-Solares, M. Griffin, M. Hardcastle, E. Hatziminaoglou, D. Herranz, D. Hughes, E. Ibar, W.-S. Jeong, C. Lacey, A. Lapi, A. Lawrence, M. Lee, L. Leeuw, J. Liske, M. López-Caniego, T. Müller, K. Nandra, P. Panuzzo, A. Papageorgiou, G. Patanchon, J. Peacock, C. Pearson, S. Phillipps, M. Pohlen, C. Popescu, S. Rawlings, E. Rigby, M. Rigopoulou, A. Robotham, G. Rodighiero, A. Sansom, B. Schulz, D. Scott, D. J. B. Smith, B. Sibthorpe, I. Smail, J. Stevens, W. Sutherland, T. Takeuchi, J. Tedds, P. Temi, R. Tuffs, M. Trichas, M. Vaccari, I. Valtchanov, P. van der Werf, A. Verma, J. Vieria, C. Vlahakis, and G. J. White. The Herschel ATLAS. *PASP*, 122:499–515, May 2010. doi: 10.1086/653086. 76, 187

D. O. Edge, J. R. Shakeshaft, W. B. McAdam, J. E. Baldwin, and S. Archer. A survey of radio sources at a frequency of 159 Mc s^{-1}. *Memoirs of the RAS*, 68:37–60, 1959. 105

R. D. Ekers. Error Recognition. In G. B. Taylor, C. L. Carilli, and R. A. Perley, editors, *Synthesis Imaging in Radio Astronomy II*, volume 180 of *Astronomical Society of the Pacific Conference Series*, page 321, 1999. 93

A. C. Fabian, J. S. Sanders, S. Ettori, G. B. Taylor, S. W. Allen, C. S. Crawford, K. Iwasawa, R. M. Johnstone, and P. M. Ogle. Chandra imaging of the complex X-ray core of the Perseus cluster. *MNRAS*, 318:L65–L68, November 2000. doi: 10.1046/j.1365-8711.2000.03904.x. 14

J. T. Falder, J. A. Stevens, M. J. Jarvis, M. J. Hardcastle, M. Lacy, R. J. McLure, E. Hatziminaoglou, M. J. Page, and G. T. Richards. The environments of z ˜ 1 active galactic nuclei at 3.6μm. *MNRAS*, 405:347–358, June 2010. doi: 10.1111/j.1365-2966.2010.16444.x. 21, 145, 146, 161, 173

B. L. Fanaroff and J. M. Riley. The morphology of extragalactic radio sources of high and low luminosity. *MNRAS*, 167:31P–36P, May 1974. 19

A. Feltre, E. Hatziminaoglou, A. Hernán-Caballero, J. Fritz, and A. Franceschini. AGN and Star Formation in HerMES-IRS sources. In *IAU Symposium*, volume 304 of *IAU Symposium*, pages 52–55, July 2014. doi: 10.1017/S1743921314003305. 153, 181

C. A. C. Fernandes, M. J. Jarvis, S. Rawlings, A. Martínez-Sansigre, E. Hatziminaoglou, M. Lacy, M. J. Page, J. A. Stevens, and E. Vardoulaki. Evidence for a maximum jet efficiency for the most powerful radio galaxies. *MNRAS*, 411:1909–1916, March 2011. doi: 10.1111/j.1365-2966.2010.17820.x. 20, 21, 22, 68, 72, 150

L. Ferrarese and D. Merritt. A Fundamental Relation between Supermassive Black Holes and Their Host Galaxies. *ApJL*, 539:L9–L12, August 2000. doi: 10.1086/312838. 5, 25

F. Fiore, S. Puccetti, A. Grazian, N. Menci, F. Shankar, P. Santini, E. Piconcelli, A. M. Koekemoer, A. Fontana, K. Boutsia, M. Castellano, A. Lamastra, C. Malacaria, C. Feruglio, S. Mathur, N. Miller, and M. Pannella. Faint high-redshift AGN in the Chandra deep field south: the evolution of the AGN luminosity function and black hole demography. *A&A*, 537:A16, January 2012. doi: 10.1051/0004-6361/201117581. 8

E. B. Fomalont and R. A. Perley. Calibration and Editing. In G. B. Taylor, C. L. Carilli, and R. A. Perley, editors, *Synthesis Imaging in Radio Astronomy II*, volume 180 of *Astronomical Society of the Pacific Conference Series*, page 79, 1999. 102

K. Gebhardt, R. Bender, G. Bower, A. Dressler, S. M. Faber, A. V. Filippenko, R. Green, C. Grillmair, L. C. Ho, J. Kormendy, T. R. Lauer, J. Magorrian, J. Pinkney, D. Richstone, and S. Tremaine. A Relationship between Nuclear Black Hole Mass and Galaxy Velocity Dispersion. *ApJL*, 539:L13–L16, August 2000. doi: 10.1086/312840. 5, 25

R. Genzel and C. J. Cesarsky. Extragalactic Results from the Infrared Space Observatory. *ARA&A*, 38:761–814, 2000. doi: 10.1146/annurev.astro.38.1.761. 83

R. Gilli, A. Comastri, and G. Hasinger. The synthesis of the cosmic X-ray background in the Chandra and XMM-Newton era. *A&A*, 463:79–96, February 2007. doi: 10.1051/0004-6361:20066334. 184

J. Glenn, A. Conley, M. Béthermin, B. Altieri, A. Amblard, V. Arumugam, H. Aussel, T. Babbedge, A. Blain, J. Bock, A. Boselli, V. Buat, N. Castro-Rodríguez, A. Cava, P. Chanial, D. L. Clements, L. Conversi, A. Cooray, C. D. Dowell, E. Dwek, S. Eales, D. Elbaz, T. P. Ellsworth-Bowers, M. Fox, A. Franceschini, W. Gear, M. Griffin, M. Halpern, E. Hatziminaoglou, E. Ibar, K. Isaak, R. J. Ivison, G. Lagache, G. Laurent, L. Levenson, N. Lu, S. Madden, B. Maffei, G. Mainetti, L. Marchetti, G. Marsden, H. T. Nguyen, B. O'Halloran, S. J. Oliver, A. Omont, M. J. Page, P. Panuzzo, A. Papageorgiou, C. P. Pearson, I. Pérez-Fournon, M. Pohlen, D. Rigopoulou, D. Rizzo, I. G. Roseboom, M. Rowan-Robinson, M. S. Portal, B. Schulz, D. Scott, N. Seymour, D. L. Shupe, A. J. Smith, J. A. Stevens, M. Symeonidis, M. Trichas, K. E. Tugwell, M. Vaccari, I. Valtchanov, J. D. Vieira, L. Vigroux, L. Wang, R. Ward, G. Wright, C. K. Xu, and M. Zemcov. HerMES: deep galaxy number counts from a P(D) fluctuation analysis of SPIRE Science Demonstration Phase observations. *MNRAS*, 409:109–121, November 2010. doi: 10.1111/j.1365-2966.2010.17781.x. 186

F. Governato, C. B. Brook, A. M. Brooks, L. Mayer, B. Willman, P. Jonsson, A. M. Stilp, L. Pope, C. Christensen, J. Wadsley, and T. Quinn. Forming a large disc galaxy from a $z < 1$ major merger. *MNRAS*, 398:312–320, September 2009. doi: 10.1111/j.1365-2966.2009.15143.x. 2

M. J. Griffin, A. Abergel, A. Abreu, P. A. R. Ade, P. André, J.-L. Augueres, T. Babbedge, Y. Bae, T. Baillie, J.-P. Baluteau, M. J. Barlow, G. Bendo, D. Benielli, J. J. Bock, P. Bonhomme, D. Brisbin, C. Brockley-Blatt, M. Caldwell, C. Cara, N. Castro-Rodriguez, R. Cerulli, P. Chanial, S. Chen, E. Clark, D. L. Clements, L. Clerc, J. Coker, D. Communal, L. Conversi, P. Cox, D. Crumb, C. Cunningham, F. Daly, G. R. Davis, P. de Antoni, J. Delderfield, N. Devin, A. di Giorgio, I. Didschuns, K. Dohlen, M. Donati, A. Dowell, C. D. Dowell, L. Duband, L. Dumaye, R. J. Emery, M. Ferlet, D. Ferrand, J. Fontignie, M. Fox, A. Franceschini, M. Frerking, T. Fulton, J. Garcia, R. Gastaud, W. K. Gear, J. Glenn, A. Goizel, D. K. Griffin, T. Grundy, S. Guest, L. Guillemet, P. C. Hargrave, M. Harwit, P. Hastings, E. Hatziminaoglou, M. Herman, B. Hinde, V. Hristov, M. Huang, P. Imhof, K. J. Isaak, U. Israelsson, R. J. Ivison, D. Jennings, B. Kiernan, K. J. King, A. E. Lange, W. Latter, G. Laurent, P. Laurent, S. J. Leeks,

E. Lellouch, L. Levenson, B. Li, J. Li, J. Lilienthal, T. Lim, S. J. Liu, N. Lu, S. Madden, G. Mainetti, P. Marliani, D. McKay, K. Mercier, S. Molinari, H. Morris, H. Moseley, J. Mulder, M. Mur, D. A. Naylor, H. Nguyen, B. O'Halloran, S. Oliver, G. Olofsson, H.-G. Olofsson, R. Orfei, M. J. Page, I. Pain, P. Panuzzo, A. Papageorgiou, G. Parks, P. Parr-Burman, A. Pearce, C. Pearson, I. Pérez-Fournon, F. Pinsard, G. Pisano, J. Podosek, M. Pohlen, E. T. Polehampton, D. Pouliquen, D. Rigopoulou, D. Rizzo, I. G. Roseboom, H. Roussel, M. Rowan-Robinson, B. Rownd, P. Saraceno, M. Sauvage, R. Savage, G. Savini, E. Sawyer, C. Scharmberg, D. Schmitt, N. Schneider, B. Schulz, A. Schwartz, R. Shafer, D. L. Shupe, B. Sibthorpe, S. Sidher, A. Smith, A. J. Smith, D. Smith, L. Spencer, B. Stobie, R. Sudiwala, K. Sukhatme, C. Surace, J. A. Stevens, B. M. Swinyard, M. Trichas, T. Tourette, H. Triou, S. Tseng, C. Tucker, A. Turner, M. Vaccari, I. Valtchanov, L. Vigroux, E. Virique, G. Voellmer, H. Walker, R. Ward, T. Waskett, M. Weilert, R. Wesson, G. J. White, N. Whitehouse, C. D. Wilson, B. Winter, A. L. Woodcraft, G. S. Wright, C. K. Xu, A. Zavagno, M. Zemcov, L. Zhang, and E. Zonca. The Herschel-SPIRE instrument and its in-flight performance. *A&A*, 518: L3, July 2010. doi: 10.1051/0004-6361/201014519. 86

B. Guiderdoni, E. Hivon, F. R. Bouchet, and B. Maffei. Semi-analytic modelling of galaxy evolution in the IR/submm range. *MNRAS*, 295:877–898, April 1998. doi: 10.1046/j.1365-8711.1998.01308.x. 158

D. Guidetti, M. Bondi, I. Prandoni, R. J. Beswick, T. W. B. Muxlow, N. Wrigley, I. Smail, and I. McHardy. e-MERLIN observations at 5 GHz of the GOODS-N region: pinpointing AGN cores in high-redshift galaxies. *MNRAS*, 432:2798–2807, July 2013. doi: 10.1093/mnras/stt633. 187

K. Gültekin, D. O. Richstone, K. Gebhardt, T. R. Lauer, S. Tremaine, M. C. Aller, R. Bender, A. Dressler, S. M. Faber, A. V. Filippenko, R. Green, L. C. Ho, J. Kormendy, J. Magorrian, J. Pinkney, and C. Siopis. The M-σ and M-L Relations in Galactic Bulges, and Determinations of Their Intrinsic Scatter. *ApJ*, 698:198–221, June 2009. doi: 10.1088/0004-637X/698/1/198. 7, 25

S. D. J. Gwyn. The Canada-France-Hawaii Telescope Legacy Survey: Stacked Images and Catalogs. *AJ*, 143:38, February 2012. doi: 10.1088/0004-6256/143/2/38. 33

M. Haas, R. Chini, K. Meisenheimer, M. Stickel, D. Lemke, U. Klaas, E. Kreysa, and S. Muller. On the far-infrared emission of quasars. In P. Cox and M. Kessler, editors, *The Universe as Seen by ISO*, volume 427 of *ESA Special Publication*, page 887, March 1999. 160

A. A. Hakobyan, V. Z. Adibekyan, L. S. Aramyan, A. R. Petrosian, J. M. Gomes, G. A. Mamon, D. Kunth, and M. Turatto. Supernovae and their host galaxies. I. The SDSS DR8 database and statistics. *A&A*, 544:A81, August 2012. doi: 10.1051/0004-6361/201219541. 28

J. P. Hamaker, J. D. Bregman, and R. J. Sault. Understanding radio polarimetry. I. Mathematical foundations. *A&AS*, 117:137–147, May 1996. 99

C. Haniff. Ground-based optical interferometry: A practical primer. *New Astron. Rev.*, 51:583–596, October 2007. doi: 10.1016/j.newar.2007.06.004. 97

M. J. Hardcastle and M. G. H. Krause. Numerical modelling of the lobes of radio galaxies in cluster environments. *MNRAS*, 430:174–196, March 2013. doi: 10.1093/mnras/sts564. 173

M. J. Hardcastle, D. A. Evans, and J. H. Croston. The X-ray nuclei of intermediate-redshift radio sources. *MNRAS*, 370:1893–1904, August 2006. doi: 10.1111/j.1365-2966.2006.10615.x. 150

M. J. Hardcastle, J. H. Y. Ching, J. S. Virdee, M. J. Jarvis, S. M. Croom, E. M. Sadler, T. Mauch, D. J. B. Smith, J. A. Stevens, M. Baes, I. K. Baldry, S. Brough, A. Cooray, A. Dariush, G. De Zotti, S. Driver, L. Dunne, S. Dye, S. Eales, R. Hopwood, J. Liske, S. Maddox, M. J. Michałowski, E. E. Rigby, A. S. G. Robotham, O. Steele, D. Thomas, and E. Valiante. Herschel-ATLAS/GAMA: a difference between star formation rates in strong-line and weak-line radio galaxies. *MNRAS*, 429:2407–2424, March 2013. doi: 10.1093/mnras/sts510. 18, 25, 152, 159

E. Hatziminaoglou, I. Pérez-Fournon, M. Polletta, A. Afonso-Luis, A. Hernán-Caballero, F. M. Montenegro-Montes, C. Lonsdale, C. K. Xu, A. Franceschini, M. Rowan-Robinson, T. Babbedge, H. E. Smith, J. Surace, D. Shupe, F. Fang, D. Farrah, S. Oliver, E. A. González-Solares, and S. Serjeant. Sloan Digital Sky Survey Quasars in the Spitzer Wide-Area Infrared Extragalactic Survey (SWIRE) ELAIS N1 Field: Properties and Spectral Energy Distributions. *AJ*, 129:1198–1211, March 2005. doi: 10.1086/428003. 38

E. Hatziminaoglou, A. Omont, J. A. Stevens, A. Amblard, V. Arumugam, R. Auld, H. Aussel, T. Babbedge, A. Blain, J. Bock, A. Boselli, V. Buat, D. Burgarella, N. Castro-Rodríguez, A. Cava, P. Chanial, D. L. Clements, A. Conley, L. Conversi, A. Cooray, C. D. Dowell, E. Dwek, S. Dye, S. Eales, D. Elbaz, D. Farrah, M. Fox, A. Franceschini, W. Gear, J. Glenn, E. A. González Solares, M. Griffin, M. Halpern, E. Ibar, K. Isaak, R. J. Ivison, G. Lagache, L. Levenson, N. Lu, S. Madden, B. Maffei, G. Mainetti, L. Marchetti, A. M. J. Mortier, H. T. Nguyen, B. O'Halloran, S. J. Oliver, M. J. Page, P. Panuzzo, A. Papageorgiou, C. P. Pearson, I. Pérez-Fournon, M. Pohlen, J. I. Rawlings, D. Rigopoulou, D. Rizzo, I. G. Roseboom, M. Rowan-Robinson, M. Sanchez Portal, B. Schulz, D. Scott, N. Seymour, D. L. Shupe, A. J. Smith, M. Symeonidis, M. Trichas, K. E. Tugwell, M. Vaccari, I. Valtchanov, L. Vigroux, L. Wang, R. Ward, G. Wright, C. K. Xu, and M. Zemcov. HerMES: Far infrared properties of known AGN in the HerMES fields. *A&A*, 518:L33, July 2010. doi: 10.1051/0004-6361/201014679. 153

B. Häussler, D. H. McIntosh, M. Barden, E. F. Bell, H.-W. Rix, A. Borch, S. V. W. Beckwith, J. A. R. Caldwell, C. Heymans, K. Jahnke, S. Jogee, S. E. Koposov, K. Meisenheimer, S. F. Sánchez, R. S. Somerville, L. Wisotzki, and C. Wolf. GEMS: Galaxy Fitting Catalogs and Testing Parametric Galaxy Fitting Codes: GALFIT and GIM2D. *ApJS*, 172:615–633, October 2007. doi: 10.1086/518836. 35

G. Helou, B. T. Soifer, and M. Rowan-Robinson. Thermal infrared and nonthermal radio - Remarkable correlation in disks of galaxies. *ApJL*, 298:L7–L11, November 1985. doi: 10.1086/184556. 24, 27

R. C. Hickox, J. R. Mullaney, D. M. Alexander, C.-T. J. Chen, F. M. Civano, A. D. Goulding, and K. N. Hainline. Black Hole Variability and the Star Formation-Active Galactic Nucleus Connection: Do All Star-forming Galaxies Host an Active Galactic Nucleus? *ApJ*, 782:9, February 2014. doi: 10.1088/0004-637X/782/1/9. 8, 16

R. H. Hildebrand. The Determination of Cloud Masses and Dust Characteristics from Submillimetre Thermal Emission. *Quarterly Journal of the RAS*, 24:267, September 1983. 152

D. W. Hogg, I. K. Baldry, M. R. Blanton, and D. J. Eisenstein. The K correction. *ArXiv Astrophysics e-prints*, October 2002. 53

M. A. Holdaway and T. T. Helfer. Interferometric Array Design. In G. B. Taylor, C. L. Carilli, and R. A. Perley, editors, *Synthesis Imaging in Radio Astronomy II*, volume 180 of *Astronomical Society of the Pacific Conference Series*, page 537, 1999. 96

E. J. Hooper, C. D. Impey, C. B. Foltz, and P. C. Hewett. The Radio Properties of Optically Selected Quasars. III. Comparison between Optical and X-Ray Selected Samples. *ApJ*, 473:746, December 1996. doi: 10.1086/178186. 9, 22, 63

A. M. Hopkins and J. F. Beacom. On the Normalization of the Cosmic Star Formation History. *ApJ*, 651:142–154, November 2006. doi: 10.1086/506610. 25

A. M. Hopkins, B. Mobasher, L. Cram, and M. Rowan-Robinson. The PHOENIX Deep Survey: 1.4-GHz source counts. *MNRAS*, 296:839–846, June 1998. doi: 10.1046/j.1365-8711.1998.01403.x. 72

A. M. Hopkins, J. Afonso, B. Chan, L. E. Cram, A. Georgakakis, and B. Mobasher. The Phoenix Deep Survey: The 1.4 GHz Microjansky Catalog. *AJ*, 125:465–477, February 2003. doi: 10.1086/345974. 27

P. F. Hopkins, L. Hernquist, T. J. Cox, and D. Kereš. A Cosmological Framework for the Co-Evolution of Quasars, Supermassive Black Holes, and Elliptical Galaxies. I. Galaxy Mergers and Quasar Activity. *ApJS*, 175:356–389, April 2008. doi: 10.1086/524362. 12, 13, 185

E. Hubble. No. 304. N.G.C. 6822, a remote stellar system. *Contributions from the Mount Wilson Observatory / Carnegie Institution of Washington*, 304:1–25, 1925. 1

E. Hubble. A Relation between Distance and Radial Velocity among Extra-Galactic Nebulae. *Proceedings of the National Academy of Science*, 15:168–173, March 1929. doi: 10.1073/pnas.15.3.168. 1

E. P. Hubble. *Realm of the Nebulae*. 1936. 3

M. Huynh and J. Lazio. An Overview of the Square Kilometre Array. *ArXiv e-prints*, November 2013. 188

O. Ilbert, S. Arnouts, H. J. McCracken, M. Bolzonella, E. Bertin, O. Le Fèvre, Y. Mellier, G. Zamorani, R. Pellò, A. Iovino, L. Tresse, V. Le Brun, D. Bottini, B. Garilli, D. Maccagni, J. P. Picat, R. Scaramella, M. Scodeggio, G. Vettolani, A. Zanichelli, C. Adami, S. Bardelli, A. Cappi, S. Charlot, P. Ciliegi, T. Contini, O. Cucciati, S. Foucaud, P. Franzetti, I. Gavignaud, L. Guzzo, B. Marano, C. Marinoni, A. Mazure, B. Meneux, R. Merighi, S. Paltani, A. Pollo, L. Pozzetti, M. Radovich, E. Zucca, M. Bondi, A. Bongiorno, G. Busarello, S. de La Torre, L. Gregorini, F. Lamareille, G. Mathez, P. Merluzzi, V. Ripepi, D. Rizzo, and D. Vergani. Accurate photometric redshifts for the CFHT legacy survey calibrated using the VIMOS VLT deep survey. *A&A*, 457:841–856, October 2006. doi: 10.1051/0004-6361:20065138. 38, 50

O. Ilbert, H. J. McCracken, O. Le Fèvre, P. Capak, J. Dunlop, A. Karim, M. A. Renzini, K. Caputi, S. Boissier, S. Arnouts, H. Aussel, J. Comparat, Q. Guo, P. Hudelot, J. Kartaltepe, J. P. Kneib, J. K. Krogager, E. Le Floc'h, S. Lilly, Y. Mellier, B. Milvang-Jensen, T. Moutard, M. Onodera, J. Richard, M. Salvato, D. B. Sanders, N. Scoville, J. D. Silverman, Y. Taniguchi, L. Tasca, R. Thomas, S. Toft, L. Tresse, D. Vergani, M. Wolk, and A. Zirm. Mass assembly in quiescent and star-forming galaxies since z $\simeq$ 4 from UltraVISTA. *A&A*, 556:A55, August 2013. doi: 10.1051/0004-6361/201321100. 8

W. Ishibashi and A. C. Fabian. Active galactic nucleus feedback and triggering of star formation in galaxies. *MNRAS*, 427:2998–3005, December 2012. doi: 10.1111/j.1365-2966.2012.22074.x. 181

Z. Ivezić, G. Richards, P. Hall, R. Lupton, A. Jagoda, G. Knapp, J. Gunn, M. Strauss, D. Schlegel, W. Steinhardt, and R. Siverd. Quasar Radio Dichotomy: Two Peaks, or not Two Peaks, that is the Question. In G. T. Richards and P. B. Hall, editors, *AGN Physics with the Sloan Digital Sky Survey*, volume 311 of *Astronomical Society of the Pacific Conference Series*, page 347, June 2004. 20

R. J. Ivison, D. M. Alexander, A. D. Biggs, W. N. Brandt, E. L. Chapin, K. E. K. Coppin, M. J. Devlin, M. Dickinson, J. Dunlop, S. Dye, S. A. Eales, D. T. Frayer, M. Halpern, D. H. Hughes, E. Ibar, A. Kovács, G. Marsden, L. Moncelsi, C. B. Netterfield, E. Pascale, G. Patanchon, D. A. Rafferty, M. Rex, E. Schinnerer, D. Scott, C. Semisch, I. Smail, A. M. Swinbank, M. D. P. Truch, G. S. Tucker, M. P. Viero, F. Walter, A. Weiß, D. V. Wiebe, and Y. Q. Xue. BLAST: the far-infrared/radio correlation in distant galaxies. *MNRAS*, 402:245–258, February 2010a. doi: 10.1111/j.1365-2966.2009.15918.x. 153

R. J. Ivison, B. Magnelli, E. Ibar, P. Andreani, D. Elbaz, B. Altieri, A. Amblard, V. Arumugam, R. Auld, H. Aussel, T. Babbedge, S. Berta, A. Blain, J. Bock, A. Bongiovanni, A. Boselli, V. Buat, D. Burgarella, N. Castro-Rodríguez, A. Cava, J. Cepa, P. Chanial, A. Cimatti, M. Cirasuolo, D. L. Clements, A. Conley, L. Conversi, A. Cooray, E. Daddi, H. Dominguez, C. D. Dowell, E. Dwek, S. Eales, D. Farrah, N. Förster Schreiber, M. Fox, A. Franceschini, W. Gear, R. Genzel, J. Glenn, M. Griffin, C. Gruppioni, M. Halpern, E. Hatziminaoglou, K. Isaak, G. Lagache, L. Levenson, N. Lu, D. Lutz, S. Madden, B. Maffei, G. Magdis, G. Mainetti, R. Maiolino, L. Marchetti, G. E. Morrison, A. M. J. Mortier, H. T. Nguyen, R. Nordon, B. O'Halloran, S. J. Oliver, A. Omont, F. N. Owen, M. J. Page, P. Panuzzo, A. Papageorgiou, C. P. Pearson, I. Pérez-Fournon, A. M. Pérez García, A. Poglitsch, M. Pohlen, P. Popesso, F. Pozzi, J. I. Rawlings, G. Raymond, D. Rigopoulou, L. Riguccini, D. Rizzo, G. Rodighiero, I. G. Roseboom, M. Rowan-Robinson, A. Saintonge, M. Sanchez Portal, P. Santini, B. Schulz, D. Scott, N. Seymour, L. Shao, D. L. Shupe, A. J. Smith, J. A. Stevens, E. Sturm, M. Symeonidis, L. Tacconi, M. Trichas, K. E. Tugwell, M. Vaccari, I. Valtchanov, J. Vieira,

L. Vigroux, L. Wang, R. Ward, G. Wright, C. K. Xu, and M. Zemcov. The far-infrared/radio correlation as probed by Herschel. *A&A*, 518:L31, July 2010b. doi: 10.1051/0004-6361/201014552. 169

M. Jarvis, N. Seymour, J. Afonso, P. Best, R. Beswick, I. Heywood, M. Huynh, E. Murphy, I. Prandoni, E. Schinnerer, C. Simpson, M. Vaccari, and S. White. The star-formation history of the Universe with the SKA. *Advancing Astrophysics with the Square Kilometre Array (AASKA14)*, art. 68, 2015. 188

M. J. Jarvis. Multi-wavelength Extragalactic Surveys and the Role of MeerKAT and SALT. *African Skies*, 16:44, March 2012. 188

M. J. Jarvis and S. Rawlings. The accretion history of the universe with the SKA. *New Astron. Rev.*, 48:1173–1185, December 2004. doi: 10.1016/j.newar.2004.09.006. 22

M. J. Jarvis, S. Rawlings, M. Lacy, K. M. Blundell, A. J. Bunker, S. Eales, R. Saunders, H. Spinrad, D. Stern, and C. J. Willott. A sample of 6C radio sources designed to find objects at redshift z > 4 - II. Spectrophotometry and emission-line properties. *MNRAS*, 326:1563–1584, October 2001. doi: 10.1111/j.1365-8711.2001.04726.x. 72

M. J. Jarvis, D. G. Bonfield, V. A. Bruce, J. E. Geach, K. McAlpine, R. J. McLure, E. González-Solares, M. Irwin, J. Lewis, A. K. Yoldas, S. Andreon, N. J. G. Cross, J. P. Emerson, G. Dalton, J. S. Dunlop, S. T. Hodgkin, F. O. Le, M. Karouzos, K. Meisenheimer, S. Oliver, S. Rawlings, C. Simpson, I. Smail, D. J. B. Smith, M. Sullivan, W. Sutherland, S. V. White, and J. T. L. Zwart. The VISTA Deep Extragalactic Observations (VIDEO) survey. *MNRAS*, 428:1281–1295, January 2013. doi: 10.1093/mnras/sts118. 33, 35, 54

R. C. Jennison. A phase sensitive interferometer technique for the measurement of the Fourier transforms of spatial brightness distributions of small angular extent. *MNRAS*, 118:276, 1958. 95

R. Johnston, M. Vaccari, M. Jarvis, M. Smith, E. Giovannoli, B. Häußler, and M. Prescott. The evolving relation between star-formation rate and stellar mass in the VIDEO Survey since $z=3$. *ArXiv e-prints*, July 2015. 161

E. Kalfountzou, M. J. Jarvis, D. G. Bonfield, and M. J. Hardcastle. Star formation in high-redshift quasars: excess [O II] emission in the radio-loud population. *MNRAS*, 427:2401–2410, December 2012. doi: 10.1111/j.1365-2966.2012.22093.x. 14, 184

E. Kalfountzou, J. A. Stevens, M. J. Jarvis, M. J. Hardcastle, D. J. B. Smith, N. Bourne, L. Dunne, E. Ibar, S. Eales, R. J. Ivison, S. Maddox, M. W. L. Smith, E. Valiante, and G. de Zotti. Herschel-ATLAS: far-infrared properties of radio-loud and radio-quiet quasars. *MNRAS*, 442:1181–1196, August 2014. doi: 10.1093/mnras/stu782. 14, 152, 184

M. Karouzos, M. Im, M. Trichas, T. Goto, M. Malkan, A. Ruiz, Y. Jeon, J. H. Kim, H. M. Lee, S. J. Kim, N. Oi, H. Matsuhara, T. Takagi, K. Murata, T. Wada, K. Wada, H. Shim, H. Hanami, S. Serjeant, G. J. White, C. Pearson, and Y. Ohyama. A Tale of Two Feedbacks: Star Formation in the Host Galaxies of Radio AGNs. *ApJ*, 784:137, April 2014. doi: 10.1088/0004-637X/784/2/137. 76

G. Kauffmann, T. M. Heckman, C. Tremonti, J. Brinchmann, S. Charlot, S. D. M. White, S. E. Ridgway, J. Brinkmann, M. Fukugita, P. B. Hall, Ž. Ivezić, G. T. Richards, and D. P. Schneider. The host galaxies of active galactic nuclei. *MNRAS*, 346:1055–1077, December 2003. doi: 10.1111/j.1365-2966.2003.07154.x. 28

K. I. Kellermann and F. N. Owen. *Radio galaxies and quasars*, pages 563–602. 1988. 27

K. I. Kellermann, R. Sramek, M. Schmidt, D. B. Shaffer, and R. Green. VLA observations of objects in the Palomar Bright Quasar Survey. *AJ*, 98:1195–1207, October 1989. doi: 10.1086/115207. 9, 63

B. C. Kelly and A. Merloni. Mass Functions of Supermassive Black Holes across Cosmic Time. *Advances in Astronomy*, 2012:970858, 2012. doi: 10.1155/2012/970858. 74

R. C. Kennicutt, Jr. Star Formation in Galaxies Along the Hubble Sequence. *ARA&A*, 36:189–232, 1998. doi: 10.1146/annurev.astro.36.1.189. 160

L. J. Kewley, M. A. Dopita, R. S. Sutherland, C. A. Heisler, and J. Trevena. Theoretical Modeling of Starburst Galaxies. *ApJ*, 556:121–140, July 2001. doi: 10.1086/321545. 28

A. E. Kimball, K. I. Kellermann, J. J. Condon, Ž. Ivezić, and R. A. Perley. The Two-component Radio Luminosity Function of Quasi-stellar Objects: Star Formation and Active Galactic Nucleus. *ApJL*, 739:L29, September 2011. doi: 10.1088/2041-8205/739/1/L29. 22, 27, 61, 68, 69, 72, 81, 82, 181

A. King. Black Holes, Galaxy Formation, and the M_{BH}-σ Relation. *ApJL*, 596:L27–L29, October 2003. doi: 10.1086/379143. 6

A. R. King, J. E. Pringle, and J. A. Hofmann. The evolution of black hole mass and spin in active galactic nuclei. *MNRAS*, 385:1621–1627, April 2008. doi: 10.1111/j.1365-2966.2008.12943.x. 20

A. Kirkpatrick, A. Pope, D. M. Alexander, V. Charmandaris, E. Daddi, M. Dickinson, D. Elbaz, J. Gabor, H. S. Hwang, R. Ivison, J. Mullaney, M. Pannella, D. Scott, B. Altieri, H. Aussel, F. Bournaud, V. Buat, D. Coia, H. Dannerbauer, K. Dasyra, J. Kartaltepe, R. Leiton, L. Lin, G. Magdis, B. Magnelli, G. Morrison, P. Popesso, and I. Valtchanov. GOODS-Herschel: Impact of Active Galactic Nuclei and Star Formation Activity on Infrared Spectral Energy Distributions at High Redshift. *ApJ*, 759:139, November 2012. doi: 10.1088/0004-637X/759/2/139. 26

H. A. Kobulnicky, K. H. Nordsieck, E. B. Burgh, M. P. Smith, J. W. Percival, T. B. Williams, and D. O'Donoghue. Prime focus imaging spectrograph for the Southern African large telescope: operational modes. In M. Iye and A. F. M. Moorwood, editors, *Instrument Design and Performance for Optical/Infrared Ground-based Telescopes*, volume 4841 of *Society of Photo-Optical Instrumentation Engineers (SPIE) Conference Series*, pages 1634–1644, March 2003. doi: 10.1117/12.460315. 45

C. Lacey and S. Cole. Merger rates in hierarchical models of galaxy formation. *MNRAS*, 262:627–649, June 1993. 4

M. Lacy, S. A. Laurent-Muehleisen, S. E. Ridgway, R. H. Becker, and R. L. White. The Radio Luminosity-Black Hole Mass Correlation for Quasars from the FIRST Bright Quasar Survey and a "Unification Scheme" for Radio-loud and Radio-quiet Quasars. *ApJL*, 551:L17–L21, April 2001. doi: 10.1086/319836. 20

M. Lacy, L. J. Storrie-Lombardi, A. Sajina, P. N. Appleton, L. Armus, S. C. Chapman, P. I. Choi, D. Fadda, F. Fang, D. T. Frayer, I. Heinrichsen, G. Helou, M. Im, F. R. Marleau, F. Masci, D. L. Shupe, B. T. Soifer, J. Surace, H. I. Teplitz, G. Wilson, and L. Yan. Obscured and Unobscured Active Galactic Nuclei in the Spitzer Space Telescope First Look Survey. *ApJS*, 154:166–169, September 2004. doi: 10.1086/422816. 43, 44, 185

G. Lagache, H. Dole, and J.-L. Puget. Modelling infrared galaxy evolution using a phenomenological approach. *MNRAS*, 338:555–571, January 2003. doi: 10.1046/j.1365-8711.2003.05971.x. 155

A. Laor and E. Behar. On the origin of radio emission in radio-quiet quasars. *MNRAS*, 390:847–862, October 2008. doi: 10.1111/j.1365-2966.2008.13806.x. 184

O. Le Fèvre, P. Cassata, O. Cucciati, B. Garilli, O. Ilbert, V. Le Brun, D. Maccagni, C. Moreau, M. Scodeggio, L. Tresse, G. Zamorani, C. Adami, S. Arnouts, S. Bardelli, M. Bolzonella, M. Bondi, A. Bongiorno, D. Bottini, A. Cappi, S. Charlot, P. Ciliegi, T. Contini, S. de la Torre, S. Foucaud, P. Franzetti, I. Gavignaud, L. Guzzo, A. Iovino, B. Lemaux, C. López-Sanjuan, H. J. McCracken, B. Marano, C. Marinoni, A. Mazure, Y. Mellier, R. Merighi, P. Merluzzi, S. Paltani, R. Pellò, A. Pollo, L. Pozzetti, R. Scaramella, L. Tasca, D. Vergani, G. Vettolani, A. Zanichelli, and E. Zucca. The VIMOS VLT Deep Survey final data release: a spectroscopic sample of 35 016 galaxies and AGN out to z ~ 6.7 selected with $17.5 \leq i_{AB} \leq 24.75$. *A&A*, 559:A14, November 2013. doi: 10.1051/0004-6361/201322179. 33

C. Leipski, K. Meisenheimer, F. Walter, U. Klaas, H. Dannerbauer, G. De Rosa, X. Fan, M. Haas, O. Krause, and H.-W. Rix. Spectral Energy Distributions of QSOs at $z > 5$: Common Active Galactic Nucleus-heated Dust and Occasionally Strong Star-formation. *ApJ*, 785:154, April 2014. doi: 10.1088/0004-637X/785/2/154. 153

Y. Li and G. L. Bryan. Modeling Active Galactic Nucleus Feedback in Cool-core Clusters: The Balance between Heating and Cooling. *ApJ*, 789:54, July 2014. doi: 10.1088/0004-637X/789/1/54. 15

S. J. Lilly, C. M. Carollo, A. Pipino, A. Renzini, and Y. Peng. Gas Regulation of Galaxies: The Evolution of the Cosmic Specific Star Formation Rate, the Metallicity-Mass-Star-formation Rate Relation, and the Stellar Content of Halos. *ApJ*, 772:119, August 2013. doi: 10.1088/0004-637X/772/2/119. 6

Y.-T. Lin, Y. Shen, M. A. Strauss, G. T. Richards, and R. Lunnan. On the Populations of Radio Galaxies with Extended Morphology at z < 0.3. *ApJ*, 723:1119–1138, November 2010. doi: 10.1088/0004-637X/723/2/1119. 20

C. J. Lonsdale, H. E. Smith, M. Rowan-Robinson, J. Surace, D. Shupe, C. Xu, S. Oliver, D. Padgett, F. Fang, T. Conrow, A. Franceschini, N. Gautier, M. Griffin, P. Hacking, F. Masci, G. Morrison, J. O'Linger, F. Owen, I. Pérez-Fournon, M. Pierre, R. Puetter, G. Stacey, S. Castro, M. d. C. Polletta, D. Farrah, T. Jarrett, D. Frayer, B. Siana, T. Babbedge, S. Dye, M. Fox, E. Gonzalez-Solares, M. Salaman, S. Berta, J. J. Condon, H. Dole, and S. Serjeant. SWIRE: The SIRTF Wide-Area Infrared Extragalactic Survey. *PASP*, 115:897–927, August 2003. doi: 10.1086/376850. 34

P. Madau and M. Dickinson. Cosmic Star-Formation History. *ARA&A*, 52:415–486, August 2014. doi: 10.1146/annurev-astro-081811-125615. 26

P. Madau, H. C. Ferguson, M. E. Dickinson, M. Giavalisco, C. C. Steidel, and A. Fruchter. High-redshift galaxies in the Hubble Deep Field: colour selection and star formation history to z˜4. *MNRAS*, 283:1388–1404, December 1996. 25, 181

N. Maddox, P. C. Hewett, S. J. Warren, and S. M. Croom. Luminous K-band selected quasars from UKIDSS. *MNRAS*, 386:1605–1624, May 2008. doi: 10.1111/j.1365-2966.2008.13138.x. 34, 38, 42

N. Maddox, P. C. Hewett, C. Péroux, D. B. Nestor, and L. Wisotzki. The large area KX quasar catalogue - I. Analysis of the photometric redshift selection and the complete quasar catalogue. *MNRAS*, 424:2876–2895, August 2012. doi: 10.1111/j.1365-2966.2012.21427.x. 41

B. Magnelli, P. Popesso, S. Berta, F. Pozzi, D. Elbaz, D. Lutz, M. Dickinson, B. Altieri, P. Andreani, H. Aussel, M. Béthermin, A. Bongiovanni, J. Cepa, V. Charmandaris, R.-R. Chary, A. Cimatti, E. Daddi, N. M. Förster Schreiber, R. Genzel, C. Gruppioni, M. Harwit, H. S. Hwang, R. J. Ivison, G. Magdis, R. Maiolino, E. Murphy, R. Nordon, M. Pannella, A. Pérez García, A. Poglitsch, D. Rosario, M. Sanchez-Portal, P. Santini, D. Scott, E. Sturm, L. J. Tacconi, and I. Valtchanov. The deepest Herschel-PACS far-infrared survey: number counts and infrared luminosity functions from combined PEP/GOODS-H observations. *A&A*, 553:A132, May 2013. doi: 10.1051/0004-6361/201321371. 155

A. Martínez-Sansigre, S. Rawlings, M. Lacy, D. Fadda, M. J. Jarvis, F. R. Marleau, C. Simpson, and C. J. Willott. A population of high-redshift type 2 quasars - I. Selection criteria and optical spectra. *MNRAS*, 370:1479–1498, August 2006. doi: 10.1111/j.1365-2966.2006.10563.x. 185

K. L. Masters. A Zoo of Galaxies. *ArXiv e-prints*, March 2013. 2, 3

J. S. Mathis. Interstellar dust and extinction. *ARA&A*, 28:37–70, 1990. doi: 10.1146/annurev.aa.28.090190.000345. 26

K. McAlpine, D. J. B. Smith, M. J. Jarvis, D. G. Bonfield, and S. Fleuren. The likelihood ratio as a tool for radio continuum surveys with Square Kilometre Array precursor telescopes. *MNRAS*, 423:132–140, June 2012. doi: 10.1111/j.1365-2966.2012.20715.x. 34

K. McAlpine, I. Prandoni, M. Jarvis, N. Seymour, P. Padovani, P. Best, C. Simpson, D. Guidetti, E. Murphy, M. Huynh, M. Vaccari, S. White, R. Beswick, J. Afonso, M. Magliocchetti, and M. Bondi. The SKA view of the Interplay between SF and AGN Activity and its role in Galaxy Evolution. *Advancing Astrophysics with the Square Kilometre Array (AASKA14)*, art. 83, 2015. 188

R. J. McLure and J. S. Dunlop. The cosmological evolution of quasar black hole masses. *MNRAS*, 352:1390–1404, August 2004. doi: 10.1111/j.1365-2966.2004.08034.x. 12, 74, 77

R. J. McLure and M. J. Jarvis. Measuring the black hole masses of high-redshift quasars. *MNRAS*, 337:109–116, November 2002. doi: 10.1046/j.1365-8711.2002.05871.x. 73, 161

R. J. McLure and M. J. Jarvis. The relationship between radio luminosity and black hole mass in optically selected quasars. *MNRAS*, 353:L45–L49, October 2004. doi: 10.1111/j.1365-2966.2004.08305.x. 20

R. J. McLure, M. J. Jarvis, T. A. Targett, J. S. Dunlop, and P. N. Best. On the evolution of the black hole: spheroid mass ratio. *MNRAS*, 368:1395–1403, May 2006. doi: 10.1111/j.1365-2966.2006.10228.x. 73

R. G. McMahon, M. Banerji, E. Gonzalez, S. E. Koposov, V. J. Bejar, N. Lodieu, R. Rebolo, and VHS Collaboration. First Scientific Results from the VISTA Hemisphere Survey (VHS). *The Messenger*, 154:35–37, December 2013. 188

J. P. McMullin, B. Waters, D. Schiebel, W. Young, and K. Golap. CASA Architecture and Applications. In R. A. Shaw, F. Hill, and D. J. Bell, editors, *Astronomical Data Analysis Software and Systems XVI*, volume 376 of *Astronomical Society of the Pacific Conference Series*, page 127, October 2007. 103

B. R. McNamara and P. E. J. Nulsen. Heating Hot Atmospheres with Active Galactic Nuclei. *ARA&A*, 45:117–175, September 2007. doi: 10.1146/annurev.astro.45.051806.110625. 14

L. Miller, J. A. Peacock, and A. R. G. Mead. The bimodal radio luminosity function of quasars. *MNRAS*, 244:207–213, May 1990. 63

K. J. Mitchell and J. J. Condon. A confusion-limited 1.49-GHz VLA survey centered on alpha = 13 H 00 M 37 s, delta = + 30 deg 34 arcmin. *AJ*, 90:1957–1966, October 1985. doi: 10.1086/113899. 23

K. Mitchell-Wynne, M. G. Santos, J. Afonso, and M. J. Jarvis. Beyond stacking: a maximum-likelihood method to constrain radio source counts below the detection threshold. *MNRAS*, 437:2270–2278, January 2014. doi: 10.1093/mnras/stt2035. 63, 186

K. D. Moller. *Optics*. University Science Books: Mill Valley, Ca., 1988. 89

R. Morganti, W. Frieswijk, R. J. B. Oonk, T. Oosterloo, and C. Tadhunter. Tracing the extreme interplay between radio jets and the ISM in IC 5063. *A&A*, 552:L4, April 2013. doi: 10.1051/0004-6361/201220734. 14

D. J. Mortlock, M. Patel, S. J. Warren, P. C. Hewett, B. P. Venemans, R. G. McMahon, and C. Simpson. Probabilistic selection of high-redshift quasars. *MNRAS*, 419:390–410, January 2012. doi: 10.1111/j.1365-2966.2011.19710.x. 34

B. P. Moster, A. V. Macciò, R. S. Somerville, P. H. Johansson, and T. Naab. Can gas prevent the destruction of thin stellar discs by minor mergers? *MNRAS*, 403:1009–1019, April 2010. doi: 10.1111/j.1365-2966.2009.16190.x. 2

J. Moustakas, A. L. Coil, J. Aird, M. R. Blanton, R. J. Cool, D. J. Eisenstein, A. J. Mendez, K. C. Wong, G. Zhu, and S. Arnouts. PRIMUS: Constraints on Star Formation Quenching and Galaxy Merging, and the Evolution of the Stellar Mass Function from z = 0-1. *ApJ*, 767:50, April 2013. doi: 10.1088/0004-637X/767/1/50. 8

E. J. Murphy. The Far-Infrared-Radio Correlation at High Redshifts: Physical Considerations and Prospects for the Square Kilometer Array. *ApJ*, 706:482–496, November 2009. doi: 10.1088/0004-637X/706/1/482. 169

P. J. Napier. The Primary Antenna Elements. In G. B. Taylor, C. L. Carilli, and R. A. Perley, editors, *Synthesis Imaging in Radio Astronomy II*, volume 180 of *Astronomical Society of the Pacific Conference Series*, page 37, 1999. 91

P. J. Napier, A. R. Thompson, and R. D. Ekers. The Very Large Array - Design and performance of a modern synthesis radio telescope. *IEEE Proceedings*, 71:1295–1320, November 1983. 86

H. Netzer. Accretion and star formation rates in low-redshift type II active galactic nuclei. *MNRAS*, 399:1907–1920, November 2009. doi: 10.1111/j.1365-2966.2009.15434.x. 17

H. Netzer, D. Lutz, M. Schweitzer, A. Contursi, E. Sturm, L. J. Tacconi, S. Veilleux, D.-C. Kim, D. Rupke, A. J. Baker, K. Dasyra, J. Mazzarella, and S. Lord. Spitzer Quasar and ULIRG Evolution Study (QUEST). II. The Spectral Energy Distributions of Palomar-Green Quasars. *ApJ*, 666:806–816, September 2007. doi: 10.1086/520716. 27

H. T. Nguyen, B. Schulz, L. Levenson, A. Amblard, V. Arumugam, H. Aussel, T. Babbedge, A. Blain, J. Bock, A. Boselli, V. Buat, N. Castro-Rodriguez, A. Cava, P. Chanial, E. Chapin, D. L. Clements, A. Conley, L. Conversi, A. Cooray, C. D. Dowell, E. Dwek, S. Eales, D. Elbaz, M. Fox, A. Franceschini, W. Gear, J. Glenn, M. Griffin, M. Halpern, E. Hatziminaoglou, E. Ibar, K. Isaak, R. J. Ivison, G. Lagache, N. Lu, S. Madden, B. Maffei, G. Mainetti, L. Marchetti, G. Marsden, J. Marshall, B. O'Halloran, S. J. Oliver, A. Omont, M. J. Page, P. Panuzzo, A. Papageorgiou, C. P. Pearson, I. Perez Fournon, M. Pohlen, N. Rangwala, D. Rigopoulou, D. Rizzo, I. G. Roseboom, M. Rowan-Robinson, D. Scott, N. Seymour, D. L. Shupe, A. J. Smith, J. A. Stevens, M. Symeonidis, M. Trichas, K. E. Tugwell, M. Vaccari, I. Valtchanov, L. Vigroux, L. Wang, R. Ward, D. Wiebe, G. Wright, C. K. Xu, and M. Zemcov. HerMES: The SPIRE confusion limit. *A&A*, 518:L5, July 2010. doi: 10.1051/0004-6361/201014680. 155

K. G. Noeske, B. J. Weiner, S. M. Faber, C. Papovich, D. C. Koo, R. S. Somerville, K. Bundy, C. J. Conselice, J. A. Newman, D. Schiminovich, E. Le Floc'h, A. L. Coil, G. H. Rieke, J. M. Lotz, J. R. Primack, P. Barmby, M. C. Cooper, M. Davis, R. S. Ellis, G. G. Fazio, P. Guhathakurta, J. Huang, S. A. Kassin, D. C. Martin, A. C. Phillips, R. M. Rich, T. A. Small, C. N. A. Willmer, and G. Wilson. Star Formation in AEGIS Field Galaxies since z=1.1: The Dominance of Gradually Declining Star Formation, and the Main Sequence of Star-forming Galaxies. *ApJL*, 660:L43–L46, May 2007. doi: 10.1086/517926. 68, 73, 74, 76, 161

R. P. Norris, A. M. Hopkins, J. Afonso, S. Brown, J. J. Condon, L. Dunne, I. Feain, R. Hollow, M. Jarvis, M. Johnston-Hollitt, E. Lenc, E. Middelberg, P. Padovani, I. Prandoni, L. Rudnick, N. Seymour, G. Umana, H. Andernach, D. M. Alexander, P. N. Appleton, D. Bacon, J. Banfield, W. Becker, M. J. I. Brown, P. Ciliegi, C. Jackson, S. Eales, A. C. Edge, B. M. Gaensler, G. Giovannini, C. A. Hales, P. Hancock, M. T. Huynh, E. Ibar, R. J. Ivison, R. Kennicutt, A. E. Kimball, A. M. Koekemoer, B. S. Koribalski, Á. R.

López-Sánchez, M. Y. Mao, T. Murphy, H. Messias, K. A. Pimbblet, A. Raccanelli, K. E. Randall, T. H. Reiprich, I. G. Roseboom, H. Röttgering, D. J. Saikia, R. G. Sharp, O. B. Slee, I. Smail, M. A. Thompson, J. S. Urquhart, J. V. Wall, and G.-B. Zhao. EMU: Evolutionary Map of the Universe. *PASA*, 28:215–248, August 2011. doi: 10.1071/AS11021. 188

J. B. Oke and A. Sandage. Energy Distributions, K Corrections, and the Stebbins-Whitford Effect for Giant Elliptical Galaxies. *ApJ*, 154:21, October 1968. doi: 10.1086/149737. 53

S. J. Oliver, J. Bock, B. Altieri, A. Amblard, V. Arumugam, H. Aussel, T. Babbedge, A. Beelen, M. Béthermin, A. Blain, A. Boselli, C. Bridge, D. Brisbin, V. Buat, D. Burgarella, N. Castro-Rodríguez, A. Cava, P. Chanial, M. Cirasuolo, D. L. Clements, A. Conley, L. Conversi, A. Cooray, C. D. Dowell, E. N. Dubois, E. Dwek, S. Dye, S. Eales, D. Elbaz, D. Farrah, A. Feltre, P. Ferrero, N. Fiolet, M. Fox, A. Franceschini, W. Gear, E. Giovannoli, J. Glenn, Y. Gong, E. A. González Solares, M. Griffin, M. Halpern, M. Harwit, E. Hatziminaoglou, S. Heinis, P. Hurley, H. S. Hwang, A. Hyde, E. Ibar, O. Ilbert, K. Isaak, R. J. Ivison, G. Lagache, E. Le Floc'h, L. Levenson, B. L. Faro, N. Lu, S. Madden, B. Maffei, G. Magdis, G. Mainetti, L. Marchetti, G. Marsden, J. Marshall, A. M. J. Mortier, H. T. Nguyen, B. O'Halloran, A. Omont, M. J. Page, P. Panuzzo, A. Papageorgiou, H. Patel, C. P. Pearson, I. Pérez-Fournon, M. Pohlen, J. I. Rawlings, G. Raymond, D. Rigopoulou, L. Riguccini, D. Rizzo, G. Rodighiero, I. G. Roseboom, M. Rowan-Robinson, M. Sánchez Portal, B. Schulz, D. Scott, N. Seymour, D. L. Shupe, A. J. Smith, J. A. Stevens, M. Symeonidis, M. Trichas, K. E. Tugwell, M. Vaccari, I. Valtchanov, J. D. Vieira, M. Viero, L. Vigroux, L. Wang, R. Ward, J. Wardlow, G. Wright, C. K. Xu, and M. Zemcov. The Herschel Multi-tiered Extragalactic Survey: HerMES. *MNRAS*, 424:1614–1635, August 2012. doi: 10.1111/j.1365-2966.2012.20912.x. 86

D. E. Osterbrock. Seyfert galaxies with weak broad H alpha emission lines. *ApJ*, 249: 462–470, October 1981. doi: 10.1086/159306. 12

P. Padovani, M. Bonzini, N. Miller, K. I. Kellermann, V. Mainieri, P. Rosati, P. Tozzi, and S. Vattakunnel. The AGN content of deep radio surveys and radio emission in radio-quiet AGN. Why every astronomer should care about deep radio fields. In *IAU Symposium*, volume 304 of *IAU Symposium*, pages 79–85, July 2014. doi: 10.1017/S1743921314003391. 22, 23, 76

I. Pâris, P. Petitjean, É. Aubourg, N. P. Ross, A. D. Myers, A. Streblyanska, S. Bailey, P. B. Hall, M. A. Strauss, S. F. Anderson, D. Bizyaev, A. Borde, J. Brinkmann, J. Bovy, W. N. Brandt, H. Brewington, J. R. Brownstein, B. A. Cook, G. Ebelke, X. Fan, N. Filiz Ak, H. Finley, A. Font-Ribera, J. Ge, F. Hamann, S. Ho, L. Jiang, K. Kinemuchi, E. Malanushenko, V. Malanushenko, M. Marchante, I. D. McGreer, R. G. McMahon, J. Miralda-Escudé, D. Muna, P. Noterdaeme, D. Oravetz, N. Palanque-Delabrouille, K. Pan, I. Perez-Fournon, M. Pieri, R. Riffel, D. J. Schlegel, D. P. Schneider, A. Simmons, M. Viel, B. A. Weaver, W. M. Wood-Vasey, C. Yèche, and D. G. York. The Sloan Digital Sky Survey quasar catalog: tenth data release. *A&A*, 563:A54, March 2014. doi: 10.1051/0004-6361/201322691. 53

G. Patanchon, P. A. R. Ade, J. J. Bock, E. L. Chapin, M. J. Devlin, S. R. Dicker, M. Griffin, J. O. Gundersen, M. Halpern, P. C. Hargrave, D. H. Hughes, J. Klein, G. Marsden, P. Mauskopf, L. Moncelsi, C. B. Netterfield, L. Olmi, E. Pascale, M. Rex, D. Scott, C. Semisch, N. Thomas, M. D. P. Truch, C. Tucker, G. S. Tucker, M. P. Viero, and D. V. Wiebe. Submillimeter Number Counts from Statistical Analysis of BLAST Maps. *ApJ*, 707:1750–1765, December 2009. doi: 10.1088/0004-637X/707/2/1750. 186

J. A. Peacock, L. Miller, and M. S. Longair. The statistics of radio emission from quasars. *MNRAS*, 218:265–278, January 1986. 9

P. J. E. Peebles. Large-scale background temperature and mass fluctuations due to scale-invariant primeval perturbations. *ApJL*, 263:L1–L5, December 1982. doi: 10.1086/183911. 2

C. Y. Peng, C. D. Impey, L. C. Ho, E. J. Barton, and H.-W. Rix. Probing the Coevolution of Supermassive Black Holes and Quasar Host Galaxies. *ApJ*, 640:114–125, March 2006. doi: 10.1086/499930. 73

Y.-j. Peng, S. J. Lilly, K. Kovač, M. Bolzonella, L. Pozzetti, A. Renzini, G. Zamorani, O. Ilbert, C. Knobel, A. Iovino, C. Maier, O. Cucciati, L. Tasca, C. M. Carollo, J. Silverman, P. Kampczyk, L. de Ravel, D. Sanders, N. Scoville, T. Contini, V. Mainieri, M. Scodeggio, J.-P. Kneib, O. Le Fèvre, S. Bardelli, A. Bongiorno, K. Caputi, G. Coppa, S. de la Torre, P. Franzetti, B. Garilli, F. Lamareille, J.-F. Le Borgne, V. Le Brun, M. Mignoli, E. Perez Montero, R. Pello, E. Ricciardelli, M. Tanaka, L. Tresse, D. Vergani, N. Welikala, E. Zucca, P. Oesch, U. Abbas, L. Barnes, R. Bordoloi, D. Bottini, A. Cappi, P. Cassata, A. Cimatti, M. Fumana, G. Hasinger, A. Koekemoer, A. Leauthaud, D. Maccagni, C. Marinoni, H. McCracken, P. Memeo, B. Meneux, P. Nair, C. Porciani, V. Presotto, and R. Scaramella. Mass and Environment as Drivers of Galaxy Evolution in SDSS and zCOSMOS and the Origin of the Schechter Function. *ApJ*, 721:193–221, September 2010. doi: 10.1088/0004-637X/721/1/193. 6

R. A. Perley and B. J. Butler. An Accurate Flux Density Scale from 1 to 50 GHz. *ApJS*, 204:19, February 2013. doi: 10.1088/0067-0049/204/2/19. 105, 106

B. M. Peterson. *An Introduction to Active Galactic Nuclei*. February 1997. 9

G. L. Pilbratt, J. R. Riedinger, T. Passvogel, G. Crone, D. Doyle, U. Gageur, A. M. Heras, C. Jewell, L. Metcalfe, S. Ott, and M. Schmidt. Herschel Space Observatory. An ESA facility for far-infrared and submillimetre astronomy. *A&A*, 518:L1, July 2010. doi: 10.1051/0004-6361/201014759. 86

A. Poglitsch, C. Waelkens, N. Geis, H. Feuchtgruber, B. Vandenbussche, L. Rodriguez, O. Krause, E. Renotte, C. van Hoof, P. Saraceno, J. Cepa, F. Kerschbaum, P. Agnèse, B. Ali, B. Altieri, P. Andreani, J.-L. Augueres, Z. Balog, L. Barl, O. H. Bauer, N. Belbachir, M. Benedettini, N. Billot, O. Boulade, H. Bischof, J. Blommaert, E. Callut, C. Cara, R. Cerulli, D. Cesarsky, A. Contursi, Y. Creten, W. De Meester, V. Doublier, E. Doumayrou, L. Duband, K. Exter, R. Genzel, J.-M. Gillis, U. Grözinger, T. Henning, J. Herreros, R. Huygen, M. Inguscio, G. Jakob, C. Jamar, C. Jean, J. de Jong, R. Katterloher, C. Kiss, U. Klaas, D. Lemke, D. Lutz, S. Madden, B. Marquet, J. Martignac, A. Mazy, P. Merken, F. Montfort, L. Morbidelli, T. Müller, M. Nielbock, K. Okumura, R. Orfei, R. Ottensamer, S. Pezzuto, P. Popesso, J. Putzeys, S. Regibo, V. Reveret,

P. Royer, M. Sauvage, J. Schreiber, J. Stegmaier, D. Schmitt, J. Schubert, E. Sturm, M. Thiel, G. Tofani, R. Vavrek, M. Wetzstein, E. Wieprecht, and E. Wiezorrek. The Photodetector Array Camera and Spectrometer (PACS) on the Herschel Space Observatory. *A&A*, 518:L2, July 2010. doi: 10.1051/0004-6361/201014535. 86

M. Polletta, M. Tajer, L. Maraschi, G. Trinchieri, C. J. Lonsdale, L. Chiappetti, S. Andreon, M. Pierre, O. Le Fèvre, G. Zamorani, D. Maccagni, O. Garcet, J. Surdej, A. Franceschini, D. Alloin, D. L. Shupe, J. A. Surace, F. Fang, M. Rowan-Robinson, H. E. Smith, and L. Tresse. Spectral Energy Distributions of Hard X-Ray Selected Active Galactic Nuclei in the XMM-Newton Medium Deep Survey. *ApJ*, 663:81–102, July 2007. doi: 10.1086/518113. 38

M. d. C. Polletta, B. J. Wilkes, B. Siana, C. J. Lonsdale, R. Kilgard, H. E. Smith, D.-W. Kim, F. Owen, A. Efstathiou, T. Jarrett, G. Stacey, A. Franceschini, M. Rowan-Robinson, T. S. R. Babbedge, S. Berta, F. Fang, D. Farrah, E. González-Solares, G. Morrison, J. A. Surace, and D. L. Shupe. Chandra and Spitzer Unveil Heavily Obscured Quasars in the Chandra/SWIRE Survey. *ApJ*, 642:673–693, May 2006. doi: 10.1086/500821. 185

I. Prandoni and N. Seymour. Revealing the Physics and Evolution of Galaxies and Galaxy Clusters with SKA Continuum Surveys. *Advancing Astrophysics with the Square Kilometre Array (AASKA14)*, art. 67, 2015. 187

W. H. Press and P. Schechter. Formation of Galaxies and Clusters of Galaxies by Self-Similar Gravitational Condensation. *ApJ*, 187:425–438, February 1974. doi: 10.1086/152650. 5

B. Punsly. High Jet Efficiency and Simulations of Black Hole Magnetospheres. *ApJL*, 728:L17, February 2011. doi: 10.1088/2041-8205/728/1/L17. 68

B. Punsly and S. Zhang. The Jet Power and Emission-line Correlations of Radio-loud Optically Selected Quasars. *ApJL*, 735:L3, July 2011. doi: 10.1088/2041-8205/735/1/L3. 68, 148

S. Rawlings and R. Saunders. Evidence for a common central-engine mechanism in all extragalactic radio sources. *Nature*, 349:138–140, January 1991. doi: 10.1038/349138a0. 25

R. B. Rengelink, Y. Tang, A. G. de Bruyn, G. K. Miley, M. N. Bremer, H. J. A. Roettgering, and M. A. R. Bremer. The Westerbork Northern Sky Survey (WENSS), I. A 570 square degree Mini-Survey around the North Ecliptic Pole. *A&AS*, 124:259–280, August 1997. doi: 10.1051/aas:1997358. 84

C. S. Reynolds, D. Garofalo, and M. C. Begelman. Trapping of Magnetic Flux by the Plunge Region of a Black Hole Accretion Disk. *ApJ*, 651:1023–1030, November 2006. doi: 10.1086/507691. 183

G. T. Richards, X. Fan, D. P. Schneider, D. E. Vanden Berk, M. A. Strauss, D. G. York, J. E. Anderson, Jr., S. F. Anderson, J. Annis, N. A. Bahcall, M. Bernardi, J. W. Briggs, J. Brinkmann, R. Brunner, S. Burles, L. Carey, F. J. Castander, A. J. Connolly, J. H. Crocker, I. Csabai, M. Doi, D. Finkbeiner, S. D. Friedman, J. A. Frieman, M. Fukugita, J. E. Gunn, R. B. Hindsley, Ž. Ivezić, S. Kent, G. R. Knapp, D. Q. Lamb, R. F. Leger, D. C. Long, J. Loveday, R. H. Lupton, T. A. McKay, A. Meiksin, A. Merrelli, J. A. Munn, H. J. Newberg, M. Newcomb, R. C. Nichol, R. Owen, J. R. Pier, A. Pope, M. W. Richmond, C. M. Rockosi, D. J. Schlegel, W. A. Siegmund, S. Smee, Y. Snir, C. Stoughton, C. Stubbs, M. SubbaRao, A. S. Szalay, G. P. Szokoly, C. Tremonti, A. Uomoto, P. Waddell, B. Yanny, and W. Zheng. Colors of 2625 Quasars at 0<Z<5 Measured in the Sloan Digital Sky Survey Photometric System. *AJ*, 121:2308–2330, May 2001. doi: 10.1086/320392. 38

G. T. Richards, M. Lacy, L. J. Storrie-Lombardi, P. B. Hall, S. C. Gallagher, D. C. Hines, X. Fan, C. Papovich, D. E. Vanden Berk, G. B. Trammell, D. P. Schneider, M. Vestergaard, D. G. York, S. Jester, S. F. Anderson, T. Budavári, and A. S. Szalay. Spectral Energy Distributions and Multiwavelength Selection of Type 1 Quasars. *ApJS*, 166:470–497, October 2006a. doi: 10.1086/506525. 34, 53

G. T. Richards, M. A. Strauss, X. Fan, P. B. Hall, S. Jester, D. P. Schneider, D. E. Vanden Berk, C. Stoughton, S. F. Anderson, R. J. Brunner, J. Gray, J. E. Gunn, Ž. Ivezić, M. K.

Kirkland, G. R. Knapp, J. Loveday, A. Meiksin, A. Pope, A. S. Szalay, A. R. Thakar, B. Yanny, D. G. York, J. C. Barentine, H. J. Brewington, J. Brinkmann, M. Fukugita, M. Harvanek, S. M. Kent, S. J. Kleinman, J. Krzesiński, D. C. Long, R. H. Lupton, T. Nash, E. H. Neilsen, Jr., A. Nitta, D. J. Schlegel, and S. A. Snedden. The Sloan Digital Sky Survey Quasar Survey: Quasar Luminosity Function from Data Release 3. *AJ*, 131:2766–2787, June 2006b. doi: 10.1086/503559. 150

Gordon T. Richards, Xiaohui Fan, Heidi Jo Newberg, Michael A. Strauss, Daniel E. Vanden Berk, Donald P. Schneider, Brian Yanny, Adam Boucher, Scott Burles, Joshua A. Frieman, James E. Gunn, Patrick B. Hall, Željko Ivezić, Stephen Kent, Jon Loveday, Robert H. Lupton, Constance M. Rockosi, David J. Schlegel, Chris Stoughton, Mark SubbaRao, and Donald G. York. Spectroscopic target selection in the sloan digital sky survey: The quasar sample. *The Astronomical Journal*, 123(6):2945, 2002. URL `http://stacks.iop.org/1538-3881/123/i=6/a=2945`. 85

D. J. Rosario, P. Santini, D. Lutz, L. Shao, R. Maiolino, D. M. Alexander, B. Altieri, P. Andreani, H. Aussel, F. E. Bauer, S. Berta, A. Bongiovanni, W. N. Brandt, M. Brusa, J. Cepa, A. Cimatti, T. J. Cox, E. Daddi, D. Elbaz, A. Fontana, N. M. Förster Schreiber, R. Genzel, A. Grazian, E. Le Floch, B. Magnelli, V. Mainieri, H. Netzer, R. Nordon, I. Pérez Garcia, A. Poglitsch, P. Popesso, F. Pozzi, L. Riguccini, G. Rodighiero, M. Salvato, M. Sanchez-Portal, E. Sturm, L. J. Tacconi, I. Valtchanov, and S. Wuyts. The mean star formation rate of X-ray selected active galaxies and its evolution from z ˜ 2.5: results from PEP-Herschel. *A&A*, 545:A45, September 2012. doi: 10.1051/0004-6361/201219258. 16, 17, 181

D. J. Rosario, B. Trakhtenbrot, D. Lutz, H. Netzer, J. R. Trump, J. D. Silverman, M. Schramm, E. Lusso, S. Berta, A. Bongiorno, M. Brusa, N. M. Förster-Schreiber, R. Genzel, S. Lilly, B. Magnelli, V. Mainieri, R. Maiolino, A. Merloni, M. Mignoli, R. Nordon, P. Popesso, M. Salvato, P. Santini, L. J. Tacconi, and G. Zamorani. The mean star-forming properties of QSO host galaxies. *A&A*, 560:A72, December 2013. doi: 10.1051/0004-6361/201322196. 27, 76, 77, 161

I. G. Roseboom and P. N. Best. Cosmic star formation probed via parametric stackfitting of known sources to radio imaging. *MNRAS*, 439:1286–1293, April 2014. doi: 10.1093/mnras/stt2452. 186

M. Rowan-Robinson. A new model for the infrared emission of quasars. *MNRAS*, 272: 737–748, February 1995. 83, 160

D. B. Sanders and I. F. Mirabel. Luminous Infrared Galaxies. *ARA&A*, 34:749, 1996. doi: 10.1146/annurev.astro.34.1.749. 153, 159

D. B. Sanders, B. T. Soifer, J. H. Elias, G. Neugebauer, and K. Matthews. Warm ultraluminous galaxies in the IRAS survey - The transition from galaxy to quasar? *ApJL*, 328:L35–L39, May 1988. doi: 10.1086/185155. 12

D. B. Sanders, E. S. Phinney, G. Neugebauer, B. T. Soifer, and K. Matthews. Continuum energy distribution of quasars - Shapes and origins. *ApJ*, 347:29–51, December 1989. doi: 10.1086/168094. 160

M. Schartmann, K. Meisenheimer, M. Camenzind, S. Wolf, K. R. W. Tristram, and T. Henning. Three-dimensional radiative transfer models of clumpy tori in Seyfert galaxies. *A&A*, 482:67–80, April 2008. doi: 10.1051/0004-6361:20078907. 9

J. Schaye, R. A. Crain, R. G. Bower, M. Furlong, M. Schaller, T. Theuns, C. Dalla Vecchia, C. S. Frenk, I. G. McCarthy, J. C. Helly, A. Jenkins, Y. M. Rosas-Guevara, S. D. M. White, M. Baes, C. M. Booth, P. Camps, J. F. Navarro, Y. Qu, A. Rahmati, T. Sawala, P. A. Thomas, and J. Trayford. The EAGLE project: simulating the evolution and assembly of galaxies and their environments. *MNRAS*, 446:521–554, January 2015. doi: 10.1093/mnras/stu2058. 4, 15

P. A. G. Scheuer. A statistical method for analysing observations of faint radio stars. *Mathematical Proceedings of the Cambridge Philosophical Society*, 53(03):764–773, 1957. doi: 10.1017/S0305004100032825. URL `http://dx.doi.org/10.1017/S0305004100032825`. 186

D. P. Schneider, X. Fan, P. B. Hall, S. Jester, G. T. Richards, C. Stoughton, M. A. Strauss, M. SubbaRao, D. E. Vanden Berk, S. F. Anderson, W. N. Brandt, J. E. Gunn,

J. Gray, J. R. Trump, W. Voges, B. Yanny, N. A. Bahcall, M. R. Blanton, W. N. Boroski, J. Brinkmann, R. Brunner, S. Burles, F. J. Castander, M. Doi, D. Eisenstein, J. A. Frieman, M. Fukugita, T. M. Heckman, G. S. Hennessy, Ž. Ivezić, S. Kent, G. R. Knapp, D. Q. Lamb, B. C. Lee, J. Loveday, R. H. Lupton, B. Margon, A. Meiksin, J. A. Munn, H. J. Newberg, R. C. Nichol, M. Niederste-Ostholt, J. R. Pier, M. W. Richmond, C. M. Rockosi, D. H. Saxe, D. J. Schlegel, A. S. Szalay, A. R. Thakar, A. Uomoto, and D. G. York. The Sloan Digital Sky Survey Quasar Catalog. II. First Data Release. *AJ*, 126:2579–2593, December 2003. doi: 10.1086/379174. 54, 85

D. P. Schneider, P. B. Hall, G. T. Richards, D. E. Vanden Berk, S. F. Anderson, X. Fan, S. Jester, C. Stoughton, M. A. Strauss, M. SubbaRao, W. N. Brandt, J. E. Gunn, B. Yanny, N. A. Bahcall, J. C. Barentine, M. R. Blanton, W. N. Boroski, H. J. Brewington, J. Brinkmann, R. Brunner, I. Csabai, M. Doi, D. J. Eisenstein, J. A. Frieman, M. Fukugita, J. Gray, M. Harvanek, T. M. Heckman, Ž. Ivezić, S. Kent, S. J. Kleinman, G. R. Knapp, R. G. Kron, J. Krzesinski, D. C. Long, J. Loveday, R. H. Lupton, B. Margon, J. A. Munn, E. H. Neilsen, H. J. Newberg, P. R. Newman, R. C. Nichol, A. Nitta, J. R. Pier, C. M. Rockosi, D. H. Saxe, D. J. Schlegel, S. A. Snedden, A. S. Szalay, A. R. Thakar, A. Uomoto, W. Voges, and D. G. York. The Sloan Digital Sky Survey Quasar Catalog. III. Third Data Release. *AJ*, 130:367–380, August 2005. doi: 10.1086/431156. 85

P. Schneider. *Extragalactic Astronomy and Cosmology: An Introduction*. Springer, 2014. 165

N. Z. Scoville. *Secular Evolution of Galaxies, Evolution of star formation and gas*, page 491. Cambridge University Press, October 2013. 26

S. Serjeant, S. Rawlings, M. Lacy, S. J. Maddox, J. C. Baker, D. Clements, and P. B. Lilje. The radio-optical correlation in steep-spectrum quasars. *MNRAS*, 294:494, March 1998. doi: 10.1046/j.1365-8711.1998.01303.x. 68, 148

N. Seymour, M. Huynh, T. Dwelly, M. Symeonidis, A. Hopkins, I. M. McHardy, M. J. Page, and G. Rieke. Investigating the far-IR/radio correlation of star-forming Galaxies to z = 3. *MNRAS*, 398:1573–1581, September 2009. doi: 10.1111/j.1365-2966.2009.15224.x. 167

F. Shankar, D. H. Weinberg, and J. Miralda-Escudé. Self-Consistent Models of the AGN and Black Hole Populations: Duty Cycles, Accretion Rates, and the Mean Radiative Efficiency. *ApJ*, 690:20–41, January 2009. doi: 10.1088/0004-637X/690/1/20. 26

T. Shanks, N. Metcalfe, B. Chehade, J. R. Findlay, M. J. Irwin, E. Gonzalez-Solares, J. R. Lewis, A. K. Yoldas, R. G. Mann, M. A. Read, E. T. W. Sutorius, and S. Voutsinas. The VLT Survey Telescope ATLAS. *MNRAS*, 451:4238–4252, August 2015. doi: 10.1093/mnras/stv1130. 188

R. K. Sheth and G. Tormen. Large-scale bias and the peak background split. *MNRAS*, 308:119–126, September 1999. doi: 10.1046/j.1365-8711.1999.02692.x. 5

M. Sikora, M. Błażejowski, M. C. Begelman, and R. Moderski. Modeling the Production of Flares in Gamma-Ray Quasars. *ApJ*, 554:1–11, June 2001. doi: 10.1086/321329. 10

J. Silk. Feedback in Galaxy Formation. In C. Carignan, F. Combes, and K. C. Freeman, editors, *IAU Symposium*, volume 277 of *IAU Symposium*, pages 273–281, December 2011. doi: 10.1017/S1743921311022939. 6

J. Silk. Unleashing Positive Feedback: Linking the Rates of Star Formation, Supermassive Black Hole Accretion, and Outflows in Distant Galaxies. *ApJ*, 772:112, August 2013. doi: 10.1088/0004-637X/772/2/112. 14

J. Silk and G. A. Mamon. The current status of galaxy formation. *Research in Astronomy and Astrophysics*, 12:917–946, August 2012. doi: 10.1088/1674-4527/12/8/004. 6, 181

J. Silk and M. J. Rees. Quasars and galaxy formation. *A&A*, 331:L1–L4, March 1998. 5

J. D. Silverman, F. Lamareille, C. Maier, S. J. Lilly, V. Mainieri, M. Brusa, N. Cappelluti, G. Hasinger, G. Zamorani, M. Scodeggio, M. Bolzonella, T. Contini, C. M. Carollo, K. Jahnke, J.-P. Kneib, O. Le Fèvre, A. Merloni, S. Bardelli, A. Bongiorno, H. Brunner, K. Caputi, F. Civano, A. Comastri, G. Coppa, O. Cucciati, S. de la Torre, L. de Ravel, M. Elvis, A. Finoguenov, F. Fiore, P. Franzetti, B. Garilli, R. Gilli, A. Iovino,

P. Kampczyk, C. Knobel, K. Kovač, J.-F. Le Borgne, V. Le Brun, M. Mignoli, R. Pello, Y. Peng, E. Perez Montero, E. Ricciardelli, M. Tanaka, L. Tasca, L. Tresse, D. Vergani, C. Vignali, E. Zucca, D. Bottini, A. Cappi, P. Cassata, M. Fumana, R. Griffiths, J. Kartaltepe, A. Koekemoer, C. Marinoni, H. J. McCracken, P. Memeo, B. Meneux, P. Oesch, C. Porciani, and M. Salvato. Ongoing and Co-Evolving Star Formation in zCOSMOS Galaxies Hosting Active Galactic Nuclei. *ApJ*, 696:396–410, May 2009. doi: 10.1088/0004-637X/696/1/396. 27

C. Simpson, A. Martínez-Sansigre, S. Rawlings, R. Ivison, M. Akiyama, K. Sekiguchi, T. Takata, Y. Ueda, and M. Watson. Radio imaging of the Subaru/XMM-Newton Deep Field - I. The 100-μJy catalogue, optical identifications, and the nature of the faint radio source population. *MNRAS*, 372:741–757, October 2006. doi: 10.1111/j.1365-2966.2006.10907.x. 22, 23, 29, 182

D. J. B. Smith, M. J. Hardcastle, M. J. Jarvis, S. J. Maddox, L. Dunne, D. G. Bonfield, S. Eales, S. Serjeant, M. A. Thompson, M. Baes, D. L. Clements, A. Cooray, G. De Zotti, J. Gonzàlez-Nuevo, P. van der Werf, J. Virdee, N. Bourne, A. Dariush, R. Hopwood, E. Ibar, and E. Valiante. Isothermal dust models of Herschel-ATLAS galaxies. *MNRAS*, 436:2435–2453, December 2013. doi: 10.1093/mnras/stt1737. 152, 159

D. J. B. Smith, M. J. Jarvis, M. J. Hardcastle, M. Vaccari, N. Bourne, L. Dunne, E. Ibar, N. Maddox, M. Prescott, C. Vlahakis, S. Eales, S. J. Maddox, M. W. L. Smith, E. Valiante, and G. de Zotti. The temperature dependence of the far-infrared-radio correlation in the Herschel-ATLAS. *MNRAS*, 445:2232–2243, December 2014. doi: 10.1093/mnras/stu1830. 165, 166

V. Smolčić, E. Schinnerer, M. Scodeggio, P. Franzetti, H. Aussel, M. Bondi, M. Brusa, C. L. Carilli, P. Capak, S. Charlot, P. Ciliegi, O. Ilbert, Ž. Ivezić, K. Jahnke, H. J. McCracken, M. Obrić, M. Salvato, D. B. Sanders, N. Scoville, J. R. Trump, C. Tremonti, L. Tasca, C. J. Walcher, and G. Zamorani. A New Method to Separate Star-forming from AGN Galaxies at Intermediate Redshift: The Submillijansky Radio Population in the VLA-COSMOS Survey. *ApJS*, 177:14–38, July 2008. doi: 10.1086/588028. 23, 182

V. Smolčić, P. Padovani, J. Delhaize, I. Prandoni, N. Seymour, M. Jarvis, J. Afonso,

M. Magliocchetti, M. Huynh, M. Vaccari, and A. Karim. Exploring AGN Activity over Cosmic Time with the SKA. *Advancing Astrophysics with the Square Kilometre Array (AASKA14)*, art. 69, 2015. 188

V. Springel, S. D. M. White, A. Jenkins, C. S. Frenk, N. Yoshida, L. Gao, J. Navarro, R. Thacker, D. Croton, J. Helly, J. A. Peacock, S. Cole, P. Thomas, H. Couchman, A. Evrard, J. Colberg, and F. Pearce. Simulations of the formation, evolution and clustering of galaxies and quasars. *Nature*, 435:629–636, June 2005. doi: 10.1038/nature03597. 4

A. T. Steffen, A. J. Barger, L. L. Cowie, R. F. Mushotzky, and Y. Yang. The Changing Active Galactic Nucleus Population. *ApJL*, 596:L23–L26, October 2003. doi: 10.1086/379142. 6

D. Stern, P. Eisenhardt, V. Gorjian, C. S. Kochanek, N. Caldwell, D. Eisenstein, M. Brodwin, M. J. I. Brown, R. Cool, A. Dey, P. Green, B. T. Jannuzi, S. S. Murray, M. A. Pahre, and S. P. Willner. Mid-Infrared Selection of Active Galaxies. *ApJ*, 631:163–168, September 2005. doi: 10.1086/432523. 43, 44, 185

A. Tchekhovskoy, R. Narayan, and J. C. McKinney. Efficient generation of jets from magnetically arrested accretion on a rapidly spinning black hole. *MNRAS*, 418:L79–L83, November 2011. doi: 10.1111/j.1745-3933.2011.01147.x. 68

A. R. Thompson. Fundamentals of Radio Interferometry. In G. B. Taylor, C. L. Carilli, and R. A. Perley, editors, *Synthesis Imaging in Radio Astronomy II*, volume 180 of *Astronomical Society of the Pacific Conference Series*, page 11, 1999. 90

E. Treister, J. H. Krolik, and C. Dullemond. Measuring the Fraction of Obscured Quasars by the Infrared Luminosity of Unobscured Quasars. *ApJ*, 679:140–148, May 2008. doi: 10.1086/586698. 184

Y. Ueda, M. Akiyama, K. Ohta, and T. Miyaji. Cosmological Evolution of the Hard X-Ray Active Galactic Nucleus Luminosity Function and the Origin of the Hard X-Ray Background. *ApJ*, 598:886–908, December 2003. doi: 10.1086/378940. 25, 181

J. S. Ulvestad, R. R. J. Antonucci, and R. Barvainis. VLBA Imaging of Central Engines in Radio-Quiet Quasars. *ApJ*, 621:123–129, March 2005. doi: 10.1086/427426. 187

C. M. Urry and P. Padovani. Unified Schemes for Radio-Loud Active Galactic Nuclei. *PASP*, 107:803, September 1995. doi: 10.1086/133630. 11

S. van Velzen and H. Falcke. The contribution of spin to jet-disk coupling in black holes. *A&A*, 557:L7, September 2013. doi: 10.1051/0004-6361/201322127. 20

T. Vernstrom, D. Scott, J. V. Wall, J. J. Condon, W. D. Cotton, E. B. Fomalont, K. I. Kellermann, N. Miller, and R. A. Perley. Deep 3 GHz number counts from a P(D) fluctuation analysis. *MNRAS*, 440:2791–2809, May 2014. doi: 10.1093/mnras/stu470. 186

M. Vestergaard. Determining Central Black Hole Masses in Distant Active Galaxies. *ApJ*, 571:733–752, June 2002. doi: 10.1086/340045. 73

M. Vestergaard and P. S. Osmer. Mass Functions of the Active Black Holes in Distant Quasars from the Large Bright Quasar Survey, the Bright Quasar Survey, and the Color-selected Sample of the SDSS Fall Equatorial Stripe. *ApJ*, 699:800–816, July 2009. doi: 10.1088/0004-637X/699/1/800. 74

M. Volonteri, M. Sikora, and J.-P. Lasota. Black Hole Spin and Galactic Morphology. *ApJ*, 667:704–713, October 2007. doi: 10.1086/521186. 20

A. Wandel, B. M. Peterson, and M. A. Malkan. Central Masses and Broad-Line Region Sizes of Active Galactic Nuclei. I. Comparing the Photoionization and Reverberation Techniques. *ApJ*, 526:579–591, December 1999. doi: 10.1086/308017. 73

S. J. Warren, P. C. Hewett, and C. B. Foltz. The KX method for producing K-band flux-limited samples of quasars. *MNRAS*, 312:827–832, March 2000. doi: 10.1046/j.1365-8711.2000.03206.x. 35

R. B. Wayth, E. Lenc, M. E. Bell, J. R. Callingham, K. S. Dwarakanath, T. M. O. Franzen, B.-Q. For, B. Gaensler, P. Hancock, L. Hindson, N. Hurley-Walker, C. A.

Jackson, M. Johnston-Hollitt, A. D. Kapińska, B. McKinley, J. Morgan, A. R. Offringa, P. Procopio, L. Staveley-Smith, C. Wu, Q. Zheng, C. M. Trott, G. Bernardi, J. D. Bowman, F. Briggs, R. J. Cappallo, B. E. Corey, A. A. Deshpande, D. Emrich, R. Goeke, L. J. Greenhill, B. J. Hazelton, D. L. Kaplan, J. C. Kasper, E. Kratzenberg, C. J. Lonsdale, M. J. Lynch, S. R. McWhirter, D. A. Mitchell, M. F. Morales, E. Morgan, D. Oberoi, S. M. Ord, T. Prabu, A. E. E. Rogers, A. Roshi, N. U. Shankar, K. S. Srivani, R. Subrahmanyan, S. J. Tingay, M. Waterson, R. L. Webster, A. R. Whitney, A. Williams, and C. L. Williams. GLEAM: The GaLactic and Extragalactic All-Sky MWA Survey. *PASA*, 32:e025, June 2015. doi: 10.1017/pasa.2015.26. 188

K. E. Whitaker, P. G. van Dokkum, G. Brammer, and M. Franx. The Star Formation Mass Sequence Out to z = 2.5. *ApJL*, 754:L29, August 2012. doi: 10.1088/2041-8205/754/2/L29. 76, 77, 161

R. L. White, R. H. Becker, D. J. Helfand, and M. D. Gregg. A Catalog of 1.4 GHz Radio Sources from the FIRST Survey. *ApJ*, 475:479, February 1997. doi: 10.1086/303564. 62, 84, 187

V. Wild, T. Heckman, and S. Charlot. Timing the starburst-AGN connection. *MNRAS*, 405:933–947, June 2010. doi: 10.1111/j.1365-2966.2010.16536.x. 184

P. Wilkinson. The SKA and the Unknown Unknowns. In *Advancing Astrophysics with the Square Kilometre Array*. Proceedings of Science, 2014. 189

P. N. Wilkinson, A. K. Tzioumis, J. M. Benson, R. C. Walker, R. S. Simon, and F. D. Kahn. A disrupted radio jet inside the host galaxy of the quasar 3C48. *Nature*, 352: 313–315, July 1991. doi: 10.1038/352313a0. 106

C. J. Willott, S. Rawlings, K. M. Blundell, and M. Lacy. The emission line-radio correlation for radio sources using the 7C Redshift Survey. *MNRAS*, 309:1017–1033, November 1999. doi: 10.1046/j.1365-8711.1999.02907.x. 72

R. J. Wilman, L. Miller, M. J. Jarvis, T. Mauch, F. Levrier, F. B. Abdalla, S. Rawlings, H.-R. Klöckner, D. Obreschkow, D. Olteanu, and S. Young. A semi-empirical simulation of the extragalactic radio continuum sky for next generation radio telescopes. *MNRAS*, 388:1335–1348, August 2008. doi: 10.1111/j.1365-2966.2008.13486.x. 23, 27, 69, 71, 72, 82, 182, 185

R. J. Wilman, M. J. Jarvis, T. Mauch, S. Rawlings, and S. Hickey. An infrared-radio simulation of the extragalactic sky: from the Square Kilometre Array to Herschel. *MNRAS*, 405:447–461, June 2010. doi: 10.1111/j.1365-2966.2010.16453.x. 69

A. S. Wilson and E. J. M. Colbert. The difference between radio-loud and radio-quiet active galaxies. *ApJ*, 438:62–71, January 1995. doi: 10.1086/175054. 20

Thomas L. Wilson, Kristen. Rohlfs, and Susanne. Hüttemeister. *Tools of Radio Astronomy*. Springer Berlin Heidelberg,, Berlin, Heidelberg :, 2009. 95

C. Wolf, L. Wisotzki, A. Borch, S. Dye, M. Kleinheinrich, and K. Meisenheimer. The evolution of faint AGN between z =˜ 1 and z =˜ 5 from the COMBO-17 survey. *A&A*, 408:499–514, September 2003. doi: 10.1051/0004-6361:20030990. 25

L. Woltjer. Emission Nuclei in Galaxies. *ApJ*, 130:38, July 1959. doi: 10.1086/146694. 8

C. Xu, M. Livio, and S. Baum. Radio-loud and Radio-quiet Active Galactic Nuclei. *AJ*, 118:1169–1176, September 1999. doi: 10.1086/301007. 9

X. Yang, H. J. Mo, and F. C. van den Bosch. Constraining galaxy formation and cosmology with the conditional luminosity function of galaxies. *MNRAS*, 339:1057–1080, March 2003. doi: 10.1046/j.1365-8711.2003.06254.x. 5

H. K. C. Yee and R. F. Green. An imaging survey of fields around quasars. II - The association of galaxies with quasars. *ApJ*, 280:79–90, May 1984. doi: 10.1086/161969. 173

D. G. York, J. Adelman, J. E. Anderson, Jr., S. F. Anderson, J. Annis, N. A. Bahcall, J. A. Bakken, R. Barkhouser, S. Bastian, E. Berman, W. N. Boroski, S. Bracker, C. Briegel, J. W. Briggs, J. Brinkmann, R. Brunner, S. Burles, L. Carey, M. A. Carr, F. J. Castander, B. Chen, P. L. Colestock, A. J. Connolly, J. H. Crocker, I. Csabai, P. C. Czarapata, J. E. Davis, M. Doi, T. Dombeck, D. Eisenstein, N. Ellman, B. R. Elms, M. L. Evans, X. Fan, G. R. Federwitz, L. Fiscelli, S. Friedman, J. A. Frieman,

M. Fukugita, B. Gillespie, J. E. Gunn, V. K. Gurbani, E. de Haas, M. Haldeman, F. H. Harris, J. Hayes, T. M. Heckman, G. S. Hennessy, R. B. Hindsley, S. Holm, D. J. Holmgren, C.-h. Huang, C. Hull, D. Husby, S.-I. Ichikawa, T. Ichikawa, Ž. Ivezić, S. Kent, R. S. J. Kim, E. Kinney, M. Klaene, A. N. Kleinman, S. Kleinman, G. R. Knapp, J. Korienek, R. G. Kron, P. Z. Kunszt, D. Q. Lamb, B. Lee, R. F. Leger, S. Limmongkol, C. Lindenmeyer, D. C. Long, C. Loomis, J. Loveday, R. Lucinio, R. H. Lupton, B. MacKinnon, E. J. Mannery, P. M. Mantsch, B. Margon, P. McGehee, T. A. McKay, A. Meiksin, A. Merelli, D. G. Monet, J. A. Munn, V. K. Narayanan, T. Nash, E. Neilsen, R. Neswold, H. J. Newberg, R. C. Nichol, T. Nicinski, M. Nonino, N. Okada, S. Okamura, J. P. Ostriker, R. Owen, A. G. Pauls, J. Peoples, R. L. Peterson, D. Petravick, J. R. Pier, A. Pope, R. Pordes, A. Prosapio, R. Rechenmacher, T. R. Quinn, G. T. Richards, M. W. Richmond, C. H. Rivetta, C. M. Rockosi, K. Ruthmansdorfer, D. Sandford, D. J. Schlegel, D. P. Schneider, M. Sekiguchi, G. Sergey, K. Shimasaku, W. A. Siegmund, S. Smee, J. A. Smith, S. Snedden, R. Stone, C. Stoughton, M. A. Strauss, C. Stubbs, M. SubbaRao, A. S. Szalay, I. Szapudi, G. P. Szokoly, A. R. Thakar, C. Tremonti, D. L. Tucker, A. Uomoto, D. Vanden Berk, M. S. Vogeley, P. Waddell, S.-i. Wang, M. Watanabe, D. H. Weinberg, B. Yanny, N. Yasuda, and SDSS Collaboration. The Sloan Digital Sky Survey: Technical Summary. *AJ*, 120:1579–1587, September 2000. doi: 10.1086/301513. 31

M. S. Yun, N. A. Reddy, and J. J. Condon. Radio Properties of Infrared-selected Galaxies in the IRAS 2 Jy Sample. *ApJ*, 554:803–822, June 2001. doi: 10.1086/323145. 76, 78, 160

N. L. Zakamska and J. E. Greene. Quasar feedback and the origin of radio emission in radio-quiet quasars. *MNRAS*, 442:784–804, July 2014. doi: 10.1093/mnras/stu842. 27, 183

J. T. L. Zwart, M. Santos, and M. J. Jarvis. Far beyond stacking: Fully bayesian constraints on sub-microJy radio source populations over the XMM-LSS-VIDEO field. *ArXiv e-prints*, March 2015. 186